UNIVERSITÉ DE GENÈVE

Département de Physique
Nucléaire et Corpusculaire

FACULTÉ DES SCIENCES
Dr. Alessandro Bravar

Development, Construction, and Characterization of a Timing Detector based on Scintillating Fibers with Silicon Photomultiplier readout for the Mu3e Experiment at PSI

THÈSE

Présentée à la Faculté des sciences de l'Université de Genève
Pour obtenir le grade de Docteur ès sciences, mention physique

Par

Yannick DEMETS

de

Kortrijk (Belgique)

Thèse N°5817

GENÈVE
Atelier d'impression ReproMail
2024

UNIVERSITÉ DE GENÈVE

FACULTÉ DES SCIENCES

DOCTORAT ÈS SCIENCES, MENTION PHYSIQUE

Thèse de Monsieur Yannick DEMETS

intitulée :

«Development, Construction, and Characterization of a Timing Detector based on Scintillating Fibers with Silicon Photomultiplier readout for the Mu3e Experiment at PSI»

La Faculté des sciences, sur le préavis de

Monsieur A. BRAVAR, docteur et directeur de thèse
Département de physique nucléaire et corpusculaire

Monsieur D. DELLA VOLPE, professeur associé
Département de physique nucléaire et corpusculaire

Monsieur C. GRAB, professeur
Department de physique, Ecole polytechnique fédérale de Zurich (EPFZ),
Zurich, Suisse

autorise l'impression de la présente thèse, sans exprimer d'opinion sur les propositions qui y sont énoncées.

Genève, le 30 avril 2024

Thèse - 5817 -

La Doyenne

N.B. - La thèse doit porter la déclaration précédente et remplir les conditions énumérées dans les "Informations relatives aux thèses de doctorat à l'Université de Genève".

ABSTRACT

The Mu3e experiment is designed to search for the rare charged lepton flavor violating muon decay $\mu^+ \to e^+e^-e^+$. The goal is to observe this decay, if its branching fraction is larger than 10^{-16}, or to exclude it. Since this process is heavily suppressed in the Standard Model of particle physics, observing this decay would be a clear indication of new physics. The experiment, located at the Paul Scherrer Institute (PSI) in Villigen (Switzerland), will use the most intense continuous surface muon beam in the world to produce the muons at a rate of 10^8 muons per second. To achieve this goal, the detector requires wide acceptance, good momemtum and vertex resolution, as well as precise timing information. This experiment is based on thin high-voltage monolithic active silicon pixel sensors (HV-MAPS) for precise tracking in conjuction with a scintillating fiber (SciFi) and a tile detector for precise timing information.

This thesis presents the work done in the development of the SciFi detector, one of the timing detectors of the Mu3e experiment. Different 250 µm diameter round scintillating fibers have been studied and compared, with a primary focus on their timing performances. The NOL-11 fiber has the best timing with a time resolution of $\simeq$250 ps. Additionally, the importance of maximizing the number of detected photons to enhance the timing performance of the fibers is discussed. The mean time analysis further demonstrated as a reliable time measurement observable, independent of the particle's crossing point.

Next, the performance of the SciFi detector with different scintillating fiber ribbons and configurations has been studied. In the study, a time resolution of 245 ps with an efficiency of 97% has been achieved with a 3-layer ribbon using SCSF-78 fibers assembled with black epoxy. Further studies have shown that the addition of a fourth layer of fibers to the ribbon improved the time resolution by around 15%. Other studies are also presented, such as the effect on the time resolution and the efficiency when the number of fiber layers or the crossing angle change.

Moreover the development of the latest SciFi readout board, SciFi Module Board (SMB), is presented. The SMB is designed to host 4 MuTRiGv3 ASICs within a compact size due to space limitations in the Mu3e experiment. A description of the design, components and integration process of the SMB into the SciFi detector are provided. A description of the calibration and verification procedures to ensure the proper functioning of the SMB are also outlined. The MuTRiG ASICs are also detailed and characterized with additional studies.

In summary, this thesis significantly contributes to understanding the potential of the SciFi detector in high-precision, high-rate particle physics experiments like the Mu3e experiment. It identifies key areas for optimization in scintillating fibers and detectors, setting a basis for future enhancements.

RÉSUMÉ

L'expérience Mu3e est conçue pour l'étude de la violation de saveur des leptons chargés dans la désintégration $\mu^+ \to e^+e^-e^+$. L'objectif est d'observer cette désintégration ou de l'exclure. Puisque ce processus est fortement réprimé dans le Modèle Standard de la physique des particules, observer cette désintégration serait un signe pour de nouvelle physique. L'expérience, située à l'institut Paul Scherrer (PSI) à Villigen (Suisse), utilisera le faisceau de muons de surface continu le plus intense du monde pour produire des muons à un taux de 10^8 muons par seconde. Pour atteindre cet objectif, le détecteur nécessite une large acceptation, une bonne résolution d'impulsion et de vertex d'interactions, et des informations temporelles précises. Ce détecteur est basée sur des pixels en silicium (HV-MAPS) pour un suivi de trajectoire des particules, en conjonction avec un détecteur à fibres scintillantes (SciFi) et un détecteur en tuiles scintillantes pour des informations de temporel précises.

Cette thèse présente le travail effectué dans le développement du détecteur à fibres scintillantes de l'expérience Mu3e. Différentes fibres scintillantes rondes de diamètre 250 µm ont été étudiées et comparées, en se concentrant principalement sur leurs performances temporelles. La fibre NOL-11 présente la meilleure résolution temporelle d'environ 250 ps. De plus, l'importance de maximiser le nombre de photons détectés pour améliorer la performance temporelle des fibres est discuté. L'analyse du temps moyen a également été démontré comme un observable de mesure de temps fiable, indépendant du point de croisement de la particule.

Ensuite, la performance du détecteur avec différentes configurations et rubans de fibres scintillantes a été étudiée. Dans l'étude, une résolution temporelle de 245 ps avec une efficacité de 97% a été atteinte avec un ruban de 3 couches utilisant des fibres SCSF-78 assemblées avec de l'époxy noir. De plus, les études ont montré que l'ajout d'une quatrième couche de fibres au ruban améliore la résolution temporelle d'environ 15%. D'autres études sont également présentées, telles que l'effet sur la résolution temporelle et l'efficacité lorsque le nombre de couches de fibres ou l'angle de croisement change.

De plus, la mise au point de la dernière carte de lecture SciFi, le SciFi Module Board (SMB), est présentée. Elle est conçu pour accueillir 4 ASICs MuTRiGv3 dans un format compact et répond aux contraintes d'espace de l'expérience Mu3e. Une description du design, des composants et du processus d'intégration du SMB dans le détecteur sont fournis. Une description des procédures de calibration et de vérification pour assurer le bon fonctionnement du SMB est également décrite. Les ASICs MuTRiG sont aussi détaillés et caractérisés par des études supplémentaires.

En résumé, cette thèse contribue de manière significative à la compréhension du potentiel des détecteurs à fibres scintillantes dans des expériences de physique des particules à haute précision et à haut taux, comme l'expérience Mu3e. Elle identifie les domaines clés pour l'optimisation des fibres scintillantes et des détecteurs, posant ainsi une base solide pour les améliorations futures.

ACKNOWLEDGMENTS

The completion of this thesis would not have been possible without the support and encouragement of many people. This part is the hardest to write as words can only express a fraction of the gratitude I feel.

I would like to express my sincere gratitude to Alessandro Bravar for his guidance and support throughout my PhD. He made it possible for me to work on the Mu3e experiment, and with his expertise and knowledge, he helped me shape my research and academic growth. Additionally, I thank Domenico Della Volpe and Christoph Grab for being my co-examiners.

I would like to thank the SciFi group members and everyone in the Mu3e collaboration for all the help and support. Their collaboration is greatly appreciated. Special thanks to Lukas, Cristina, and Annarita, with whom we shared many test beam days and helped me during the journey. Thanks to Konrad, who helped me and provided me with valuable advice and expertise. Also, thanks to Yifeng, Robert, Benjamin, and Gentian for their help and contributions to the SciFi group. Also, special thanks to Marius, Martin, Alex, and Nik for their valuable insights on the data acquisition system.

I would like to thank all the people from the DPNC at the University of Geneva, without whom this work would not have been possible. A special thank you to Franck Cadoux for all his work and help with the test beams and SciFi mechanics. Also, a thank you to Coralie, Sylvain, and Laurent for their work in the mechanical workshop. I thank the electronic engineers Daniel La Marra and Stéphane Débieux for their help in the development of the readout boards and for giving me answers to all the questions I had. I would also like to thank Gabi and Javier for their work on all things electronic related. Thank you to Philipp Azzarello for teaching me how to use the probing stations and giving me knowledge about SiPM arrays. I would like to thank the secretaries, especially Liliane and Nathalie, for all their help regarding the administrative work. Also, I would like to thank Yann for all the IT-related help and support. Personally, I would like to express my sincere appreciation to the entire DPNC for fostering a collaborative, supportive, and positive work environment. I firmly believe that this positive and humanistic atmosphere plays a pivotal role in the success of all projects undertaken within the DPNC. Please maintain this atmosphere.

Of course, I could not forget all the physicists and friends that are at the DPNC, with whom I shared great moments. A good part of the positive atmosphere at the DPNC is due to these people. Special thanks to Robert, Benjamin, Gentian, Lorenzo, Dana, Svetlana, Vedantha, Mathias, Emanuele, Stefania, Adrien, Nicolas, Enzo, Pokhee, Caspar, Thanh, Saba, Stéphanie, Marco, Sergio, Matthieu and Leïla for their company and friendship.

Finally, I would like to thank my friends who knew me already all those years during my life here in Geneva. I would like to thank my family for their support and encouragement throughout my life. I guess acts of kindness and love speak louder than words, and the support and love I receive are, I hope, a reflection of my positive attitude and love I always try to keep in work and in everyday life. L&R

CONTENTS

LIST OF FIGURES

LIST OF TABLES

1 CHARGED LEPTON FLAVOR VIOLATION

The Standard Model (SM) of particle physiscs is a sophisticated theory that unites our present understanding of elementary particles and their interactions. While it has proven to be astonishingly accurate in predicting a multitude of experimental observations, it is still an incomplete theory. The SM falls short in explaining several phenomena, including neutrino masses, gravitational interactions, and matter-antimatter asymmetry. In order to construct more comprehensive models, scientists are conducting experiments to investigate futher, in search for new physics.

This chapter presents a brief overview of the SM with some hints to new physics. Introdusing in the discussion charge lepton violation as new physics and presenting the main experiments exploring this field.

1.1 THE STANDARD MODEL

The Standard Model of particle physics is a quantum field theory describing the known constituents of our universe, that make up matter and their interactions. It is a single theory[1], that explains how three of the four fundamental forces in the universe (electromagnetic, weak, and strong) interact with matter [1]. The last force, gravity, cannot be consistently unified with any renormalizable quantum field theory and therefore, at present, is excluded from the SM model. Gravity, as described by Einstein's theory of General Relativity, presents a classical framework that contrasts sharply with the quantum nature of the other forces [2]. This divergence highlights the ongoing quest for a quantum theory of gravity, with approaches like String Theory and Loop Quantum Gravity being prominent [3]. Furthermore, phenomena such as black holes and gravitational waves, offer unique insights into extreme gravitational conditions and potential quantum effects. Gravity's role in cosmology, particularly regarding dark energy and dark matter, underscores its importance in the universe's evolution [4, 5]. The black hole information paradox and experimental efforts to detect gravitons or observe quantum effects in macroscopic objects further reflects the complexities in integrating gravity with quantum mechanics [5]. These challenges expands the frontier of theoretical physics, where the reconciliation of gravity with quantum field theory remains an elusive yet fundamental goal.

Despite the absence of gravity, the SM is a remarkably successful theory. It describes three of the four fundamental interactions known in physics, each mediated by their respective gauge bosons. In a more specific and mathematical framework, the SM is represented by a gauge theory with the symmetry group $SU(3)_C \times SU(2)_L \times U(1)_Y$.

1 Striclty speaking it is a single Lagrangian

The electromagnetic interaction is described by Quantum Electrodynamics (QED). QED is a theory that combines quantum mechanics with the classical theory of electromagnetism. It explains how light and matter interact and is the first theory in which full agreement between quantum mechanics and special relativity is achieved. In QED, photons (γ) are the force carriers that mediate electromagnetic forces between electrically charged particles. This force not only governs the structure and dynamics of atoms but also underlies the vast array of electromagnetic phenomena in the universe, from visible light to radio waves [1].

The weak force is described by the theory of Electroweak interaction, which unifies the weak force with electromagnetism. This unification represented the first successful merging of two fundamental forces under the same theoretical framework. This theory was a groundbreaking step in particle physics, predicting also the existence of the W^+,W^- and Z^0 bosons, particles that were later experimentally confirmed [6]. The Electroweak Theory is particularly notable for its role in explaining processes like beta decay, a type of radioactive decay in which a neutron in an atomic nucleus is transformed into a proton [1]. Here the symmetry group $\mathrm{SU}(2)_\mathrm{L} \times \mathrm{U}(1)_\mathrm{Y}$ corresponds to the Electroweak interaction. $\mathrm{SU}(2)_\mathrm{L}$ represents the weak isospin symmetry, where L indicates that this symmetry applies only to left-handed particles and right-handed antiparticles. This part of the group structure is crucial for understanding the weak force and its chiral nature. On the other hand, $\mathrm{U}(1)_\mathrm{Y}$ denotes the weak hypercharge, a quantum number that, along with weak isospin, defines the electromagnetic and weak interactions properties.

Quantum Chromodynamics (QCD) is the theory that describes the strong force. QCD is a part of the Standard Model that deals with the interactions between quarks and gluons (g), the particles responsible for mediating the strong force. This theory explains how quarks are bound together to form protons, neutrons, and other hadrons and is essential for understanding the structure of the atomic nucleus. The strong force, as explained by QCD, is characterized by the property of color charge and the phenomenon of confinement, which prevents the isolation of individual quarks [1]. The $\mathrm{SU}(3)_\mathrm{C}$ part of the gauge group represents the theory of QCD. In this context, $\mathrm{SU}(3)$ refers to the special unitary group of degree 3 which is a Lie group of 3×3 unitary matrices with determinant equal to 1 [7]. This Lie group reflects the symmetry properties of the strong force, specifically the way quarks change under transformations related to color charge, the property responsible for the strong force. The subscript C stands for color, indicating the type of charge carried by quarks and gluons, the mediator particles of the strong force.

The $\mathrm{SU}(2)_\mathrm{L} \times \mathrm{U}(1)_\mathrm{Y}$ symmetry is spontaneously broken by the Higgs mechanism, resulting in the W^+ and W^- and Z^0 bosons acquiring non-zero masses [8]. This process is important as it explains how these gauge bosons, which mediate the weak force, become massive. A direct consequence of the Higgs mechanism is the existence of the Higgs boson itself, a particle that was the final piece of the Standard Model puzzle to be experimentally confirmed. This landmark discovery occurred in 2012 at the Large Hadron Collider (LHC) [9, 10]. Furthermore, the Higgs mechanism is essential for giving mass to fermions. Through Yukawa interactions, fermion fields interact with the

Higgs field, acquiring mass. This aspect of the Higgs field is crucial, as it provides a comprehensive explanation for the mass properties of fundamental particles.

Fermions, with spin 1/2, are categorized into quarks and leptons, further divided into three generations:

- 1^{st} generation: up (u) and down (d) quarks, electron (e) and electron neutrino (ν_e).
- 2^{nd} generation: charm (c) and strange (s) quarks, muon (μ) and muon neutrino (ν_μ).
- 3^{rd} generation: top (t) and bottom (b) quarks, tau (τ) and tau neutrino (ν_τ).

The mass increases with each generation. Quarks interact via all four fundamental forces, while leptons, lacking color charge, interact through weak, electromagnetic, and gravitational forces. Each of the so called upper quarks - namely the u, c, and t quarks - possesses an electric charge $+2/3$e. In contrast, the lower quarks, which include the d, s, and b quarks, have an electric charge of $-1/3$e. Additionally, in the realm of leptons, there is a clear differentiation based on electric charge. Charged leptons, such as the electron, muon, and tau, carry a charge of -1e. In contrast, neutral leptons, the electron neutrino, muon neutrino, and tau neutrino, bear no electric charge.

The absence of observed transitions between leptons of different generations in the SM inspired the introduction of the lepton flavor (LF) number [11]. Consequently, lepton flavor numbers for each generation (L_e, L_μ, L_τ) are assigned values of $+1$ to negatively charged leptons and neutrinos, -1 to their corresponding antiparticles, and 0 to all other particles.

1.2 LEPTON FLAVOR VIOLATION

Lepton flavor does not emerge as a fundamental conserved quantity in the SM, while most of the other quantum numbers do. The experimental observation of neutrino oscillations, where neutrinos change between different flavors (electron, muon, and tau), is a clear violation of lepton flavor conservation. This phenomenon contradicts the original SM framework that treated neutrinos as massless particles.

1.2.1 *Neutrino Oscillation and Mixing Matrices*

Despite their initial classification as massless particles in the SM, where they are inherently massless by design, neutrino oscillations provide concrete evidence that neutrinos actually have mass. This phenomenon involves a neutrino created with a specific lepton flavor (electron, muon, or tau) later being detected with a different flavor. In this context, the SM has been expanded and is more referred to as the νSM.

Central to this is the Pontecorvo-Maki-Nakagawa-Sakata (PMNS) matrix, analogous to the CKM matrix for quarks. The PMNS matrix, U_{li} (l = e, μ, τ; i = 1, 2, 3), describes neutrino mixing between flavor and mass states. It translates the probability of a neutrino's mass state detection as a specific flavor. Neutrinos exist in mass eigenstates

(ν_1, ν_2, ν_3) and flavor eigenstates (ν_e, ν_μ, ν_τ), where mass eigenstates have definite mass, and flavor eigenstates relate to neutrino production and detection via weak interactions. The PMNS matrix links these states, allowing flavor oscillation during their journey.

The discovery of neutrino oscillation and the PMNS matrix's development have significant implications. They confirm non-zero neutrino masses and non-degenerate mass eigenstates, with ongoing research to determine their exact values. First suggested by the solar neutrino problem and confirmed by experiments on atmospheric, reactor neutrinos and in accelerators, neutrino oscillation aligns with the disappearance of muon neutrinos and appearance of tau neutrinos, supporting the theory [12, 13].

1.2.2 *Charged lepton flavor violation*

Within the Standard Model, charged lepton flavor violation (cLFV) processes are forbidden at tree level but can occur in higher order processes due to neutrino oscillations, see Figure 1.1. In other words, the νSM[1] theoretically allows for cLFV processes. However, the branching ratios, seen in equation 1.1, for such processes (e.g., $\mu^+ \to e^+\gamma$ or $\mu^+ \to e^+e^-e^+$) are extremely small, making them practically unobservable with current experimental capabilities.

$$B_{SM}(\mu^+ \to e^+e^-e^+) \sim B_{SM}(\mu^+ \to e^+\gamma) \propto \left| \sum_{2,3} U^*_{\mu i} U_{ei} \frac{\Delta m^2_{i1}}{\Delta m^2_W} \right|^2 < 10^{-54} \tag{1.1}$$

This extreme suppression is due to the tiny neutrino mass differences and the absence of tree-level flavor-changing neutral currents.

The current experimental sensitivity to cLFV processes is orders of magnitude lower than the predictions within νSM. This gap highlights the challenge of observing cLFV experimentally and is practically impossible with current experimental capabilities. Alternatively, this gap might hint at the need for new theoretical frameworks that predict higher rates of cLFV, more accessible to experimental observation.

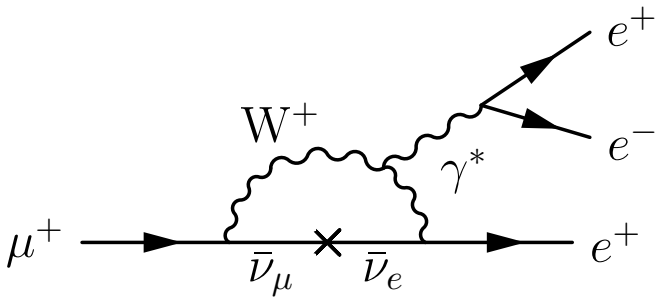

Figure 1.1: Diagram showing the decay $\mu^+ \to e^+e^-e^+$ via neutrino oscillation leading to cLFV.

1 refers to the extended SM with neutrino oscillation

1.2.3 *Beyond the Standard Model*

While the Standard Model has been incredibly successful in explaining a wide array of particle interactions, it shows signs of incompleteness, especially in the context of cosmological phenomena. For instance, cosmological studies, such as those examining the universe's expansion and the Cosmic Microwave Background (CMB), suggest that the majority of the universe's mass-energy composition, including dark matter and dark energy, cannot be explained by the SM particles. These inconsistencies, alongside unanswered questions about the specific characteristics of neutrino masses and the number of fermion generations, underscore the limitations of the SM and the necessity for new theories beyond the Standard Model (BSM).

The search for new physics beyond the SM involves diverse experimental strategies. One approach, shown at the Large Hadron Collider (LHC), seeks to directly discover new particles by colliding protons at very high energies, up to 13 TeV. This direct approach contrasts with more precision-oriented strategies, which focus on detecting subtle deviations from the SM's predictions. These deviations, although small, could indicate the presence of new physics at energy scales that are currently beyond the capabilities of existing colliders.

Some BSM theories suggest that cLFV could emerge naturally if there are supersymmetric particles, as in left of Figure 1.2, or new types of interactions like on the right of Figure 1.2 [14]. Such theories lead to various lepton flavor violating processes, each offering potential clues to new discoveries.

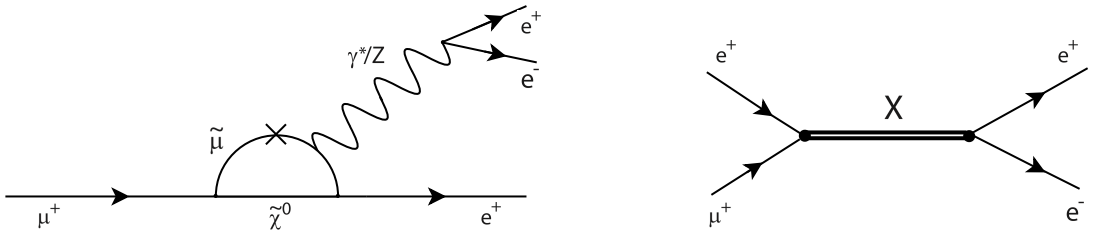

Figure 1.2: Loop diagrams of $\mu^+ \to e^+e^-e^+$ in BSM. Left) In SUSY models a supersymmetric particle is exchanged in the loop. Right) Tree diagram with new bosons coupling to the muon and electron.

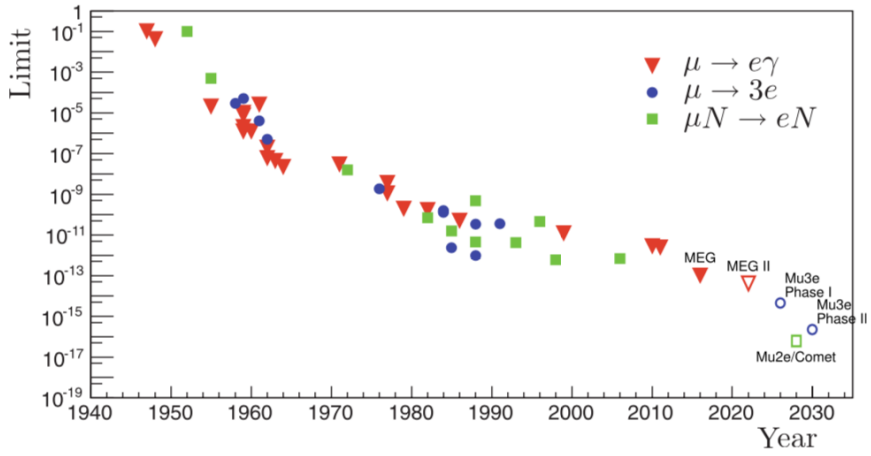

Figure 1.3: History of cLFV searches showing the upper limits on the branching ratios and projected ones. From [15].

1.3 PROBING FOR CLFV IN MUON DECAYS

Rare muon decay studies offer a unique window into cLFV due to several reasons. First, muons are relatively easy to produce in large quantities in particle accelerators, providing ample opportunities for study. Second, the decay products of muons (such as electrons and photons) are well-understood and can be precisely detected, allowing for clear identification of cLFV events. Finally, the specific properties of muon decay processes, like energy and momentum distributions, provide distinct signatures that can be differentiated from other standard particle interactions. This makes it possible to set good limits on cLFV processes and might detect rare events that possibly indicates for BSM new physics. Investigations into muon decays as a method for probing cLFV typically focus on three muon decay channels, called "golden" channels. Table 1.1 shows the current experimental upper limits at 90% confidence level on the branching ratios of the three "golden" channels.

Channel	Experiment	Present limit (90% CL on branching ratio)
$\mu^+ \to e^+\gamma$	MEG II	3.1×10^{-13} [16]
$\mu^+ \to e^+e^-e^+$	SINDRUM	1.0×10^{-12} [17]
$\mu^- Au \to e^- Au$	SINDRUM II	7×10^{-13} [18]

Table 1.1: Current experimental upper limits at 90% confidence level on the branching ratios of the three golden channels.

$\mu^+ \to e^+\gamma$

The distinctive characteristic of this decay is that both decay products should carry half the rest mass energy of the muon, and they should be emitted back-to-back. This

decay channel is central to the MEG experiment [19] and its successor, MEG II [20], at the Paul Scherrer Institute (PSI). Central to the experiment is the production of a continuous high-intensity beam of positive muons, which are directed towards a thin target and stopped to decay at rest. The key to detecting this decay lies in accurately measuring the energy, timing, and direction of the decay products. For photon detection, the MEG experiment employs a liquid xenon calorimeter. This detector captures the scintillation light produced when a photon enters, allowing for precise measurement of the photon's energy and timing. Simultaneously, the experiment uses a combination of drift chambers and timing counters made of scintillating materials to track the positron. These detectors reconstruct the positron's trajectory and momentum, while also measuring its time of flight. The experiment relies on the principle that in the $\mu \to e\gamma$ decay, the positron and photon are emitted back-to-back, each with momentum equal to half the muon mass, as required by conservation laws in a two-body decay. By measuring these properties, the MEG experiment aims to either observe the $\mu \to e\gamma$ decay or set stringent limits on its occurrence, thus contributing to the understanding of lepton flavor violation and the potential for BSM new physics. The current limit set by MEG on the branching ratio of this decay is 4.2×10^{-13} [21].

$\mu^- N \to e^- N$

In this process, a negative muon (μ^-) captured by a nucleus is converted directly into an electron (e^-) without producing neutrinos, which would be a clear sign of new physics. The electron is expected to have an energy slightly less than the rest mass of the muon, making it distinguishable from other decay processes. An upper limit (90 %) on the branching ratio of this process was set by the SINDRUM II experiment [18] at 7×10^{-13} in 2006. At present, several experiments are focused on this conversion, notably Mu2e [22] at Fermilab and COMET [23] at J-PARC. Mu2e aims to improve the sensitivity to $\mu^- \to e^-$ conversion by a factor of 10^5 compared to previous experiments, using an intense pulsed muon beam and a sophisticated detection system. COMET (COherent Muon to Electron Transition) experiment at J-PARC in Japan also aims to achieve a similar level of sensitivity, employing different experimental techniques. The projected limits for these experiments are shown in Table 1.2.

Channel	Experiment	Planned sensitivity
$\mu^+ \to e^+\gamma$	MEG II	[1] 6×10^{-14} [20]
$\mu^+ \to e^+e^-e^+$	Mu3e Phase I	2×10^{-15} [24]
	Mu3e Phase II	$\sim 10^{-16}$ [24]
$\mu^- Al \to e^- Al$	COMET	2.7×10^{-17} [22]
	Mu2e	2.9×10^{-17} [23]

Table 1.2: Projected single event sensitivity (SES) for the three "golden" channels.

1 Projected upper limit of the branching ratio at 90% CL.

$\mu^+ \to e^+e^-e^+$

The most recent constraints on the branching ratio for the decay process $\mu \to eee$ were established by the SINDRUM [17] experiment at PSI. The Mu3e experiment, described in the next chapter, is at the forefront of investigating this decay. It aims to achieve an unparalleled level of sensitivity, potentially identifying such decays with a much lower frequency than previously possible.

2

THE MU3E EXPERIMENT

Mu3e is a experiment searching for the rare charge Lepton Flavor Violating neutrinoless muon decay $\mu^+ \to e^+e^-e^+$. It's goal is to observe this decay if its branching fraction is larger than 10^{-16}, or to exclude it with a branching fraction of $> 10^{-16}$ at the 90% confidence level. The experiement is located at the Paul Scherrer Institute (PSI) in Switzerland and is currently under construction. It will have two phases, Phase I and Phase II. During Phase I of the experiment, the goal is to achieve a Single Event Sensitivity (SES) of 2×10^{-15} , utilizing the PiE5 beamline currently operational at PSI. The experiment will be upgraded to Phase II, with a SES of $\sim 10^{-16}$. To attain this degree of sensitivity for Phase I, a total of 2.5×10^{15} muons need to be stopped within the Mu3e detector.

The focus of this study is centered on Phase I of the experiment. This chapter delves into the fundamental physics concepts and the challenges associated with the Mu3e experiment.

2.1 THE CONCEPTUAL IDEA

The experiment involves stopping surface antimuons on a target to observe decay products. Surface antimuons are muons which have all the same momentum of 29.8 Mev/c. Charged decay products create signals, or hits, in pixel trackers, allowing for track reconstruction. Timing detectors record the instance when each decay product passes through them. This time information is used to reduce the backgrounds. The decay products' momentum is determined by measuring the path curvature in a 1 T magnetic field, parallel to the beam's direction.

2.1.1 *The signal and backgrounds*

Looking into a more detailed description of the signal, the $\mu^+ \to e^+e^-e^+$ decay products are three electrons, which are emitted from a common vertex in space, all simultaneous in time. In Mu3e the muons are stoped in thin target before decaying, so the muons are at rest. This leads to a scenario where the momenta of the three electrons sum are coplanar and that their total energy equals the muon mass at rest $m_\mu = 105.6$ MeV/c [25] :

$$\vec{p}_{tot} = \sum_{i=1}^{3} \vec{p}_i = \vec{0} \tag{2.1}$$

$$E_{tot} = \sum_{i=1}^{3} E_i = m_\mu \tag{2.2}$$

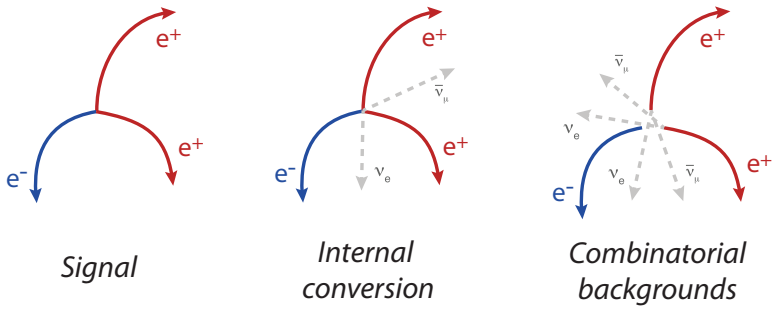

Figure 2.1: Signal topology for the $\mu^+ \to e^+e^-e^+$ decay. The three electrons are emitted from a common vertex in space, all simultaneous in time. Internal conversion mimics the signal but has two extra neutrinos that cannot be detected and thus manifest as missing energy. Other backgrounds are accidental ones and consist of particles from independent processes (sources) that, in combination, mimic the signal.

adhering to the convention that the speed of light and the reduced Planck constant are set to one in natural units ($c = \hbar = 1$).

Backgrounds that mimic the signal are present and should be suppressed below the target sensitivity, see Figure 2.1. Internal conversion decay $\mu^+ \to e^+e^-e^+\nu_e\bar{\nu}_\mu$ produces the same decay signature as the signal, Figure 2.1. It is the main source of background with a branching ratio of $(3.4 \pm 0.5) \times 10^{-5}$ [25]. If the neutrinos carry a fraction of the energy, the signal can be distinguished from the background with kinetics. In this case, the decay differs from the signal decay in the reconstructed rest mass of the three electrons $m_{eee} < m_\mu$ and the total momentum $\sum_{i=1}^{3} \vec{p}_i \neq 0$. The only way to supress this background is to have a high momentum and energy resolution since the three electrons are emitted simultaneously in time and space. Figure 2.2 shows the contamination of the signal region with the internal conversion background as a function of the reconstructed mass resolution. To aim for a sensitivity of 2×10^{-15}, the resolution of the reconstructed rest mass of the muon has to be better than 1 MeV/c^2. This can be only achieved by sufficient momentum resolution of the charged particle tracks.

Another background is accidental ones and consists of particles from independent processes (sources) that, in combination, mimic the signal. The most common muon decay is the Michel decay $\mu^+ \to e^+\nu_e\bar{\nu}_\mu$ with a branching ratio close to 100%, is the main source of positrons [25]. The electrons can come from Bhabha scattering, photon conversion or Compton scattering. Photons from the radiative muon decay $\mu^+ \to e^+\nu_e\bar{\nu}_\mu\gamma$ or via bremsstrahlung can convert to e^+e^- pairs and also provide an electron. So a lot of combinations of three independent or two correlated and one independent particles can mimic the signal. Also, if there are inefficiencies in the track reconstruction or presence of fake tracks, this can lead to an increase in this type of background. As the beam intensity is increased, the number of accidental background events increases.

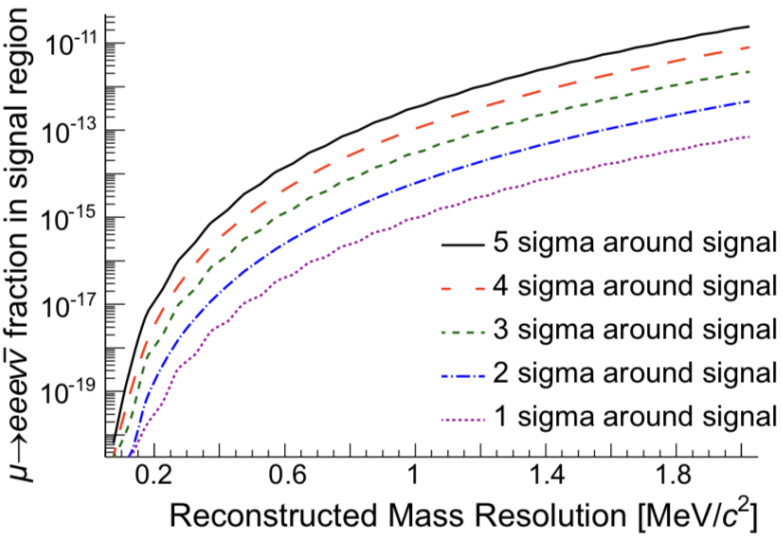

Figure 2.2: Contamination of the signal region with the internal conversion background as a function of the reconstructed mass resolution. From [24].

Therefore, to conduct a meaningful measurement within a feasible timeframe (1 year), the high muon stopping rates must be countered by precise momentum, vertex, and time resolutions to suppress the accidental backgrounds.

2.2 THE MU3E DETECTOR

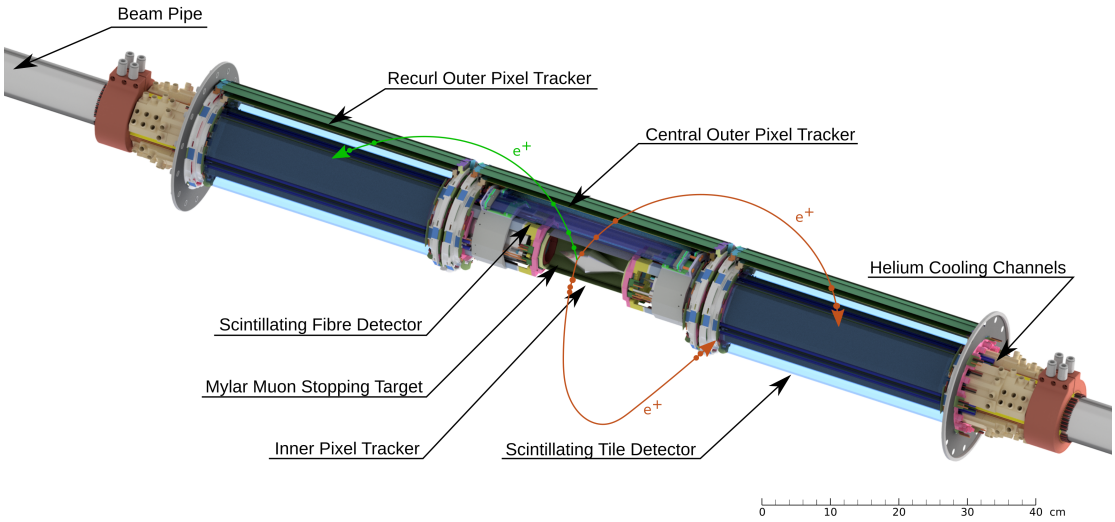

Figure 2.3: Active part of the Mu3e detector, with the central inner pixel vertex tracker and the SciFi detector surrounding the targer, and the upstream and downstream recurl stations. From [26].

The Mu3e detector, see Figure 2.4, is based on 50 µm thick high-voltage monolithic active silicon pixel sensors (HV-MAPS) for very precise tracking in conjunction with scintillating fibers (SciFi) and scintillating tiles coupled to silicon photomultipliers (SiPMs) for accurate timing measurements. The detector is designed to operate at very high rates in excess of 10^8 muons decays per second. Low momentum positive muons are stopped in a 5 µm thick hollow double cone target. The muons' relatively long lifetime of 2.2 µs ensures their survival until they reach the target, where they stop and decay. All subdetectors are barrel-shaped and concentric around the beam axis. The detector is inserted into a 2.7 m long 1T solenoidal homogeneous magnetic field.The full experiment is embedded in a helium atmosphere at atmospheric pressure cooling the pixel sensors. Also, since helium has a low atomic number, it minimizes multiple scattering of the decay products. A longitudinal and transverse view of the detector is shown in Figure 2.4.

The detector consists of one central and two recurl stations. At the central station, a cylindrical pair of the thin pixel trackers is placed directly around the target at 23.3 mm and 29.8 mm respectively. To achieve good vertex resultion the pixel sensors are placed as close as possible to the target. A second pair of pixel tracker layers with an inner radius of 73.9 mm and 86.3 mm provides a second set of measurements for the track reconstructions. Because of the magnetic field, the electrons follow a helical path so outer pixel tracker layers are further duplicated on both sides of the central stations to improve the momentum resolution of the tracks. Those outer pixel tracker layers form the recurl stations for the electrons which curl back towards the beam axis. Two type of timing detectors, the scintillating fibers and scintillating tiles are place at the

central and recurl stations and placed at a radius of 60 mm. The scintillating fibers are placed just below the outer pixel layers and are designed to be as thin as possible. The tiles are placed at the outermost layer of the pixel trackers and deliver a precise time measurement at the expense of more material.

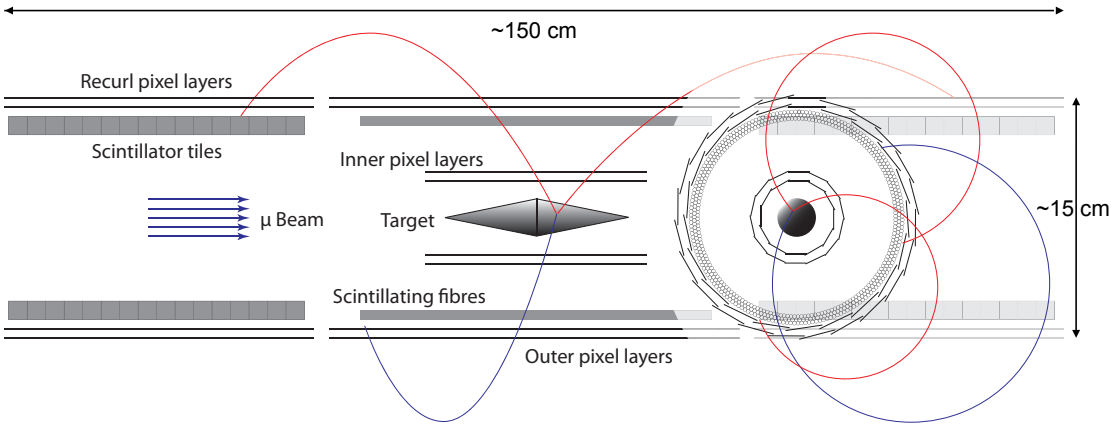

Figure 2.4: Schematic view of the Mu3e apparatus in the side and transverse projections (not to scale) [24]. The Phase I setup consists of a central part and recurl stations up- and down-stream. The central part comprises, from inside out, a hollow double cone muon stopping target, a silicon pixel inner double layer, the scintillating fiber detector, and a second silicon pixel outer double layer. The apparatus is inserted in a 2.7 m long solenoid providing a 1 T homogeneous magnetic field.

To optimize for precise momentum resolution, the material budget of all the subdetectors must be minimized to avoid multiple Coulomb scattering. Also, the resolution is affected by the uncertainty on the position measurement, so smaller pixels sizes with respect to the scattering angle are needed.

When a particle is deflected by an angle Ω, multiple scattering by an angle θ_{MS} limits the momemtum resolution (see Figure 2.5 left) and in a first order approximation:

$$\frac{\sigma_p}{p} \propto \frac{\theta_{MS}}{\Omega} \tag{2.3}$$

But in an interesting way, if the particle makes half a turn ($\Omega \sim \pi$), the effect of multiple scattering in the last pixel layer cancels out at first order and the momentum is determined with a higher precision (right Figure 2.5). This is the reason why the pixel tracker layers are placed at the recurl and central stations to make advantage of this effect when the tracks are detected a second time after they curl back towards the beam axis.

2.2.1 *Pixel tracker*

The pixel vertex tracker is based on high-voltage monolithic active silicon pixel sensors (HV-MAPS), called MuPix [28]. In HV-MAPS, the readout electronics is placed in the

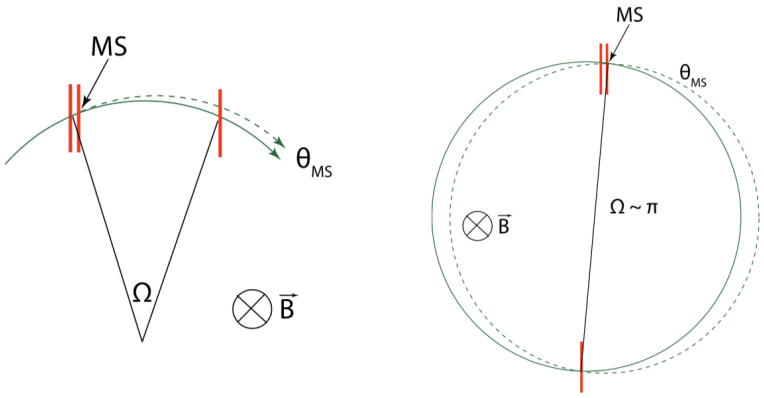

Figure 2.5: Illustration of multiple scattering as seen in the plane transverse to the magnetic field direction (left). Particle momentum is deduced by the deflection angle Ω, the momentum resolution is limited by the multiple scattering by θ_{MS}. Multiple scattering for a semi-circular trajectory (right). The red lines indicate measurement planes.

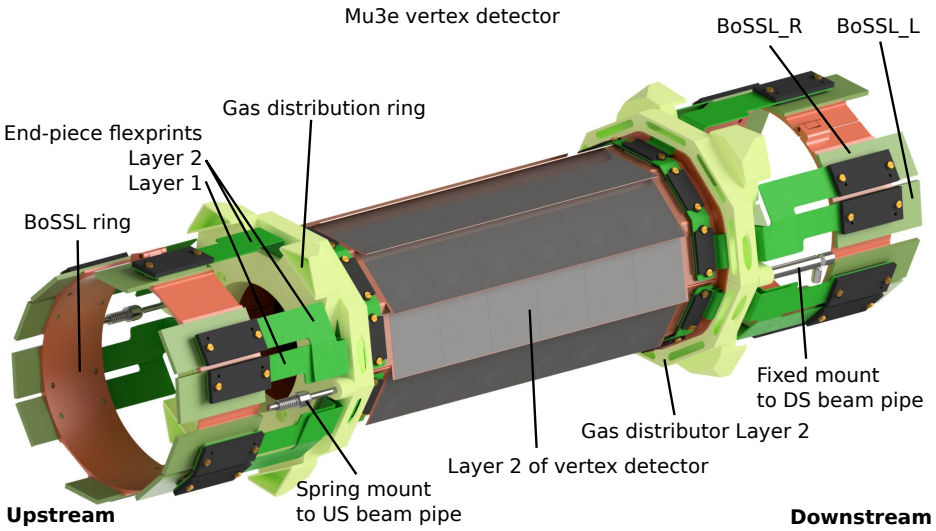

Figure 2.6: CAD rendering of the Mu3e pixel vertex tracker [27].

deep N-wells directly on top of each pixel diode. This offers a large geometrical fill factor. A reversed bias of the order of 60 V is applied. The dimension of a MuPix11 chip, the latest version of the MuPix to this date, is around 21×23 mm^2 and the charge collection is in the order a few nanoseconds. The sensor is 50 µm thick. The chip is divided into an active matrix and a periphery containing the readout structure. Integrated charge-sensitive amplifier is in the active part of the chip. In the periphery each pixel is discriminated by two thresholds. The maximum power consumption of a pixel sensor is 350 mW/cm^2. The cooling is done via the helium flows between the detector layers.

The pixel vertex detector for Mu3e, see Figure 2.6, is composed of ladders. Each ladder is made of 6 MuPix chips glued on a high-density interconnect (HDI) provided by a company. HDIs are flex circuits made of aluminum-polyimide laminates. The HDIs provide the supply voltages, HV, clock and the lines for configuring and reading out the chips. The ladders are mounted on end pieces made of polyetherimide which are mounted on an end ring that is connected to the gas distribution ring. Two pixels layers of pixel ladders are placed in close proximity of the traget in the central region. Their lenght is around 120 mm and their radii are around 23 mm and 30 mm.

Two outer pixel layers are installed at radii of 74 mm and 86 mm at the central and recurl stations as well. The outer tracking layers are composed in the similar way as the inner ones. They used 70 µm thick sensors. This unables to measure electrons with a transverse momentum of minimum 10 MeV/c.

2.2.2 *Timing Detectors*

The timing detectors are based on scintillating fibers and scintillating tiles coupled to silicon photomultipliers (SiPMs). They are used to suppress the accidental backgrounds. Successfully matching all three tracks from a vertex to hits in fiber or tile detectors reduces accidental backgrounds by a factor of 75 with a fiber detector time resolution of 250 ps [29]. Figure 2.7 shows the suppression of Bhabha e^+/e^- pairs plus Michel e^+ accidental background as a function of SciFi detector time resolution if only the SciFi detector is used or both timing detectors are used. A time resolution of 60 ps for the tile detector and a working point with a 90% overall signal efficiency is assumed. The vertical line corresponds to a 250 ps time resolution for the SciFi detector. It can be seen that only a combined use of both timing detectors can suppress the background to a desired level. In addition to timing, the SciFi detector will also determine the sense of rotation (i.e. the charge) of the recurling tracks in the central region of the aparatus. This can be done by using the time of flight between consecutive crossings of the SciFi detector. At the central region the amount of material needs to be minimzed so a very thin scinitllating fiber detector has been developed. At the recurl station the material budget is less critical since the momemtum measurements are completed and so a thicker scintillating tile detector can be installed. The tile detector is installed under the outer pixel tracker layers to provide better time resolution. Both subdetectors are

coupled to silicon photomultipliers but in a different configuration. To readout both subdetectors, a dedicated ASIC the MuTRiG is used (see section 8.1).

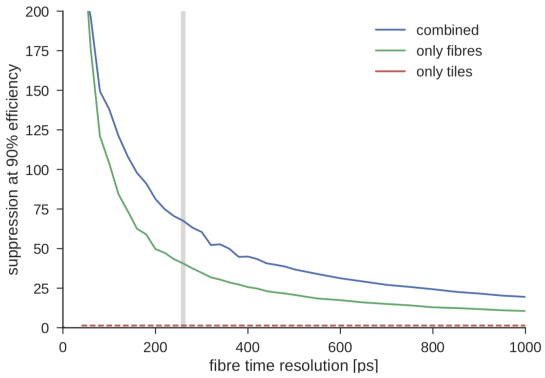

Figure 2.7: Simulation of the suppression of Bhabha e^+/e^- pairs plus Michel e^+ accidental background as a function of fibre detector time resolution if only the fibre detector (green) is used or both timing detectors (blue) are used. A time resolution of 60 ps for the tile detector and a working point with a 90% overall signal efficiency is assumed. The vertical line (in grey) corresponds to a 250 ps time resolution for the SciFi detector. From [24].

2.2.3 *Scintillating Tiles*

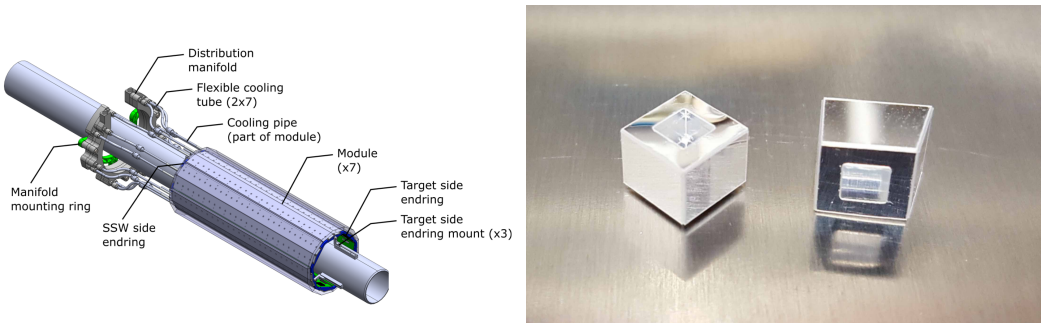

Figure 2.8: On the left a CAD rendering of one station of Tile detector with cooling manifold. Both stations at both sides are built identical. On the left a picture of a prototype scintillating tile wrapped with ESR foil. Rendering and picture from [26, 27].

The scintillating tile detector, see left of Figure 2.8, situated between the recurl outer pixel layers and the beam pipe, provides precise timing information. It is composed of two identical recurl stations placed upstream and downstream of the target. Constructed from EJ-228 plastic scintillator, each tile measures $6.3 \times 6.2 \times 5.0$ mm^3 individually enclosed in an Enhanced Specular Reflector (ESR) foil with 3×3 mm^2 (right Figure 2.8) opening at the bottom for coupling to the SiPM sensors. Each recurl station consists of 7 modules assembled on a pair of endrings. Each module has 26 sensor matrices assembled on an aluminium cooling plate and one tile module board

hosting 13 MuTRiG ASICs for readout. Each sensor matrix consists of 16 scintillating tiles and silicon photomultipliers, considered as channels. The Tile detector is cooled down by the liquid cooling system which is operated down to $\sim -20\,^{\circ}\mathrm{C}$.

2.2.4 *Scintillating Fibers*

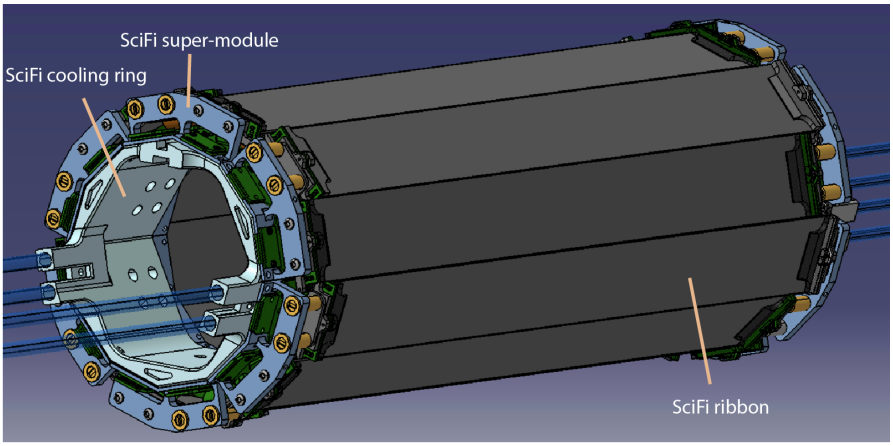

Figure 2.9: CAD rendering of the full scintillating fiber detector. 12 SciFi ribbons are arranged in a cylindrical shape and coupled to SiPMs on both sides.

The scintillating fiber detector (SciFi) is placed between the inner and outer pixel layers, as above the outer pixel layers would lead to additional multiple scattering. The optimal location is either just outside the second pixel layer or inside the third, with the latter preferred due to its larger radius, which reduces detector occupancy and pile-up events. The detector's design includes twelve 32.5 mm (Figure 7.2) wide fiber ribbons in a cylindrical arrangement, each 300 mm long and composed of staggered fibers with a diameter of 250 µm. SiPM arrays are attached to both ends of each fiber ribbon for light detection using the MuTRiG ASICs. In chapter 7 the SciFi detector is described in more detail.

2.2.5 *Detector readout*

`Mu3e` will use a continuous, triggerless readout. As described above, it employs specific ASICs for each subdettectors which streams out compressed digital hit data. This data is gathered by FPGA's on front end boards and then transmitted optically to switching boards. These boards distribute the data to computer farms which allows to access complete detector data for specific time intervals. The reconstruction of the decays uses graphics processing units to identify interesting events for storage. More about the DAQ system is explained in section 8.4.

2.3 BEAMLINE

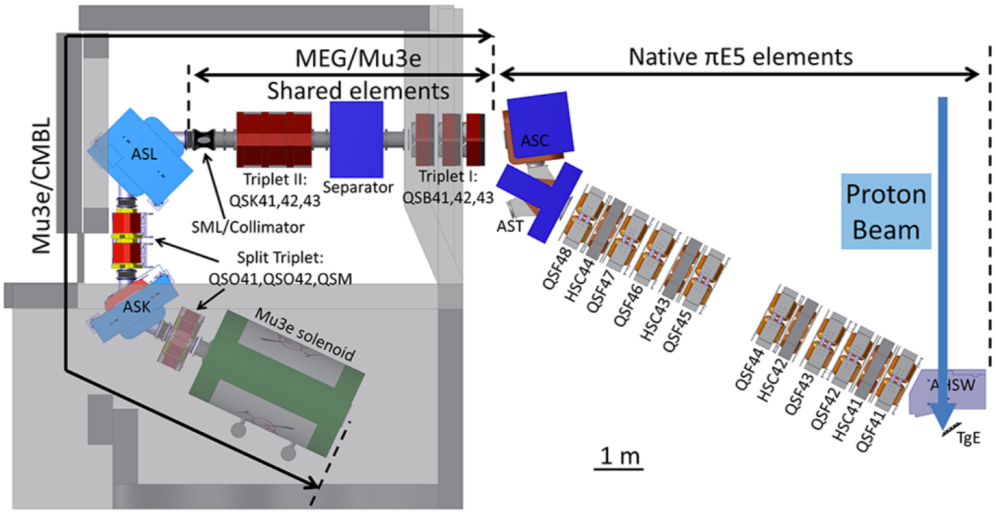

Figure 2.10: CAD model of the PiE5 beamline in the Compact Muon Beam Line configuration used for the Mu3e [24].

Mu3e will be installed in the PiE5 beamline at Paul Scherrer Institute (PSI) which delivers the highest intensity continuous muon beam currently available, around 10^8 muons per second. A 1.3 MW cyclotron accelerates protons to 590 MeV/c which are then directed to a primary target. This target, TgE, made of polycrystalline graphite, produce pions, some of which decay near the target surface into surface muons. These surface muons, with a momentum peak around 28 MeV/. A special beamline configuration is designed to select and transport particles with a momentum of 28 MeV/c to the Mu3e detector.

Mu3e shares the beamline with the MEG II experiment and an additional compact muon beam line (CMBL) is needed to transport muons to the Mu3e detector (Figure 2.10). The beam line also contains positrons and electrons, originating either from muon decays along the beam line or from electron-positron showers triggered by photon emitted in π^0 decay at the primary target.

3

SCINTILLATING FIBERS

Scintillating fibers are a specialized type of scintillating material with unique properties for photon detection and tracking applications. This chapter covers the basics of scintillators, the distinct characteristics of scintillating fibers, and their use in assembling scintillating fiber ribbons for the `Mu3e` experiment. Their performance and effectiveness will be discussed in the next chapters.

3.1 BASIC OF SCINTILLATORS

Scintillators are materials in which some fractions of incident energy carried by incoming particles or radiation, are absorbed and transformed into detectable photons (visible or near visible light). In other words, they exhibit the property of luminescence, which when exposed to certain forms of energy, for example, light, ionizong particles, etc., absorb and reemit the energy in the form of visible light (or near visible light). There are two different scintillation mechanisms:

- Fluorescence is when the scintillation material absorbs the energy and reemits the energy in a short time scale of the order of 10 ns.
- Phosphorescence is when the remission of the energy is delayed because the excited state is metastable. In such case, the delay time between absorption and remission can vary from few µs to several hours, depending on the material.

There are different types of scintillating materials. In general, they can be classified in two main categories: organic and inorganic scintillators. Different mechanisms are responsible for the scintillation process in each of these two categories. For organic scintillators, the scintillation process is based on a molecular effect. On the other hand, for inorganic scintillators, the scintillation process is based on a lattice effect.

3.1.1 *Inorganic scintillators*

Inorganic scintillators, primarily alkali halide crystals doped with activator impurities, include common types like NaI(Tl), CsI(Tl), BGO, LSO, and LYSO. The scintillation process is governed by the crystal's electronic band structure, where ionizing radiation generates electron-hole pairs or excitons. Activators create intermediate energy levels, enabling electron-hole pair recombination and light emission.

Though inorganic scintillators generally are slower in response than organic ones because of the *long decay times* of their emission spectra, they exhibit *rapid rise times*. CsF is an exception with its notably fast decay. The decay is typically exponential, single or dual in nature. A drawback of some inorganic scintillators, like NaI, is their hygroscopic

nature, requiring airtight enclosures to prevent moisture damage. In contrast, materials like BGO and BaF2 are non-hygroscopic and more durable [30].

The key advantage of inorganic scintillators is their high stopping power due to their density and atomic number, which, combined with their high light output, provides superior energy resolution. This makes them well-suited for detecting gamma rays, electrons, and positrons.

3.1.2 *Organic molecules*

Organic scintillators display luminescence because of the electronic configurations of aromatic organic molecules. A key component of these molecules is the benzene ring molecules (C_6H_6), whose atomic structure is shown in Figure 3.1. These molecules differ from inorganic ones in their luminescence mechanism, which is rooted in the carbon-based structure. Carbon atoms, with their electron configuration of $1s^2 2s^2 2p^2$, can form various bonding arrangements with different valencies observed in molecules like saturated hydrocarbons, and double or triple-bonded hydrocarbons.

Key configurations of carbon atoms in organic scintillators include:

- Tetrahedral Configuration (sp3 Hybridization): Common in non-luminescent compounds like diamond and methane.
- Trigonal Configuration (sp2 Hybridization): Found in luminescent aromatic hydrocarbons like, as mentioned , benzene (C_6H_6), characterized by a hexagonal ring structure. In benzene, σ bonds form through the direct overlap of atomic orbitals, while π bonds result from side-to-side overlap. The delocalized π electrons across the benzene ring contribute to its stability and luminescence.
- Diagonal Configuration (sp Hybridization): Present in luminescent molecules like acetylene (C_2H_2), involving two equivalent hybrid σ bonds.

In each carbon atom within an organic scintillator, three out of four valence electrons are present in $sp2$ orbitals. These electrons engage in covalent bonds (σ bonds) with adjacent carbon atoms and a hydrogen atom (H), creating a planar ring structure. The remaining valence electron is in a $2p$ orbital and forms a π bond through overlapping with a $2p$ electron from a neighboring carbon atom. This configuration results in six

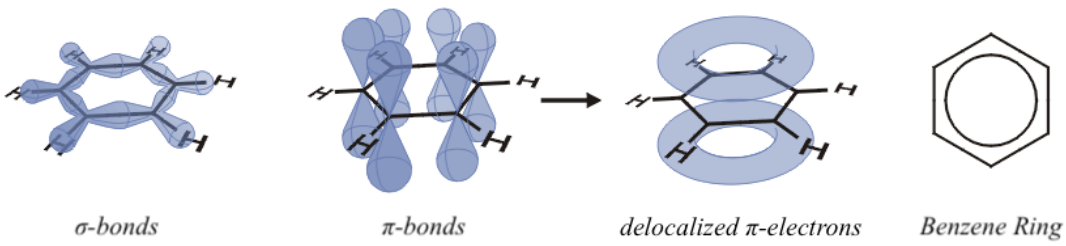

Figure 3.1: Structure of benzene molecule. Adaped from [31].

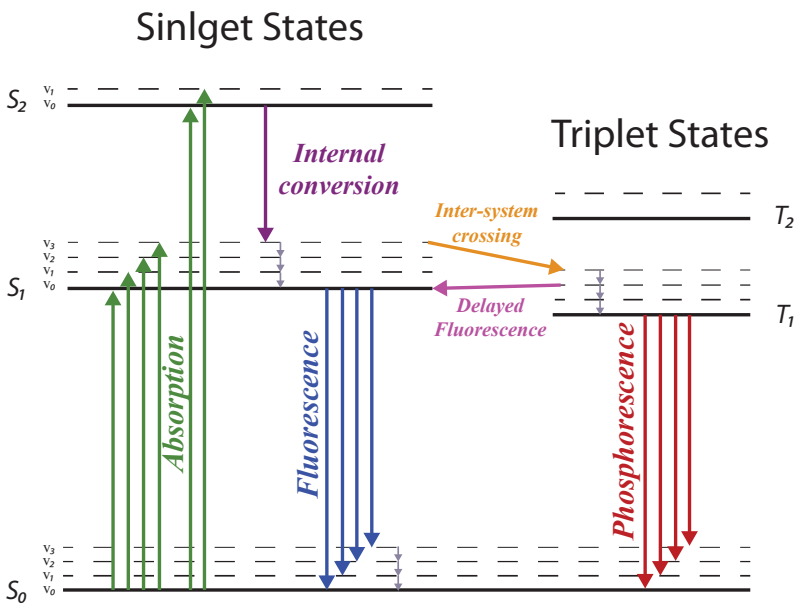

Figure 3.2: Electronic energy level structure of organic molecules. Adaped from [32].

electrons that are not fixed in place but are rather delocalized. They have the ability to move between different energy levels associated with the π bonds. This movement of electrons is a key factor in enabling luminescence in the organic scintillator material.

The electronic structure of organic molecules containing a π electron, such as benzene, is shown in Figure 3.2. There is a sequence of energy levels, where the π electrons are in singlet states (S_0, S_1, S_2, etc) up to the ionization level. Superimposed on this sequence are vibrational sub-levels (v_0, v_1, v_2, etc). The spacing in energy between the vibrational sub-levels is of the order of 0.1 eV. The spacing of the singlet states is of the order of 3 eV. Also a sequence of excited π triplet states (T_1, T_2, etc) is present, with each triple state being lower in energy than the corresponding single state.

Through the deposition of energy by ionizing radiation, electrons within the molecules are excited to higher energy levels. Since transitions from the ground state S_0 to higher triplet states T_1 are spin-forbidden, the excited electrons can only be excited to higher singlet states S_1, S_2, etc, green arrows in Figure 3.2. After the initial excitation, the molecules relax back to their lower energy states. The relaxation process occurs rapidly within the vibrational states, during which the initially excited vibrational levels undergo a fast decay to reach the lowest vibrational level within the same electronic state. Furthermore, there is a notable overlap of vibrational energy levels across distinct electronic states, facilitating fast transitions to the first excited state S_1. This quick relaxation process is known as internal conversion or internal degradation, purple arrows in Figure 3.2. However, from the first excited state S_1, the molecule can also retun to the ground state by emitting a photon, which is known as *fluorescence*, blue arrows Figure 3.2. This emitted light typically has a longer wavelength than the absorbed radiation, a

phenomenon known as the *Stokes shift* [32]. In addition to fluorescence, molecules like benzene can also exhibit *phosphorescence*, red arrows in Figure 3.2. Phosphorescence occures when an π electron first moves to a triplet state T_1, through the process called inter-system crossing, orange arrow in Figure 3.2. The triplet state, which is relatively long-lived due to spin conservations rules, eventually decays back to the ground state S_0, resulting in the phenomenon of phosphorescence. Howerever, a π electron in this long-lived triplet state T_1 can also revert to a singlet state and then decay to the ground state, emitting a so called delayed fluorescence, pink arrow in Figure 3.2 . This triplet state T_1 is refered to as a metastable state [32, 33].

3.1.3 *Plastic scintillators*

Plastic scintillators are essentially solutions made by embedding fluorescent molecules into solid plastic solvents, such as polystyrene (PS) or polyvinyltoluene (PVT). These polymers are primarily composed of benzene units and are known for their low quantum efficiencies, resulting in poor light yield. The emitted photons by PS are in the UV region (280 nm - 400 nm). At the peak of the emission spectrum, photons are absorbed back by the PS due to various effects such as Rayleigh scattering and molecular vibrations. To enhance the performance and mitigate these inefficiencies, an organic fluorescent dye, called an *activator*, is added to the plastic solvent. This fluorescent dye has energy levels that are compatible with the energy levels of the plastic solvent. Common activators include p-terphenyl, 2,5-diphenyloxazole (PPO), and 1,4-bis-2-methylstyrylbenzene (bis-MSB). Typically, the activator concentration is about $\mathcal{O}(1\,\%)$ by weight, ensuring that the molecules of the scintillator dye are no further than $\mathcal{O}(1\,\text{nm})$ apart from the benzene rings of the plastic solvent. This proximity is key to efficient intermolecular energy transfer, which occurs through a non-radiative *Förster transfer* [34, 35]. This process involves a non-radiative dipole-dipole interaction, transferring energy from benzene excitation to the activator. The efficiency (ϵ_F) of this energy transfer is expressed as [34, 35]:

$$\epsilon_F = \frac{1}{1 + \left(\frac{r}{R_0}\right)^6} \tag{3.1}$$

Here, r represents the distance between benzene molecules and the activator, and R_0 is the Förster radius - the distance where the energy transfer efficiency is 50%. If r exceeds R_0, the probability of a non-radiative energy transfer decreases. However, distance is not the only important parameter for the energy transfer efficiency. The Förster radius depends on the spectral overlap between the emission and absorption spectra of benzene and activator respectively, as well as the relative orientation of dipole moments of donor and acceptor molecules. Hence, factors beyond distance play a role in determining Förster transfer occurrence. Consequently of this transfer, photons are emitted from the activator dye. The activator dye's emission spectrum is selected to shift the photon wavelengths away from the absorption peaks of the PS. In cases where *fast decay times* (<1 ns) are necessary, the emitted fluorescent photons

exhibit wavelengths in the UV spectrum and higher. A second dye, the *spectral shifter*, is often added at a concentration of about $\mathcal{O}(0.05\,\%)$ by weight. This shifter absorbs UV photons and shifts their wavelengths to higher values, enhancing the transparency of the scintillator and aligning with the absorption spectrum of available photosensors. Each step of shifting the wavelenghts introduces inefficiencies in the scintillation process. Precise concentration balancing of the activator and spectral shifter is crucial to prevent inefficiencies in energy transfers and self-absorption. A spectral shifter with a large difference between its absorption and emission spectra (Stokes shift) can help mitigate these issues [36, 37]. Some scintillators use Nanostructured Organosilicon Luminophores (NOL) [38] which bond the activator and the spectral shifter dye to a silicon atom to allow non-radiative energy transfer between the two through the Förster mechanism. This process makes the shifting of the wavelenghts of the photons faster and more efficient.

3.2 CHARACTERISTICS OF SCINTILLATING FIBERS

Scintillating fibers have two main functions:

1. to convert the energy that ionizing particles deposit into optical photons, essentially turning particle interactions into light;
2. to transport this light to the extremities of the fiber, where it can be detected

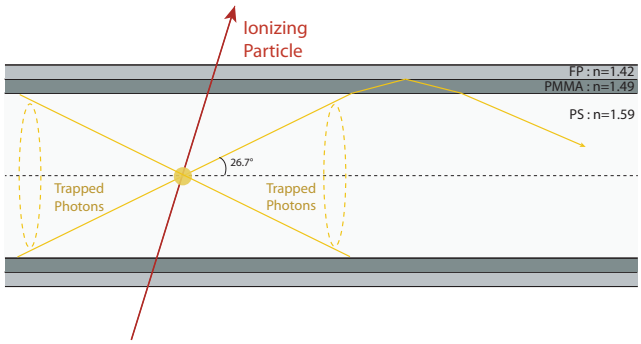

Figure 3.3: A longitudinal view of the trapping efficiency for a double clad fiber. The additional cladding increases the internal reflection angle.

Most common fibers have a circular or square cross-section. For the circular cross-section, the diameter of the fiber is typically in the range of 250 µm. While there are fibers with larger diameters, such as 500 µm up to 5 mm. The fibers are composed of a core made of polystyrene (PS), surrounded by a single or double layer cladding. Those layers are used to enhance the scintillation light trapping efficiency, given that light propagates in the fiber via total internal reflection. Polymethyl-methacrylate (PMMA) is typically used for the cladding material. In double clad fibers, an additional outer layer of fluorinated polymer (FP) is incorporated. The cladding layers have a decreased refractive index compared to the polystyrene core, see Figure 3.3. In the core of the

fibers are embedded activators and spectral shifters, which are responsible for the scintillation process, as decribed in the previous section.

Scintillating fibers are used for developping a Scintillating Fiber (SciFi) detector. The performace of a SciFi detector, including its efficiency and time resultion, is predominantly determined by the amplitude $A(\lambda)$ of the measured signal, which is a direct measurement of the number of detected photons $n_{ph.e.}$:

$$A(\lambda) = Y_S(\lambda) \cdot \epsilon_{trap}(\lambda) \cdot \epsilon_{trans}(\lambda) \cdot PDE(\lambda) \cdot \Delta E \tag{3.2}$$

where $Y_S(\lambda)$ is the ionization light yield, $\epsilon_{trap}(\lambda)$ and $\epsilon_{trans}(\lambda)$ are the trapping efficiency and the transport efficiency, respectively, and $PDE(\lambda)$ is the photon detection efficiency of the photodetector. All of these factors depend on the scintillation wavelenght λ, expect for the energy deposit ΔE.

The ionization light yield $Y_S(\lambda)$ is an intrinsic property of the fiber and is expressed in terms of generated visible photons per deposited amount of energy ΔE. It depends on the core material of the fiber, the concentration and type of dissolved dyes, the spectral compatibility between the activator and the spectral shifter, and the quantum efficieny of spectral shifter.

Photon emission in these fibers occurs isotropically at the interaction point. However, only a fraction of these photons, given by $\epsilon_{trap}(\lambda)$, are captured and transported through the fiber via total internal reflection. Total internal reflection is fuffilled only if the photon incidence angle θ relative to the normal to the surface upon which the photon reflects, satisfies the following condition (Snell's law):

$$\theta < \theta_c = \arcsin\left(\frac{n_{core}}{n_{clad}}\right) \tag{3.3}$$

where n_{core} and n_{clad} are the refractive indices of the core and the cladding respectively. The trapping efficiency is defined as the ratio of the number of photons trapped in the fiber to the number of photons emitted isotropically at the interaction point. So by adding more layers of cladding with decreasing refractive indices the critical angle θ_c, as seen from the core, deacreases leading to a higher trapping efficiency. The fibers used in this work have a double cladding, with a refractive index of the core material, PS, $n_{core} = 1.59$. The inner cladding is made of PMMA with a refractive index of $n_{clad_{PMMA}} = 1.49$, while the outer cladding is made of FP with a refractive index of $n_{clad_{FP}} = 1.42$. With those materials and structure of double cladding, the trapping efficiency $\epsilon_{trap}(\lambda)$ of a fiber is around 5 % per hemisphere with critical angle of 26.7°.

The transport of these photon through the fiber is subject to losses due to several factors, listed below.

- Disturbances in the internal reflection caused by imperfections in the core material and defects in the cladding.
- Light absorption in the fiber due to the overlapping emission and absorption bands of the dyes. This should be avoided by using dyes with large Stoke's shift of the wavelength shifter. Imperfections in the fiber can also contribute to light absorption.

- Photon scattering losses, notably Rayleigh scattering, arise from fluctuations in the material's density or compositional uniformity within the fiber. These variations can scatter light away from the path that would normally lead to internal reflection, causing a loss of light intensity.
- In some cases, the molecular orientation of the polymers in the fiber core can impact the light transmission. For instance, a high degree of molecular orientation might increase mechanical strength but could also reduce optical transparency.
- When a fiber is bent, some of the light rays may no longer meet the conditions for total internal reflection (equation 3.3) and thus can escape from the fiber.
- External factors such as temperature fluctuations, mechanical stress, and exposure to chemicals or radiation can degrade the fiber over time, leading to increased losses.

The loss of light during propagation over distance d is characterized by the light attenuation length $\Lambda(\lambda)$, which is related to transport efficiency by $\epsilon_{trans} = 1 - \exp(d/\Lambda(\lambda))$. The attenuation length $\Lambda(\lambda)$ indicates the distance d at which $1/e$ of the initial number of photons survives.

The light intensity $I(\lambda, d)$ along the fiber, as a function of the propagation distance d, is usually described in terms of a short and a long component:

$$I(\lambda, d) = I_0^{short}(\lambda) \cdot \exp\left(-d/\Lambda^{short}(\lambda)\right) + I_0^{long}(\lambda) \cdot \exp\left(-d/\Lambda^{long}(\lambda)\right) \tag{3.4}$$

The light instensity is characterized by respective attenuation lengths $\Lambda^{short}(\lambda)$ for the short component and $\Lambda^{long}(\lambda)$ for the long component. This behavior is attributed to the different photon trajectories within the fiber, which can be either meridional (along the fiber) or non-meridional (at an angle relative to the fiber's axis). The meridional trajectories predominantly suffer from core related effects, while non-meridional trajectories are more susceptible to interface effects, such as cladding induced light losses. The short component, primarily non-meridional, tends to diminish rapidly, often within a span of 10-20 cm. Furthermore, shorter wavelengths face more intense reabsorption than longer wavelengths due to spectral overlaps between absorption and re-emission spectra of the spectral shifters, leading to a wavelength shift in the emission spectrum over longer distances.

Concerning time resolution σ_t, the fundamental limitations for thin (low mass) scintillation detectors are determined by the statistical nature of light signal generation and inconsistencies within the light detection apparatus. The time resolution of a relatively low light yield SciFi detector is dependent on the spectral shifter's decay time τ_d and on the number of detected photons n_{ph}:

$$\sigma_t \sim \sqrt{\frac{\tau_d \cdot \tau_r}{n_{ph}}} \tag{3.5}$$

where τ_r is the rise time of the light pulse. Shorter the decay time of the spectral shifter the better the time resolution but also the number of detected photons n_{ph} is important, as will be seen in chapter 5.

Equaly important is the signal amplitude $A(\lambda)$, i.e. the number of detected photons n_{ph}. The number of detected photons n_{ph} is proportional to the energy deposited ΔE in the fiber. Presuming that the detection of the initial photon corresponds to the time of the particle's passage through the fiber, an increase in the number of detected photons n_{ph} significantly increases the probability that this first photon is close to the fiber's initial time of excitation. In cases where fluorescent states are formed instantaneously (similar to UV LED excitation), the light pulse over time exhibits a fast leading edge followed by an exponential decay defined by τ.

Therefore, the intensity over time can be described as [32]:

$$I(t) = I_0 \exp(-t/\tau) \tag{3.6}$$

where I_0 is the initial intensity of the light at $t = 0$ and τ is the decay time. In contrast, an excitation by an ionizing particle the porcess of signal formation is more complex, as it involves multiple step. First initiating with the transfer of energy from the ionizing radiation to an intermediate fluorescent state, the activator. This initial step is followed by a transfer of energy from the activator to the spectral shifter. The culmination of this sequence is the final emission of light. Therefore, it is essential to consider the finite rise time required to *populate the intermediate fluorescent states*. If the assumption is made that the population of these intermediate fluorescent states behaves exponentially, then the overall shape of the emitted light pulse of this two-step process can be written as [32, 39]:

$$I(t) \sim I_0 \frac{\tau}{\tau - \tau_a} \left(exp(-t/\tau) - exp(-t/\tau_a)\right) \tag{3.7}$$

where τ is the decay time of the spectral shifter as in equation 3.6 and τ_a describes the population of fluorescenct state with values around 1 ns.

Another way to describe the shape of the light pulse is to conclude that a Gaussian function captures better the energy transfer from the radiation source to the activator [40, 41]. Consequently, the time profile of the light pulse is best characterized by a convolution of this Gaussian distribution with a two-step exponential decay function. The Gaussian distribution describes the time spread of the light pulse generation process (and also the fluctuations in the light collection). The two step exponential decay function describing the light emission by the spectral shifter. So, this gives :

$$I(t) \sim \frac{I_0}{\sqrt{2\pi\sigma^2}} exp\left(\frac{(t - t_0)^2}{2\sigma^2}\right) * \frac{\tau}{\tau - \tau_a} \left(exp(-t/\tau) - exp(-t/\tau_a)\right) \tag{3.8}$$

The parameter σ represents the time spread associated with the light generation process and the detection. For very fast organic scintillators, an accurate description of their timing performance is achieved by simultaneously reporting both the time spread of the light pulse σ, and the decay time of the spectral shifter τ.

Table 5.1 provides a detailed summary of the physical properties of various double-clad round scintillating fibers that have been examined and used in this study. The data compiled in this table are derived from specifications provided by the manufacturers

Table 3.1: Properties of blue-emitting, high-purity round scintillating fibers from Kuraray[38, 42] and Saint-Gobain [43], typically for 1 mm diameter fibers. Saint-Gobain specifies the light yield, while Kuraray labels SCSF-78 and NOL-11 as "high light yield" fibers.

Fiber Type	**SCSF−78**	**SCSF−81**	**NOL−11**	**BCF−12**
Cladding thickness [% fiber radius]		$3-3$		$3-1$
Trapping efficiency [%]		5.4		≥ 5.6
Numerical aperture		0.72		0.74
Emission peak [nm]	450	437	421	435
Decay time [ns]	2.8	2.4	1.3	3.2
Attenuation length [m]	> 4.0	> 3.5	> 2.5	> 2.7
Light yield [ph/MeV]	high		high	~ 8000
Refractive index (inside out)	$1.59-1.49-1.42$			$1.60-1.49-1.42$
Density (inside out) [g/cm^2]	$1.05-1.19-1.43$			1.05
Core	Polystyrene (PS)			
Inner cladding	PMMA			
Outer cladding	Fluorinated polymer (FP)			

and from values reported in relevant literature. These properties are typically representative of fibers with a diameter of 1 mm. Specifically, the peak emission wavelengths for the fibers are as follows: for Kuraray's SCSF−78, the peak emission is at 450 nm; for SCSF−81 it is at 437 nm; NOL−11 features a peak at 421 nm; and for Saint Gobain's BCF−12, the peak is observed at 435 nm.

Additionally Figure 3.4, illustrates the emission spectra for two of these fibers, SCSF-78 and NOL-11, shows how the emission varies at different distances from the point of excitation.

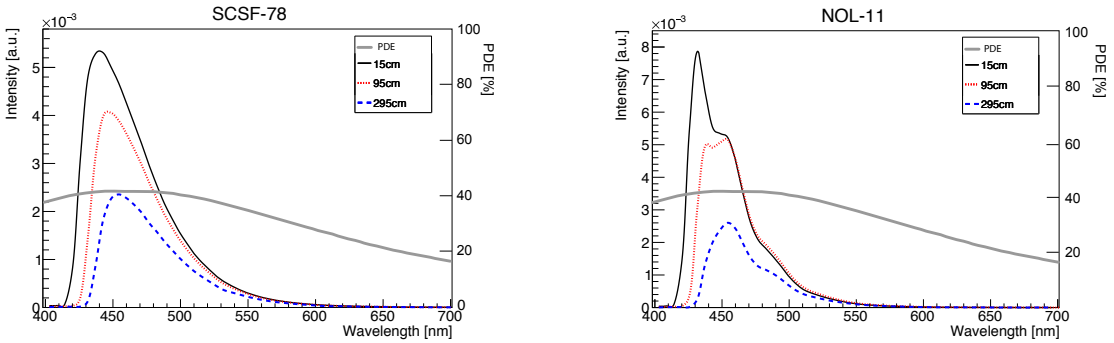

Figure 3.4: Emission spectra at various distances from the excitation point for SCSF-78 (left) and NOL-11 (right) fibers. Spectra are not normalized. Gray line represents the SIPM `S13360-1350CS` photon detection efficiency (PDE) at an overbias of 3 V.

Figure 3.5: Various full size SciFi ribbon prototypes formed by staggering 250 µm diameter round scintillating fibers. The fibers are assembled with different adhesives (the black epoxy gives the black color to the ribbons).

3.3 SCINTILLATING FIBER RIBBONS

For the SciFi detector, the 250 µm fibers are arranged in a ribbon structure. They consist of staggered layers of round, high-purity, double-clad scintillating fibers. Different scintillating fiber materials and assembly procedures (i.e. the number of staggered SciFi layers) have been evaluated in this thesis, to achieve the best performance compatible with the Mu3e requirements (see chapter 5).

In the Mu3e baseline design, SciFi ribbons are formed by staggering 3 layers of 250 µm diameter fibers from Kuraray [42], type SCSF-78. The ribbons have a length of 300 mm and a width of 32.5 mm, resulting in 128 fibers in the bottom layer. POLYTEC EP 601-Black a two-component low-viscosity black-colored adhesive was selected for its advantageous handling properties. One can see the various full size SciFi ribbons with end pieces attached for coupling to the photo-sensors in Figure 3.5.

The necessity for thin scintillating fibers, driven by material budget constraints, occupancy, and position resolution requirements, led to the examination of different blue-emitting 250 µm diameter round double-cladded scinfitllating fibers, including Kuraray's SCSF-78 and SCSF-81, NOL-11 fibers, and Saint-Gobain's BCF-12 fibers. Characteristics of these fibers are summarized in Table 5.1 and performances studies of single fibers are presented in chapter 5. Ribbons comprising two to six staggered scintillating fiber layers were produced and evaluated, utilizing different adhesives for assembly. The comprehensive results of these ribbon studies are presented in performance chapter 5, with a focus on high-yield fibers SCSF-78 and NOL-11 since the results for low light yield fibers SCSF-81 and BCF-12 is much worse. Notably, the novel NOL fibers, based on Nanostructured Organosilicon Luminophores with very short decay times (approximately 1 ns), demonstrated the best timing performance. However, these fibers were not available in sufficient quantities at the time of construction of the SciFi detector.

3.3.1 *Assembling of scintillating fiber ribbons*

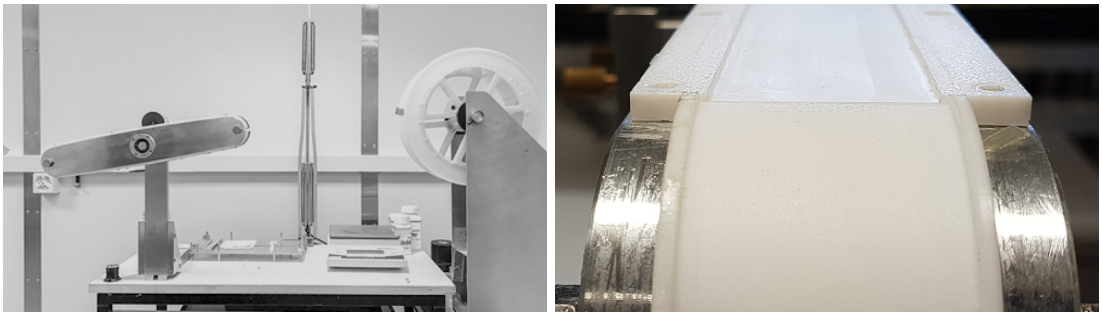

Figure 3.6: Left: winding tool for the preparation of the SciFi ribbons (the fiber is not visible in the photo). Up to 6 SciFi layers can be staggered using this tool. Right: detail of the U-channel. Winding tool designed by Franck Cadoux.

The fibers are assembled[1] with the help of a winding tool, see Figure 3.6 (left). They are methodically arranged into ribbons, ranging from two to six staggered layers. The assembling process was executed in a layer-by-layer method. Initially, as shown in Figure 3.6 (right), a Teflon made U-channel is used to hold and group the fibres in place. The fibers, coming from a spool, are placed in the U-channel one by one next to each other. This U-channel which is 0.5 mm deep, packs uniformily the first fiber layer. To facilitates the removal of the ribbons afterwards, the U-channel is coated with a thin layer of Trennspray P6. This Trennspray is a wax based spray, formulated to prevent materials from sticking to surfaces during processing. Such sprays are for example, commonly used in molding. The precise alignment of the fibers, crucial for achieving good tracking resolution, is ensured by tightly packing them in the U-channel to an alignment accuracy exceeding 10 µm [44]. The fibers are positioned manually.

Following this, a thin layer of glue is applied, carefully controlled in quantity to minimize the addition of non-active material to the ribbon. While the glue is still setting, the second layer of fibers is placed on top. This layering process, where each preceding layer assists in the alignment and staggering of the next, is repeated until the desired number of layers, up to six, is achieved. The manufacturing process is designed to create two ribbons at once.

To address potential edge-related issues, primarily due to the small amount use of the adhesive, the ribbons are initially formed slightly wider than their final intended width. After being removed from the winding tool, these ribbons are then trimmed off, down to their specified width of 32.5 mm, by removing the surplus fibers along the edges. This meticulous method ensures the ribbons are constructed to the precise specifications needed for their application.

The bottom ribbon layer is composed of 128 fibers. These ribbons are then secured in a jig, where the so called SciFi end-pieces are glued to each of the ribbon ends. Figure 3.7 shows the jig and the end-pieces of the ribbon. The jig positions the ribbon

1 SciFi ribbons assembled by Coralie Husi, technical assistant of the mechanics group at the University of Geneva. Technique developed by A. Damyanova, PhD at the University of Geneva

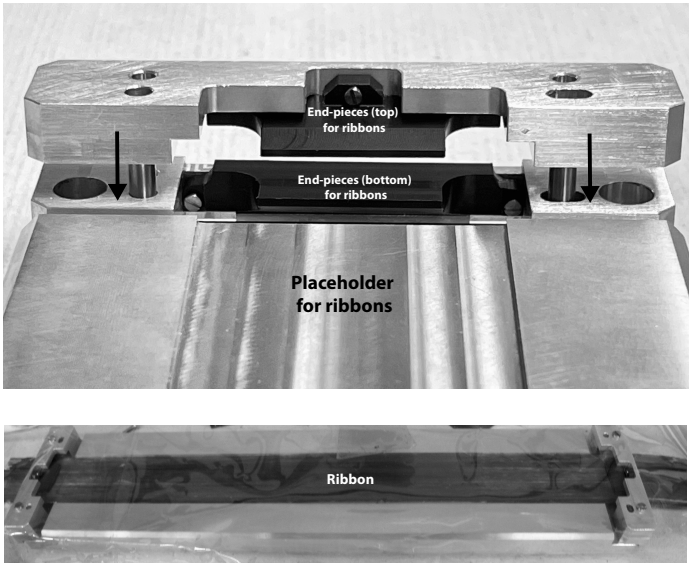

Figure 3.7: Top: close up of the jig used to glue the end-pieces to the ribbons. The jig is made of aluminium and has a placeholder for the ribbon. Two pieces of aluminium are used as clamps to press the end-pieces to the ribbon while the glue is setting. The end-pieces are made of a black plastic material, POM-C. Bottom: SciFi ribbon with end-pieces being glued on the jig. Jig designed by Franck Cadoux.

in the placeholder and two aluminium clamps serves to press the end-pieces to the ribbon while the glue is setting. The end-pieces are made of black plastic material POM-C, which is a polyoxymethylene copolymer. This material is used for its mechanical properties, such as its high stiffness, hardness, and strength. The end-pieces are glued to the ribbons using the same black epoxy as used for the ribbon assembly. Subsequently, the ribbons are cut to their designated length of 300 mm and undergo a diamond polishing process for a smooth finish. This cutting and especially the polishing process is done using a monocrystalline diamond cutting tool placed on a milling machine. Firstly, a rough cut is done to remove the extra fiber lenght and then a fine cut with the diamond tool. The cutting is done dry, so no lubrifiant used.

To evaluate the performance of the ribbons, three distinct adhesives have been tested. The initial set of ribbons was assembled using POLYTEC EP 601 epoxy, a two-component transparent adhesive with low viscosity. This adhesive solidifies at room temperature over a period of 12 hours.

For the second set, TiO_2 powder, was blended with the transparent epoxy constituting 20 % by weight. TiO_2 is a white pigment with a high refractive index, which is used for mainly two reasons:

1. to increase efficiency of the total internal reflection within the fibers by minimizing light losses, ultimately increasing the light yield;

2. to reduce the optical cross-talk between fibers by providing a reflective coating.

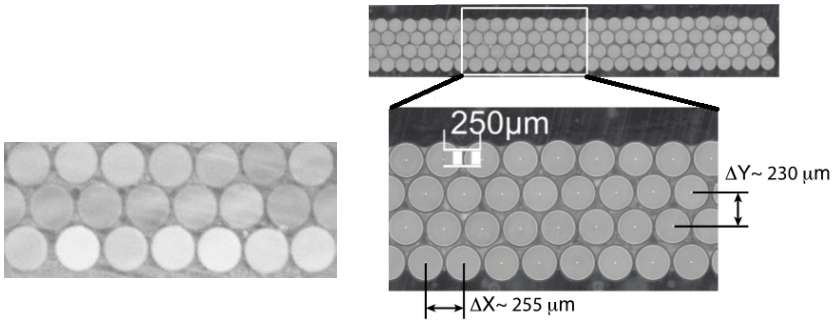

Figure 3.8: Left: close up cut view of a diamond polished 3-layer SciFi ribbon. Right: cut view of a diamond polished 4-layer SciFi ribbon with a close up, from [44].

Though incorporating TiO_2 to the adhesive is a common practice for assembling SciFi ribbons, its high atomic number (Z) is not compatible with the material budget restrictions of the Mu3e detector.

The final set of ribbons was constructed using POLYTEC EP 601-Black adhesive. This adhesive, similar to the first in being a two-component, low viscosity type, differs in its black color. This black adhesive was selected for the final assembly of the Mu3e fiber ribbons. It was found to reduce optical cross-talk between fibers. The reduction is attributed to the adhesive's enhanced ability to absorb non-reflected photons, thanks to its dark color.

3.3.2 *Fiber alignment*

Displayed in Figure 3.8 are the diamond-polished cross-section of 3-layer and 4-layer SciFi ribbon prototypes. The fibers within a layer exhibit a center-to-center spacing of 255 µm, maintaining remarkable uniformity across the ribbon. This specific 255 µm spacing results from the slight irregularities in the fiber cross-sections, which compensate when multiple fibers are arranged in the same layer. As indicated in Figure 3.8, the gap between layers is approximately 230 µm. Consequently, the total thickness reaches about 710 µm for a 3-layer ribbon and 940 µm for a 4-layer ribbon. Including the adhesive, the thickness of a 3-layer ribbons accounts for less then 0.2 % of a radiation length X_0. So the comparison of the ribbon's thickness to the radiation length indicates that the ribbon is thin enough to minimally affect the passage of a particle. The ribbon's fill factor stands at 82 %, slightly less than the 87 % that would be achieved in the tightest possible configuration where fibers are in direct contact. This suggests a high but not maximal density of scintillating fibers within the ribbon's cross-section, influenced by the practical necessities of ribbon construction and the inclusion of other materials like adhesives.

Within the Mu3e experiment, the magnetic field will bend the electrons/positrons from the muons decays, seen in Figure 2.4 . They will travel through the SciFi ribbons at angles ranging from 10° to 90°, with an average incidence angle of 27°. Figure 3.9 illustrates the effective thickness of the active scintillating material within the

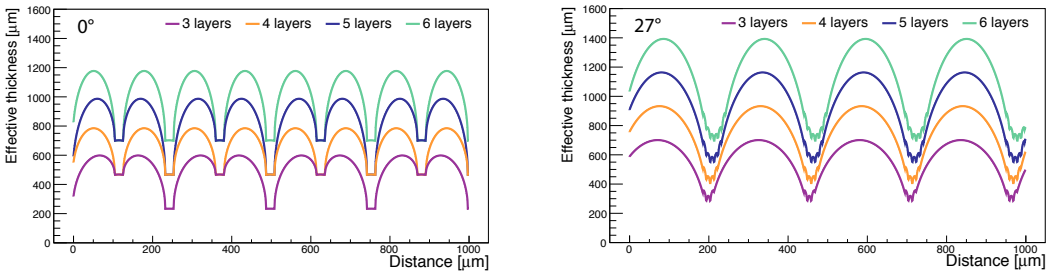

Figure 3.9: Showing the active material thickness within scintillating fibers traversed by particles at incidence angles of 0° (left) and 27° (right), plotted against various impact points along the ribbon. Varying numbers of staggered fiber layers, assuming an effective fiber diameter of 230 µm that excludes the cladding is shown.

fibers traversed by particles at incidence angles of 0° and 27°, relative to the ribbon's perpendicular axis. This thickness varies with the number of staggered fiber layers and the particle's impact location on the ribbon. The scintillating fibers are assumed to have an effective diameter of 230 µm, excluding the cladding. The quantity of light produced in scintillation, and thus the number of photons detected, is proportional to the thickness of the active material that the particles traverse within the ribbon. At a 0° angle incidence, the average active material thickness is 510 µm in a 3-layer ribbon and 680 µm in a 4-layer ribbon. This thickness tends to increase as the angle of incidence grows larger. At 27° angle incidence, which is an angle closely aligning with `Mu3e`'s average crossing angle, a effect is observed which accentuates the structure of the ribbon, seen in Figure 3.9 right. This effect can be called a resonance effect and is a consequence of the staggered structure of the ribbon. This resonance effect results in an average active material thickness of 580 µm for a 3-layer ribbon and 780 µm for a 4-layer ribbon at 27°. Additionally, as shown in Figure 3.9, it is apparent that achieving 100 % efficiency in the detector is not feasible.

4

SILICON PHOTOMULTIPLIERS

This chapter focuses on Silicon Photo-Multipliers (SiPMs), beginning with semiconductor basics, exploring the evolution of photo-detectors, and ending with SiPM arrays. These SiPM arrays are 128 channel devices, are the ones used for the Scintillating Fiber detector and are characterized at the end of the chapter.

4.1 SEMICONDUCTORS AND DOPED SEMICONDUCTORS

Semiconductors have an energy band structure with closely spaced levels, forming a continuum with a distinct energy gap (E_g). Governed by the Pauli exclusion principle, this structure is divided into the conduction band, which consists of free electrons, and the valence band, comprising bound electrons. The energy gap is the amount of energy required to excite an electron from the valence band to the conduction band. Typically, the energy gap for silicon (Si), which is the most comon semiconductor, is $E_g = 1.12\,\text{eV}$ and for germanium (Ge) is $E_g = 0.66\,\text{eV}$. It can happen from thermal excitation that electrons get excited into the condictive band.

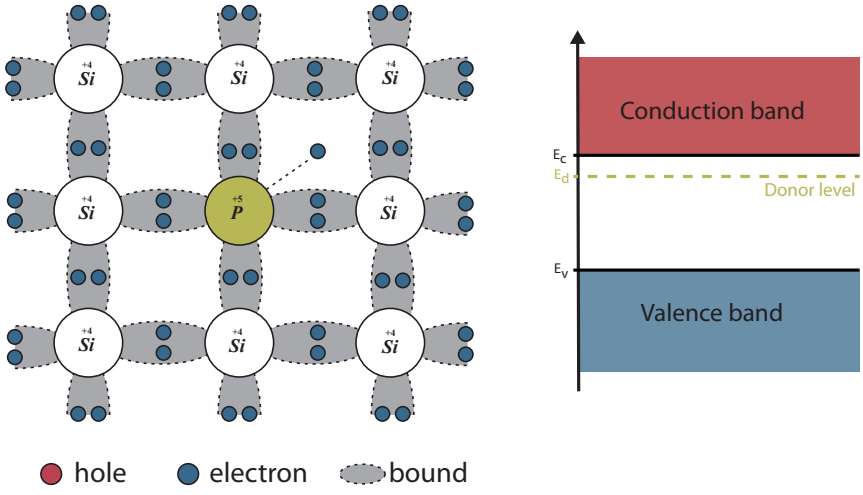

Figure 4.1: Donor impurity in a semiconductor, called n-doped semicondcutor. The donor (e.g. phosphorus) impurity has one more electron than the host atom (silicon) and therefore the electron is not bound to the atom and can move freely through the lattice. It creates a donor bound level just below the conduction band.

In a pure semiconductor, electron and hole concentrations are equal, where holes represent the absence of electrons in the valence band. Doping, or the process of adding impurities, disrupts this balance, increasing free electrons or holes, and so creating an

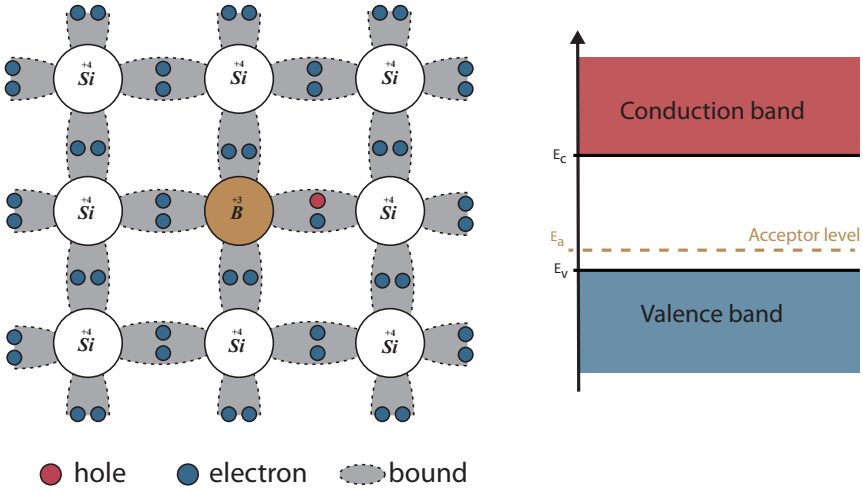

Figure 4.2: Acceptor impurity in a semiconductor, called p-doped semicondcutor. The acceptor (e.g. Boron) impurity has one less electron than the host atom (Silicon) and therefore the electron is bound to the atom. It creates an acceptor bound level just above the valence band.

extrinsic semiconductor. This involves introducing other atoms into the crystal lattice. Silicon, for example, can be doped with Group V elements (e.g., Phosphorous, Arsenic, Antimony) or Group III elements (e.g., Boron, Aluminium, Gallium). Dopants are either donors (e.g., Phosphorus) or acceptors (e.g., Boron). Group V doping creates n-type semiconductors with excess of electrons, while Group III doping leads to p-type semiconductors with more holes. Donor impurities add an extra electron compared to the host atom, making this electron not bound and free to move through the lattice. This results in a donor energy level just below the conduction band, close enough to allow easy excitation of the electron to the conduction band, leading to the formation of an n-type semiconductor. In contrast, acceptor impurities lack an electron, creating a bound hole. This generates an acceptor energy level just above the valence band, very close to it, thus creating a p-type semiconductor. Both doping types are shown in Figures 4.1 and 4.2.

4.2 THE PN-JUNCTION

When these doped semiconductors are put in contact with each other, electrons diffuse from the n-type to the p-type side, and holes from the p-type to the n-type side. The diffusion of charge carriers continues until the Fermi levels across the junction align. This migration leads to a depletion region with no mobile charge carriers. Because of the potential difference at both sides, an internal electric field is formed in the depletion region which acts as a barrier to stop the diffusion of electrons and holes and the net current flow becomes zero. This junction between p-type and n-type semiconductors (pn-junction) is fundamental for photo-detectors.

Applying an external voltage from the p to the n side, is called a foward bias. Doing this and if exceeding the built-in potential, allows current to flow and the pn-junction becomes conductive. On the contrary, a reverse bias (from the n side to the p side) strengthens the internal electric field, resulting in negligible current flow, provided the bias voltage stays below the breakdown voltage V_{bd}. Exceeding V_{bd} leads to an exponential increase in reverse current. Importantly, in the case of reverse bias, the width of the depletion region increases as the external voltage increases the internal electric field, further restricting the movement of charge carriers across the junction.

4.3 PN PHOTODIODE

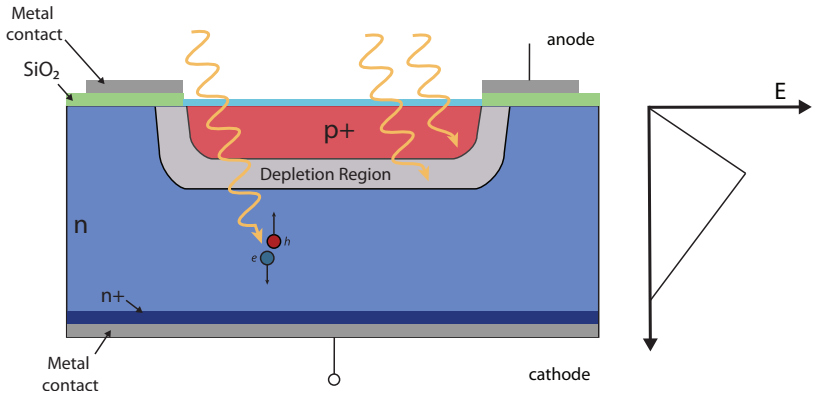

Figure 4.3: Schematic of a generic photodiode. Three different regions are shown where the electron-hole pair can be generated by the incident photon. The electrons and holes drift towards the cathode and anode whitout multiplication.

The base of a solid-state photodiode is the pn-junction which works in reverse bias. A generic PN photodiode is shown in Figure 4.3. The foundation of such a device is a n-type doped silicon with a p-type shallow diffused at a active surface. This forms the pn-junction. On the front and back side of the photodiode, a metal layer is deposited to create the contact pads. To reduce the reflection of light across specific wavelenghts, the active area is coated with an anti-reflective layer. This anti-reflective layer is usully made of silicon dioxide (SiO_2).

When a photon with an energy greater than the energy gap E_g of Si, hits the photodiode, the photon interacts with a bound electron in the valence band via the photoelectric effect and its energy is transferred to the electron. This creates an electron-hole pair in the p-type layer, depletion region, or in the n-type layer depending on the wavelenght of the incendent photon. For short wavelenghts, the photon is absorbed in the p-type layer and for long wavelenghts, the photon is absorbed in the n-type layer.

The electric field in the pn-junction is mostly in the depletion region, so the charge carries generation is confined in it. Electron-hole pair in a photodiode can be generated in one of three distinct locations by an incident photon, shown in Figure 4.3, each affecting the device's photo-current differently:

- In the depletion region: in this region, the electric field causes the electrons and holes to drift in opposite directions: electrons from the p-side towards the n-side, and holes are driven from the n-side towards the p-side. Recombination is unlikely, so each photo-generated carrier adds a charge q to the current flowing to the device's electrodes.
- Far away from the depletion region: the electron-hole pair recombines after some time without contributing to the signal, thus having no impact.
- Close to the depletion region: pairs created near the depletion region can diffuse into it due to random movement. An electron originating from the p-side or a hole from the n-side may quickly cross the junction. When this happens, it contributes to a charge q.

The collected charges result in a output current which is proportional to the intensity of the incident light. Also no multiplication of the charge carriers occurs in a PN photodiode.

4.3.1 *Characteristics of photodiodes*

Current-voltage

The current in a photodiode can initially be approximated using the Shockley ideal diode equation:

$$I_{photodiode} = I_{sat}\left(\exp(\frac{qV_{bias}}{nk_BT}) - 1\right) \tag{4.1}$$

where I_{sat} is the saturation current, V_{bias} is the bias voltage across the diode, n is the ideality factor, k_B is the Boltzmann constant and T is the temperature. The factor n, influenced by the fabrication process and semiconductor material, typically ranges from 1 to 2. The reverse bias saturation current, I_{sat}, results from the diffusion of minority carriers: electrons (minority carriers in the p-region) moving from the p-side to the n-side, and holes (minority carriers in the n-region) moving from the n-side to the p-side. Consequently, it is dependent on both the density of these minority carriers and the diffusion coefficients of electrons and holes. In Si based pn diodes, the ideal Shockley equation provides only a qualitative agreement with the reverse current-voltage characteristics of actual devices. This is due to effects such as surface effects, carrier generation in the depletion region through thermal effects, and tunneling currents.

The current of a PN photodiode in function of the voltage (IV) curve operated in dark, is shown in Figure 4.4. When a photodiode is exposed to light, it's IV curve shifts by the value of the photo-current I_{ph} which is proporional to the photon flux. So the total current when exposed with light can be written as:

$$I = I_{sat}\left(\exp(\frac{qV_{bias}}{nk_BT}) - 1\right) - I_{ph} \tag{4.2}$$

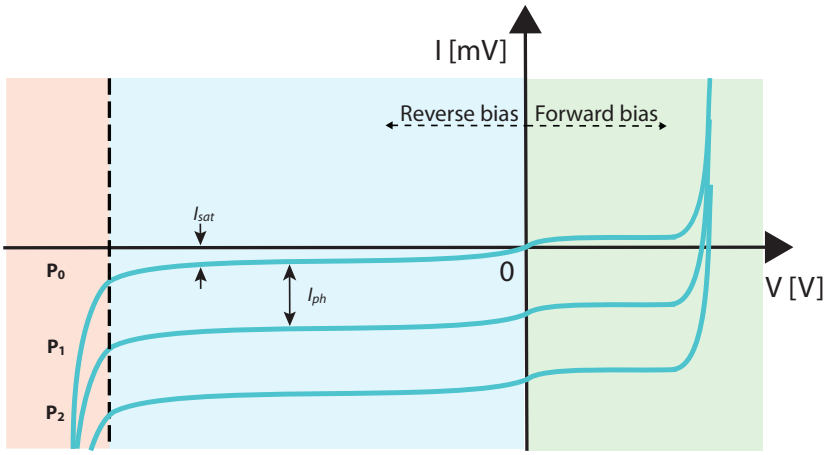

Figure 4.4: Current-voltage (IV) characteristics of a photodiode. I_{sat} is the saturation current. I_{ph} is the photo-current. P shows current at different light levels (P_0 is for no incident light). The reverse bias section (in blue) with the breakdown voltage next to it (in red) and the forward bias section (in green) are also shown.

Depending on the bias voltage applied, a photodiode can function in either photovoltaic mode (with no reverse bias) or photo-conductive mode (with a few volts of reverse bias). The photo-conductive mode has a very linear response.

Responsivity

The responsivity R_λ of a photodiode indicates how effectively it converts light power into electrical current. It is the ratio of the photo-current I_{ph} to the incident optical power P_{opt}:

$$R_\lambda = \frac{I_{ph}}{P_{opt}} \tag{4.3}$$

Responsivity varies with the wavelength of the incident light, and it slightly increases with applied reverse bias and changes with temperature. It has usually the units of amperes per watt (A/W).

Quantum efficiency

The quantum efficiency of a photodiode is the fraction of incident photons contributing to the photo-current, and it is related to the responsivity.

$$QE = R_\lambda \frac{hc}{\lambda e} \tag{4.4}$$

where λ is the wavelength of the incident light in nm, R_λ the responsivity and e is the electron charge (h is the Planck constant, c is the speed of light). A Si photodiode is considered linear, if the generated photo-current increases linearly with incident light

power. In other words, linearity reflects consistent responsivity over a range of light power.

Noise

Photodiodes have a light detection lower limit set by their noise characteristics. Total noise combines thermal (or Johnson noise) and shot noise. The Johnson noise is determined by the thermal generation of the charge carriers in the shunt resistance, which represents the resistance of a unbiased photodiode junction. The thermal noise is predominant in photovoltaic mode. The shot noise, dominant in photo-conductive mode, is related to the statistical fluctuations in both the diode dark current and the photo-current.

4.4 PIN PHOTODIODE

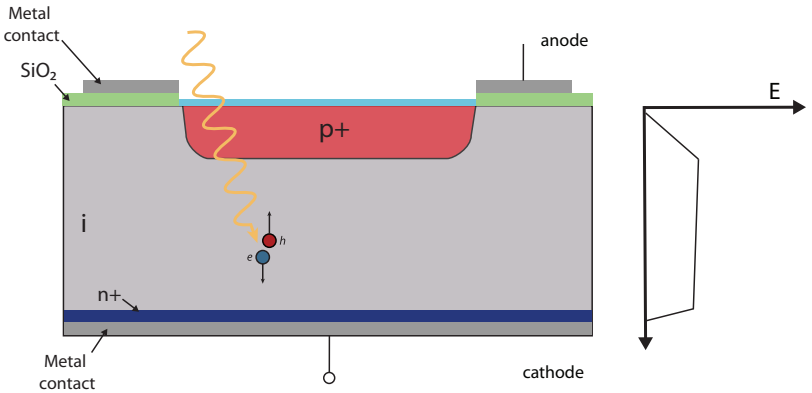

Figure 4.5: Schematic of a PIN photodiode. The depletion region is now located in the lightly n-doped intrinsic layer.

A PIN photodiode is a pn junction with a wide, lightly n-doped intrinsic (*i*) region between the p-type and n-type layers. The depletion region is now located in the *i* layer. Most of the photons are absorbed in the intrinsic layer and the carriers generated in this region contribute to the current. The PIN photodiode is shown in Figure 4.5.

In comparison to the PN photodiode, the PIN variant has an larger depletion region which allows for a more efficient collection of the charge carriers and therefore has a higher quantum efficiency for incident photons with longer wavelenghts (because a wider sensitive area). Furthermore, it has no internal amplification (the gain is equal to one) meaning that the number of charge carriers is determined by the number of incident photons and the quantum efficiency.

4.5 AVALANCHE PHOTODIODE

An avalanche photodiode (APD) is essentially a PIN photodiode designed to operate at higher reverse bias. This design allows photo-electrons, which are valence electrons excited to the conduction band by incident photons, to be accelerated by the electric field in the depletion region. When they gain enough kinetic energy, they collide with other atoms in the semiconductor, triggering impact ionization. This process creates additional electron-hole pairs, which are also accelerated and produce additional charge carriers. This process occuring repeatedly, is called the avalanche effect. Those devices have increased light sensitivity since the signal (even small) are amplified by a certain mulitplication factor (gain).

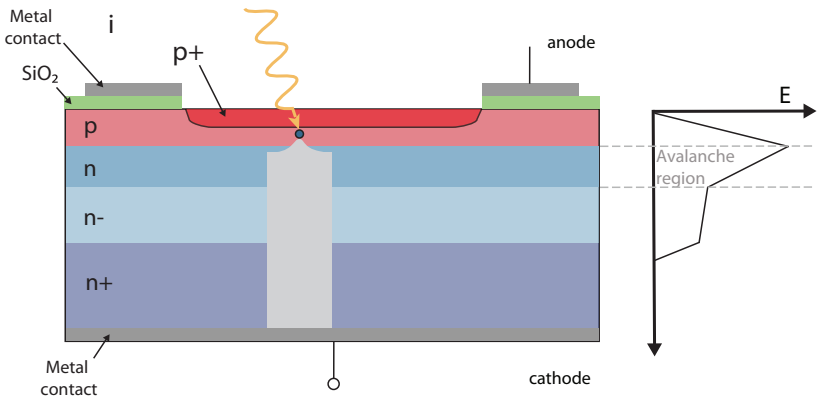

Figure 4.6: Schematic of an avalanche photodiode (APD). An APD is operated under rever bias voltage that is sufficient to enable the avalanche mulitplication.

The structure of a APD is shown in Figure 4.6. Incident photons interact with the upper layer which is a p-type layer. Around the pn junction an avalanche is formed and the multiplied charge carries drift through the n- and n+ type layers. The n-layer role is to reduce the capacitance of the device and the gain dependence on the bias voltage as well. Advanced APDs are capable of detecting single photons but can be a challenge. The key to detecting single photons lies in maximizing the signal-to-noise ratio (SNR). This can be done by cooling the APD to reduce thermal noise and using low-noise electronics. Also, they need amplification stages as the current generated by a single photon is small even with the gain.

4.5.1 *Characteristics of a APD*

Gain of an APD

As an APD offers internal amplification, the output signal (I_{signal}) current is :

$$I_{signal} = MR_0(\lambda)P_{opt} \tag{4.5}$$

where M is the gain of the APD, R_λ is his responsivity and P_{opt} is the incident optical power. The gain is a function of the applied bias voltage V_{bias} to the APD. Typical gains are in the range of 50 to 10^3. To increase SNR and especially achieve single photon detection, amplifiers are used to further amplify the signal since internal gain is not enough.

Dark current

The dark (leakage) current in an APD is composed of two main components:

- the surface leakage current, $I_{surface}$, which flows through the interface between the PN junction and the Si oxide layer on the diode surface;
- the internal current, I_{bulk}, generated within the Si substrate.

The surface leakage current isn't amplified since it doesn't pass through the avalanche region, whereas the internal current, flowing in this region, is multiplied by a multiplication factor M. As a result, the total dark current is given by:

$$I_{leakage} = I_{surface} + MI_{bulk} \tag{4.6}$$

Noise critical parameters

As an APD is designed to be operated under a reverse bias, sensitivity at low light levels will be limited by the shot noise and the APDs leakage current. Dark current shot noise is normally given, for PIN photodiode, by $i_{sn_{dark}} = \sqrt{2eI_{leakage}B}$, where B is the bandwidth of the system. In a APD this is different, as the bulk leakage current I_{bulk} is amplified by the gain of the APD (equation 4.6). Moreover, due to the fact that the avalanche process is a random process, the gain and consequently the output signal can exhibit fluctuations. This is called the excess noise factor (F) and the APD performance is degraded by this compared to a PIN photodiode. The excess noise factor is a function of the carrier ionization ratio, k, where k is usually defined as the ratio of hole to electron ionization probabilities ($k < 1$). The total noise current for an APD in dark conditions is thus given by:

$$i_{sn_{dark}} = \sqrt{2e(I_{surface} + I_{bulk}M^2F)B} \tag{4.7}$$

When exposed to light, the device transitions to the photon shot noise limited regime. In this regime the sensitivity is limited by photon shot noise on the current generated by the optical signal. Total noise from the APD exposed to light, will therefore equal the quadratic sum of the detector noise ($i_{sn_{dark}}$) with the signal shot noise $i_{sn_{signal}} = \sqrt{2qI_{signal}B}$:

$$i_{sn_{total}} = \sqrt{2e(I_{surface} + (I_{bulk}M^2 + R_0(\lambda)M^2P_{opt})F)B} \tag{4.8}$$

Conclusion is that an APD, without other noise sources, offers a signal-to-noise ratio (SNR) that is $\sqrt{F}$ lower than that of a PIN photodiode with equivalent quantum

efficiency. However, an APD can achieve a superior overall system SNR compared to a PIN detector when its internal gain amplifies the signal without significantly increasing the system noise.

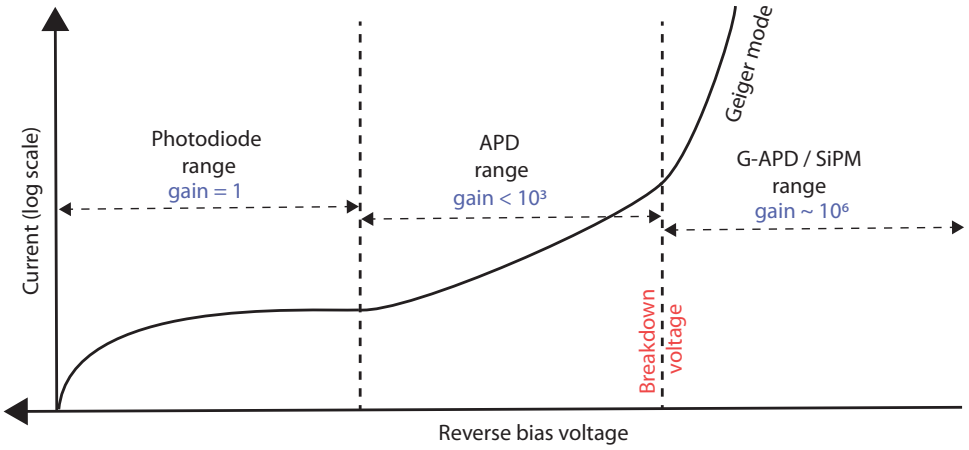

Figure 4.7: Schematic of the voltage-current characteristic of the previous and G-APD devices. A G-APD is a APD which is operated in reverse bias above the breakdown voltage (V_{bd}).

4.6 GEIGER MODE OPERATED APD

To increase the gain of an APD, a high and stable electric field within the depletion region is required. This high electrical field is achieved by operating the APD in Geiger mode. An APD in Geiger mode (G-APD) is operated in a reverse bias voltage above the breakdown voltage (V_{bd}) (Figure 4.7). In this mode, the avalanche is saturated and both electrons and holes trigger a discharge while accelerating towards the anode and the cathode. This process leads to a self-sustaining avalanche or discharge, with the population of electrons and holes in the high electric field and the associated current increasing exponentially to very high values. This discharge is called a Geiger discharge.

To make the G-APD detect next photon events this current growth must be stopped. To do so, a quenching mechanism is used by implementing in series a quenching resistor (R_q) within the device. This R_q in series interupts this growth of the current (I_{G-APD}) by reducing the voltage across the junction.

$$V_{bias} = V_{bd} + \Delta V - (I_{G-APD} R_q) \tag{4.9}$$

where ΔV (or V_{ob}) is the voltage applied above the breakdown voltage V_{bd}, called the overbias. Once the voltage across the junction falls below the breakdown voltage V_{bd}, the electric field in the depletion region is no longer strong enough to sustain the avalanche process. The generation of new charge carriers ceases, effectively stopping the avalanche.

Following the quenching, a brief recovery phase (or recharge) is required re-establishing its initial state with the bias voltage reset above the breakdown level. The different steps are illustrated in Figure 4.8. If the recovery time is too long then the G-APD is not able to detect another photon because the G-APD is still in the Geiger discharge. Having a short recovery time is therefore important for the G-APD. The recovery time (τ_{rec}) is determined by the quenching resistor (R_q) and the capacitance of the APD ($C_{\mu cell}$) :

$$\tau_{rec} = \exp\left(\frac{-t}{R_q C_{\mu cell}}\right) \tag{4.10}$$

With a small quenching resistor, the recovery time is shorter making the G-APD able to detect high rates. However, the noise is also larger because the quenching resistor is smaller. So there is a trade-off between the recovery time and the noise. Also the capcitance of the APD is important. The capacitance of the APD is proportional to the sensitive area of the APD and therefore the capacitance increases with the sensitive area. It is also proportional to the excess noise factor and therefore the noise is larger for a larger sensitive area. So there is also a trade-off between the sensitive area and the noise for the APD operated in Geiger mode.

When biased above the breakdown voltage, the state of the device remains in an OFF state. With no current flowing, until an electron or hole triggers an avalanche, switching it to the ON state. Avalanche initiation has a turn-on probability, representing the likelihood of a carrier initiating a current pulse that grows exponentially under constant conditions. Real-world factors like contact resistance or diode heating limit this current growth. The G-APD has a high gain $\mathcal{O}(10^6)$. Howerever, a G-APD is a binary device so it cannot differentiate between events involving one or two incident photons once a discharge is initiated. Consequently, the recovery time of these devices becomes again a critical factor.

In both APDs and G-APDs, the electric field within the depletion region is the primary factor determining the gain and an important factor to consider when designing these devices. For APDs in linear mode, the electric field is designed to be high enough to accelerate charge carriers and induce impact ionization, thereby amplifying the photo-current. However, the field strength remains below the threshold that would lead to a self-sustaining avalanche. In contrast, G-APDs are biased above the breakdown voltage, creating an electric field intense enough to not only accelerate carriers but also sustain an avalanche from a single photon interaction, a Geiger discharge. The precise control over the electric field distribution ensures efficient carrier multiplication while minimizing noise and dark counts, thereby maximizing the device's performance

4.7 SILICON PHOTOMULTIPLIER

Also known as Multi-Pixel Photon Counters (MPPC), SiPMs consists of arrays of APDs operating in Geiger mode. SiPMs address the limitations of G-APDs by enabling single-photon detection, exhibiting low dark count rates (DCR), and providing high photon detection efficiency. They use a large number of small APDs in a matrix structure,

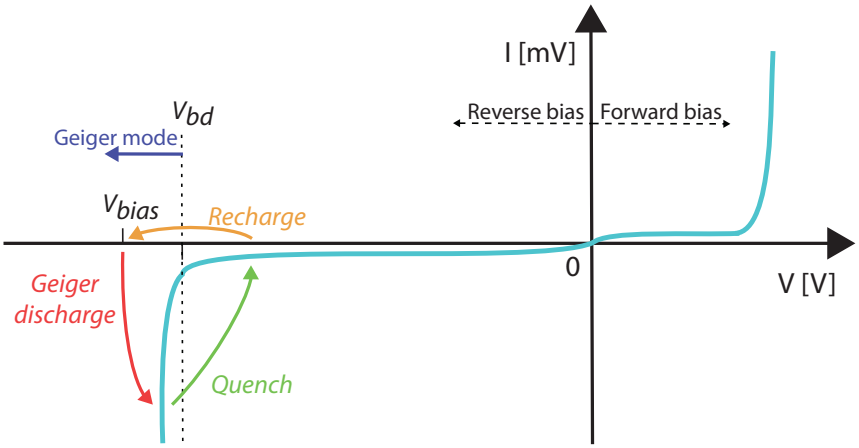

Figure 4.8: Illustration of the biasing mechanism in APD cells, focusing on the Geiger mode operation. Exceeding the breakdown voltage in a cell leads to a Geiger discharge initiated by photon interaction in the active area, followed by quenching through a resistor. This causes a reduction in the electric field, necessitating a brief period of recovery before the formation of subsequent avalanches.

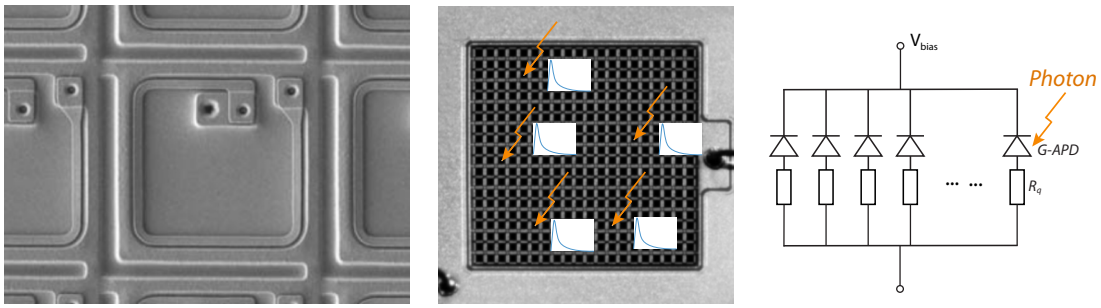

Figure 4.9: One channel SiPM device with the micro-cells (pitch 25 µm) visible. Picture of individual micro-cells with a metal-composite quenching resistor fabricated around each micro-cell on then left. In the middle, all the micro-cells in one channel. On the right, a simplified circuit of the SiPM, where each micro-cell is represented as a diode in series with a quenching resistor. All the micro-cells are connected in parallel.

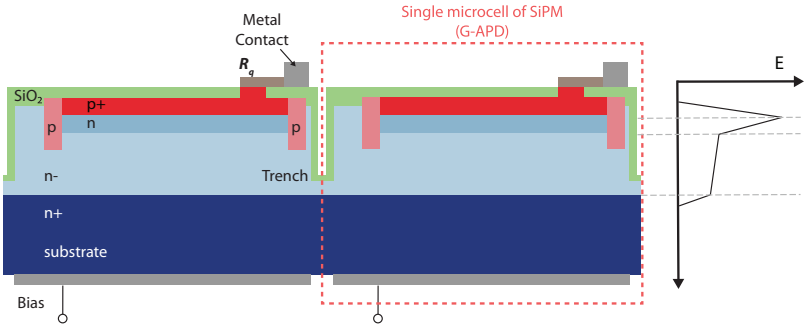

Figure 4.10: Schematic of a SiPM. The SiPM is an array of avalanche photodiodes (APD) operated in Geiger mode.

called micro-cells or pixels, operating in Geiger mode and connected in parallel with a common cathode. Each micro-cell's output is independent, allowing parallel readout. The output signal is the sum of the signals from all the fired micro-cells and so the total current is proportional to the number of incident photons. A picture of the matrix and a single micro-cell of a single channel SiPM is shown in Figure 4.9.

When a photon hits the SiPM, it triggers a Geiger discharge in a micro-cell. The output signal of each micro-cell when operated in Geiger mode is very close to the same amplitude, which is determined by the uniformity of each micro-cell and the individual quenching resistors R_q. Because all the micro-cells work together in parallel on a common load, the output signal is the sum of the signals from all the fired micro-cells. As seen in the left of Figure 4.9, each micro-cell of a channel can be simplified as a diode in series with a quenching resistor. So the device, where each micro-cell behaves as a binary element, works analogously as an analog device and can measure the light intensity. The output charge is in principle, proportional to the number of incident photons in different micro-cells. The limitation lies in the number of micro-cells in the device and the probability that two or more photons strike the same micro-cell, which is determined by the micro-cell's size.

A schematic of two micro-cell in a SiPM is shown in Figure 4.10. A photon is absorbed in a highly doped (p+) silicon layer in one micro-cell, triggering the Geiger discharge. The micro-cells which are build in a thin layer, are represented by the pn-junction and a quenching resistor (R_q). The micro-cells are connected in parallel through a common Si substrate, a hilghy doped (n+ type) layer, which is $\simeq 300\,\mu m$ thick to make the device more robust. Guard rings (p) situated between the micro-cells, are used to prevent a too high electric field at the edges of the micro-cells and to reduce the cross-talk between the micro-cells. The guard rings are also used to reduce the dark current and to reduce the afterpulsing (see later). The anti-reflective coating, made from SiO_2, covers the active surface and is used to improve the light transmission.

4.7.1 *Characteristics of a SiPM*

4.7.1.1 *Breakdown voltage*

The breakdown voltage is the voltage at which the electric field in the depletion zone is strong enough to create a Geiger discharge. To determine the breakdown voltage, the dark current can be measured as a function of the voltage and when the dark current starts to increase exponentially, the breakdown voltage is reached. In general, SiPMs are operated with a few volts higher than the breakdown voltage to ensure that all the micro-cells are operating in Geiger mode.

4.7.1.2 *Gain*

The gain of a SiPM is the ratio of the number of charge carriers created to the number of incident photons. In other words, it is defined as the amount of charge collected induced by a single photon. It can be expressed as followed:

$$G = \frac{Q}{e} = \frac{C_{\mu cell}\Delta V}{e} \tag{4.11}$$

where Q is the amount of charge collected, , $C_{\mu cell}$ is the capacitance of the micro-cell (also know as junction capacitance) and ΔV is the overbias. Typical values for the gain of a SiPM are $\mathcal{O}(10^6)$ [47]. As can be seen in equation 4.11, the gain depends linearly on the overbias ΔV and on the capacitance $C_{\mu cell}$ of the micro-cell. In fact, the capacitance of a micro-cell is proportional to the sensitive area of the cell. For a bigger surface area, the capacitance is larger. The range of the capacitance of a single micro-cell varies from a few femtofarads to tens of femtofarads[47, 48]. Additionally, it's worth noting that increasing the quenching resistor (R_q) to allow for a higher overbias can lead to an increase in gain.

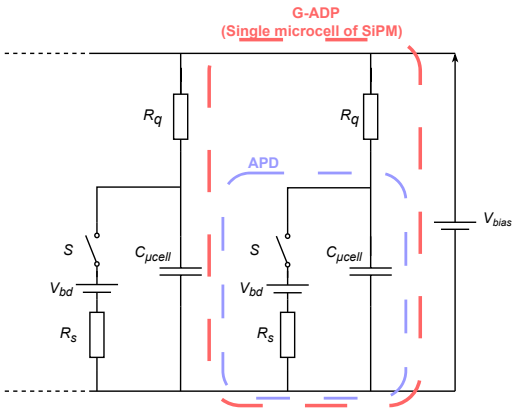

Figure 4.11: Equivalent circuit of the SiPM according to the Corsi model [45, 46].

4.7.1.3 *Pulse Shape*

To understand better, the SiPM can be represented with an equivalent circuit as shown in Figure 4.11. This simplified and equivalent circuit is called the Corsi model [45, 46]. All the micro-cells in Figure 4.11 are connected in parallel and are biased via a common cathode. The quenching resistor is represented by R_q. The circuit is a parallel combination of a capacitor $C_{\mu cell}$ with a series combination of a switch S, V_{bd} representing the breakdown voltage and a resistor representing the full single micro-cell resistance during the Geiger discharge R_S. In the absence of light and excluding the influence of dark counts that generate dark current, this system remains in an open state, represented by the switch S. During this state, the voltage across the component $C_{\mu cell}$ is maintained at a constant value of V_{bias}, where V_{bias} exceeds the breakdown voltage V_{bd}.

This state reflects the light sensitivity of the micro-cell and the operation of the avalanche photodiode (APD) in Geiger mode. Upon absorption of a photon by the micro-cell, an electron-hole pair is generated, and one of these charge carriers migrates towards the avalanche region, where it can initiate an avalanche process. When the avalanche begins, the switch S transitions to a closed state, leading to the discharge of the capacitor $C_{\mu cell}$ through the resistor R_S (R_S significantly smaller than R_q) with a time constant $R_S C_{\mu cell}$. Consequently, the voltage across the capacitor $C_{\mu cell}$ diminishes, reducing the likelihood to start an avalanche process. By optimizing the value of R_q, the probability of initiating an avalanche becomes so small that the avalanche quenches. At this point, the switch S returns to an open state, and the V_{bias} recharges the capacitor $C_{\mu cell}$ with time constant $\tau_{rec} \sim R_q C_{\mu cell}$, thereby restoring the initial state of the micro-cell.

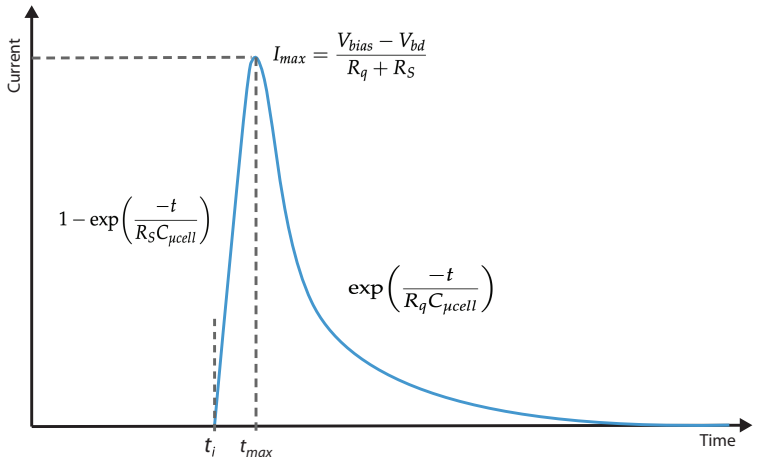

Figure 4.12: Pulse shape of a SiPM. The pulse starts at the time t_i and quenches at the time t_{max}. The rise time τ_r is proportional to the capacitance of the micro-cell $C_{\mu cell}$ and the resistor R_S. The recovery time τ_{rec} is proportional to the quenching resistor R_q and the capacitance of the micro-cell $C_{\mu cell}$.

A pulse of a SiPM is shown in Figure 4.12. One can see that the pulse and therefore the avalanche starts at the time t_i and quenches at the time t_{max}. The rise time of this leading edge strating at t_i is proportional to the capacitance of the micro-cell $C_{\mu cell}$ and the resistor R_S, seen in the equation 4.12.

$$t_i = \tau_r = 1 - \exp\left(\frac{-t}{R_S C_{\mu cell}}\right) \tag{4.12}$$

After the quenching, the recovery time τ_{rec} starts which is the time needed to recharge the micro-cell. This decline is proportional to the quenching resistor R_q and the capacitance of the micro-cell $C_{\mu cell}$, seen in the equation 4.13.

$$\tau_{rec} = \exp\left(\frac{-t}{R_q C_{\mu cell}}\right) \tag{4.13}$$

4.7.1.4 *Photon detection efficiency*

The photon detection efficiency (PDE) is the probability that a photon is detected by the SiPM. It is the ratio of the number of detected photons $N_{detected}$ to the number of incident photons $N_{incident}$. It is defined as followed:

$$PDE = \frac{N_{detected}}{N_{incident}} = QE(\lambda)\, \epsilon(\Delta V)\, f \tag{4.14}$$

where $QE(\lambda)$ is the quantum efficiency which depends on the wavelenght λ , $\epsilon(V_{ob})$ is the probability of Geiger discharge wich depends on the overbias ΔV and f is the geometrical fill factor.

The quantum efficiency $QE(\lambda)$ of a given photon with a given wavelenght λ is the probability that the photon generates a electron-hole pair capable of triggering a Geiger discharge in the depletion region of the SiPM. In the SiPM, the desired range of wavelenght means optimizing the thickness of the depletion zone. For each material the QE is different. The fill factor (f) is the ratio of the sensitive area of the SiPM to the total area of the SiPM. Because some regions of the SiPM are not sensitive to light some inefficiencies are introduced. They can come from the guard rings, the micro-cell gaps, the inactive edges, the inactive corners as the quench resistors and the bonding pads. Different SiPMs have different fill factors. The values ranges from 30% to 80% [49]. The probability of a Geiger discharge $\epsilon(\Delta V)$ is the probability that a micro-cell is operated in Geiger mode. Note that this probability is proportional to the overbias and the QE depends on the wavelenght of the incoming photon. Considering that PDE is linked to overbias, using a higher quenching resistor may indirectly enhance the SiPM's PDE.

4.7.2 *Dark count rate and afterpulsing*

The Dark Count Rate (DCR) is the number of pulses per second in dark conditions and determines the minimum count rate at which the signal is dominantly caused by real

photons. The main cause is the thermal generation of carriers in the depletion region. This happens when an electron in the valence band gains enough kinetic energy by interaction with a phonon of the lattice and is excited to the conduction band. This leaves a hole in the valence band. From the Bose-Einstein distribution, the number of phonons generally increases as the temperature T increases. [1] Therfore this occurence is proportional to the temperature and to the number of charge carriers in the depletion region. Typically, for a $\Delta T = 10\,^{\circ}\mathrm{C}$, a factor of 2 in the DCR is observed.

In the case of tunneling, the carriers are able to tunnel through the band gap of the semiconductor. This can lead to a avalanche process because the carries that tunneled to the conduction band can be accelerated by the electric field [50].

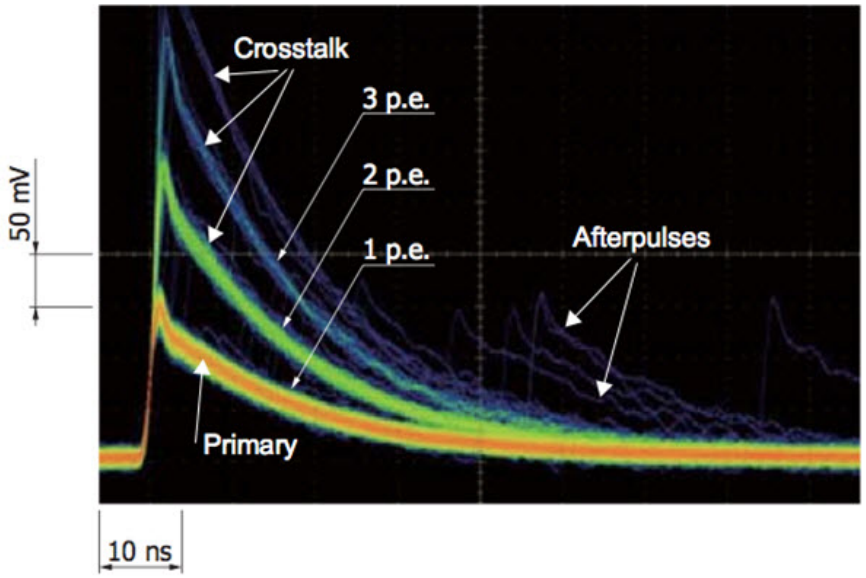

Figure 4.13: Example of an output signal of a SiPM. The oscilloscope trace is set to persistence mode to see the different pulses. In this example a high gain has been used and the signals have a slow rise time. Image from [49].

Afterpulsing, another factor in DCR, occurs when pulses are triggered during the recovery time of a previous pulse. This happens due to the release of carriers trapped in the primary avalanche, initiating a new avalanche (see Figure 4.13). Afterpulses typically have a smaller amplitude than primary pulses, as they involve fewer charge carriers. Their amplitude is related to the voltage difference between breakdown voltage and micro-cell capacitance $C_{\mu cell}$, and their probability, being proportional to the number of charge carriers, is relatively low. Minimizing afterpulsing can be achieved by using a larger quenching resistor, which extends the recovery time but reduces the likelihood of detecting subsequent photons during this period. Longer recovery times also increase the detector's dead time, presenting a trade-off between

1 However, it's important to note that the relationship is not linear, and it depends on the specific energy level of the vibrational mode being considered. It is not a simple direct proportionality.

reducing afterpulsing and increasing the dead time. Also direct and delayed cross-talk can contribute to the DCR.

4.7.2.1 *Optical cross-talk*

A significant source of noise also arises from optical cross-talk between the micro-cells. During an initial avalanche which is triggered by a photon, accelerated electrons whitin the high field region can emit photons, which induce secondary avalanches in a neighboring micro-cell. This process is called optical cross-talk. There are three types of optical cross-talk.

- Direct cross-talk occurs almost instantaneously with the primary avalanche that give the primary pulse (Figure 4.13). It is caused when photons generated from the primary avalanche in one micro-cell directly trigger an avalanche in a neighboring micro-cell without any significant delay. This process is facilitated by the very short distance between the micro-cells and the high probability of photon absorption in neighboring cells. The main charaterictic is that the signal from direct crosstalk appears almost simultaneously with the signal from the primary avalanche, making it challenging to distinguish between the two.
- Delayed cross-talk occurs when the photon generated in one micro-cell doesn't immediately affect a neighboring micro-cell. Instead, it creates an electron-hole pair near a neighboring micro-cell. These charge carriers can then diffuse or migrate to the nearby micro-cell over a short period of time. Once they reach the neighboring micro-cell, they can contribute to an avalanche. This process introduces a delay compared to direct cross-talk. Delayed cross-talk signals are temporally separated from the primary event, usually by a few nanoseconds to even microseconds in some cases.
- Indirect cross-talk involves the photon being reflected at one of the layer interfaces within the sensor. This reflected photon can then travel to a neighboring micro-cell through a more complex, indirect path. The indirect cross-talk pathway may involve multiple reflections or interactions before reaching the neighboring micro-cell. This type of cross-talk can have a wider range of time delays compared to direct or delayed crosstalk and can affect micro-cells farther away from the original avalanche site.

The probability of optical cross-talk is proportional to the number of charge carriers created in the avalanche process. Therfore, the optical cross-talk is proportional to the overbias and the probability of a Geiger discharge. By adding trenches or guard rings around the micro-cells, the optical cross-talk can be reduced but this reduces the fill factor and therefore the PDE.

4.7.2.2 *Dynamic range*

The dynamic range of a SiPM is defined as the spectrum of light intensities it can effectively handle, from the lowest detectable level to the highest without saturation or

accuracy loss. A large dynamic range is essential for simultaneous multiple photons counting and is achieved by using many micro-cells. The SiPM's response to incident photons should ideally be linear, though saturation occurs at high light levels due to limited micro-cells and recovery time constraints. If photons arrive in close succession, the SiPM might not differentiate them. The dynamic range relates to the ratio of fired micro-cells $N_{\mu cell}$:

$$N_{\mu cell_{fired}} = N_{\mu cell}\left(1 - \exp\left(\frac{-PDE\ N_{ph}}{N_{\mu cell}}\right)\right) \tag{4.15}$$

where N_{ph} is the number of incident photons and PDE is the photon detection efficiency. It can be seen that the dynamic range is proportional to the number of micro-cells and to the PDE.

4.7.2.3 *Time Resolution*

SiPM have a very good time resolution, owing to their small size and rapid Geiger discharge. Their intrinsic time resolution is described with the parameter called single photon timing resolution (SPTR). The SPTR for Hammatshu SiPMs ranges from 10 ps to 220 ps [51]. The resolution improves with more incident light due to the statistical nature of photon detection. The SPTR of the SiPM array `S13552-HRQ` is ∼220 ps.

4.7.2.4 *Temperature dependence*

Temperature impacts the breakdown voltage of an APD, influencing the gain and overbias of a SiPM. An increase in temperature leads to a decrease in breakdown voltage, resulting in reduced gain. Specifically, the breakdown voltage of Hamamatsu SiPMs rises linearly with temperature at approximately 54 mV/°C [52]. Additionally, both the DCR and afterpulsing rates increase with temperature due to a rise in the number of charge carriers. The PDE is also temperature-dependent, as it is influenced by the QE, which varies with temperature.

4.8 SIPM READOUT

In the course of the measurements, various types of SiPMs have been employed to suit the specific measurement objectives and applications at hand. In the initial phase of the investigation involving single scintillating fibers, single-channel devices are used. As the study progressed to examine scintillating fiber ribbons and, ultimately, the development of the scintillating fiber tracker, multi-channel SiPM arrays are employed. The acquisition of data from the SiPMs was done with dedicated readout electronics, the details of which will be elaborated in subsequent sections.

4.8.1 *Single-channel SiPM*

The single-channel SiPMs used in this work are the Hamamatsu devices `S13360-1350CS` and `S13360-3050CS`. The `S13360-1350CS` is a 1.3 mm × 1.3 mm SiPM with the micro-cells size of 50 µm × 50 µm and with a fill factor of 74 %[53]. These sensors will be directly coupled to the scintillating fibers as explained later, and readout with amplifiers direclty via the anode and the cathode. A picture of this SiPM is shown in figure 4.14.

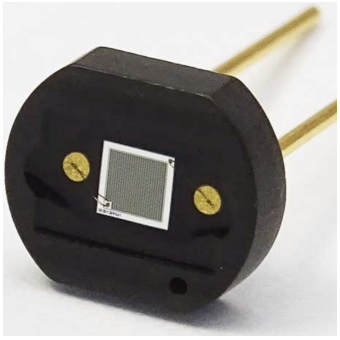

Figure 4.14: A picture of the Hamamatsu `S13360-1350CS` single-channel SiPM. The device constists of a matrix of 3600 micro-cells, each measuring 50 µm in width.

The PDE of SiPMs, like the `S13360-1350CS`, is consistent across much of the light spectrum emitted by scintillating fibers (see Figure 3.4). Operating these SiPMs at an overbias of 3 V results in a PDE of around 40 %. The `S13360-3050CS`, with a 3 mm × 3 mm size, is used for reading out the trigger scintillator and exhibits a similar PDE of about 40 % [53].

4.8.2 *Multi-channel SiPM array*

The SiPM used in the second phase of this work, namely the Hamamatsu device `S13552-HRQ`, is a multi-channel SiPM array [54]. This SiPM array consists of 128 channels and has a high quench resistance $R_q = 500\,\text{k}\Omega$ to be able to operate at high overbias. By operating at high overbias, the gain and the PDE of the sensor are increased. The drawback is that the recovery time is less optimal for very high rates.

The arrays is formed by 2 dies of 64 channels each with a 220 µm gap between the dies. Each channel has 4 columns of 26 micro-cells with a micro-cell size of 57.5 µm × 62.5 µm. The micro-cells are divided by trenches utilizing the fifth-generation Hamamatsu low-crosstalk development (LCT5). The segmentation can be seen in a close up view of the SiPM in figure 4.15. A 20 µm gap seperates the columns which results in a 250 µm readout pitch.

The devices are supplied in a configuration where they are wire bonded onto a printed wiring board (PWB). This PWB features Ball Grid Array (BGA) soldering balls on its rear side, and the sensors are further protected by a layer of epoxy resin with a thickness of 105 µm. This guarantees protection for the wire bonds, and also provides a flat surface for the SiPMs to couple the scintillating fibers to. The individual channels

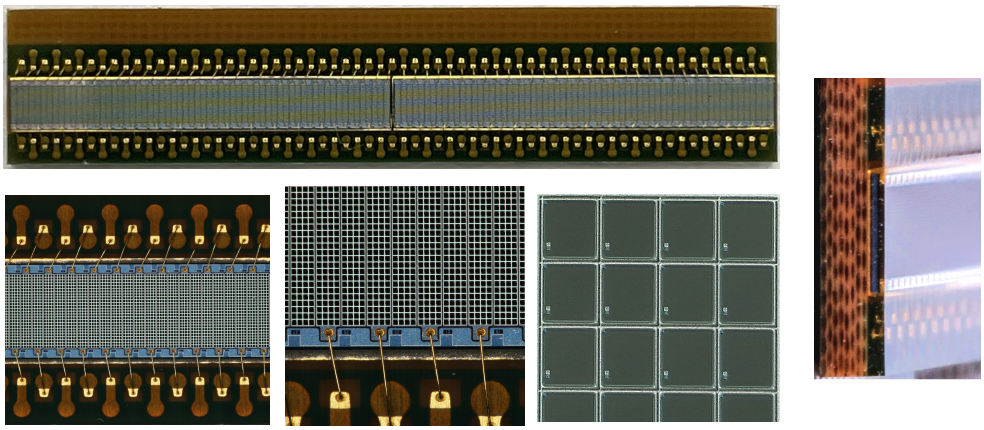

Figure 4.15: A visual representation of the Hamamatsu S13552-HRQ multi-channel Silicon Photomultiplier (SiPM) column array, featuring detailed close-up views that reveal the sensor's cell structure. The array consists of 4 rows and 26 columns of cells, each measuring 250 µm in width, resulting in a longitudinal segmentation of the sensor. The figure also presents the side profile of the sensor, showing the epoxy coating, as depicted on the right.

from each die share a common cathode, while the anodes are connected to the BGA soldering balls. The sensor has a gain of 3.8×10^6, a peak photon detection efficiency (PDE) of 48 %, and a 3 % cross-talk probability when operated at an overbias voltage of 3.5 V. At 25°C, non-irradiated sensors exhibit a dark count rate (DCR) of approximately 15 kHz per channel at a 0.5 photoelectron equivalent threshold and around 0.5 kHz at a 1.5 photoelectron equivalent threshold.

This sensor, as indicated in reference [55], was originally designed for the LHCb experiment and is well-suited to meet the specific demands of the Mu3e fiber detector. The key characteristics essential for application in the Mu3e experiment include the sensor's capability for single photon detection, its fast intrinsic time response, with a single photon transit time jitter of around 220 ps, and its insensitivity to magnetic fields.

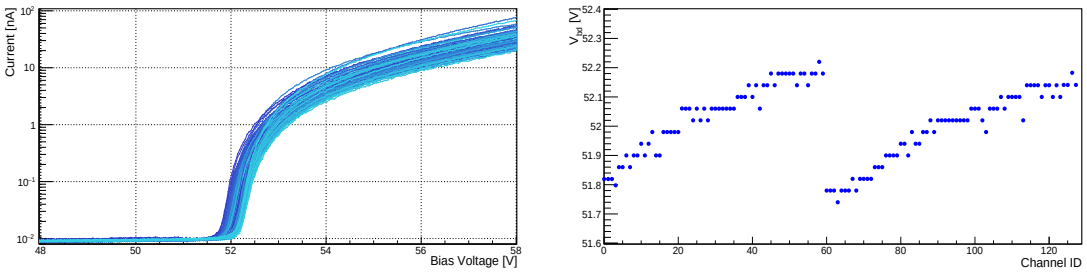

Figure 4.16: I-V curve (left) and breakdown voltage (right) for all 128 channels of one S13552-HRQ multi-channel SiPM array. The breakdown voltage is measured for each of the 128 channels. The variation in the breakdown voltage is within ± 0.3 V across the entire array.

characteristic	value
breakdown voltage V_{bd}	52.1 V
V_{bd} variation per sensor	$\pm$300 mV
V_{bd} variation between sensor	$\pm$500 mV
temperature coeficcient(*)	53.7 mV/K
gain(*)	3.8×10^6
DCR	15 kHz
peak PDE (*)	48 %
max PDE wavelength (*)	450 nm
quench resistance R_q	(500 ± 10) kΩ
recovery time τ_{rec}	(69 ± 2) ns
rise time τ_r	$<$ 1ns
short decay component τ_{short}	$\sim$ 1 ns
long decay component τ_{long}	(50 ± 4) ns

Table 4.1: Characteristics of the multichannel SiPM array, Hamamatsu device `S13552-HRQ`, at an overbias voltage of 3.5 V and at 25 °C. Most of the values have been measured for this work at the Universiy of Geneva while those with (*) are from [54].

I-V measurements were performed on the SiPMs to determine the breakdown voltage over the 128 channels. The variation in the breakdown voltage is within $\pm$0.3 V across the entire array, as can bee seen in figure 4.16. The central value of the breakdown voltage around 52 V. V_{bd} exhibits a gradual drift from 52.2 V at one end of the sensor to 51.8 V at the opposite end. This recurring pattern, seen in the right Figure 4.16 can be attributed to the sensor's construction, where a single device comprises two distinct dies. V_{bd} varies from sensor to sensor within $\pm$500 mV.

As mentioned all the channels share a common cathode and are therefore operated at the same bias voltage. Because of the small variation in the breakdown voltage, small gain differences between the channels are present. One way to reduce this small differences in gain is to adjust the bias voltage (or the overbias) for each channel individually. This is possible by using one of the features of the MuTRiG ASIC which can adjust the bias voltage for each channel individually around a common bias voltage (discussed in chapter 8).

In figure 4.17, a waveform of a SiPM channel of the `S13552-HRQ` multi-channel SiPM array is shown. The waveform is a digitiezed pulse over a 800 ns acquisition window for each channel. The SiPM array has been excited with a pulsed laser with a wavelength of 405 nm. From the shape of the pulse different charactieritics can be extracted. The fast rise time, with τ_r being less than 1 ns, is primarily attributed to the fast response of the micro-cells and is constrained by the amplifier's speed. After the rapid rise, there is a two-component decay, and a kink is observed in the decay profile. The short component has a decay time τ_{short} of approximatively 1 ns while the long component

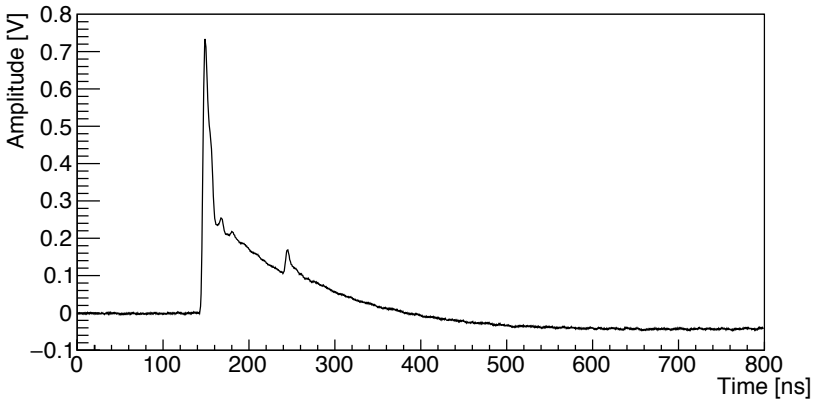

Figure 4.17: Waveform of a SiPM channel of the S13552-HRQ multi-channel SiPM array. The waveform is obtained by illuminating the SiPM with a pulsed laser with a wavelength of 405 nm.

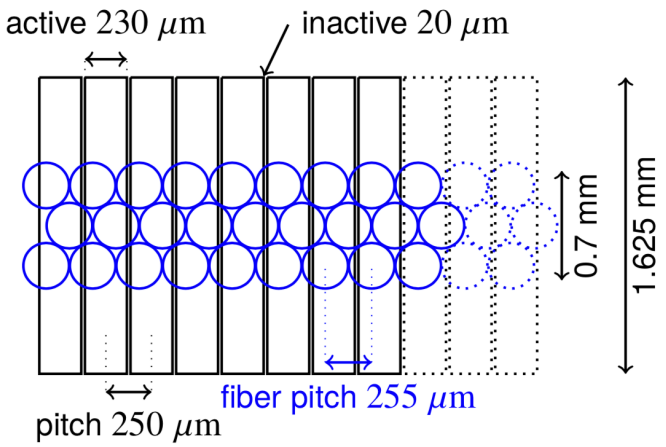

Figure 4.18: Mapping of the SciFi ribbon on the SiPM array. No one to one matching is possible between the fibers and the SiPM columns and the light signal will be spread over several columns. Schematic from [44].

has a decay time τ_{long} of around 50 ns. The short component of the decay is attributed to the recovery time of the micro-cells. The long decay component is determined by the recovery time attributed to the presence of a large quenching resistor $R_q = 500\,\text{k}\Omega$, indicating a slower discharge process. In this example one can observe some additional peaks, which are from delayed cross-talk between the micro-cells of the same channel.

The scintillating fiber ribbons are directly connected to the surface of multi-channel SiPM arrays, see figure 4.18. However, there isn't a one-to-one correspondence between the fibers and the multi-channel SiPM arrays due to the staggered arrangement of fibers and different pitches between the ribbon fibers and the SiPM array. Additionally, there is a dead area between the columns of the SiPM array, which results in an efficiency loss of $(1 - \epsilon_{\text{fill-factor}}) = 8\,\%$. This leads to an overall PDE of 44 %. To simplify the detector assembly, the coupling will be done exclusively through mechanical pressure applied by fixation screws. There are no plans for spring-loading the ribbons onto the SiPMs or using optical interfaces to minimize the spread of light signals (i.e., the optical cross-talk) at the SciFi ribbon-sensor interface.

During the studies, the potential for investigating a SiPM array with a reduced height was considered. For example halving the height of the SiPM array would still provide adequate coverage for the full thickness of the scintillating fiber ribbon. Such a reduction could potentially double the radiation hardness of the SciFi detector, offering significant improvements in its durability and performance under high-radiation conditions.

A summary table of the characteristics of the SiPMs used in this study is shown in table 4.2.

	`S13360-1350CS`	`S13360-3050CS`	`S13552-HRQ`
Sensitive area	1.3 mm × 1.3 mm	3 mm × 3 mm	230 µm × 1625 µm
micro-cell size	50 µm × 50 µm	50 µm × 50 µm	57.5 µm × 62.5 µm
Number of micro-cell/channel	667	3600	4 × 26
Fill factor	74 %	74 %	78 %
Peak PDE	40 %	40 %	48 %
Max PDE wavelenght	450 nm	450 nm	450 nm
Refractice index	1.41	1.41	1.55
Gain	1.7×10^6	1.7×10^6	3.8×10^6
Recommended overbias	3 V	3 V	3.5 V

Table 4.2: Summary of characteristics for the SiPMs used in this work: `S13360-1350CS`, `S13360-3050CS` and `S13552-HRQ`. [53, 56]

5

CHARACTERISTICS OF SCINFITLLATING FIBERS

This chapter focuses on evaluating the properties and performance of different types of scintillating fibers such as the light yield, attenuation length, and timing properties. These scintillating fibers are round fibers with a diameter of 250 µm. Table 5.1 is shown again to recall the properties of the fibers used in this study. This work has been published [39].

Table 5.1: Properties of blue-emitting, high-purity round scintillating fibers from Kuraray[38, 42] and Saint-Gobain [43], typically for 1 mm diameter fibers. Saint-Gobain specifies the light yield, while Kuraray labels SCSF-78 and NOL-11 as "high light yield" fibers.

Fiber Type	**SCSF−78**	**SCSF−81**	**NOL−11**	**BCF−12**
Cladding thickness [% fiber radius]		$3-3$		$3-1$
Trapping efficiency [%]		5.4		≥ 5.6
Numerical aperture		0.72		0.74
Emission peak [nm]	450	437	421	435
Decay time [ns]	2.8	2.4	1.3	3.2
Attenuation length [m]	> 4.0	> 3.5	> 2.5	> 2.7
Light yield [ph/MeV]	high		high	~ 8000
Refractive index (inside out)		$1.59-1.49-1.42$		$1.60-1.49-1.42$
Density (inside out) [g/cm^2]		$1.05-1.19-1.43$		1.05
Core		Polystyrene (PS)		
Inner cladding		PMMA		
Outer cladding		Fluorinated polymer (FP)		

5.1 EXPERIMENTAL SETUP

To characterize different types of scintillating fibers, a deticated setup has been built, in which the fibers can be excited with ionizing particles. The light produced by the fibers is collected with SiPMs. The setup is shown in Figure 5.1. The setup consists of an arrangement of five fibers, each with a diameter of 250 µm. The lenght of the fibers is 60 cm. They have been assembled on top of each other to form a flat ribbon. The adhesive used to bind these fibers together is a water based TiO_2 solution (referred to

as BC-622A from Saint-Gobain), chosen for its dual propertie of maintaining structural cohesiveness and ensuring optical isolation of each fiber within the assembly.

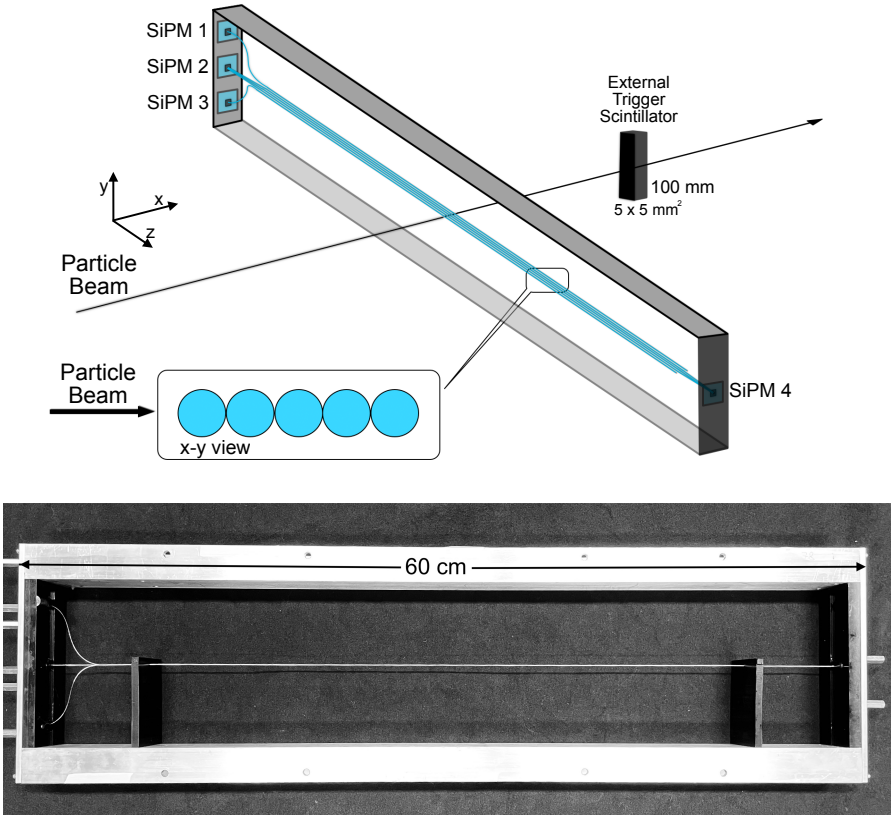

Figure 5.1: Arrangement illustration showing the mapping of the fibers to the SiPMs (top) and a photo of the frame securing the fibers (bottom). The fibers are arranged horizontally w.r.t. the direction of the incoming beam particles. For clarity in this depiction, the diameter of the fibers has been intentionally enlarged.

In this experimental framework, the beam particles traveres all five fibers perpendicularly, as detailed in Figure 5.1. The configuration of the fibers is such that the two outer fibers read out independently while the three central ones are grouped together and read out at both ends. In addition, a scintiallating bar serves as a trigger and external time reference.

The measurements were performed at the πM1 beamline of the Paul Scherrer Institute (PSI). The beamline was set at a momentum of 210 MeV/c and contained mostly pions. Additional measurements were conducted using a ^{90}Sr radioactive source. To select beta particles exceeding 1 MeV, a high threshold was set on the trigger scintillator. This approach ensured that the energy loss of β particles was equivalent to that observed with beam particles. It's important to note that all timing measurements were exclusively carried out with the beam. Furthermore, when a Minimum Ionizing Particle (MIP) traverses the entire diameter of the fiber, it deposits an energy of approximately 45 keV [39]. This can be understood by considering the energy loss of a MIP in a material, which is given by the Bethe-Bloch formula [30].

These fibers were coupled to single channel SiPMs from Hamamatsu, $1.3 \times 1.3\ \mathrm{mm}^2$, model `S13360-1350CS` detailed in the previous section 4.8.1. The SiPMs have a consistent Photon Detection Efficiency (PDE) across a substantial portion of the emission spectrum of the fibers, see Figure 3.4, nearing 40 % efficiency when operated at an overbias of 3 V. This ensures to detect a large fraction of photons. Also to ensure optimal coupling, the fibers are glued in plastic holders. These holders were designed to be compatible with the SiPMs, having a spring loaded mechanism to couple the SiPMs to the fibers. This approach not only secures the fibers but also centers them with respect to the SiPMs. The effectiveness of this alignment is further enhanced by diamond polishing the contact surfaces at the ends of the fibers.

Additional to this setup, is a scintillator bar, with a square cross-section measuring 5 mm on each side. This bar is positioned behind the fiber ribbon to function as an external trigger and provided a time reference for timing measurements. The trigger scintillator was coupled to the Hamamatsu SiPMs `S13360-3050CS` at both ends, achieving a time resolution estimated to be $\sigma_{trigger} \simeq 60\,\mathrm{ps}$.

5.1.1 *Readout electronics*

To amplify the signals received from the SiPMs, a set of fast, hybrid two-stage common emitter bipolar junction transistor (BJT) was employed. The necessity of this two-stage amplification process lies in ensuring that the signals are adequately amplified to be read by the DRS4 waveform digitizer.

The first stage is boosting the signal from the SiPM by a factor of 5 and inverts it. This initial increase is achieved through the modulation of the base current of a bipolar junction transistor (BJT). In this context, 'modulation' refers to varying the base current, which in turn controls the current flowing between the collector and emitter terminals of the BJT. This modulation is the key factor in amplifying the input signal, as a small variation in the base current results in a proportionally larger change in the collector-emitter current, thereby amplifying the signal.

Following this, the second stage of the amplifier further enhances the signal amplitude with an additional factor of 5. Here, another transistor in a common-emitter configuration amplifies the signal from the first stage.

Through these stages, the signals from the SiPMs are not only amplified to a level suitable for digital readout but are also ensured to maintain their quality and stability, essential for accurate digitization. To sum up, the use of a two-stage amplifier offers several advantages :

- The combined gain of the two stages provides significant amplification, ensuring that the signal is strong enough for subsequent processing and is fast with a rise time of $\sim 1.5\,\mathrm{ns}$.
- The amplifier can handle a wide range of signal amplitudes, from small single photon signals to larger signals generated by multiple photons with no saturation up to 20 photons.

- The two-stage configuration helps to stabilize the amplifier's response, reducing noise and ensuring consistent performance over time.

Together, the two stages provide a combined gain of about 35 dB which is sufficient for producing clear, positive signal outputs with single photon amplitudes of roughly 85 mV.

These signals are captured using the DRS4 waveform digitizer [57], which sampled the SiPM outputs at a frequency of 5 GHz. There are a total of 6 inputs in the setup, so two synchronized DRS4 Evaluation Boards are employed, both of which were read out simultaneously [58]. For every measured event, waveform data from all the SiPMs were collected. Additionally, the triggering logic required the simultaneous detection of signals in the two outer fibers and the square scintillator bar.

5.2 LIGHT YIELD AND ATTENUATION LENGTH

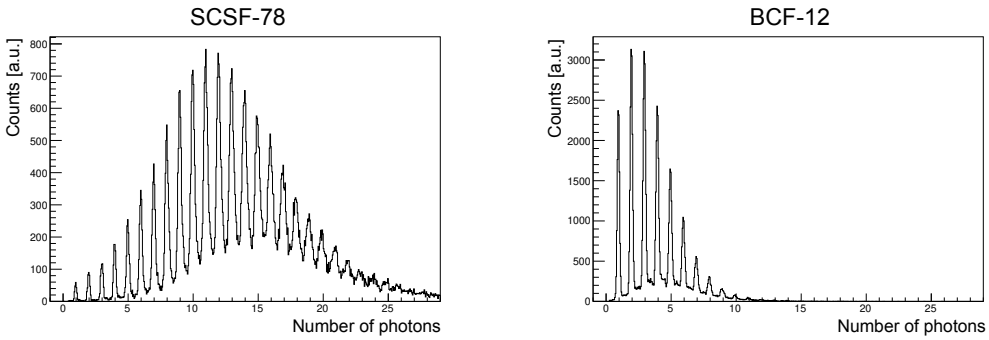

Figure 5.2: Integrated charge spectrum of a high light yield fiber (SCSF-78, left) and a low light yield fiber (BCF-12, right). This comparison is based on the charge produced by a single photon. In these measurements, particles intersect the fibers at the midpoint of the ribbon, situated 30 cm away from the ends of the fibers.

The light yield of the fibers is measured by evaluating the measured charge by integrating the recorded waveforms. This integration process occurs after baseline subtraction on a event-by-event basis, and is performed over a time window of 60 ns. The baseline is evaluated on an event by event basis by averaging the waveform over 100 consecutive samples between 25 ns and 5 ns before the start of the signal. The integration starts 5 ns before the start of the rising edge of the signal. In Figure 5.2 the integrated charge spectrum after baseline substraction of a high light yield fiber (SCSF-78) and a low light yield fiber (BCF-12) are shown. As can be seen, the high light yield fiber produces a greater number of photons compared to the low light yield fiber. The SiPMs ability to detect single photons (see section 4.8.2) enables the normalization of the charge spectrum to the charge generated by a single photon without precise knowledge of the absolute amplification (gain) of the SiPMs and readout electronics.

The charge spectra for the SCSF-78, SCSF-81, NOL-11 and BCF-12 type of fibers are shown in Figure 5.3. The charge is normalized, as explained above, and has been integrated in a region of ± 0.5 around each photon peak. Like this, each bin in the

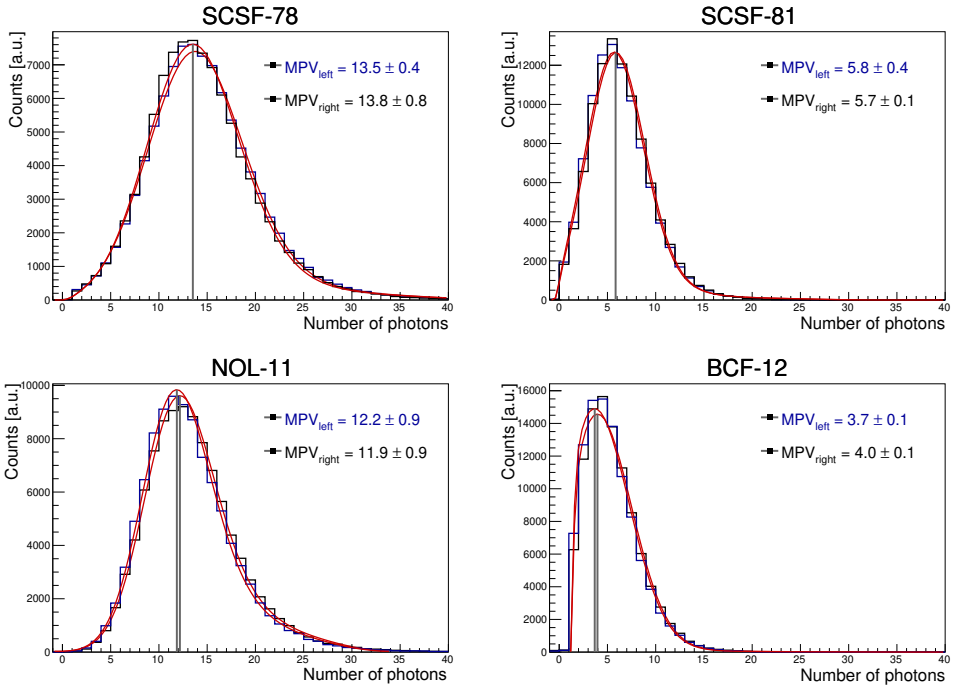

Figure 5.3: Photon yield of different fibers at both ends of the fibers are the center. The fit distribution in red, is a convolution of a Gaussian and a Landau distribution. The light yield is not corrected for the PDE of the SiPMs.

Table 5.2: Most Probable Value (MPV) for different fibers as a function of the different distances from the fiber's end. The MPV is obtained by fitting the charge spectrum with a convolution of a Gaussian and a Landau distribution. The error on the MPV is the error coming from the fit. These values are not corrected for the PDE of the SiPMs.

	Distance from excitation point				
Fiber type	10 cm	20 cm	30 cm	40 cm	50 cm
SCSF-78	16.2 ± 0.9	14.8 ± 0.7	13.7 ± 0.7	13.1 ± 0.8	12.5 ± 0.9
SCSF-81	8.1 ± 0.6	6.3 ± 0.5	5.8 ± 0.3	5.4 ± 0.3	5.2 ± 0.3
NOL-11	13.0 ± 1.0	11.5 ± 0.9	12.1 ± 0.9	10.6 ± 0.7	10.1 ± 0.7
BCF-12	6.6 ± 0.4	5.1 ± 0.2	3.8 ± 0.1	2.1 ± 0.4	1.5 ± 0.4

histogram corresponds to the detected number of photons. The resulting distribution has been fitted with a convolution of a Gaussian and a Landau distribution:

$$F(x) = \frac{1}{\sqrt{2\pi\sigma^2}} \exp\left(\frac{(x-\mu)^2}{2\sigma^2}\right) * \frac{1}{\pi}\int_0^\infty \exp\left(-t\log(t) - xt\right)\sin(\pi t)dt \tag{5.1}$$

The Landau distribution is used to describe the fluctuations in the energy deposit in a thin layer of material, which is traversed by a charged particle. The Gaussian is used because of the nature of the scintillation light generation resulting into a Poissonian distribution, which approaches a Gaussian distribution at those mean values. The Most Probable Value (MPV) of the fit is a good indicator of the number of photons produced for the different fibers. Note that the MPV values are not corrected for the PDE of the SiPMs which is around 40 %. The values for each side of the fibers are very similar, less than 1 detected photon difference. The MPV of the different fibers and at different distances from the fiber end are shown in Table 5.2. Those reported in the table are obtained by taking the mean of the left side and right side values of the fibers. The error on the MPV is the errors coming from the fits of the charge spectrum. Notice that the errors are larger than the difference between the left and right side MPV values.

In this study, the focus is set exclusively on the relative light yields of the fibers, employing a consistent normalization method. This approach enables a clear comparison among various type of scintillating fibers. However, determining the intrinsic ionization light yield $Y_S(\lambda)$, mentioned in the previous section 3.2, presents a complex challenge. Indeed, it needs an accurate knowledge of several factors, including the Photon Detection Efficiency (PDE) of the SiPMs, the efficiency of the optical coupling, light propagation within the fiber (inlcuding both trapping efficiency and attenuation), and other relevant parameters. Regardless of these challenges, a relative light yield of the fibers can be determined with a high degree of precision, as demonstrated in this study. This accurate measurement is crucial for effectively comparing various types of fibers.

To measure the attenuation length of the fibers, the light yield of the fibers is measured at different distances from the excitation point, ranging from 5 cm to 55 cm. As mentioned in the previous section 3.2, the light intensity is expected to be influenced by two attenuation lengths, the long and short component. At these lengths of fibers, the light intensity is expected to be influenced by both components.

Figure 5.4 shows the variation in the detected number of photons (MPV) relative to different distances from the fiber's end, including measurements from both ends of the fibers.

The analysis of the attenuation lenght involves fitting the measured points to a model that accounts for both the short and long attenuation lengths. The model is a double exponential distribution as detailed in the previous section 3.2:

$$F(x) = A \cdot \exp\left(-x/\Lambda^{short}\right) + B \cdot \exp\left(-x/\Lambda^{long}\right) \tag{5.2}$$

where A, B, Λ^{short} and Λ^{long} are the fit parameters. The fit is shown in Figure 5.4 as a solid line. The resulting fit parameters, and so the attenuation lengths, are reported

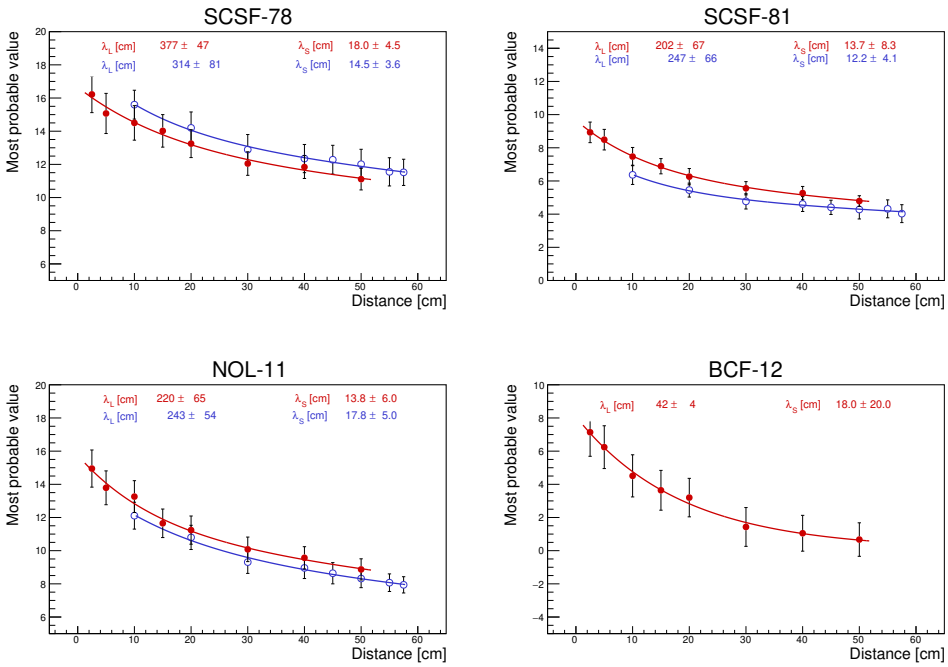

Figure 5.4: Most Probable Value (MPV) for different fibers at different distances from the fiber end. The full red circles are the MPV values from the left side of the fibers, while the empty blue circles are the MPV values from the right side of the fibers.

in Table 5.3. The reported values represent an averaged sum of measurements from both the left and right ends, except for the BCF-12 fiber, where only the left side data is included.

Table 5.3: Attenuation lengths of the different fibers. The attenuation lengths are obtained by fitting the MPV values with a double exponential distribution. The short and long attenuation lengths are reported in the table.

Fiber type	Λ^{short}[cm]	Λ^{long}[cm]
SCSF-78	16.4 ± 4.1	337 ± 62
SCSF-81	13.2 ± 6.3	224 ± 66
NOL-11	15.6 ± 5.4	230 ± 59
BCF-12	18.2 ± 20	42 ± 4

It's notable that the reported errors are large, influenced by the relatively short measurement range and the fact that the attenuation lengths are calculated in a region where both short and long components are big. Also the small number of data points contributs to the errors. As initially explained, the measured short component is around 10-20 cm while the long component corresponds with the values reported in Table 5.1, with the exception of the BCF-12 fiber.

Overall, the results are consistent with the expected values, with the attenuation lengths of the SCSF-78 and SCSF-81 fibers being comparable to each other, and the attenuation length of the NOL-11 fiber being slightly shorter. The BCF-12 fiber, on the other hand, exhibits a significantly shorter attenuation length. Those results are consistent with the previously reported values in Table 5.1.

Regarding the light yield, the results provide a valuable insight into the relative light yield of the fibers. Understanding this is crucial for the choice of the Scintillating Fiber (SciFi) detector, as it directly informs us about the detector's efficiency. Additionally, the attenuation length is a key parameter in the design process, as it dictates the optimal length of the fibers to be used. It's important to note, however, that the attenuation length is just one of several critical factors that need to be considered in the comprehensive design of the SciFi detector.

5.3 TIMING PERFORMANCE

The timing performance of the fibers is a pivotal parameter in the design of the SciFi detector. Understanding the time resolution of the fibers is essential, as it directly influences and determines the overall time resolution of the SciFi detector itself.

5.3.1 *Effective decay time*

The method for determining the effective decay time of scintillation light involves measuring the time interval between the detection of the first scintillation photon (T_{fiber}) and the external timing reference provided by the trigger scintillator ($T_{trigger}$). It is very important to note that the decay time τ that we extract does not directly measure the decay time of the spectral shifter, as seen in section 3.2. This is because the formation of the signal is a complex, multi-step process involving simultaneous excitation of many molecules by the ionizing particle. In the measurements, T_{fiber} is defined by the arrival time of the first detected photon.

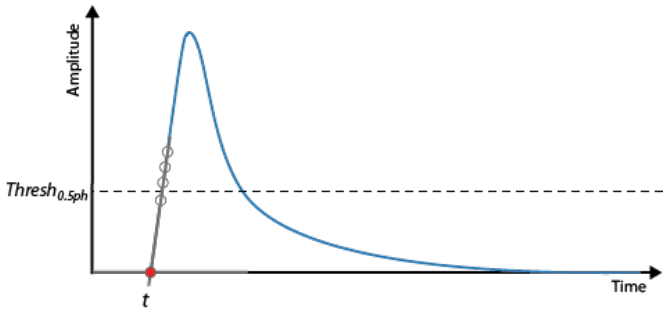

Figure 5.5: Interpolation methode used to determine the arrival time of the first photon. The sample points are exagerated for clarity.

The arrival time of the first scintillation photon is determined by the waveform. This involves a method where the rising edge of the signal is interpolated with a straight

line, which is then extended back to the baseline of the waveform, taking into account any fluctuations in the baseline. This interpolation is done on 4 waveform samples on the rising edge with the first sample being below the single photon's half amplitude and the next three samples above it. A scheme of this interpolation is shown in Figure 5.5. The sampling frequency of the DRS4 is 5 GHz which corresponds to a sampling period (the time between two samples) of 200 ps. The interpolation has a time base of 600 ps which is the time difference between the first and the last sample. The time jitter of the DRS4 is less then 5 ps [58]. The time walk for the timing algorithm used in this analysis is less than 10 ps. Additionally, various algorithms have been explored, including a leading-edge discriminator set to a very low threshold, equivalent to half a photon amplitude, and a constant fraction algorithm with adjustable ratios. Leading edge algorithms are known to be sensitive to noise and to the rise time of the signal while constant fraction algorithms are more robust but require a higher threshold. A time walk has been indeed observed for the leading edge algorithm. Note also that the time resolution of the trigger scintillator is of the order of 60 ps which does not affect significantly the time resolution of the fiber. The time difference between the first

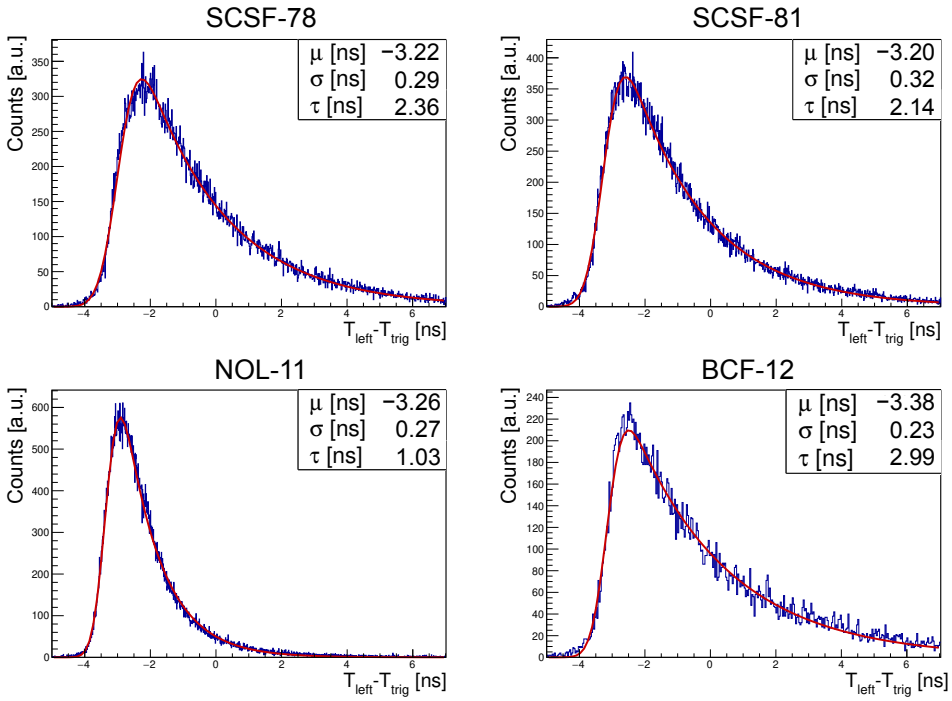

Figure 5.6: Time difference for different type of fibers. The time difference is the difference between the first photon detected in the fiber and the trigger scintillator. The fit distribution, in red, is the EMG distribution.

photon detected in the fiber and the trigger scintillator, $T_{fiber} - T_{trig}$ is shown in Figure 5.6. The distributions are fitted with a so called Exponentially Modified Gaussian

(EMG) distribution. This distribution is a convolution of a Gaussian and an exponential distribution. The EMG distribution is defined as:

$$F(t,\mu,\sigma,\tau) = A\frac{1}{2\tau}\exp\left(\frac{\mu-t}{\tau}-\frac{\sigma^2}{2\tau^2}\right) * \left[1+\mathrm{erf}\left[\frac{1}{\sqrt{2}}\left(\frac{\mu-t}{\sigma}+\frac{\sigma}{\tau}\right)\right]\right] \tag{5.3}$$

where τ is the effective decay time of the scintillating light. σ is the standard deviation of the Gaussian distribution, which accounts for the time spread of the light collection process that includes the time jitter of the trigger, the single photon transit time jitter in the SiPM , the signal formation and the response time of the electronics. It basically accounts for the time spread of all the light collection. μ is the mean of the Gaussian distribution and is the time difference between the first photon detected in the fiber and the trigger scintillator. A is a normalization factor. erf is the error function. Here t is the time difference between the first photon detected in the fiber and the trigger scintillator, so $t = T_{fiber} - T_{trigger}$. The decay times, τ in Figure 5.6, obtained are shorter than the values reported in Table 5.1, but still show a similar pattern among the different fibers. The difference may arise from the measurements focused on the arrival time of the first photon rather the collective photon ensemble. Moreover, as illustrated in Figure 5.7 and

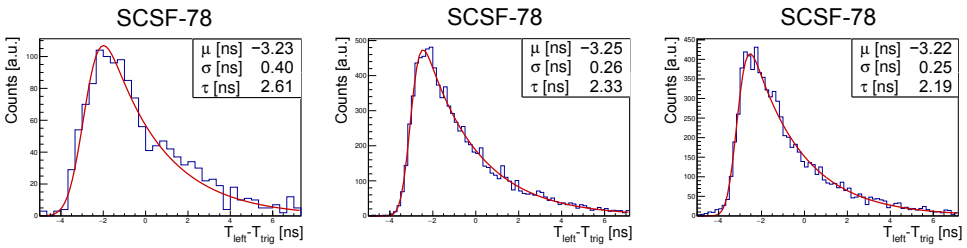

Figure 5.7: Decay time as a function of the number of detected photons fitted with the EMG distribution. From left to right : $n_{ph} \leq 5$, $10 < n_{ph} \leq 15$, $n_{ph} > 20$.

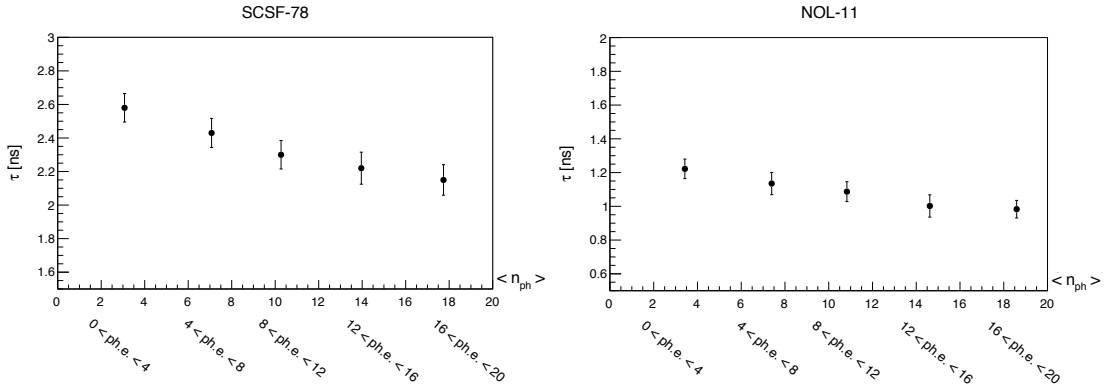

Figure 5.8: Effective decay time as a function of the number of detected photons n_{ph} for SCSF-78 on the left and NOL-11 on the right.

Figure 5.8, the decay time varies with the number of detected photons n_{ph}. Specifically, shown in Figure 5.7, the distribution becomes narrower as the number of detected

photons n_{ph} increased. The extended tail of the right side of the peak diminishes very slowly and so the decay time decreases, as well.

Additionally, Figure 5.7 also provides insight into the achievable time resolution with single-ended readout, predominantly influenced by the decay time, especially when the photon statistics is low. The variance of the EMG distribution is given by:

$$\sigma_{EMG}^2 = \sigma^2 + \tau^2 \tag{5.4}$$

where σ is the intrinsic time resolution of the system. Because of the asymmetrical shape of the distribution, σ_{EMG} is not the best indicator of the time resolution of the fibers. A more appropriate approach to quantify the time resolution, considering the shape of the distribution and the nature of light generation, would be to provide asymmetric errors. This can be done by measuring the widths of the distribution on both the left side, $\sigma_{left} = \sigma$, and the right side, $\sigma_{right} = \sqrt{\sigma^2 + \tau^2}$, of the peak separately. Like this, the time resolution can be expressed in a more appropriated way.

5.3.2 *Time difference between the two ends of the fibers*

The time resolution of scintillating fibers can be significantly improved by reading them out at both ends and combining the time measurements from each end. This method offers distinct advantages over single-ended readouts, primarily in its ability to mitigate noise and variations caused by external factors. The likelihood of noise and external disturbances impacting both ends of the fiber simultaneously is low, making reading out at both ends a more stable and dependable option for accurate time resolution.

For this reason, the initial step involves measuring the time difference between the two ends of the fibers:

$$\Delta T = T_{left} - T_{right} \tag{5.5}$$

where T_{left} and T_{right} are the time measurements from the left and right ends of the fibers, respectively. Notably, ΔT does not rely on an external time reference. However, it is very important to note that ΔT is not suitable for determining the crossing time of a particle. This limitation arises because the ΔT measurement depends on the hit position along the fiber. Subsequent results and discussions will reveal that the most accurate method to determine the crossing time of a particle through the fiber is by employing the mean time, since this is independent of the hit position along the fiber.

In Figure 5.9, the time difference ΔT for different types of fibers is shown. The beam particles are crossing the fibers at the midpoint of the ribbon, situated 30 cm away from the ends of the fibers. One can see that the mean of the distribution is not necessary center around zero. This can be explained by the different cable lengths. The large tails of the distribution, which extend symmetrically on both sides of the peak, are driven by the fiber's decay time.

The distributions are fitted with the sum of two Gaussian distributions centered around the same mean. 80 % of the events are contained in the core Gaussian distribution, while the remaining 20 % are contained in the tail of the Gaussian distribution.

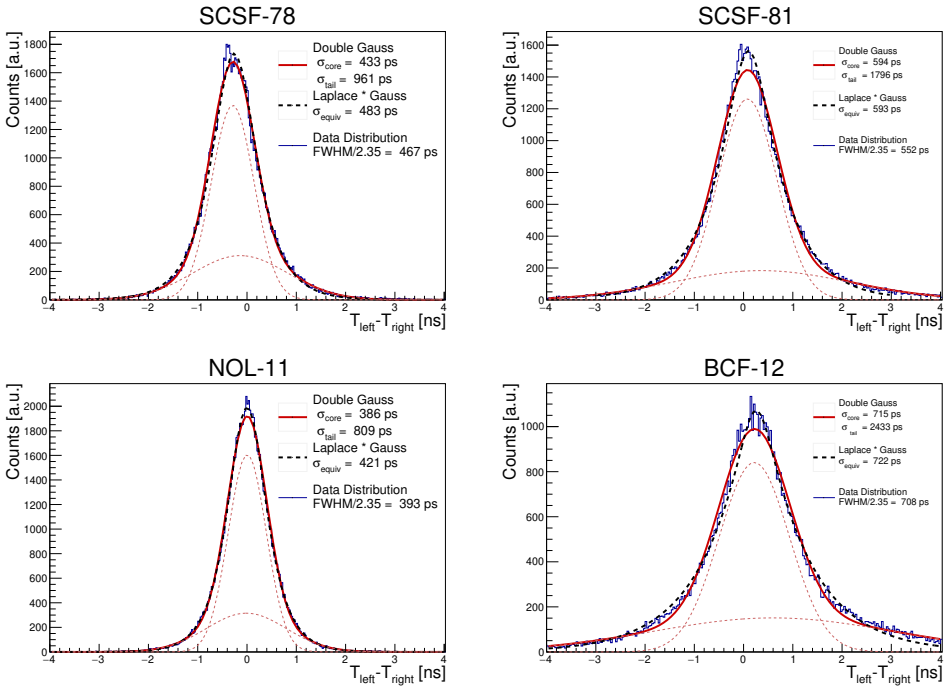

Figure 5.9: Time difference ΔT for different type of fibers. The ΔT distribution is fitted with a sum of two Gaussian distributions centered around the same mean (red solid line). The core Gaussian distribution and the tail Gaussian distribution are shown in dashed lines. The black dashed line is the convolution of a Gaussian and a Laplace distribution.

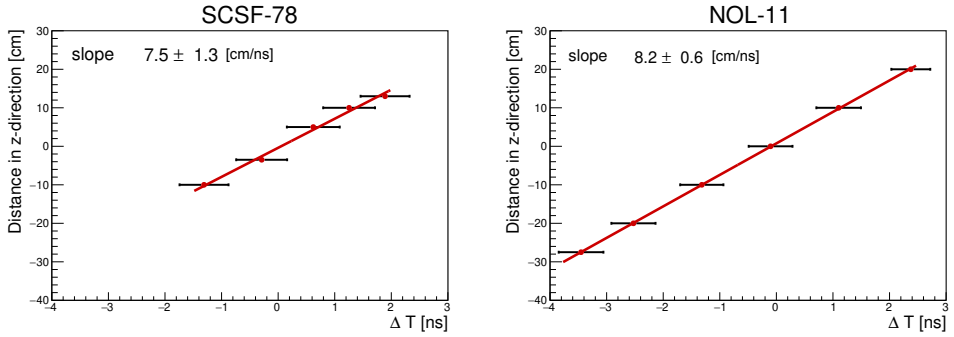

Figure 5.10: Time difference ΔT as a function of the hit position along the fiber. The time difference ΔT is the difference between the first photon detected in the fiber at the left side and right side. The fit distribution in red, is a linear interpolation of the data points.

The time difference resolution $\sigma_{\Delta T}$ is deduced from the Full Width at Half Maximum (FWHM) of the ΔT distribution as:

$$\sigma_{\Delta T} = \frac{\text{FWHM}}{2.355} \tag{5.6}$$

where the FWHM is the difference between the two points where the distribution reaches half of its maximum value. In this case, $\sigma_{\Delta T}$ is close to the width of the core Gaussian distribution σ_{core}. The values are varying between 400 ps and 700 ps depending on the fiber type. The most precise resolution, around 400 ps, is obtained with the NOl-11 fiber which is known to have the shortest decay time. It is interesting to note that the SCSF-81 fiber, although having a decay time sorter then that of the SCSF-78 fiber, exhibits notably larger tails. This is mainly due to its lower light yield, as seen in Figure 5.3. Also, the performance of the BCF-12 fiber can be attributed to its reduced light yield as well.

As seen in Figure 5.9, the ΔT distribution can also be modeled using a Laplace distribution, reflecting the Poissonian nature of the light generation within the scintillation process. Additionally, this can be refined by convoluting with a Gaussian distribution, which accounts for the time spread of the light collection. This combination offers a more comprehensive representation of the underlying physical processes, and is expressed as:

$$F(t) = A \cdot \exp\left(\frac{-|t-t_0|}{\tau}\right) * \frac{1}{\sigma\sqrt{2\pi}} exp\left(\frac{(t-t_0)^2}{2\sigma^2}\right) \tag{5.7}$$

where t_0 is the mean of the distribution, τ is the decay time and σ is the standard deviation of the Gaussian distribution. The fit is shown in Figure 5.9 as a black dashed line and models the data well for all the fibers. Especially the tails of the distribution are well described by this model.

The time difference ΔT as a function of the hit position along the fiber is shown in Figure 5.10. One can see a corresponding shift in the time difference ΔT as the hit

position along the fiber changes. The width of the distribution is found to remain constant along the fiber, showing that the time resolution is independent of the hit position along the fiber. The data points at each hit position can be interpolated with a straight line and the slope of the line as shown in Figure 5.10. This suggests and reinforces the idea that the light propagates uniformly in both directions. Near the fiber's end, any notable edge effects within the limits of the measurements resolution are seen.

The difference in photon travel distance being double the displacement allows to calculate the speed of light within the fibers, considering it is constant, denoted as v_{fiber}. This speed is determined using the slope of the straight line interpolated from the data. Interestingly, v_{fiber} is found to be around half that of light speed in vacuum, i.e. $v_{fiber} \sim 0.5 \times c$. This reduced speed, in comparison to what the fiber core's refractive index might suggest (c/n), is attributed to the increase of the effective path length due to the photons having a helical trajectory or to the multiple internal reflections they undergo within the fiber cladding. Consequently, the effective travel path length increases, leading to a reduction in the measured speed of light. This is in agreement with the results obtained in the next chapter of the thesis.

Futhermore, the ΔT measurement enables the determination of the impact position along the fiber, z, coming from the following relation, with L the fiber's full length:

$$\Delta T = \frac{z - (L - z)}{v_{fiber}} = \frac{2z - L}{v_{fiber}} \Leftrightarrow z = \frac{1}{2}L + \Delta T \times \frac{1}{2}v_{fiber} \tag{5.8}$$

with spatial resolution given by :

$$\sigma_z = \sigma_{\Delta T} \times \frac{1}{2}v_{fiber} \tag{5.9}$$

The spatial resolution is found to be $\sigma_z \sim 3.5\,\text{cm}$. Despite its modesty, this spatial resolution can be advantageous in specific applications.

Another interesting study is to examine the ΔT distribution as a function of the number of detected photons n_{ph}. In this case, instead of one side of the fiber, the

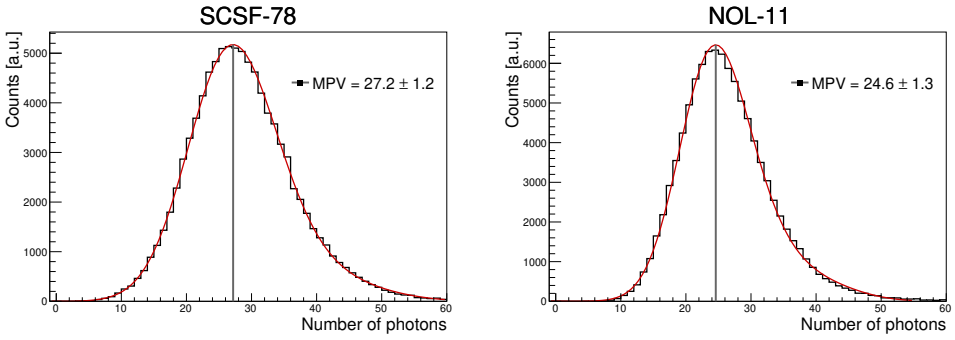

Figure 5.11: Total number of detected photons obtained by summing the number of detected photons from both ends of SCSF-78 (left) and NOL-11 (right) fibers. The fit distribution in red, is a convolution of a Gaussian and a Landau distribution.

total number of detected photons is the sum of the number of detected photons from both ends of the fiber, $\sum n_{ph}$ as shown in Figure 5.11. The fit distribution is again a convolution of a Gaussian and a Landau distribution.

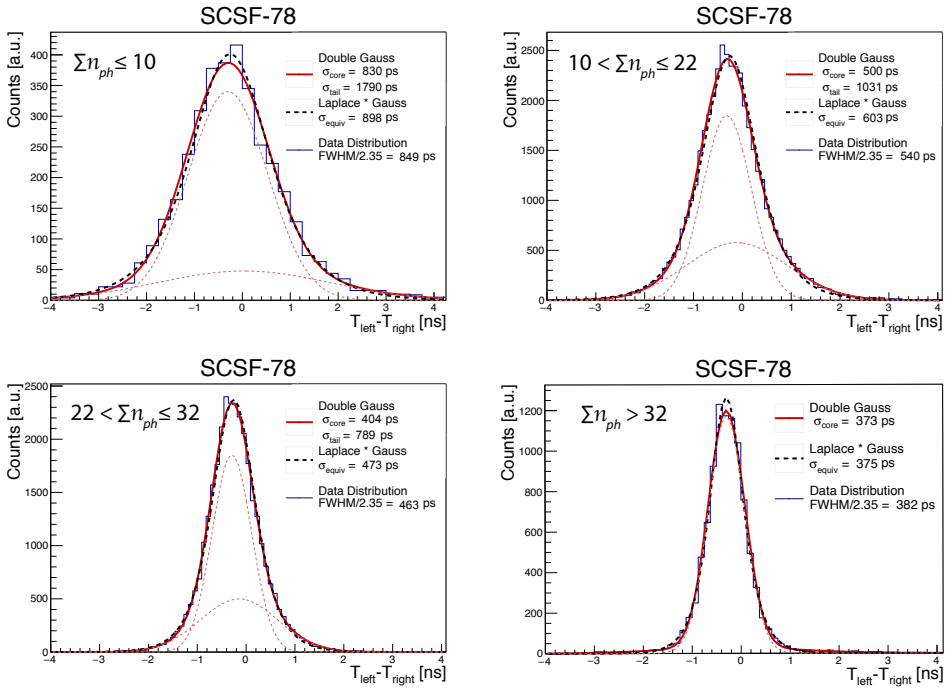

Figure 5.12: Time difference ΔT for different total number of detected photons $\sum n_{ph}$ for SCSF-78. As the total number of detected photons $\sum n_{ph}$ increases, the spread of the distribution decreases.

The Figures 5.12 and 5.13 shows the distribution of ΔT across different ranges of $\sum n_{ph}$. As $\sum n_{ph}$ increases, the spread decreases, reducing the tails of the distribution. This trend is observed for both SCSF-78 and NOL-11 fibers. Each distribution is fitted with a sum of two Gaussian distributions centered around the same mean. The distribution tends towards a Gaussian shape, enhancing the time difference resolution $\sigma_{\Delta T}$. For $\sum n_{ph} > 32$, the core Gaussian distribution absorbs the tails, resulting in a single Gaussian distribution.

Additionally, for a comprehensive analysis, the distributions are also analyzed using the convolution of a Gaussian distribution with a Landau distribution. This approach, as said previously, allows for a more understanding of the distribution characteristics by combining the properties of both Gaussian and Landau distributions in the analysis.

One can also check more carefully the dependence of the time difference resolution $\sigma_{\Delta T}$ on the total number of detected photons $\sum n_{ph}$. Plotting the time difference resolution $\sigma_{\Delta T}$ as a function of the total number of detected photons $\sum n_{ph}$, as shown in Figure 5.14, one can see that the time difference resolution $\sigma_{\Delta T}$ decreases as the total

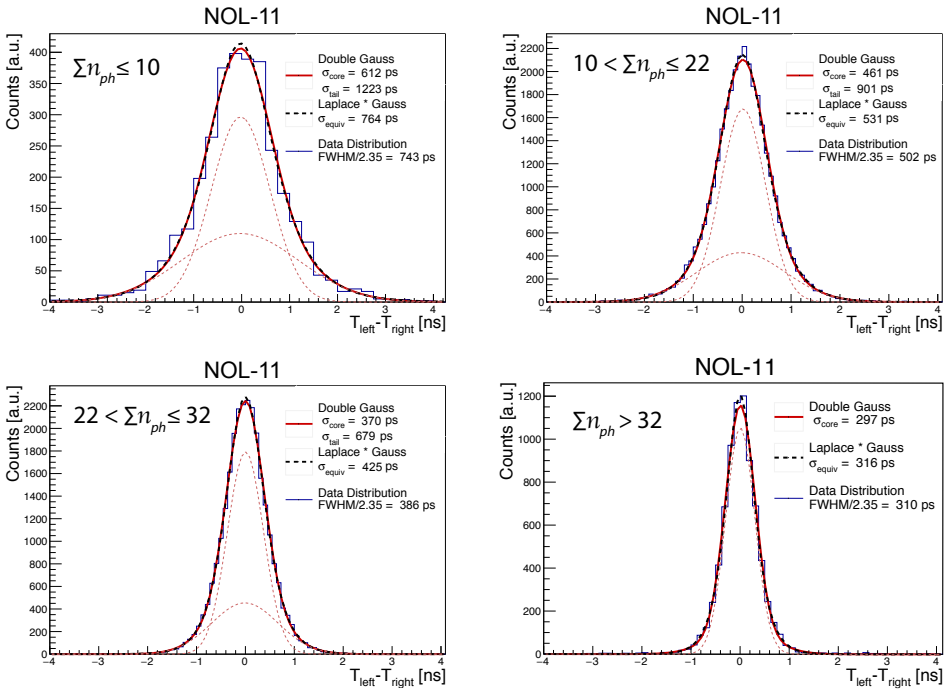

Figure 5.13: Time difference ΔT for different total number of detected photons $\sum n_{ph}$ for NOL-11 As the total number of detected photons $\sum n_{ph}$ increases, the spread of the distribution decreases.

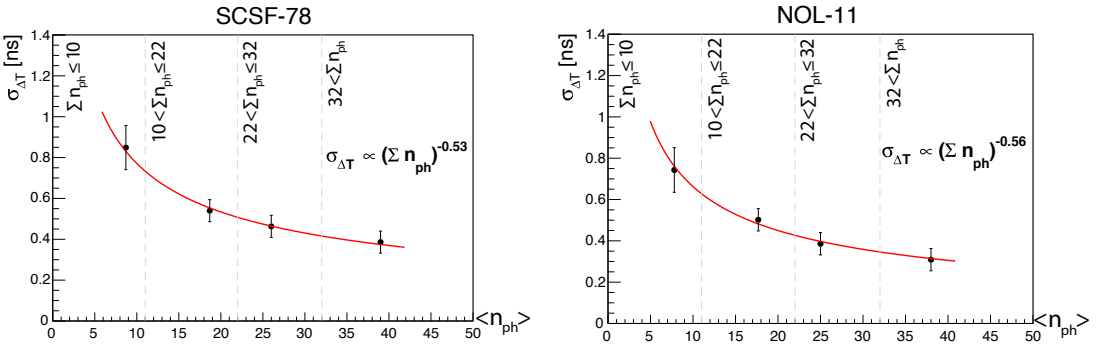

Figure 5.14: Time difference resolution $\sigma_{\Delta T}$ as a function of the total number of detected photons $\sum n_{ph}$ for SCSF-78 (left) and NOL-11 (right). The time difference resolution $\sigma_{\Delta T}$ decreases as the total number of detected photons $\sum n_{ph}$ increases and can be fitted with a power law such where α is the power law exponent.

number of detected photons $\sum n_{ph}$ increases and can be fitted with a power law such as:

$$\sigma_{\Delta T} \propto (\sum n_{ph})^{\alpha} \tag{5.10}$$

where α is the power law exponent. The power law exponent α is found to be -0.53 for the SCSF-78 fiber and -0.56 for the NOL-11 fiber, so the trend goes as $1/\sqrt{(n_{ph})}$. This analysis leads to a crucial conclusion: enhancing the time difference resolution $\sigma_{\Delta T}$ is achievable by increasing the total number of detected photons $\sum n_{ph}$. Therefore, in the persuit of the optimal timing, it becomes evident that not only is the minimization of the decay time τ important, but also the maximization of the number of detected photons n_{ph}. Those two parameters are essential for achieving the best possible timing accuracy.

5.3.3 *Mean Time*

As mentioned before when reading out both ends of a scintillating fiber, the most accurate method to determine the crossing time of a particle through the fiber is by employing the mean time. The mean time (MT) is defined as :

$$MT = \frac{1}{2}(T_{left} + T_{right}) - T_{trigger} \tag{5.11}$$

where T_{left} and T_{right} are the time measurements from the left and right end of the fibers respectively. $T_{trigger}$ serves as a reference time, which can be derived from various sources. One source can be another timing measurement, such as the trigger scintillator in this study, but it can also be obtained from the system clock. The reference time measurement can be seen as an additive constant as long as the time resolution of the reference time measurement $\sigma_{trigger}$ is smaller comparing to the MT distribution width σ_{MT}. The big advantage of using the MT is its relative independence, to a good degree, from the hit position along the scintillating fiber, eliminating the need to adjust for light propagation effects. Inherent to its design, it can be anticipated that the width of the MT distribution σ_{MT} is half of that of the ΔT distribution $\sigma_{\Delta T}$.

$$\sigma_{MT} = \frac{1}{2}\sigma_{(T_{left}+T_{right})} = \frac{1}{2}\sqrt{\sigma^2_{T_{left}} + \sigma^2_{T_{right}}} = \frac{1}{2}\sigma_{(T_{left}-T_{right})} = \frac{1}{2}\sigma_{\Delta T} \tag{5.12}$$

This above relation is true if both time measurements T_{left} and T_{right} are independent, have the same time resolution intrinsicaly and are Gaussian distributed. Figure 5.15 shows the MT distribution for different type of fibers. As for the ΔT distributions, the beam hits the fibers in the middle of the ribbon, situated 30 cm away from the ends of the fibers. For the MT distribution, a tail is visible on the right side of the peak which is driven by the decay time of the fibers because the low number of detected photons. Like for the decay time distributions in Figure 5.6, the fit distribution used is the convolution of a Gaussian and an exponential distribution, equation 5.3. The fit is shown in Figure 5.15 as a red solid line. For the case of the SCSF-78 and NOL-11 fibers, the tail is less predominant compared to the SCSF-81 and BCF-12 fibers. Therefore for those

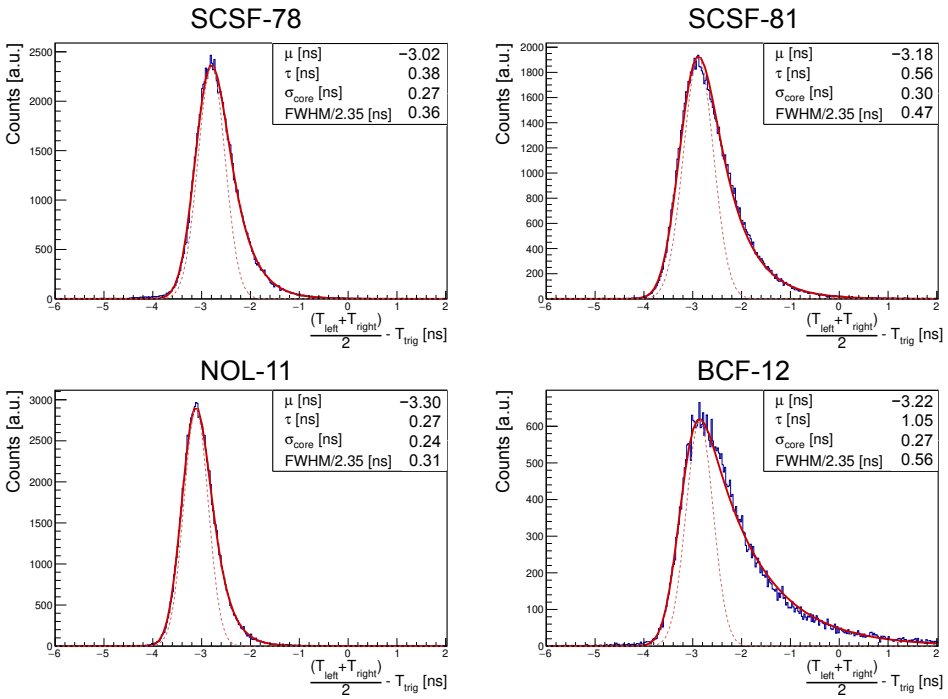

Figure 5.15: Mean time (MT) for different type of fibers.

two fibers, the σ_{core} can be used as the time resolution σ_{MT}. Alternatively, asymmetric errors for the left and the right can be used to quantify the time resolution. The best result is obtained with the NOL-11 fiber, with a time resolution of $\sigma_{MT} \simeq 250\,\text{ps}$. These measurements do not account for the external time reference's jitter, estimated to be $\simeq 60\,\text{ps}$, originating from the trigger scintillator. The results show some larger σ_{MT} values compared to $\frac{1}{2}\sigma_{\Delta T}$, but significantly smaller then $\sigma_{\Delta T}$.

Figure 5.16 shows the peak values of the mean time distribution at different hit possiiotns along the fiber. These peak values are derived through fitting with the EMG distribution, similar as before. Considering the total distance covered by light emitted from both ends of the fiber is constant, equal to the length of the fiber, it is expected that the mean time and the width of the MT distribution would remain constant throughout the fiber. This hypothesis is confrimed by the data shown in Figure 5.16, within the system's resolution. The data points at each hit position can be interpolated with a straight line and the slope, $= 0$, of the line as shown and comfirms the constancy of the mean time along the fiber. Thus, the mean time is not influenced by the hit position along the fiber, and the spread of the MT distribution σ_{MT} remains relatively unchanged throughout. This is a very important result and confirms the idea that the light propagates uniformily in both directions, and the MT distribution does not requiere to take into account the light propagation effects in the fiber. So the MT is a good observable of time measurement.

The dependence with the number of detected photons n_{ph} is shown in Figure 5.18 and Figure 5.17. As the number of detected photons n_{ph} increases, the tail on the right

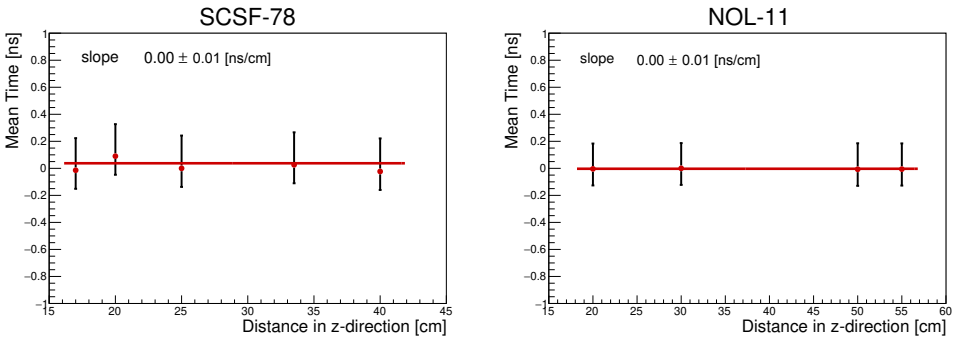

Figure 5.16: Peak values of the mean time distribution at different hit positions along the fiber. The data points at each hit position can be interpolated with a horizontal line. That comfirms the constancy of the mean time along the fiber. The width of the MT distribution σ_{MT} remains relatively unchanged throughout.

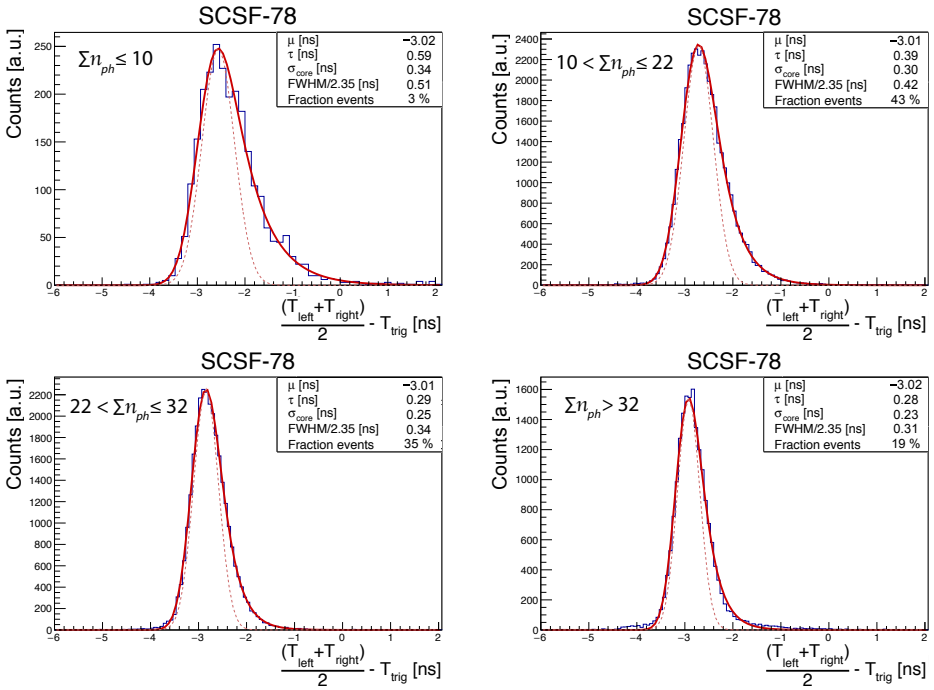

Figure 5.17: Mean time (MT) for different total number of detected photons $\sum n_{ph}$ for SCSF-78. As the total number of detected photons $\sum n_{ph}$ increases, the spread of the distribution decreases.

side of the peak diminishes and the spread of the MT distribution decreases. This is the same as for thetime difference ΔT distribution. For the case of where $\sum n_{ph} > 32$,

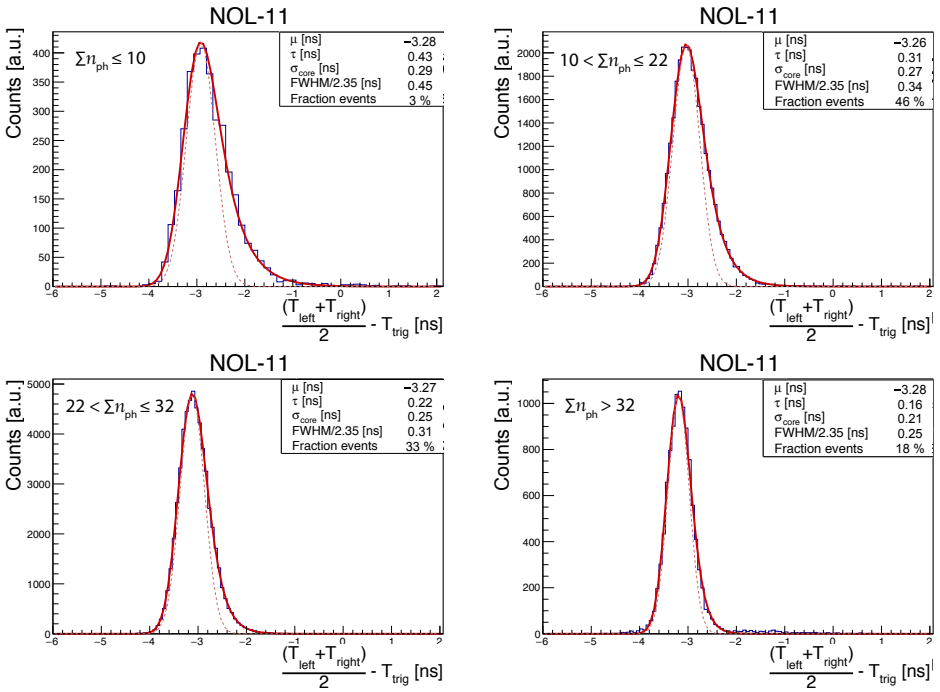

Figure 5.18: Mean time (MT) for different total number of detected photons $\sum n_{ph}$ for NOL-11. As the total number of detected photons $\sum n_{ph}$ increases, the spread of the distribution decreases.

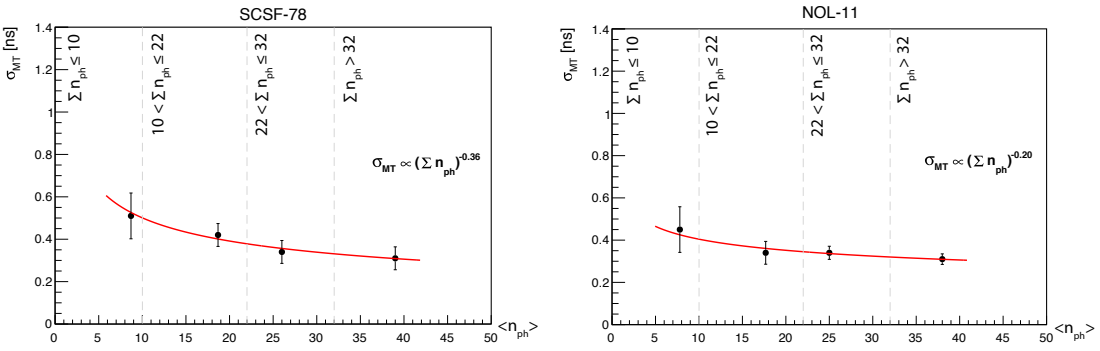

Figure 5.19: σ_{MT} as a function of the total number of detected photons $\sum n_{ph}$ for SCSF-78 (left) and NOL-11 (right).

the achievable time resolution σ_{MT} is given from the NOL-11 fiber, with a value of $\sigma_{MT} \simeq 220\,\text{ps}$. For the SCSF-78 fiber, the time resolution σ_{MT} is $\sigma_{MT} \simeq 240\,\text{ps}$.

As for the width of the time difference distribution $\sigma_{\Delta T}$, the width of the MT σ_{MT} change, less significantly with the number of detected photons n_{ph}, as shown in Figure

Table 5.4: Summary of the performance of the blue-emitting scintillating fibers studied in this work. The reported values are for measurments performed at the center of the fiber. For σ_{MT} we report the width at the half maximum of the mean time distribution for the left side and right side of the peak seperately to refelect the asymmetry of the distribution, seen in Figure 5.15.

Fiber type	$< n_{ph} >$	Λ^{short} [cm]	effective τ [ns]	$\sigma_{\Delta T}$ [ps]	σ_{MT} [ps]
SCSF−78	13.7 ± 0.6	16.4 ± 4.1	2.4 ± 0.1	467	$^{-240}_{+450}$
SCSF−81	5.8 ± 0.3	13.2 ± 6.3	2.1 ± 0.1	552	$^{-310}_{+630}$
NOL−11	12.1 ± 0.9	15.6 ± 5.4	1.0 ± 0.1	393	$^{-230}_{+380}$
BCF−12	3.8 ± 0.1	18.2 ± 20	3.0 ± 0.1	708	$^{-260}_{+860}$

5.19. It can also be fitted with a power law but in this case the slope is not so steep and therefore the exponent α is smaller.

It's important to point out that the peak positions of the Mean Time (MT) distributions, as shown in Figure 5.17 and 5.18 , remain unchanged with variations of $\sum n_{ph}$, which represents the signal's amplitude. This indicates that the timing algorithm used is unaffected by the amplitude of the signal, meaning there is no amplitude driven time walk observed. As a result, there is no necessity to apply an amplitude correction to the time measurement, ensuring the reliability of the timing irrespective of signal strength variations.

5.4 SUMMARY OF SCINTILLATING FIBER PROPERTIES

Within this study and with this setup, different types of fibers are tested and their properties are measured. More specifically, this study shows properties of various blue-emitting scintillating fibers, examining attributes such as photon yield (uncorrected for SiPM PDE), short attenuation length (Λ_{short}), effective decay time, and achievable time resolution.

Table 5.4 summarizes the results obtained for the different types of fibers. The superior timing performance of the NOL−11 fiber can be noticed with respect to the other fibers. The SCSF−78 fiber also shows good timing performance with a slightly higher light yield. The fibers with a low light yield, SCSF−81 and BCF−12, show poor timing performance therefore, are not a good candidate for timing applications. Good efficiencies can be obtained from fibers with a high light yield, such as SCSF−78 and NOL−11.

The study shows that best timing requires not just minimizing the scintillation light decay time τ of the fiber but also maximizing the number of detected photons n_{ph}.

For instance, the light yield in principle could be increased by increasing the SciFi detector's thickness through additional fiber layers, although this might be constrained by the detector's material budget. For smaller detectors (of order 10 cm), enhancing scintillation light yield could involve increasing the concentration of activator dyes, but maintaining long attenuation lengths necessitates a relatively low concentration of the spectral shifter.

Reading fibers at both ends is a must. The mean time (MT) proves to be a good observable for time measurements as it is independent of the particle's crossing point. The study found that scintillation light travels through the fibers at about half the speed of light in vacuum. This is due to the increased effective path of the photons, which is caused by their helical trajectory and the multiple internal reflections they undergo within the fiber cladding. Interestingly, no edge effects were observed near the fiber ends, which might have been expected due to varying geometrical apertures close to the fiber's end. The light is channeled in the fiber, contrary to a scintillating bar with a light guide at the end.

The asymmetry in the mean time (MT) distribution can be addressed in a likelihood analysis of the time information, incorporating the distribution's asymmetric shape. This approach is beneficial in applications like time of flight-based particle identification (PID) analysis or coincidence measurements. Enhancing the analysis with signal amplitude information could further improve results, although this data might not always be available, especially when using ASICs designed solely for time recording, such as the MuTRIG ASIC.

To sum up, these are the important points from this study:

- The best timing performance is obtained with the NOL−11 fiber, with a time resolution of $\sigma_{MT} \simeq 250\,\text{ps}$, while the SCSF−78 fiber gives a slightly higher light yield.
- Optimal timing is achieved by both minimizing fiber scintillation light decay time τ and maximizing the number of detected photons n_{ph}.
- The mean time (MT) is a good observable for time measurements as it is independent of the particle's crossing point.

6

PERFORMANCE OF SCINTILLATING FIBER RIBBONS

In this chapter, a study of the performance of scintillating fiber (SciFi) ribbons is presented. The SciFi ribbons are described in Section 3.3.

6.1 EXPERIMENTAL SETUP

As for the previous setup, the measurements of the SciFi detector, and more specifically, the SciFi ribbons, were conducted through test beam campaigns at PSI's πM1 beamline (different campaigns than for the individual fiber measurements detailed in the previous chapter).

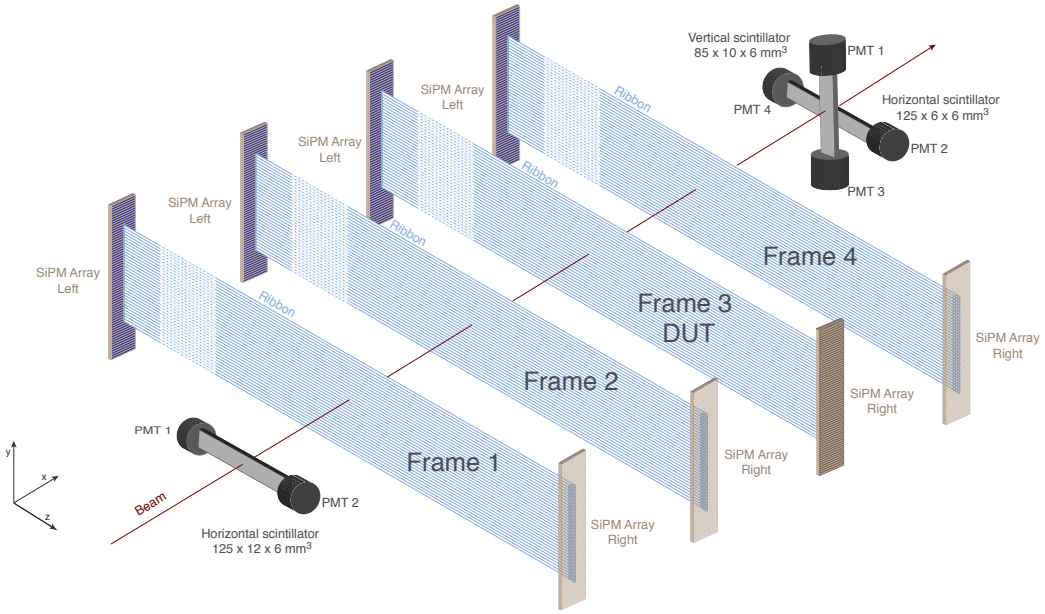

Figure 6.1: Illustration of the SciFi telescope comprising of four SciFi ribbons and three trigger scintillators bars. The third most downstream detector is referred to as Device Under Test (DUT).

A telescope consisting of four SciFi ribbons was constructed to study the SciFi detector, as shown in Figure 6.1. All detectors were placed inside a box designed to prevent light intrusion. Of the four SciFi ribbons used, three served for tracking purposes, while the third, positioned furthest downstream, is the Device Under Test (DUT). Motorized frames fix the ribbons in the setup, enabling vertical movement for alignment and vertical scanning The DUT enables angular scans by tilting around a horizontal axis perpendicular to the beam. Additionally, the entire assembly is mounted

on rails, making it possible to move it sideways relative to the beam for horizontal scanning purposes. Triggering on beam particles was accomplished using a scintillator bar measuring 125 mm × 12 mm × 6 mm positioned upstream, and a scintillator cross downstream. This cross consisted of a horizontal bar (125 mm × 6 mm × 6 mm) and a vertical bar (85 mm × 10 mm × 6 mm). All scintillators were connected at each end to Hamamatsu photomultipliers, specifically the `H6524` model. The trigger cross served as the external time reference for the time measurements, providing a time resolution of $\sigma_{trigger} \simeq 80$ ps. A 3-fold coincidence between the three trigger scintillator bars initiated the acquisition of an event, indicating that the beam particle crossed the SciFi telescope.

Figure 6.2: Photographie of a scintillating fiber ribbon on a supporting frame. This frame is placed in the telescope with the SiPMs arrays fixed at both ends.

The SciFi ribbons used in this study match the specifications of the ribbons to be used in the `Mu3e` experiment, which measure 32.5 mm in width and 300 mm in length. These prototype fiber ribbons were constructed with varying fiber types and configurations, ranging from two to six layers of staggered fibers. Different types of blue-emitting scintillating fibers and adhesives were used in the assemblies. In the telescope configuration, these SciFi ribbons were connected, as previously mentioned in Section 3.3, to Hamamatsu `S13552-HQR` SiPM arrays, featuring 128 channels, at both ends. However, not all channels of the SiPMs were instrumented: 64 channels of the DUT on each side, covering a vertical extent of 16 mm, and 32 channels for the other ribbons on each side, corresponding to an 8 mm vertical extension, all equipped with analog readout electronics.

Unless specified otherwise, the presented results relate to the `Mu3e` baseline design. This design consists of SciFi ribbons composed of three staggered layers of SCSF−78MJ scintillating fibers, each 250 µm in diameter, and assembled using POLYTEC EP 601-Black epoxy. Varying scintillating fiber types are also studied and discussed in the following. However, fiber types SCSF-81 and BCF-12 are not further discussed in this study due to their poor performance, as described in the previous chapter.

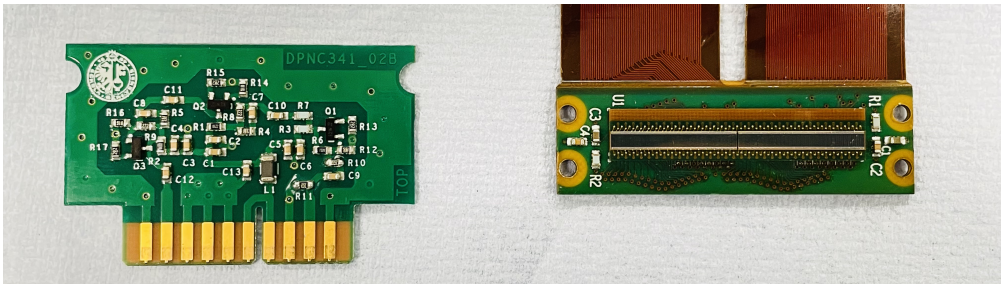

Figure 6.3: Pictures of the SiPM array module soldered to a carrier PCB with integrated flex print cables with 128 signal and ground lines (right) and the amplifier (left) used in the SciFi telescope.

6.1.1 *Readout electronics*

The SiPM arrays, model `S13552-HQR` from Hamamatsu, are soldered to a carrier PCB featuring integrated flex print lines, as shown in Figure 6.3. This setup connects each SiPM channel to a fast, transisitor-based, three-stage common emitter amplifier, shown in Figure 6.3. Different from the previous setup, this is a three-staged amplifier. Through a shunt resistor with a resistance of $R_{shunt} = 39\,\Omega$, the SiPM's current signal is converted into a voltage signal. This voltage is then capacitively coupled by a $C = 100\,\text{nF}$ capacitance to the amplifier stages. The capacitively coupled signal blocks any DC component and only allows AC components (the varying part of the signal) to pass through to the amplifier. The signal, now in voltage form, enters a three-stage common emitter amplifier. Each stage of this amplifier will increase the amplitude of the signal. The amplifier's performance is characterized by a cut-off frequency of 400 MHz. Above this frequency, the amplifier's ability to transmit signals diminishes rapidly, indicating its optimal performance is achieved at frequencies below 400 MHz. In parallel with the cut-off frequency, the amplifier has a quick rise time of approximately 1 ns. The amplifiers, with a variable gain of approximately 35 dB, are controlled by the voltage applied (typically 4.5 V), resulting in single photon amplitudes of about 100 mV. The maximum amplitude of the amplified signals did not surpass 1 V. Typically, the amplified SiPM signals exhibit a rise time of approximately 1 ns, as depicted in 4.17.

The signals are then fed into a wavefrom digitizer board, DPNC 342 [1], which is based on the DRS4 ASICs [57]. The digitizer boards are equipped with 32 analog input channels, comprising four DRS4 ASICs. The input range, between 0 V and -1 V, is inverted on the board to align with the dynamic range of the DRS4 ASIC. To facilitate precise monitoring, the baseline is shifted by 50 mV. Each DRS board connects via a USB 3.0 link for data readout. The DRS4 ASIC features nine independent capacitor arrays, each with a depth of 1024 cells. The ASICs of different boards are synchronized using the ninth channel. Waveforms are sampled at a high rate of 5 GHz, controlled by a Phase-Locked Loop (PLL) locked to a reference clock (around 2.5 MHz for 5 GHz sampling). The charges in the capacitor arrays are digitized at a much lower

1 Designed by Stéphane Débieux, electronic engeneer at the University of Geneva

frequency of 33 MHz with 12-bit Analog-to-Digital converters (ADC). An example of

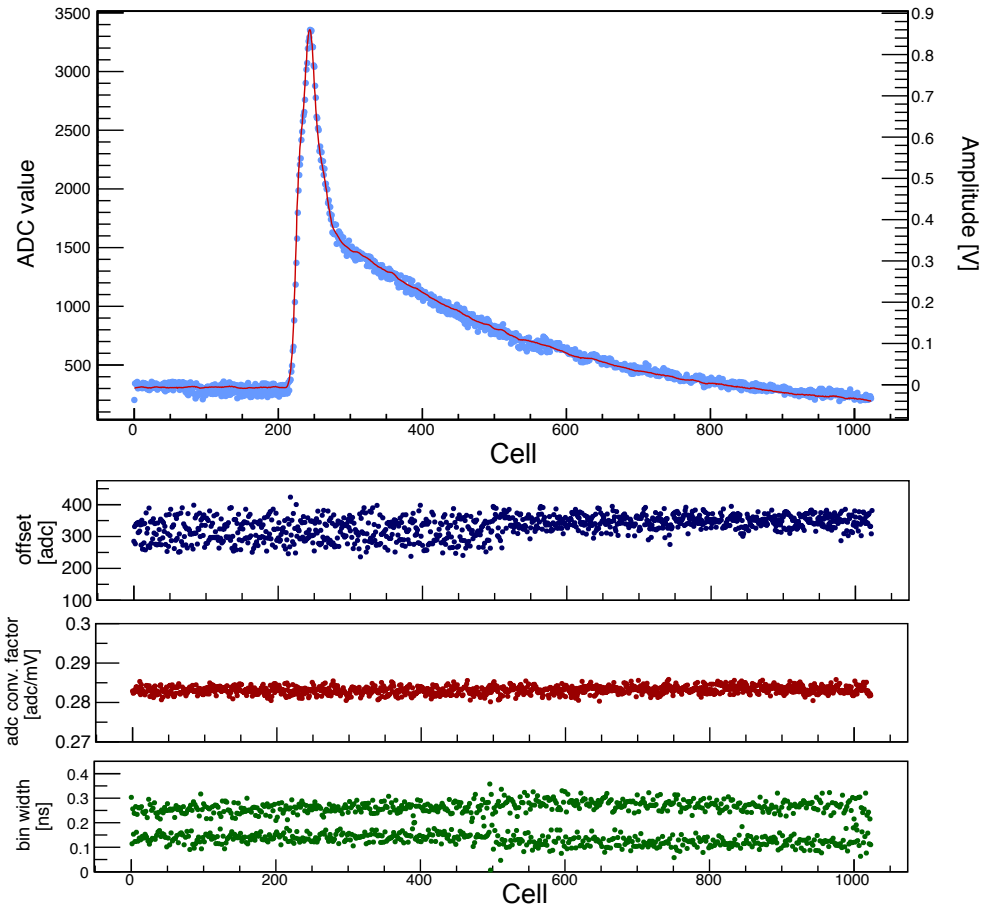

Figure 6.4: Display of a waveform recorded with the DPNC 342 board, both before and after voltage calibration. The continuous line represents the waveform after voltage calibration and the uncalibrated ADC values are depicted as dots. The baseline has been intentionally retained in this illustration to show the range of the ADC values. On the bottom figures, the details of the waveform calibration process, highlighting three key aspects: the baseline (offset), the conversion factors from ADC readings to voltage values, and the time widths associated with the cells of the digitizer.

such a digitized waveform can be seen in Figure 6.4. Each cell in the capacitor arrays undergoes voltage calibration, and the time width of each sampling cell is determined using a 100 MHz sinusoidal signal generated on the digitizer board. The capacitor arrays in the DRS4 are synchronized with an external 50 MHz sinusoidal reference signal. This reference is recorded in parallel with the data in a separate ASIC channel (channel 9). A comprehensive explanation of the calibration process is provided in [59]. On the DPNC 342 board, seen in Figure 6.5, is placed a field programmable gate array (FPGA) from the Cyclone V series of Altera [60]. The FPGA is responsible for executing the on-board data collection logic and managing connectivity between

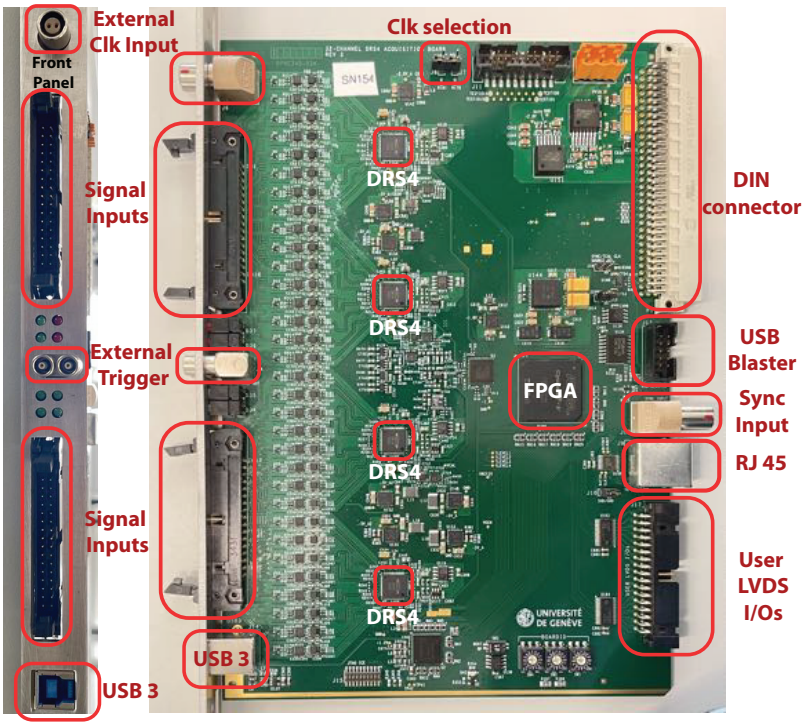

Figure 6.5: The 32 channel DPNC 342 DRS board with each components highlighted and annotated.

different components. The data transfer between the board and a host computer is achieved by a USB-3 connection. The board aligns with the exact physical dimensions of a VME 6U module.

The back of the device is equipped with a DIN connection to provide power at $\pm 6\,\mathrm{V}$. Additionally, it has different control and monitor signals for the readout and synchronization between numerous boards. A USB-blaster is used for communicating with the FPGA during the development process such as firmware updates and debugging. An RJ45 connector is provided for external communications and data transmission. Next to the RJ45 connector, is a two pole LEMO F/RA connector, which serves to receive external signals specifically for time calibration and synchronization of multiple boards. The time calibration source can be a sinusoidal wave generated by an onboard crystal oscillator or an external signal provided through this LEMO F/RA connector or via the VME P1 connection. The received external signals used for time reference, are recorded in parallel with the data in a separate ASIC channel, the 9th, to allow synchronization of multiple boards. Below that connector, a 34-pin connection is included, which contains differential pairs specifically allocated for general purpose usage. Pins on the FPGA directly connect to these pairs.

On the front side of the board, another two pole LEMO F/RA connector for the external clock is situated in the upper part of the front panel. Next to it, two 34-pin connections that allow for the connection of 2×16 single ended signal inputs, which are terminated at 50 Ohm. Between the two 34-pin connections, two coaxial LEMO

connectors are positioned in the center of the panel for the purpose of trigger input and busy output. The board is equipped with a USB type B connector, which allows for communication and data transmission to the host PC. On the board are address keys for easy board identification. Three turning switches on the board provide it with identification. The board has J7 and J8 jumpers that are used to decide the selection of the clock source.

6.1.2 *Beamline*

As for the individual fiber measurements, the majority of the measurements were performed at PSI's πM1 beamline. The beam, set to a momentum of 210 MeV/c, predominantly consisted of positive pions. Secondary particles were generated using a carbon target (target M) in a 1.8 A continuous beam of 590 MeV protons. These particles were then extracted and selected based on their p/m ratio using a combination of dipole and quadrupole magnets. The average continuous beam intensity was approximately 10^6 particles/s, focusing on a spot measuring 15 mm $\times$ 10 mm on the Device Under Test (DUT) at the center of the telescope [61].

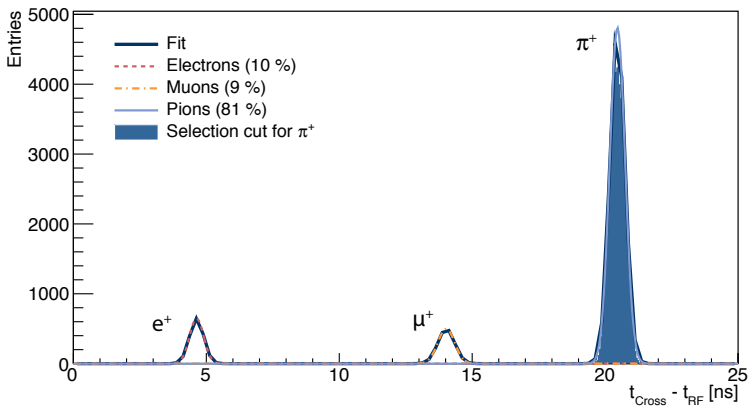

Figure 6.6: Based on the time difference between the trigger cross and the 50.63 MHz RF signal from the cyclotron accelerating cavities, time of flight particle identification is performed. The beam is composed of 81% π^+, 9% μ^+, and 10% e^+. Particle concentrations are extracted after a composite fit of three Gaussian functions. The shaded area represents the cut applied to select pions. The pattern repeats each 19.74 ns.

By recording the 50.63 MHz RF sinusoidal signal of the accelerating cavities of the proton cyclotron (the RF pattern has a length of 19.74 ns), beam particles are identified with time of flight (ToF) measurements between the trigger cross and the production target, which is located 21 m upstream of the experimental setup. Figure 6.6 provides an illustration of the beam particle identification by displaying the time difference distribution between the trigger cross signal and the RF signal. Beam particles are chosen within a 3 ns window surrounding each peak. This selection has been successful

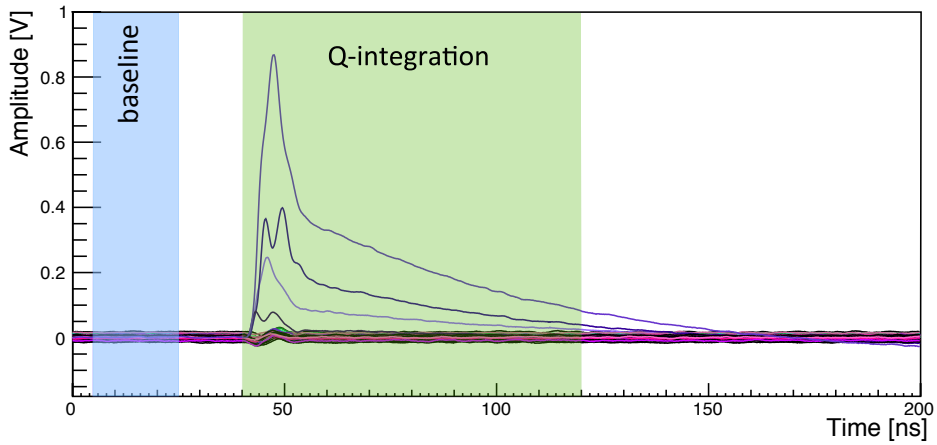

Figure 6.7: One event acquired with the 32 channels DPNC 342 DRS board. The signals of all 32 channels are shown. Four adjacent channels have a high activity (over 100 mV amplitude). A slight cross-talk of about 3 % is noticeable in inactive channels. Charge is extracted by integrating the pulse's main part in the "Q-integration" region, with the "baseline" section used for baseline assessment.

for 88% of beam particles. Particle concentrations are extracted after a composite fit of three Gaussian functions. The beam's composition is 81% π^+, 9% μ_+, and 10% e^+ at 210 MeV/c. Pions are selected for the following studies as they are the most abundant particles.

6.2 SIGNAL PROCESSING

Figure 6.4 provides an illustration of a digitized waveform, showing 1024 samples which translates into a 205 ns time window. From the recorded waveform, all the information, such as the charge and arrival time of the scintillation photons, can be extracted. Figure 6.4 shows also the ADC to voltage conversion factors and the time width for each cell of the DRS4 capacitor array. The DRS4 digitizer board was described earlier, and more details can be found in [57, 58].

6.2.1 *Waveform*

Figure 6.7 shows an example of a waveform. The figure presents voltage and time calibrated waveforms across 32 consecutive channels of a SiPM array, captured during a single event. Several adjacent channels exhibit notable activity due to the light signal from a crossing particle spreading across multiple SiPM array channels. The scintillation photons primary arrive simultaneously, creating signals starting around 40 ns after the opening of the acquisition window. The trigger delay determines this start, and it is adjustable to ensure that the pulse is captured within the acquisition window. The shape of the pulse suggests different emission and arrival times of the scintillation

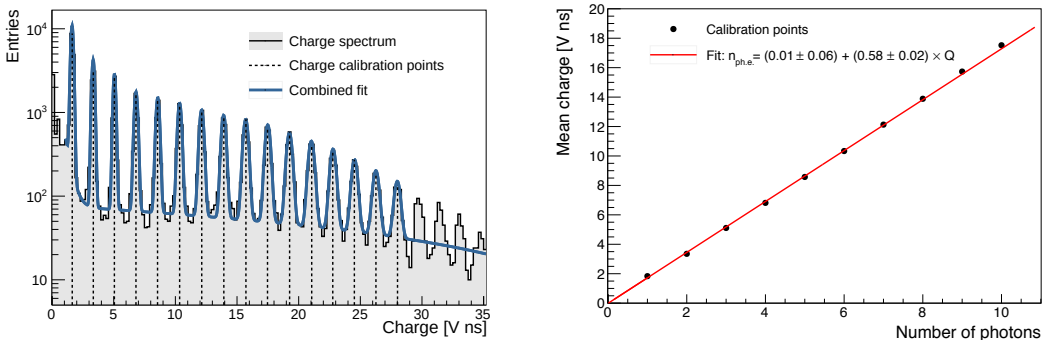

Figure 6.8: Left: Charge distribution from waveform integration. Peaks above the continuum correspond to distinct photon counts. Right: Relationship between the peak positions and the corresponding photon numbers n_{ph}.

photons, linked to the scintillating fiber's de-exitation. Cross-talk happens at about 3 percent in the readout chain, mostly from the flex prints of the electronic amplifier boards. This makes dips visible in channels that aren't being used. The time alignment of all channels is determined with respect to the 50 MHz sinusoidal reference signal injected into each DRS4 ASIC and the external trigger.

For quantifying the scintillation photon-induced charge in each SiPM channel, the method involves subtracting the baseline from the waveforms. These adjusted waveforms are then integrated over a period of 80 ns, equivalent to 400 sequential waveform samples, beginning around 5 ns before the pulse starts. The baseline is determined for each event by averaging the waveform over 100 sequential samples, or a 20 ns interval, between 25 ns and 5 ns before the signal starts. Each waveform in the process undergoes subtraction of this baseline, event by event.

The resulting charge, which includes the amplifier's gain, is initially expressed in arbitrary units. Due to the SiPMs' ability to detect single photons, this charge is normalized to the charge generated by a single photon, thereby eliminating the need for absolute amplification values of the SiPM and of the electronics. Consequently, the charge can be represented in terms of the number of detected photons or photoelectrons (ph.e.).

6.2.2 *Charge normalization*

To determine the count of detected scintillation photons, the charge distribution from waveform integration, as shown in the left Figure 6.8, is normalized against the charge produced by a single photon. Peaks above the continuum, mainly due to cross-talk within SiPM cells in the same column, correspond to distinct photon counts. These peaks are fitted with a Gaussian distribution. The relationship between the peak positions and the corresponding photon numbers n_{ph} is shown in the right Figure 6.8. The slope gives the conversion factor between the charge and the n_{ph}. Additionally, the

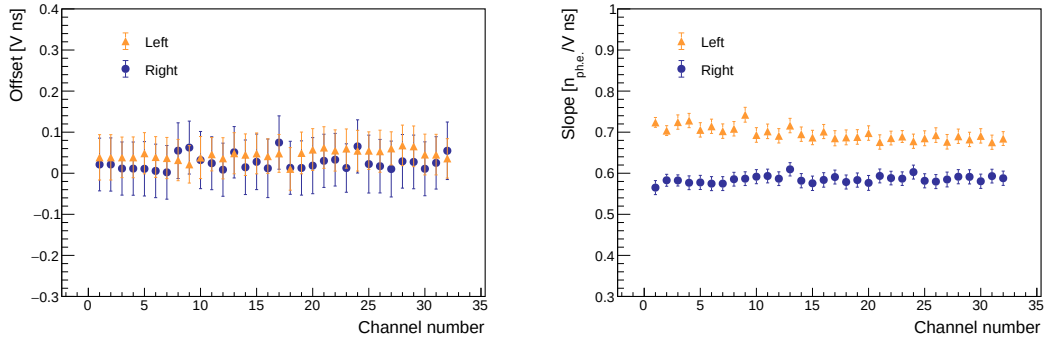

Figure 6.9: Offset (left) and slope (right) of the linear fit for the multichannel SiPM arrays at the opposite ends of a SciFi ribbon (2×32 channels). The differences within the same sensor are caused by variations in the amplifier and SiPM array channel gains. The two sensors differ from one another since they are both operated at the same bias voltage.

fit extrapolates to zero, confirming the correct baseline subtraction. This methodology is consistently applied across all channels.

The gain across channels within the same SiPM array shows an overall uniformity, as seen in the left Figure 6.9. However, there are some minor variations due to the different amplifier gains and the unifrom V_{bias} operation across all SiPM array channels. Sensors at both ends of the SciFi ribbon, operated under the same V_{bias}, exhibit differences in gain.

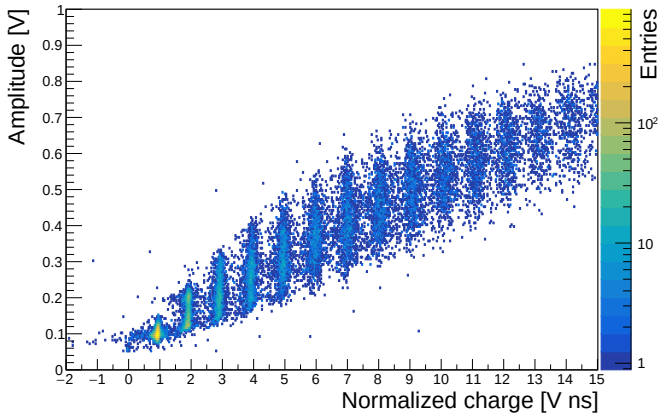

Figure 6.10: Relationship between the integrated charge and the maximum amplitude of the waveform.

The relationship between integrated charge and peak signal amplitude for all active channels of the SiPM array, connected to a specific DRS digitizer board, is presented in the Figure 6.10 post charge normalization but before amplitude normalization. The spread in the arrival of scintillation photons, which is associated with the de-excitation process of the spectral shifter, does not impact the leading edge of the peak signal

but is contributing to the charge. This explains the spread of the signal amplitudes. For comparison, the same plot is shown for the DCR in dark conditions in Figure 6.11. By integrating the charge over 400 consecutive pulse samples, a more precise

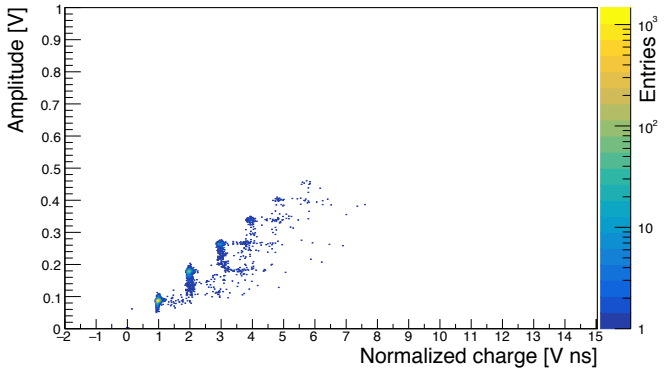

Figure 6.11: Relationship between the integrated charge and the maximum amplitude of the waveform for DCR.

representation of the number of photons detected in each event is achieved. This approach is less susceptible to fluctuations in amplitude.

6.2.3 *Thresholds determination*

In this study, the selection of hits is determined by the signal's amplitude rather than a charge threshold. This approach is favored as amplitude data is immediately accessible and can also be utilized at the trigger level. This is also the operational mode of the MuTRiG ASIC, see section 8.1. As shown in the left Figure 6.12 the maximum amplitude distribution for a single channel following baseline subtraction. In this distribution, photon peaks are distinctly observable at lower photon multiplicities, and

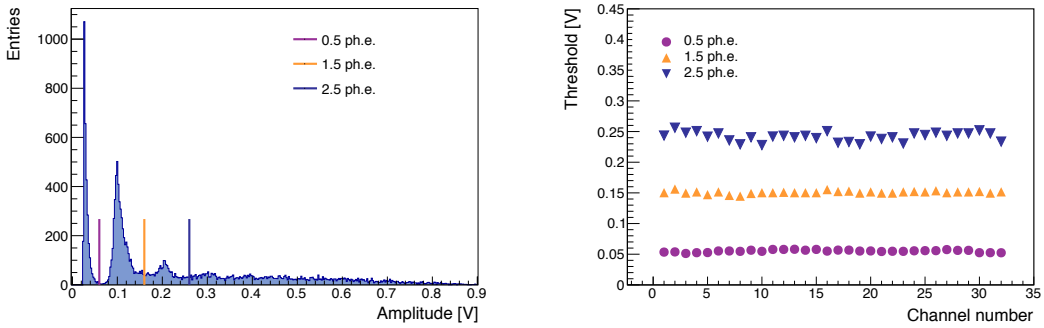

Figure 6.12: Left: Maximum amplitude distribution for a single channel following baseline subtraction. Right: Determination of thresholds for each channel.

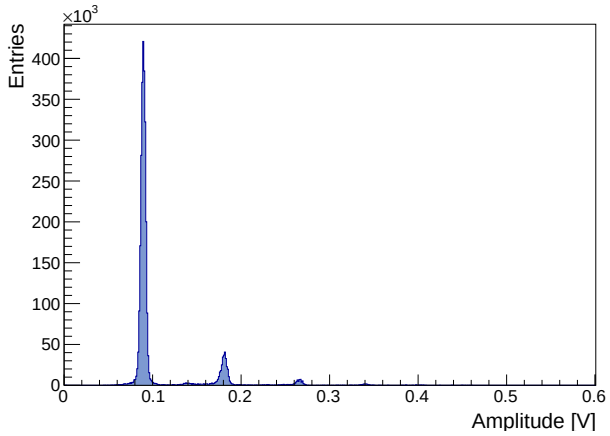

Figure 6.13: Maximum amplitude distribution for a single channel following baseline subtraction for DCR.

exhibit regular spacing. As comparison the same plot is shown for the DCR in Figure 6.13.

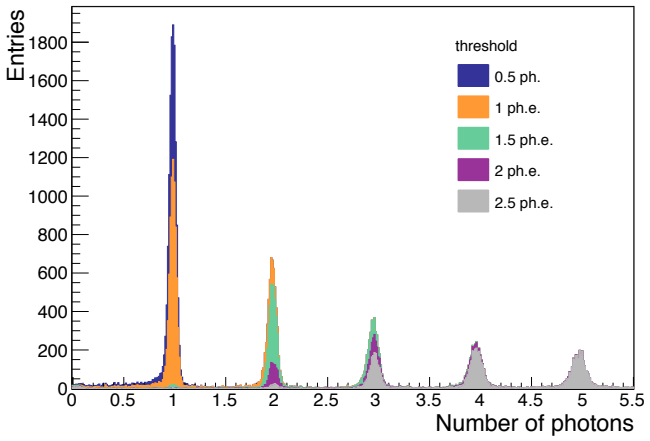

Figure 6.14: Effect of the amplitude thresholds on the integrated charge distribution for one channel.

To select a channel with a minimum detected photon count n_{ph}, amplitude thresholds are established between two successive peaks in the amplitude distribution. For example, to select an event with $n_{ph} \geq 2$ in a specific channel, the threshold is set between the peaks corresponding to 1 photon and 2 photon amplitudes, at a level called equivalent to 1.5 ph.e. amplitude. This method of determining amplitude thresholds for each channel is shown in the right Figure 6.12. The consistent spacing of these thresholds suggests a linear response from both the detector and the readout electronics. Variations observed are attributed to differing gains across each SiPM array channel.

The impact of amplitude thresholds on the charge distribution and the number of detected photons can be further explored. Figure 6.14 shows how these thresholds cut into the charge distribution. For instance, at a 1.5 ph.e. threshold, around 5 % of 1 photon event are included in this selection, whereas approximatively 20 % of 2 photon events are excluded. The use of these thresholds is significant in the context of cluster formation and the detection efficiency of the detector, discussed in later sections.

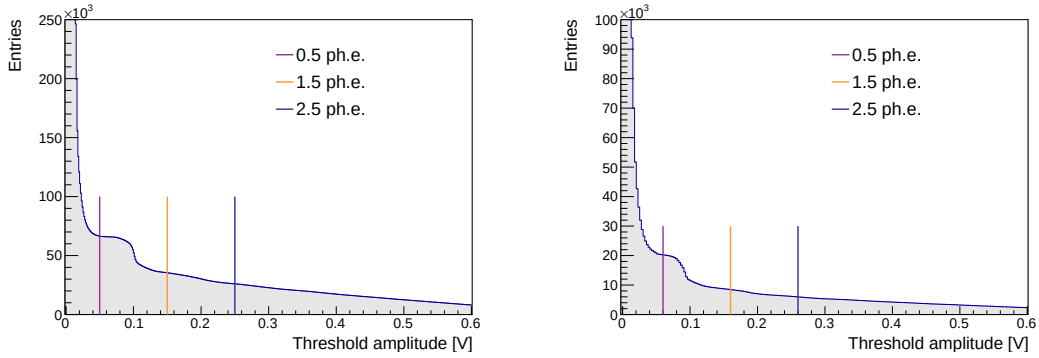

Figure 6.15: Cumulative sum of the maximum amplitude distribution of a single channel as a function of a threshold amplitude. Left: 3-layer SCSF-78 fiber ribbon assembled with black epoxy. Right: 4-layer NOL-11 fiber ribbon assembled with clear epoxy containing a 20 % TiO_2 admixture. For clarity the x-axis is limited to 0.6 V but the trend is not changing going further until 0.9 V.

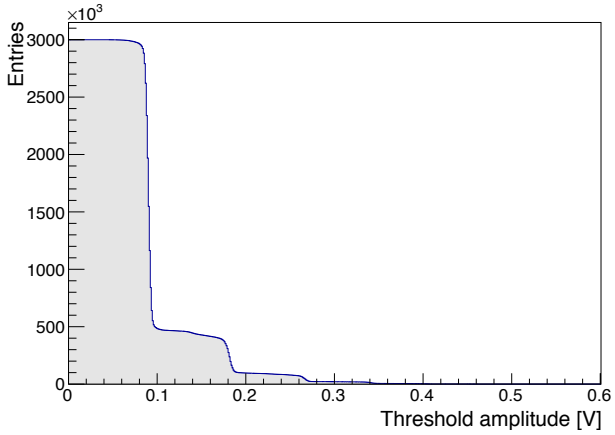

Figure 6.16: Cumulative sum of the maximum amplitude distribution of a single channel as a function of a threshold amplitude for DCR.

Figure 6.15 shows the cumulative sum of the maximum amplitude distribution of a single channel as a function of a threshold amplitude for the 3-layer SCSF-78 fiber ribbon with black epoxy and the 4-layer NOL-11 fiber ribbon with clear epoxy containing a 20 % TiO_2 admixture. The MuTRiG ASIC works with amplitude thresholds, and the rates that change based on these thresholds are controlled by DAC values. These rates give information for calibrating the ASIC, i.e., setting the correct thresholds.

The rate as a function of the amplitude thresholds can be translated to the cumulative sum of the maximum amplitude distribution. One can see that the entries, which can be considered a rate, are decreasing as the amplitude threshold is increasing. The slopes of the cumulative sum are the peak signal amplitudes, and the so called plateaus, where no variation is seen, are where the amplitude thresholds are established beforehand, as seen by the colored lines in Figure 6.15. The slope for the 1 photon can be seen, but the ones for the 2 and 3 photons are not visible. For visibility reasons, the x-axis goes until 0.6 V, but the trend is not changing going further until 0.9 V. Figure 6.16 shows the same for DCR. The data reveal a more discernible trend, with distinct plateaus evident even for the 2 and 3 photon levels. Consequently, using DCR improves the precision in determining each threshold when the maximum amplitude distribution is only available, offering an advantage over beam data. Since the MuTRiG ASIC works with amplitude thresholds the best way to set the thresholds is with DCR.

Additionally, the correlation between hits detected by the two SiPM arrays positioned at opposite ends of the SciFi ribbon is examined. Figure 6.17 illustrates correlations at amplitude thresholds of 0.5 ph.e. and 1.5 ph.e. amplitude thresholds. In the test setup, the SciFi ribbons measure hit positions vertically across the ribbon. The extent of this correlation reflects the vertical spread of the beam spot impacting the SciFi ribbon, as determined by the vertical dimension of the horizontal trigger scintillator bars. The width of these correlations also provides an estimate for the cluster width, indicating the extent to which the optical signal spreads across multiple channels of the SiPM array.

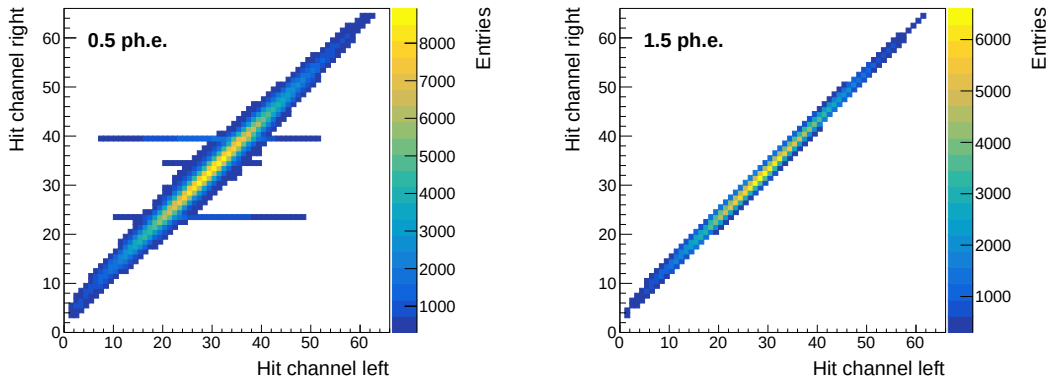

Figure 6.17: Correlation between hits detected by the two SiPM arrays at both ends of the SciFi ribbon. Left: 0.5 ph.e. amplitude threshold. Right: 1.5 ph.e. amplitude threshold.

6.3 CLUSTERING

When particles traverse the SciFi ribbon, they excite a small number of fibers , generating scintillation photons, as shown in Figure 6.18. The same fibers transmit these photons to the SiPM arrays at both ends of the ribbon. The staggering of the fibers

prevents a one-to-one mapping of the fibers to the columns of the SiPM array, causing the scintillating light signal to spread across multiple adjacent SiPM columns (channels). Other various factors such as optical cross-talk between the fibers, delta rays, the angle at which the photons exit, and light scattering at the optical junction between the SciFi ribbon and the photo-sensor contribute also to the spread of the scintillation light signal across multiple adjacent SiPM columns (channels). This spread can be illustrated as in Figure 6.7 where several consecutive channels exhibit significant activity.

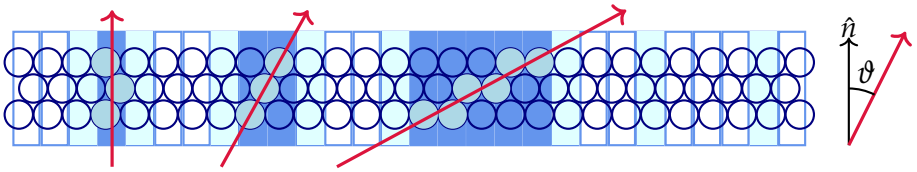

Figure 6.18: Transverse view of a 3-layer SciFi ribbon mapped to a SiPM array. When a particle (shown as a red arrow) passes through, it excites some fibers (indicated as filled circles), potentially causing avalanches in multiple SiPM channels (blue). Optical cross-talk may extend the signal to adjacent channels (light blue). The cluster's width varies with the particle's angle (0°, 30°, 50°, shown left to right).

Furthermore, in the context of the `Mu3e` experiment, particles intersect the SciFi ribbons at an average angle θ of 27° relative to the normal of the SciFi ribbon. This angular intersection further extends the spread of the light signal. Additionally, due to cross-talk among SiPM columns and dark counts, spurious signals may emerge in channels that do not actually receive a direct signal.

The clustering process aims to accurately identify and group all SiPM channels excited by the crossing particles. At the same time, it aims to eliminate any unwanted contributions from SiPM channels that are mistakenly triggered, such as those activated by DCR or cross-talk.

The clustering algorithm in this study begins with the selection of candidate SiPM channels, adhering to specific criteria:

- **Amplitude Threshold**: the amplitude of each selected channel must exceed a predefined threshold of 0.5 photo-electrons (ph.e.) or more. This threshold is uniformly applied to all channels.
- **Timing**: the peak of the channel's signal should align with the trigger time, falling within a window of -5 ns to $+10$ ns. This timing constraint effectively reduces dark counts.

Subsequent to channel selection, the cluster formation involves several steps which need to be fuffilled:

1. **Contiguity of Channels**: this involves grouping only directly contiguous channels among the selected ones into clusters. A one channel gap is allowed to account for inefficiencies and dead channels.
2. **Seed Channel Identification**: within each cluster, the channel with the highest amplitude is designated as the *seed* for further analysis.

3. **Hit Multiplicity**: a minimum hit multiplicity, generally set at two, is required for cluster formation. However, at higher threshold levels, this multiplicity requirement is waived, allowing for clusters comprising a single hit.

4. **Track Matching**: each cluster must correspond to a track reconstructed within the SciFi telescope, matching within $\pm 5\sigma_{res}$, where σ_{res} represents the width of the residual distribution showns in Figure 6.19.

5. **Cluster Timing**: the final step in the formation of a cluster is to assign its time based on the earliest time stamp among the channels that constitute it, effectively marking the time of the first detected photon.

These structured steps ensure a systematic and precise approach to forming clusters, critical for accurate data analysis in the context of the study.

Prior to the association of clusters with specific tracks, it is essential to align the SciFi telescope. Initially, the identification of clusters is independent of track matching. Following this initial identification, alignment procedures for the SciFi ribbons are carried out. After the alignment, clusters are then matched to tracks.

The alignment of the SciFi telescope (Figure 6.19) needs to detect clusters from all four SciFi ribbons. In this phase, tracks are reconstructed across the SciFi telescope using straight lines, neglecting the multiple scattering using the clusters identified above: for a hit to be selected, it must pass a predefined amplitude threshold of 0.5 photo-electrons (ph.e.). Additionally, the seed of each cluster is required to meet a more stringent threshold of 1.5 ph.e.

In scenarios where multiple clusters are present, the one closest in time to the trigger event is chosen. To mitigate edge effects, clusters that are reconstructed within 4 channels (equivalent to 1 mm) of the ribbon edges are excluded from consideration.

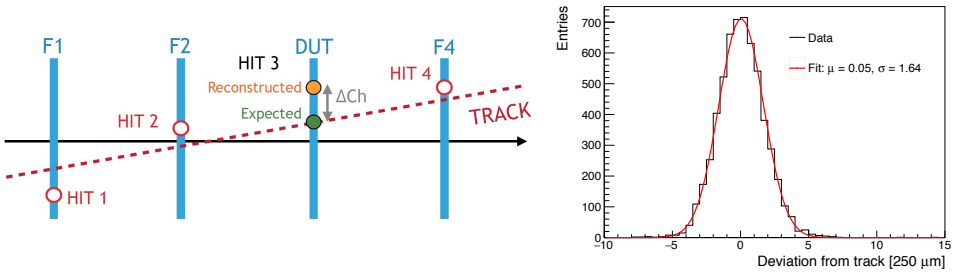

Figure 6.19: left) Illustration of the SciFi ribbon alignment procedure. right) Distribution of residuals between the clusters reconstructed in the DUT and the tracks reconstructed in the SciFi telescope. The units are expressed in terms of the SiPM array pitch of 250 nm . Note that this is not the intrinsic resolution of the detector.

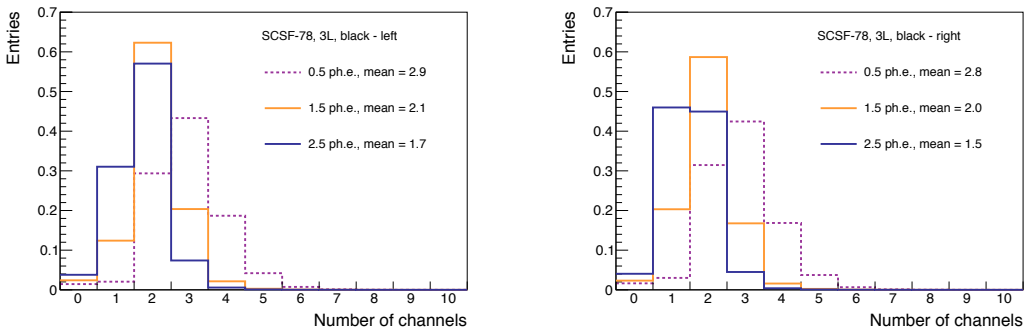

Figure 6.20: Cluster width comparison for particles crossing perpendicular a 3-layer SCSF-78 fiber black ribbon: left) 15 cm from the ribbon's left end, right) 15 cm cm from the right end, across amplitude thresholds of 0.5, 1.5, and 2.5 ph.e. Distributions are normalized to the total event count, ensuring each distribution's integral equals to 1.

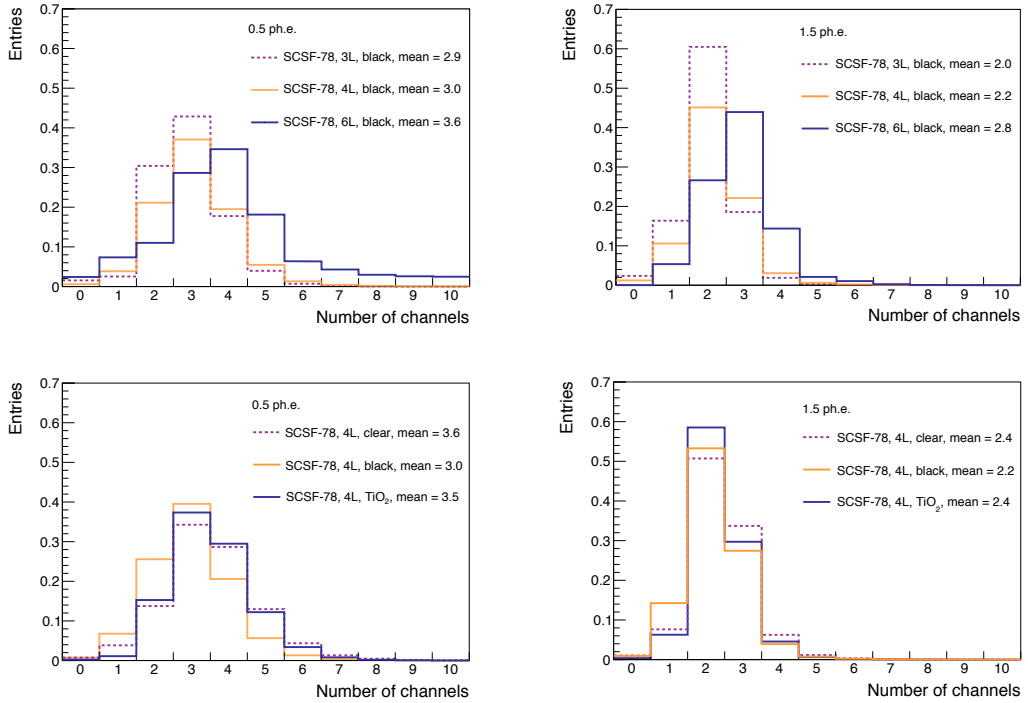

Figure 6.21: Comparison of cluster widths for amplitude thresholds of 0.5 ph.e. (Left) and 1.5 ph.e. (Right): top) 3-, 4-, and 6-Layer SCSF-78 fiber black ribbons; bot) 4−Layer SCSF−78 ribbons utilizing various adhesives (Clear, Black, and Clear with 20 % TiO_2 Admixture).

6.3.1 *Cluster width*

Figure 6.20 shows the reconstructed clusters of a 3-layer SCSF-78 fiber ribbon, which has been prepared using black epoxy. The figure illustrates the application of different amplitude thresholds, specifically 0.5, 1.5, and 2.5 photoelectrons (ph.e.), applied separately to each end of the ribbon. These ph.e. thresholds are uniformly applied across all channels within each cluster. This method aligns with the operational characteristics of the MuTRiG ASIC, which permits a single threshold setting for each channel. The beam particles intersect the SciFi ribbon centrally, approximately 15 cm from either edge, and strike the ribbon perpendicularly. The vertical axis in this and subsequent figures is normalized to the total number of analyzed events, meaning that the integral of the distribution equals one. The occurrence of zero-width entries, denoting events without cluster detection, serves as an initial indicator of the SciFi detector's detection inefficiencies, which are discussed in later sections. As the threshold value rises, a noticeable contraction in cluster width occurs. Generally, the channels at the cluster's periphery, which detect fewer photons and thus exhibit lower signal amplitudes, are eliminated. Geometrically, it is typical for two adjacent SiPM columns to be activated, although wider clusters are occasionally observed. This widening is attributed to optical cross-talk, which disperses the signal across the photo-sensor. A comparative analysis of cluster widths at both ends of the SciFi ribbon is also possible with Figure 6.20. For lower thresholds, the widths appear similar; however, a difference emerges at 2.5 ph.e, the highest threshold. This variation is likely due to the differing alignments of the SciFi ribbon relative to the SiPM array at each end of the ribbon, as seen in Figure 4.18. Since the staggering of the fibers does not alow for a one-to-one mapping of the fibers to the SiPM array, a misalignment can affect the cluster width distribution. Furthermore, given that the ribbon consists of three layers, misalignment becomes a more critical factor.

Figure 6.21 (top) features a comparative analysis of cluster widths for 3-, 4-, and 6-layer SciFi ribbons. This figure, along with subsequent ones, focuses on clusters on the left side. A notable increase in cluster width of approximately 0.5 channels is observed in 6-layer SciFi ribbons, likely attributable to their higher light yield. This increase enhances the probability of photon detection at the cluster's edges.

In Figure 6.21 (bottom), the cluster widths of ribbons made with various adhesives (clear, black, and clear with 20 % TiO_2 admixture) are compared. The most significant decrease in cluster width at the 0.5 ph.e. threshold, although only around 0.5 channels, is observed in ribbons prepared with black epoxy. This suggests that black epoxy is most effective in reducing optical cross-talk between fibers, due to its superior absorption of non-reflected photons.

Figure 6.22 illustrates the distribution of photons detected within a cluster, each exhibiting hit multiplicities of 2, 3, and 4. These clusters were analyzed in a 3-layer SCSF-78 fiber ribbon prepared using black epoxy. In each cluster, there is a channel with the highest number of photons. This asymmetrical distribution is influenced by the alignment of the SciFi ribbon relative to the SiPM array. This effect arises because the fibers cannot always be precisely aligned with the columns of the SiPM array.

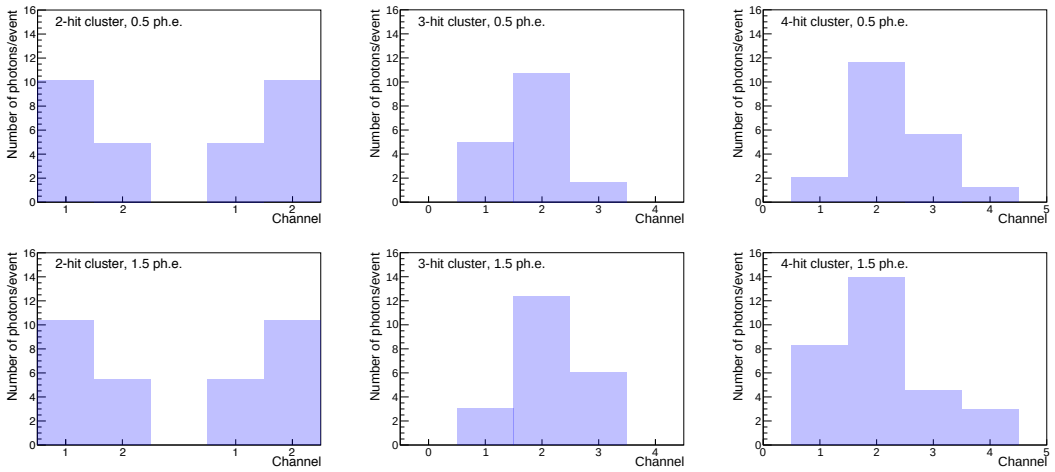

Figure 6.22: Distribution of photons detected within a cluster, each exhibiting hit multiplicities (from left to right) of 2, 3, and 4 at 0.5 ph.e. threshold (top) and 1.5 ph.e. (bottom). Two distinct distributions are shown for 2-hit clusters to separate the case when the first or the second channel has the largest number of photons.

The photon count at the periphery of these clusters tends to be lower, leading to the exclusion of these peripheral channels from the cluster analysis. This exclusion occurs, particularly when a higher threshold is set for confirming hits within the cluster.

6.3.2 *Angular Scans*

Particles emanating from the Mu3e target typically intersect the SciFi ribbons at an average angle of 27°, perpendicular to the ribbon's plane in the transverse direction. These angles vary, ranging from 0° to nearly 90°, due to the curvature induced by the 1 T solenoidal magnetic field, see Figure 6.24. This variation results in a broader distribution of the light signal across multiple columns, as depicted in 6.23 and 6.18.

Moreover, Figure 6.23 shows the variation in cluster width for different incident angles (and corresponding thresholds) when observing a 3-layer SciFi ribbon prepared with black epoxy. The cluster width demonstrates a proportional relationship to $1/cos(\theta)$, aligning with geometrical predictions. To minimize the cluster width for larger crossing angles, it is necessary to decrease the number of staggered fiber layers. This requirement underpins the choice for employing 3-layer ribbons in the design.

6.4 LIGHT YIELD

To evaluate the light yield of a SciFi ribbon, it's essential to sum up the outputs from all active channels in the SiPM array, given that the light signal extends over several channels. The process for choosing channels is the same as the one used for cluster formation. This involves ensuring channels pass a 0.5 ph.e. amplitude threshold, correspond with the trigger time, and match a track reconstructed in the SciFi telescope.

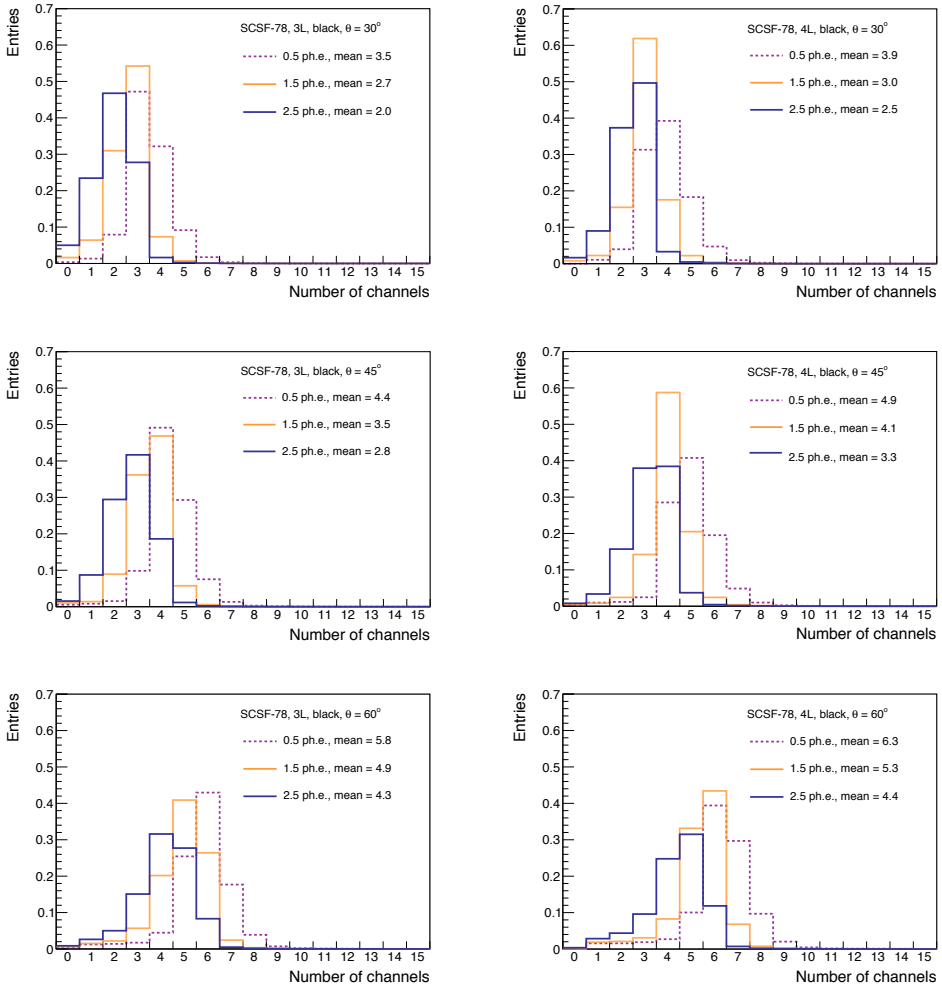

Figure 6.23: Cluster width comparison for particles intersecting a 3-layer (left column) and 4-layer (right column) SCSF-78 fiber ribbon prepared with black epoxy at angles of 30°, 45°, and 60°.

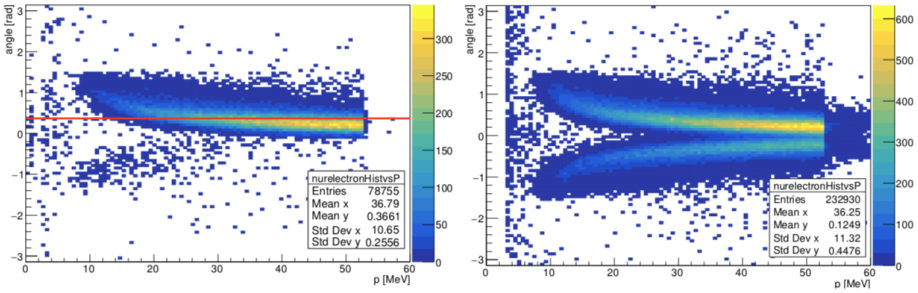

Figure 6.24: Simulation of the distribution of the crossing angle of electrons crossing the scintillating fiber detector. The data shows electrons and positrons crossings. In the left plot the crossing for all muon decay events are shown. The distribution is therefore dominated by the electrons produced by Michel decays. The mean angle is highlighted in red. As a comparison the right plot shows the distribution for $\mu^+ \rightarrow e^+e^-e^+$ events only. [62]

Table 6.1: Light yield $< n_{ph} >$ for various SciFi ribbons, consisting of a different number of staggered fiber layers, and prepared with different adhesives.

Ribbon type	$< n_{ph} >$	**Ribbon type**	$< n_{ph} >$
n/a		NOL-11 2L TiO_2	11.7 ± 1.0
SCSF-78 3L black	15.5 ± 0.8	NOL-11 3L TiO_2	19.2 ± 1.2
SCSF-78 4L black	20.9 ± 1.0	NOL-11 4L TiO_2	23.4 ± 1.2
SCSF-78 6L black	30.3 ± 1.2	n/a	
SCSF-78 4L TiO_2	23.6 ± 1.4	SCSF-78 4L clear	21.2 ± 1.3
NOL-11 4L TiO_2	23.4 ± 1.2	SCSF-78 4L black	20.9 ± 1.0
n/a		SCSF-78 4L TiO_2	23.6 ± 1.4

Interestingly, this method does not require a minimum cluster size; therefore, a cluster might consist solely of a single channel.

Figure 6.25 illustrates the integrated charge spectrum from all active channels in a cluster, normalized to the charge generated by a single photo-electron, as described in section 6.2. This analysis is conducted on a 3-layer SCSF-78 fiber ribbon prepared with black epoxy. Each peak within this spectrum signifies a distinct number of detected photons (n_{ph}), with these peaks being regularly spaced, even at higher multiplicities. This indicates a linear reponse in photon detection. To determine the n_{ph} for an event, the normalized charge distribution is integrated within a range of ± 0.5 around each peak. The resulting discrete photon count is then fitted with a Gaussian convulated with a Landau distribution, effectively modeling the characteristics of the observed spectrum as seen in the previously study done with the single fiber setup. And as in the previous study, the Most Probable Value (MPV) of the distribution is extracted to determine the light yield of the SciFi ribbon.

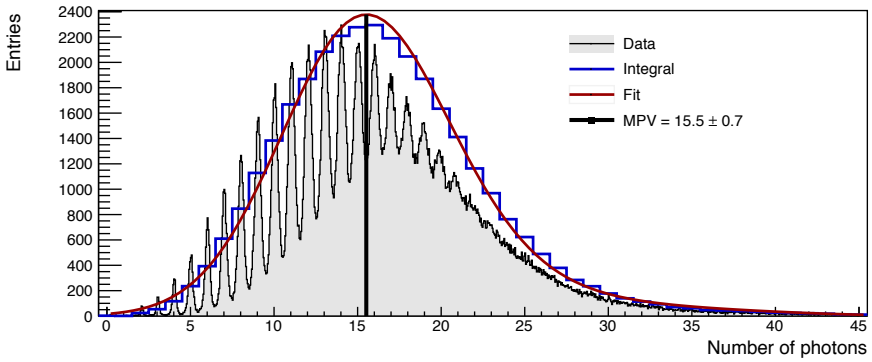

Figure 6.25: Charge spectrum integrated over all active channels passing the 0.5 ph.e. amplitude threshold in a cluster matched to a track and to the trigger time for a 3-layer SCSF-78 fiber ribbon prepared with black epoxy. The x axis is normalized to the charge generated by a single photo-electron. Beam particles cross the SciFi ribbon in the center, i.e. 15 cm from both ribbon's ends. The n_{ph} distribution (histogram) is obtained by integrating the charge in a region of ± 0.5 ph.e. around each peak. A convolution of a Gaussian with a Landau distribution is used to model the data (continuous line) and the MPV of the convolution is extracted.

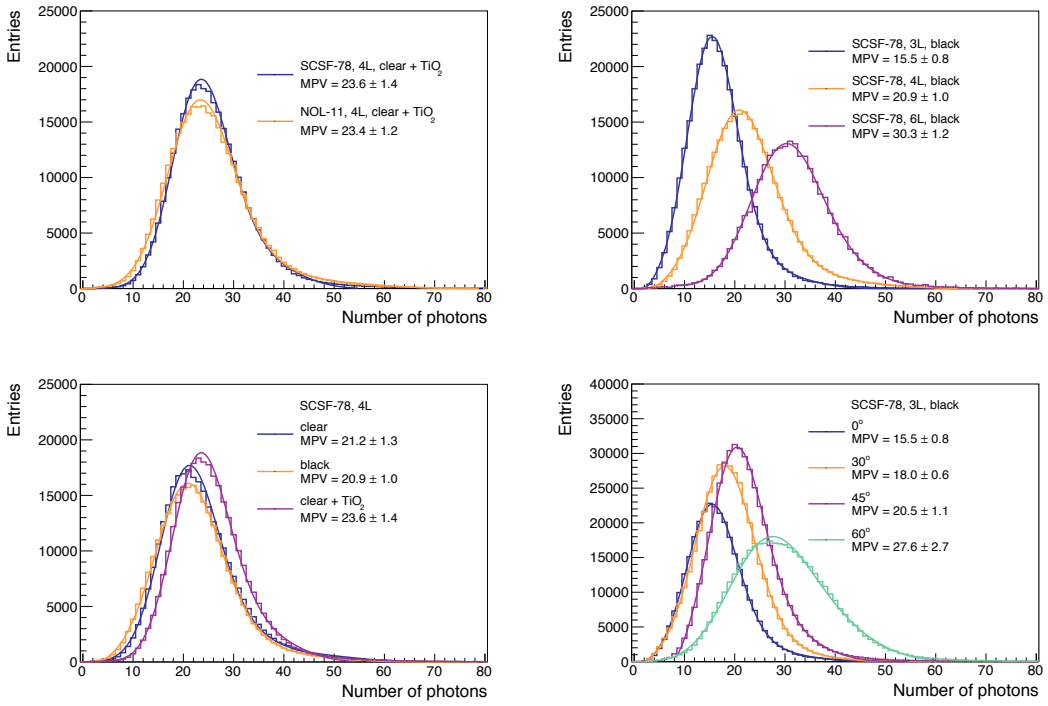

Figure 6.26: Comparison of the light yield of various SciFi ribbons: top left) SCSF-78 and NOL-11 fiber ribbons; top right) 3-, 4-, and 6-layer SCSF-78 fiber ribbons; bottom left) SCSF-78 fiber ribbons prepared with various adhesives; bottom right) SCSF-78 fiber ribbons at various crossing angles.

Figure 6.26 presents a comparative analysis of the light yield between SCSF-78 and NOL-11 fiber ribbons. These ribbons vary not only in the number of staggered fiber layers but also in the types of adhesives used in their assembly. The MPVs of the light yield fits are compiled in Table 6.1. It's important to note that these values haven't been adjusted for the PDE, as for the previous setup with the single fiber, which is approximately 44 %, when the inactive area of the photo-sensor, accounting for the fill factor, is included.

When comparing SCSF-78 and NOL-11 fiber ribbons assembled using identical adhesives, their light yields are found to be similar, as shown in the top left of Figure 6.26. However, the light yield for SCSF-81 and BCF-12 fiber ribbons is approximately 50 % lower, which explains the focus on the high light yield fibers in this study.

The light yield exhibits an almost linear increase with the ribbon's thickness, i.e., the number of staggered layers. This is depicted in the top right of Figure 6.26, where it's shown that a 6-layer fiber ribbon gives twice the light yield of a 3-layer ribbon. Additionally, SciFi ribbons coated with TiO_2 shows a 15 % higher light yield than those prepared with black epoxy (see bottom left of Figure 6.26). This increase is attributed to the enhanced reflection of scintillating photons at the fiber surface.

Furthermore, as the crossing angle θ increases, so does the thickness of the SciFi ribbon traversed by a particle, proportional to $1/cos(\theta)$. This trend is also mirrored in the measured light yield, as illustrated in the bottom right of Figure 6.26.

6.4.1 *Light Attenuation*

To investigate light attenuation in SciFi ribbons, these ribbons were scanned horizontally at various distances, ranging from 5 cm to 25 cm, from the ribbon's end. The light intensity I along the fiber, as a function of the propagation distance d, is typically characterized by both a short and a long attenuation component as can be seen in equation 3.4. At distances of 30 cm or less, light absorption is predominantly influenced by the short component λ_s which diminishes rapidly. The long component, on the other hand, remains relatively constant across the length of the SciFi ribbon.

Figure 6.27 shows the relationship between the number of detected and the the distance from the ribbon's end for two different SciFi ribbons. The data, collected from both ends of the ribbons, show slight variations due to factors like the optical couplings of the fibers to the SiPM arrays, the PDE of each SiPM array, inconsistencies in the fibers, and misalignments in the assembly of the fiber ribbons. The observed measurements were fitted using a single exponential function that represents the short attenuation component λ_s, while assuming the long component to be constant.

6.5 TIMING PERFORMANCE

The timing performance of the SciFi detector is important, particularly for charge identification of the reconstructed tracks and the effective rejection of background in the Mu3e experiment. The fundamental limit to the time resolution in low mass (or thin)

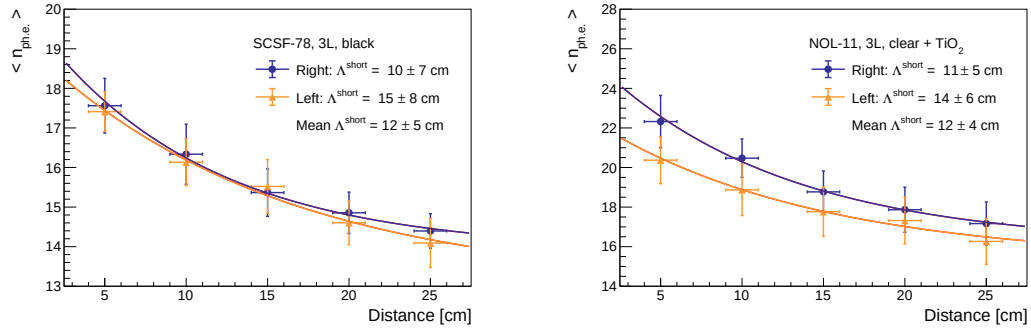

Figure 6.27: Light attenuation for a 3-layer SCSF-78 fiber ribbon (left) and a 3-layer NOL-11 fiber ribbon (right). The data is fitted with a single exponential function, representing the short attenuation component λ_s, while the long component is assumed to be constant. The resulting attenuation lengths λ_s are found to be compatible within the margin of error.

scintillating detectors is predominantly influenced by the statistical processes inherent in the generation of the light signal, along with fluctuations in the light detection.

Specifically, the time resolution of a SciFi detector with a relatively low light yield (on the order of 15 detected photons) hinges on several factors, as also seen in the previous study with the single fiber setup:

- The decay time (τ) of the spectral shifter, which is a crucial factor in determining the time resolution. Shorter decay times generally lead to better time resolution.
- The number of detected photons, which plays a significant role in determining the time resolution.

Figure 6.28 illustrates the distribution of arrival times for the first detected photon in a selected channel of the SiPM array. This distribution shows the time difference ($T_{fiber} - T_{trigger}$) between the first photon detection and an external time reference, given by the trigger. The pattern is fitted with the EMG distribution (equation 5.3), which is a convolution of the exponential and Gaussian distributions as descibed in section 5.3.1.

The method for determining the arrival time of the first scintillation photon is detailed in a previous section, but it's worth reiterating for clarity. This process involves interpolating the rising edge of digitized pulses using a straight line that is extrapolated to the waveform's baseline. This interpolation is necessary to account for any fluctuations in the baseline. The interpolation of the rising edge focuses on four consecutive samples along the rising edge of the pulse. The first of these samples falls below the half-amplitude threshold of a single photon, while the next three samples exceed this threshold. For this particular study, $\sigma_{trigger}$ has a value of 80 ps. It's noteworthy that this level of time resolution does not significantly influence the shape of the light pulse. Additionally, Figure 6.28 shows the achievable time resolution when using single-sided readout of the fiber detector. In scenarios where photon statistics are low, the time

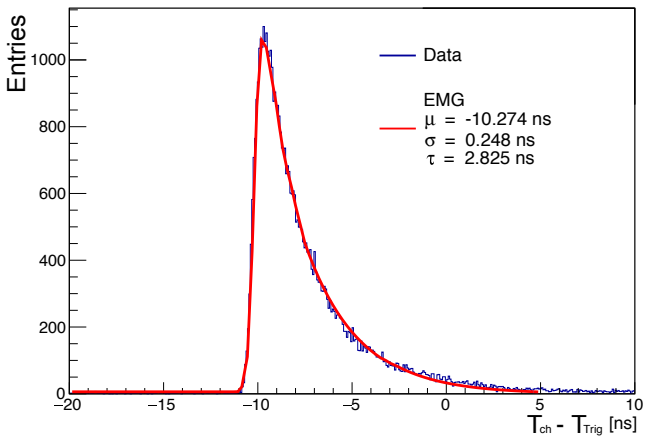

Figure 6.28: Time of arrival of the first detected photon $T_{fiber} - T_{trigger}$. The data is described by the exponentially modified Gaussian distribution (EMG), equation 5.3, with parameters σ and τ

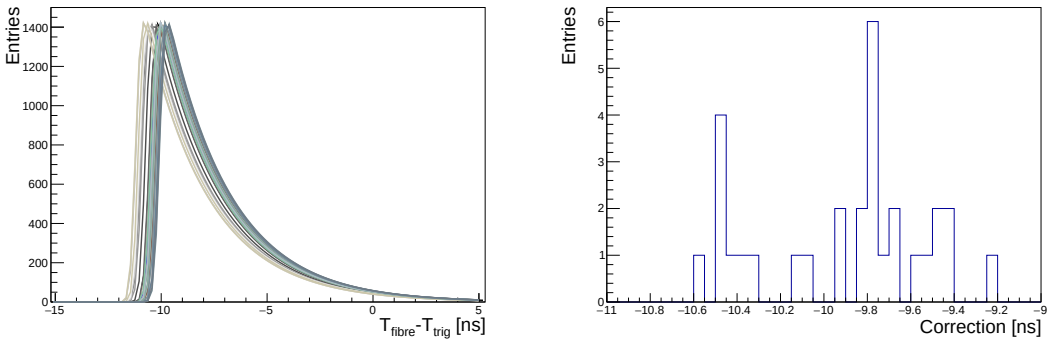

Figure 6.29: left)Paremetrized $T_{fiber} - T_{trigger}$ distribution based on fits to the data (Figure 6.28) using the EMG distribution (equation 5.3). for 32 consicutive channels of the SiPM array. right) Time shifts for each channel.

resolution is primarily governed by the decay time (τ) of the spectral shifter. This decay time is a crucial factor because it directly affects the time at which the scintillation light is re-emitted after the initial absorption, thereby influencing the overall timing accuracy of the detector.

6.5.1 *Time alignment*

Extracting timing information from the SciFi detector requires precise synchronization of all SiPM channels. Figure 6.29 shows the timing response of various SiPM channels from a single SiPM array relative to the trigger time, $T_{trigger}$. One can observe that the signals from different channels spread over a range of 1 ns in this figure. This time spread arises from a variety of factors, including variations in trace lengths on the

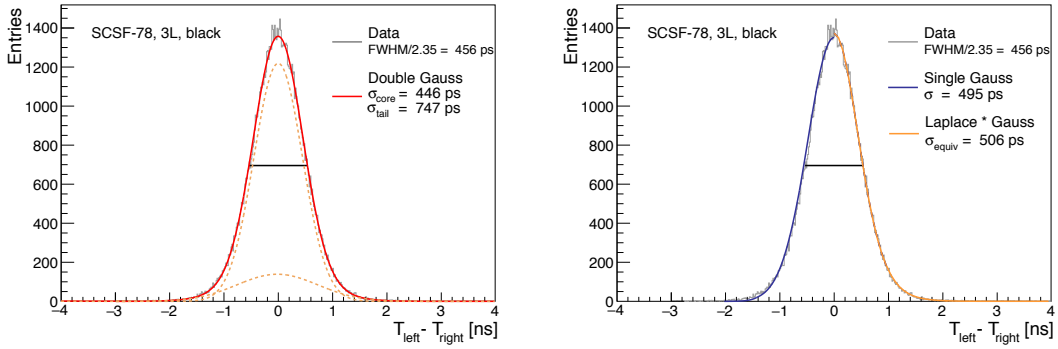

Figure 6.30: Distributions and fits of ΔT for a 3-layer SCSF-78 fiber ribbon prepared with black epoxy. This includes, on the left, a double Gaussian with a common mean, and on the right, a single Gaussian and a convolution of a Laplace distribution with a Gaussian, both fitted symmetrically around the peak. Additionally, the full width at half maximum (FWHM) of the ΔT distribution is also shown.

amplifier boards, differences in cable lengths, and disparities in the response times of the SiPMs and associated electronics.

To address this, an analysis starting from the $T_{fiber} - T_{trigger}$ distributions was done. This analysis involved determining the time shift for all channels in relation to the external time reference, $T_{trigger}$. On the right side of Figure 6.29, the time shift for each channel is shown. Once these time shifts have been accurately determined, each channel can be corrected for its individual time shift, thereby aligning the timing across all channels.

Another way, without the $T_{trigger}$ information, is to apply a more general approach, which is based on the time differences between the channels. The approach that will be developed in the future can be formulated on the premise of linear relationships between the observed time differences (ΔT) of channel pairs and the required time shifts. So without using any other external time reference.

6.5.2 *Time difference* ΔT

As said previouly also, the time resolution of the SciFi detector can be enhanced significantly by reading out the detector from both ends and using the two time readings. Unless specified otherwise, the cluster time is determined by identifying the first detected photon within the cluster, corresponding to the earliest time stamp in that cluster.

One aspect of this investigation focused on the time difference, $\Delta T = T_{left} - T_{right}$, where T_{left} and T_{right} represent the arrival times of the first detected photon in the left and right channels of the SciFi ribbon, respectively. As a reminder, ΔT can be calculated without relying on an external time reference but is not suitable for determining the exact crossing time of a particle as it lacks correlation with an external time reference.

Figure 6.30 shows the distribution of ΔT for a 3-layer SCSF-78 fiber ribbon prepared with black epoxy. Beam particles crossed this ribbon at its center, which was equidistant (15 cm) from both ends of the ribbon. The ΔT distribution is symmetric around the peak, reflecting the symmetrical addition and subtraction of timing fluctuations in T_{left} and T_{right}. The tails of the distribution, extending symmetrically around the peak, are influenced by the decay time of the fiber.

To analyze the ΔT distribution and determine the time-difference resolution $\sigma_{\Delta T}$, several models were employed. Initially, the distribution was fitted with a single Gaussian function within $\pm 4\sigma$ of the peak. While this Gaussian fit adequately describes the core of the ΔT distribution, it fails to fit the tails of the distribution. The fraction of events in these tails is relatively small, constituting less than 10 % of the total.

To account for the tails, the distribution was fitted with a sum of two Gaussian functions, see Figure 6.30, both centered around a common mean :

$$F(t) = N_1 \cdot \frac{1}{\sqrt{2\pi}\sigma_1} exp\left(\frac{(t-\mu)^2}{2\sigma_1^2}\right) + N_2 \cdot \frac{1}{\sqrt{2\pi}\sigma_2} exp\left(\frac{(t-\mu)^2}{2\sigma_2^2}\right) \tag{6.1}$$

where N_1 and N_2 represent the normalization factors for the two Gaussian functions, σ_1 and σ_2 are the corresponding standard deviations, and μ is the common mean. The first Gaussian, accounting for the core of the distribution, is thought to represent fluctuations in the excitation of the primary dye in the fibers (the activator) and in the light detection process. The second Gaussian accounts for the tails of the distribution, which are primarily influenced by the decay time of the fiber. In this example, it is observed that over 90 % of the events fall under the first Gaussian, while less than 10 % fall under the second.

Moving forward, the sum of these two Gaussians is used to characterize the ΔT distributions. This approach allows for a more accurate and representative analysis of the timing behavior in the SciFi detector. As a measure of the time difference resolution, $\sigma_{\Delta T}$, the Full Width at Half Maximum (FWHM) divided by 2.35 of the ΔT distribution is used. This metric is chosen because it closely approximates the width of the first Gaussian, which is the dominant component in the distribution. By adopting this method, a more precise understanding of the time difference resolution is achieved.

Another approach to model the ΔT distribution is by using a symmetric exponential function, like the Laplace distribution. This choice is informed by the Poissonian characteristics of the scintillation process. Additionally, a Gaussian distribution is convoluted with it to account for the time spread in the light collection process, see equation 5.7. This convolution method effectively models the ΔT distribution, particularly in fitting the tails, see Figure 6.30.

Figure 6.31 provides a comparative analysis of the ΔT distribution for 4-layer SCSF-78 and 4-layer NOL-11 fibber ribbons. The Full Width at Half Maximum (FWHM) divided by 2.35 for these distributions is observed to be around 400 ps. Notably, the best time difference resolution ($\sigma_{\Delta T}$) of 395 ps was achieved with a 4-layer SciFi ribbon composed of NOL-11 fibers, assembed with clear epoxy containing a 20 % TiO_2 admixture.

Despite the significantly shorter decay time of the NOL-11 fiber (1.1 ns), SciFi ribbons made from this fiber exhibit only a minor improvement in timing performance

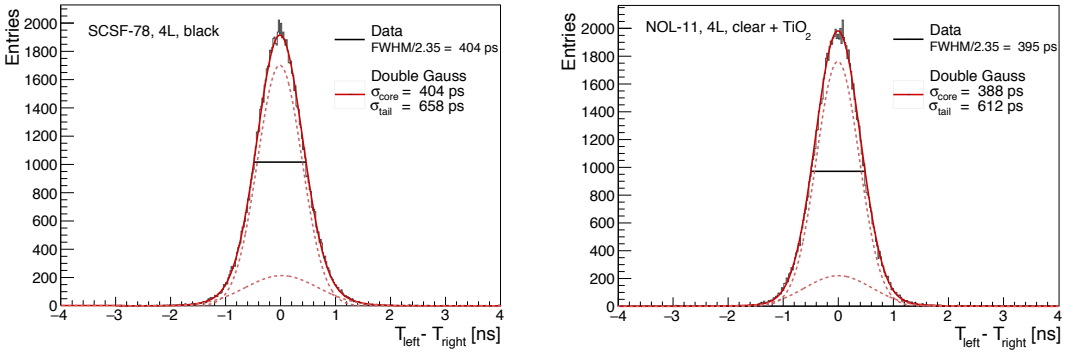

Figure 6.31: Distributions of ΔT for a 4-layer SCSF-78 fiber ribbon prepared with black epoxy (left) and a 4-layer NOL-11 fiber ribbon prepared with clear epoxy (right). The data is fitted with a double Gaussian with a common mean. The full width at half maximum (FWHM) of the ΔT distribution is shown.

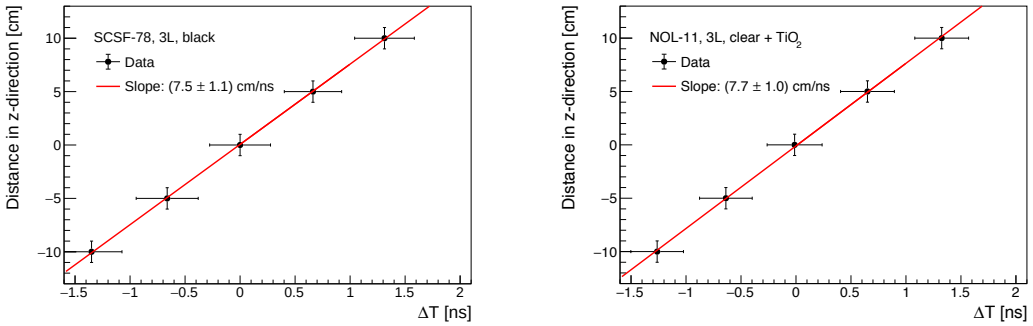

Figure 6.32: Peak position of the ΔT distribution for a 3-layer SCSF-78 fiber ribbon prepared with black epoxy (left) and a 3-layer NOL-11 fiber ribbon prepared with clear epoxy with 20 % TiO_2 admixture (right) as a function of the hit position in the ribbon. The data is fitted with a linear function.

compared to those made from SCSF-78 fiber, which has a decay time of 2.8 ns. This observation suggests that the $\sigma_{\Delta T}$ resolution is more influenced by the light yield, which is similar for both types of SciFi ribbons ((as shown in Figure 6.26), rather than by the decay time of the spectral shifter. This observation highlights the critical role of light yield in defining the timing performance of SciFi ribbons, regardless of the decay time of the fiber materials, as also demonstrated in the prior study involving individual fibers.

6.5.3 *Light propagation*

Figure 6.32 displays the peak position of the ΔT distribution for varying beam impact points along the SciFi ribbon. A key observation from this data is that the width of the ΔT distributions remains largely unchanged across different points along the ribbon,

suggesting that the time-difference resolution ($\sigma_{\Delta T}$) is not influenced by the location of the beam impact. The data points can be interpolated with a straight line supporting the idea that the light propagates uniformly in both directions within the ribbon. Moreover, within the resolution limits of this study, no edge effects are observed as the measurement approaches the ends of the fiber ribbon. This is the same conclusion as the one drawn from the previous study with the single fiber setup.

Also here, the speed of light propagation within the fibers (v_{fiber}) can be estimated. Considering that the difference in the distance traveled by the scintillation photons is twice the displacement, the speed can be deduced from the slope of the fitted data points. The formula used is $v_{fiber} = 2 \cdot \Delta z / \Delta T$, where Δz is the displacement of the beam impact point along the SciFi ribbon, and ΔT is the peak position of the ΔT distribution. This leads to the finding that the scintillation photons propagate at approximately half the speed of light in vacuum. Also, in this case, the speed is reduced compared to the theoretical speed derived from the fiber's core refractive index, but it can be attributed to the multiple internal reflections off the cladding that the photons undergo during propagation, effectively increasing their travel distance.

Furthermore, the ΔT measurement can be employed to pinpoint the crossing point (z) of a particle along the fiber. The crossing point is calculated with equation 5.8, where L is the lenght of the fiber ribbon. The spacial resolution, is approximately 3 cm, assuming a $\sigma_{\Delta T}$ of 400 ps. This level of spatial resolution highlights the capability of the SciFi detector not only in timing analysis but also in accurately determining the locations of particle interactions within the fiber ribbon.

6.5.4 *Mean time*

The standard method for timing measurement in scintillators read out at both ends involves calculating the Mean-Time (MT), defined as in 5.11 and explained in section 5.3.3. The MT distributions for 3-layer and 4-layer SCSF-78 SciFi black and NOL-11 clear + 20 % TiO_2, as shown in Figure 6.33, were taken with the beam crossing the ribbons in the middle. These MT distributions are asymmetric, showing a tail extending to the right of the peak, driven by the fiber's decay time. The distributions are well described by the Exponentially Modified Gaussian (EMG) distribution.

Since the MT distributions are not excessively skewed, the core standard deviation (σ_{core}) of the MT distribution can be used as an indicator for the time resolution, σ_{MT}. In cases of significant skewness, the Full Width at Half Maximum (FWHM) for both sides of the distribution might be reported separately.

After accounting for the jitter of the trigger time ($\sigma_{trigger} \approx 80$ ps), the achievable time resolution, σ_{MT}, with the 3-layer SCSF-78 SciFi black ribbon is approximately 245 ps, and 210 ps for a 4-layer ribbon. For the 3-layer NOL-11 SciFi clear + 20 % TiO_2 ribbon, the σ_{MT} is 235 ps, and around 200 ps for a 4-layer ribbon. The similarity in timing performance of 4-layer SCSF-78 ribbons prepared with different adhesives indicates that adhesive type does not significantly impact time resolution. Table 6.2 summarizes the timing performance of different fiber ribbons.

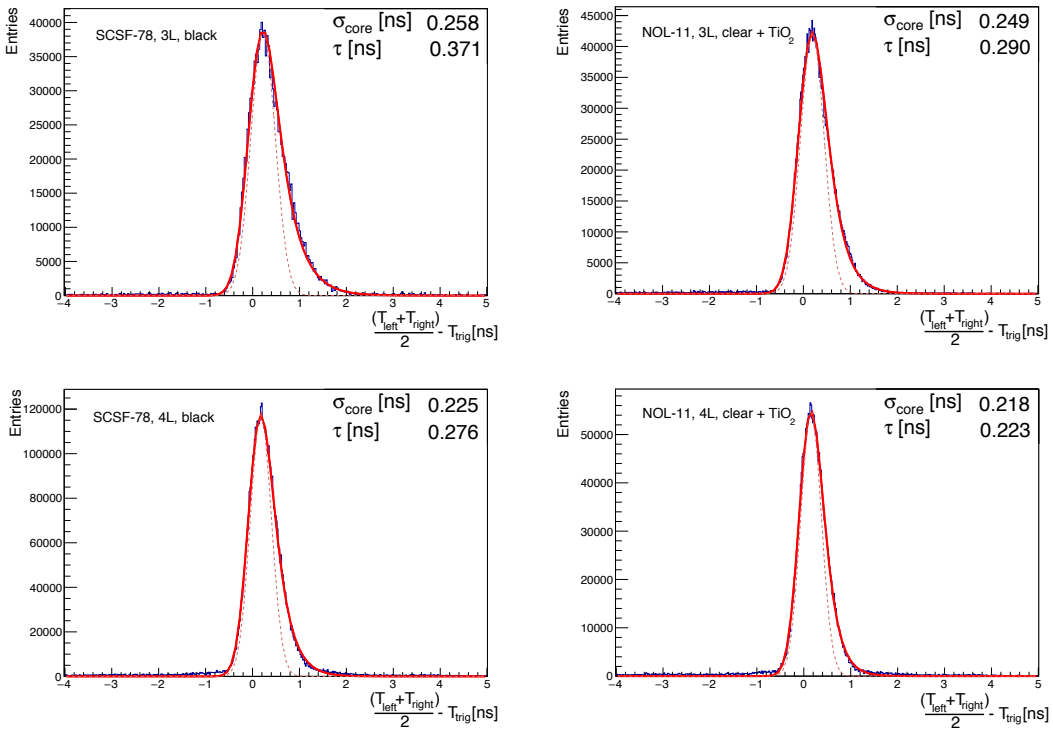

Figure 6.33: Mean-Time distribution MT $= \frac{1}{2}(T_{left} + T_{right})$ for different SciFi ribbons. The distributions are well described by the EMG distribution, i.e. a convolution of a Gaussian and an exponential function. The tails on the right of the peaks are driven by the decay time of the scintillation light. The dashed line shows the resulting Gaussian with width σ_{core}. The SCSF-78 ribbons have been prepared with black epoxy while the NOL-11 ones with clear epoxy with a 20% TiO_2 admixture.

Table 6.2: Timing performance of 3- and 4- layer SciFi ribbons made of different fibers

Fiber type	**Number of layer**	**Adhesive**	$\sigma_{\Delta T}$ **[ps]**	σ_{MT} [ps]	σ_{EMG} [ps]
SCSF-78	3	black	456 ± 9	245 ± 6	371 ± 12
SCSF-78	4	black	404 ± 9	210 ± 6	276 ± 11
SCSF-78	4	clear + 20 % TiO_2	409 ± 9	218 ± 6	275 ± 10
NOL-11	3	clear + 20 % TiO_2	409 ± 9	235 ± 6	290 ± 11
NOL-11	4	clear + 20 % TiO_2	395 ± 9	200 ± 6	223 ± 11

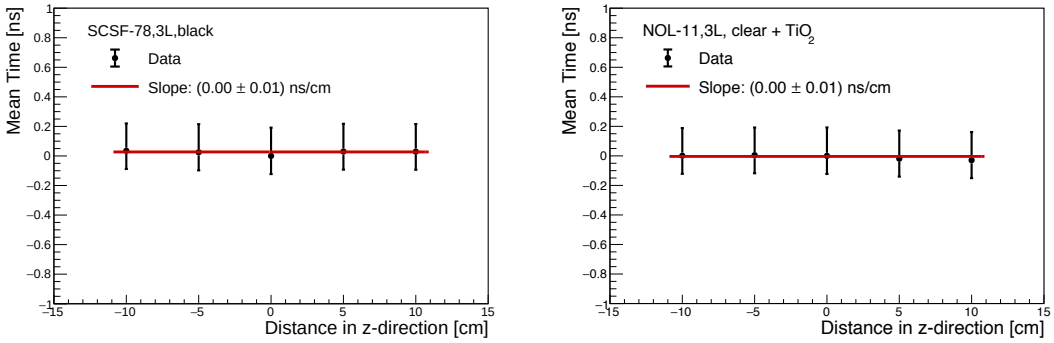

Figure 6.34: Peak position of the MT distribution for a 3-layer SCSF-78 fiber ribbon prepared with black epoxy (left) and a 3-layer NOL-11 fiber ribbon prepared with clear epoxy with 20 % TiO_2 admixture (right) as function of the hit position in the ribbon. The data is fitted with a linear function.

A notable finding is that the shorter decay time of NOL-11 fibers leads to a reduced tail in the MT distribution. However, increasing the number of staggered fiber layers from 3 to 4 has a more significant effect, improving the time resolution and underscoring the importance of light yield. The best timing performance of 200 ps was achieved with a 4-layer NOL-11 SciFi ribbon.

Figure 6.34 shows that the peak values of the MT distribution remain constant for different beam impact points along the ribbon, showing that MT is a reliable observable for timing measurements, as the width of the MT distribution does not change significantly along the ribbon. This constancy suggests that the total distance that light travels in opposite directions within the ribbon is consistent, making MT a robust observable for precise timing analysis. This is the same conclusion as the one drawn from the previous study.

6.6 DETECTION EFFICIENCY

The detection efficiency is a key parameter of the SciFi detector. To correlate a hit in the SciFi detector with a track reconstructed in the Mu3e Si-pixel tracking detectors, and to accurately extract timing information, it is essential to identify and match clusters at both ends of the SciFi ribbons in both space and time. Clusters on the left and right sides are considered matched if they share at least one common channel in the SiPM arrays at each end. Uncorrelated clusters, typically arising from dark counts, are excluded by this matching criterion. Additionally, clusters matched in time by ensuring that the time difference $|\Delta T = T_{left} - T_{right}|$ falls within a predefined time window, generally 3 or 5 times the width of the ΔT distribution $\sigma_{\Delta T}$. This selection process needs to consider the drift of ΔT along the length of the SciFi ribbon. Furthermore, this time matching also serves to reject accidental cluster combinations that may occur due to track pileup at high rates.

The efficiency estimation method, as outlined in [25], involves using the mode of the probability distribution $P(\epsilon|k, N, I)$, where k represents the observed events (the number of matched clusters), N denotes the total number of tracks reconstructed in the SciFi telescope crossing the SciFi ribbon, and I encompasses any prior knowledge before the measurement. The peak of the efficiency distribution is calculated as:

$$\hat{\epsilon} = \frac{k}{N} = \frac{\text{\# of matched clusters}}{\text{\# of reconstructed tracks}} \tag{6.2}$$

The uncertainty associated with this efficiency estimator is determined using the Fisher-Snedecor distribution [63], taking into account a 68.27 % central confidence interval. For lower event counts, these confidence intervals are asymmetric around the distribution's mode but approximate a Normal distribution's $\mu \pm 1\sigma$ range for larger numbers of events. This methodological approach ensures a robust and accurate estimation of the SciFi detector's efficiency.

The process of assessing the cluster detection and matching efficiency for the SciFi ribbon, referred to as the Device Under Test (DUT), is a rigorous operation. This ribbon is strategically placed between the second and fourth most downstream SciFi ribbons, as seen in Figure 6.1. The evaluation of its efficiency is comprehensive, covering various parameters and conditions:

- **Space and Time Intervals**: the efficiency is gauged across different spatial and temporal intervals. This variation helps to understand how efficiency varies with distance and time between detected events.
- **Hit Selection Threshold**: the threshold at which hits are selected for cluster formation is varied to determine its effect on the overall efficiency.
- **Cluster Multiplicity**: the number of hits required to form a cluster (multiplicity) is another variable in the assessment. This aspect examines how the grouping of hits into clusters impacts the detector's efficiency.
- **SiPM overbias (V_{ob})**: the efficiency is also tested against different bias voltages applied to the Silicon Photomultipliers (SiPMs). Varying the V_{ob} can affect the SiPMs' gain and, consequently, the detector's overall efficiency.
- **Scanning Orientation**: both horizontal and vertical scans over the fiber ribbons are conducted. This ensures a comprehensive evaluation of the efficiency across different orientations and positions of the beam.
- **Beam**: Normally, the beam strikes the middle of the SciFi ribbon, unless specified otherwise. This standard condition allows for a consistent basis for comparing efficiency under different test scenarios.

6.6.1 *HV Bias Dependence*

Figure 6.35 presents the singe-sided cluster detection and matching efficiencies as function of the bias voltage applied to the SiPMs, denoted as V_{bias}. The efficiency

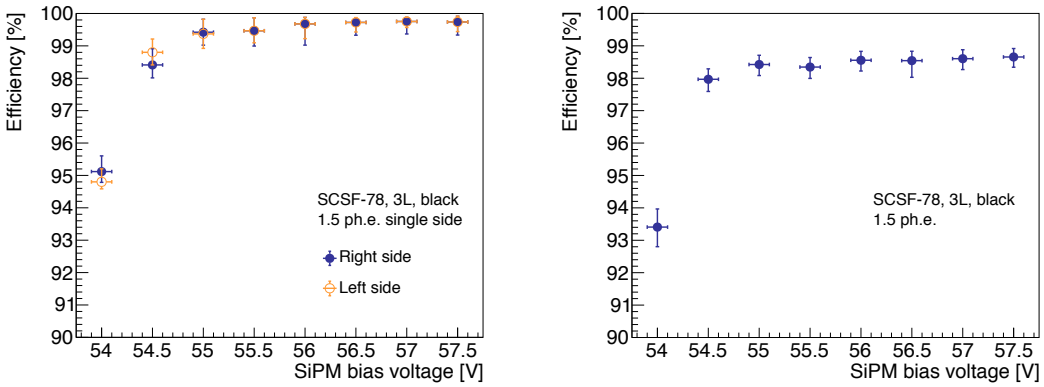

Figure 6.35: Cluster detection efficiency (left) and cluster matching efficiency (right) as a function of the bias voltage applied to the SiPM arrays. The efficiency is measured for a 3-layer SCSF-78 fiber ribbon prepared with black epoxy. The cluster selection criteria include requiring at least one channel to surpass a 1.5 ph.e. threshold, combined with the $5 \times \sigma_{\Delta T}$ timing cut for matched clusters.

analysis is conducted under specific cluster selection criteria: requiring at least one channel to surpass a 1.5 ph.e. threshold, combined with a 5 times the width of the ΔT distribution ($5 \times \sigma_{\Delta T}$) timing cut for matched clusters.

All channels of the SiPM array operate at the same V_{bias}, but they have different breakdown voltages, V_{bd}. This discrepancy leads to some inefficiencies at lower overbias voltages (V_{ob}). However, the single-sided efficiency reaches a stable plateau around $V_{ob} \approx 3\,\mathrm{V}$, and it remains relatively constant for higher values of V_{bias}. The cluster matching efficiency exhibits a similar pattern.

Consequently, the operating voltage for all SiPM arrays in this setup has been set to at least $V_{bias} = 55.5\,\mathrm{V}$, which corresponds to an overbias voltage of approximately 3 V. This choice is made to ensure optimal efficiency across the SiPM arrays while mitigating the inefficiencies that arise at lower over-bias voltages.

6.6.2 *Threshold scans*

Figure 6.36 illustrates the single-sided cluster detection efficiency as a function of the hit selection threshold for both 3-layer and 4-layer SCSF-78 black fiber ribbons. For clusters with a hit multiplicity of ≥ 2, the efficiency decreases rapidly. This trend can be attributed to the concentration of most of the light signal in a single channel. The drop in efficiency is less significant for the 4-layer SciFi ribbon compared to the 3-layer ribbon. This can be understood by the higher light yield of the 4-layer SciFi ribbon.

Figure 6.37 then examines the efficiency of left-right cluster matching under various timing selections, exhibiting behavior similar to the single-sided efficiency. The timing cut on $|T_{left} - T_{right}|$ contributes to an additional efficiency reduction. This is because such a requirement excludes events in the tails of the ΔT ditribution. A summary table

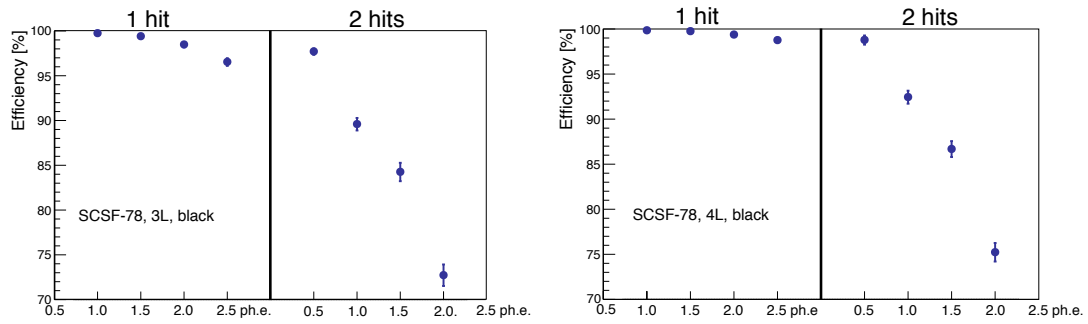

Figure 6.36: Single-sided cluster detection efficiency as a function of the hit selection threshold for a 3-layer (left) and 4-layer (right) SCSF-78 fiber ribbon prepared with black epoxy. The cluster selection criteria include a combined $5 \times \sigma_{\Delta T}$ timing cut for matched clusters.

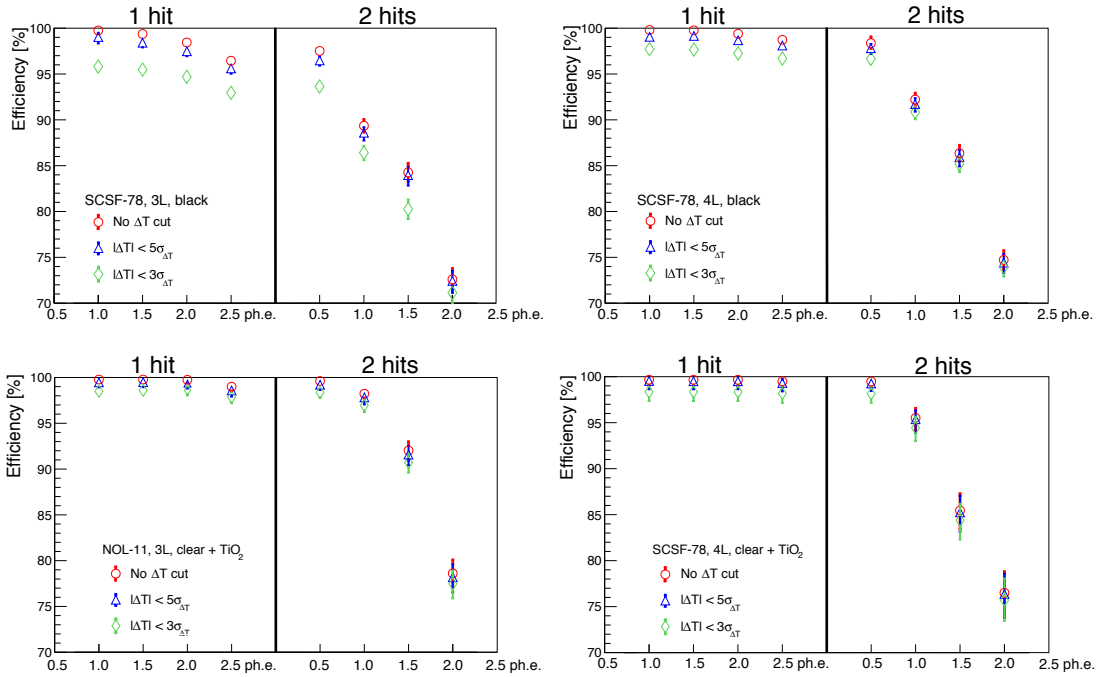

Figure 6.37: Cluster left-right matching efficiency as a function of the hit selection threshold for a 3-layer SCSF-78 fiber ribbon prepared with black epoxy (top left), a 4-layer SCSF-78 fiber ribbon prepared with black epoxy (top right), a 3-layer NOL-11 fiber ribbon prepared with clear epoxy with 20 % TiO_2 admixture (bottom left), and a 4-layer SCSF-78 fiber ribbon prepared with clear epoxy with 20 % TiO_2 admixture (bottom right). The cluster selection criteria include a $5 \times \sigma_{\Delta T}$, $3 \times \sigma_{\Delta T}$ or no timing cut for matched clusters.

Table 6.3: Cluster matching efficiency in % for different thresholds, cluster multiplicities, and different timing cuts for a 3-layer SCSF-78 (black) fiber ribbon.

thr.	**Cluster**	**Single-sided**	**Matched clusters**		
[ph.e.]	**mult.**	**cluster**	**no ΔT cut**	$\lvert\Delta T\rvert < 5\sigma_{\Delta T}$	$\lvert\Delta T\rvert < 3\sigma_{\Delta T}$
0.5	≥ 2	$97.5^{+0.3}_{-0.4}$	$97.5^{+0.3}_{-0.4}$	$96.8^{+0.4}_{-0.5}$	$93.6^{+0.5}_{-0.6}$
1.5	≥ 1	$99.4^{+0.1}_{-0.2}$	$99.4^{+0.1}_{-0.2}$	$98.3^{+0.2}_{-0.3}$	$95.5^{+0.4}_{-0.5}$
1.5	≥ 2	$84.3^{+0.6}_{-0.7}$	$84.3^{+0.6}_{-0.7}$	$83.9^{+0.7}_{-0.8}$	$80.3^{+0.7}_{-0.8}$
2.0	≥ 1	$98.4^{+0.2}_{-0.3}$	$98.4^{+0.2}_{-0.3}$	$97.3^{+0.4}_{-0.5}$	$94.7^{+0.5}_{-0.6}$
2.0	≥ 2	$72.7^{+1.1}_{-1.2}$	$72.6^{+1.1}_{-1.2}$	$72.3^{+1.1}_{-1.2}$	$71.1^{+0.2}_{-1.2}$
2.5	≥ 1	$96.6^{+0.9}_{-0.5}$	$96.5^{+0.4}_{-0.5}$	$95.5^{+0.4}_{-0.5}$	$93.9^{+0.5}_{-0.6}$
2.5	≥ 2	$66.9^{+0.9}_{-1.2}$	$66.5^{+0.8}_{-1.1}$	$66.1^{+1.1}_{-1.2}$	$64.3.5^{+0.9}_{-1.1}$

of the cluster matching efficiency for different thresholds and timing cuts is shown in Table 6.3.

From this analysis, two working points for the SciFi detector have been identified:

1. require at least two contiguous channels to surpass a 0.5 ph.e. threshold. This setting effectively reduces most dark counts, as it is highly improbable for two adjacent channels to discharge simultaneously.

2. require at least one channel to exceed a 1.5 ph.e. threshold. Higher thresholds can also be considered. This approach further suppresses dark counts since they are unlikely to pass a higher threshold. This setting is combined with a $|\Delta T|$ timing selection of $5 \times \sigma_{\Delta T}$. While more complex clustering algorithms are possible, this approach aligns closely with the operational mode of the MuTRiG ASIC, which allows setting only one threshold per channel during data collection.

6.6.3 *Position scans*

The uniformity of the cluster matching efficiency in both the longitudinal (horizontal) and transverse (vertical) directions of the SciFi ribbons has been a focus of study, essential for ensuring consistent performance across the entire detector surface. This aspect of the SciFi detector's performance was assessed by examining the efficiencies at various beam impact points along the ribbon and across consecutive groups of 8 channels in the SiPM arrays, each group corresponding to approximately 2 mm.

Figure 6.38 shows the position dependent efficiencies. One key observation from the data is that the cluster matching efficiency is uniform along the length of the SciFi ribbons. This finding is particularly important given the significant variation in light yield that typically occurs along the ribbon's length.

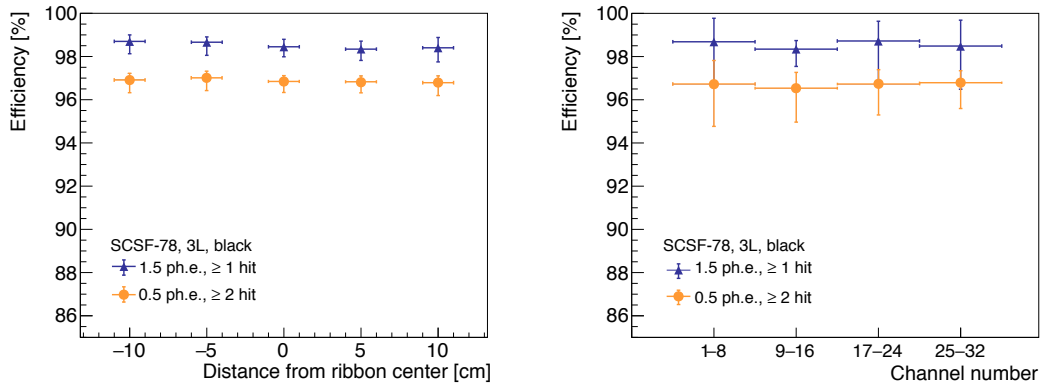

Figure 6.38: Cluster matching efficiency as a function of the beam impact point along the SciFi ribbon (left) and the SiPM channel number (right) for a 3-layer SCSF-78 fiber ribbon prepared with black epoxy. The cluster selection criteria include a combined $5 \times \sigma_{\Delta T}$ timing cut for matched clusters.

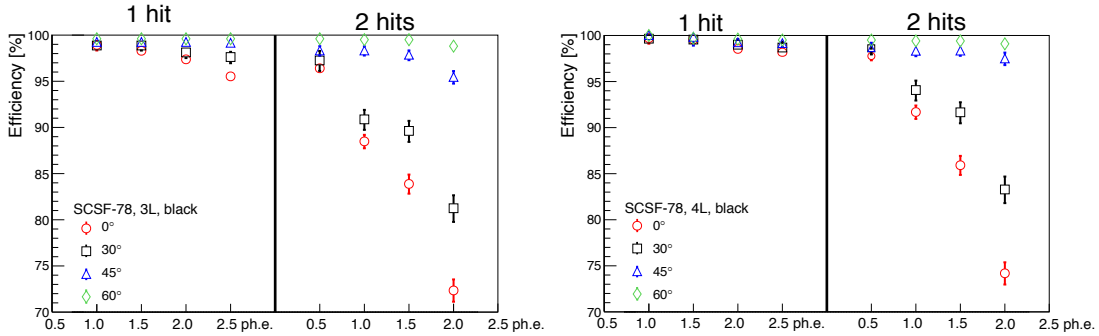

Figure 6.39: Cluster matching efficiency as a function of the particle crossing angle for a 3-layer (left) and 4-layer (right) SCSF-78 fiber ribbon prepared with black epoxy. The cluster selection criteria include a combined $5 \times \sigma_{\Delta T}$ timing cut for matched clusters.

6.6.4 *Angular scans*

Figure 6.39 in the study illustrates how the cluster matching efficiency varies with different particle crossing angles in 3- and 4-layer SCSF-78 black fiber ribbons, under various cluster selection criteria. As the crossing angle of the particle increases, the cluster width also broadens, leading to an increase in detection efficiency.

This trend is particularly relevant for the Mu3e experiment, where particles typically intersect the SciFi ribbons at an average angle of 27°. According to the data, such an angle corresponds to a higher detection efficiency. This finding is significant for the experiment's design and effectiveness, as it suggests that the SciFi detector's configuration is well-suited to the expected particle trajectories in Mu3e.

Moreover, for particles crossing at a 60° angle, the effective thickness of the SciFi ribbon essentially doubles, resulting in a detection efficiency that exceeds 99 %, regard-

less of the specific selection criteria employed. This high efficiency at steep crossing angles is advantageous, particularly in scenarios where particles intersect the detector at various angles, ensuring that the detector maintains high performance across a range of incidence angles. This capability of the SciFi detector to maintain high detection efficiency across different crossing angles is critical for its application in precision experiments like Mu3e, where accurate tracking and detection of particles are essential.

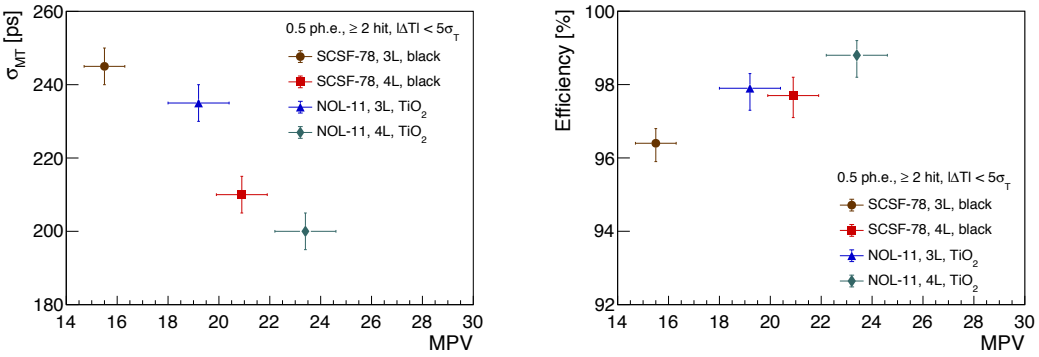

Figure 6.40: Mean time resolution, σ_{MT} (left) and detection efficiency (right) as a function of the light yield, measured by the MPV of the distribution, for SciFi ribbons consisting of either 3 or 4 staggered fiber layers. This comparison specifically utilizes SCSF-78 and NOL-11 fibers. The cluster selection criteria include a combined $5 \times \sigma_{\Delta T}$ timing cut for matched clusters.

6.7 SUMMARY AND PERFORMANCE OF THE SCIFI DETECTOR

The primary attributes of the SciFi detector crucial for the Mu3e experiment are its time resolution and detection efficiency. Figure 6.40 illustrates a comparison between the mean time resolution, σ_{MT}, and detection efficiency in relation to the light yield, measured here by the MPV of the distribution, for SciFi ribbons consisting of either 3 or 4 staggered fiber layers. This comparison specifically utilizes SCSF-78 and NOL-11 fibers.

Furthermore, Figure 6.41 displays the relationship between mean time resolution, σ_{MT} and efficiency for these ribbons, considering the two operational working points previously outlined (working point 1 with a threshold $\geq$ 0.5 ph.e. and nhits $\geq$ 2, and working point 2 with a threshold $\geq$ 1.5 ph.e. and nhits $\geq$ 1). These findings are summarized in Table 6.4.

To sum up, those are the key observations from this study:

- The best mean time resolution, σ_{MT} of 200 ps was achieved with 4-layer SciFi ribbons made of NOL-11 fibers, while the 3-layer SCSF-78 fiber ribbons with black epoxy have a σ_{MT} of 245 ps. Although NOL-11 fibers have a significantly shorter decay time (1.1 ns) compared to SCSF-78 fibers (2.8 ns), the improvement in σ_{MT} is about 5 %, with a 20 % reduction in the tail of the MT distribution.
- Adding an extra layer of fiber results in a more substantial improvement in σ_{MT} of around 15 %, emphasizing the importance of light yield for achieving good time resolution.
- The light yield of SCSF-78 and NOL-11 fibers is similar.
- The detection efficiency is around 97 % for clusters with a minimum multiplicity of two at the 0.5 ph.e. threshold, and about 98 % for clusters formed with at least

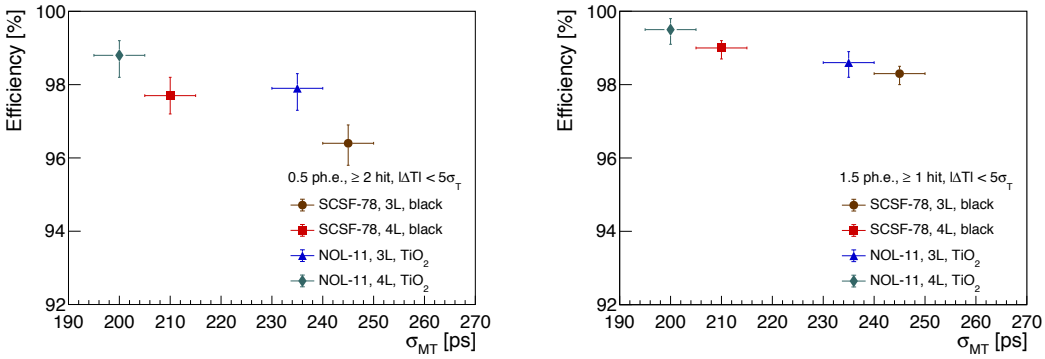

Figure 6.41: Mean time resolution σ_{MT} (left) and detection efficiency (right) as a function of the light yield, measured by the MPV of the distribution, for SciFi ribbons consisting of either 3 or 4 staggered fiber layers. This comparison specifically utilizes SCSF-78 and NOL-11 fibers. The cluster selection criteria include a combined $5 \times \sigma_{\Delta T}$ timing cut for matched clusters.

one hit surpassing the 1.5 ph.e. threshold. This efficiency decreases by roughly 3 % with a more strict time cut of $3 \times \sigma_{\Delta T}$.

- An additional fiber layer enhances the detection efficiency by 1 % to 3 %, depending on the selected working point. As the thickness of the SciFi ribbons increases, so does the light yield and consequently the detection efficiency.
- The efficiency increases with the particle's crossing angle.
- SciFi detectors made with fibers coated with TiO_2 containing epoxy show a slightly higher efficiency due to the increased light yield.
- The detector's response, including time resolution and detection efficiency, is uniformly consistent. The mean time extracted from time measurements at both ends of the SciFi ribbon is independent of the hit position, confirming the mean time as a reliable observable for time measurements.

Table 6.4: Performance of different SciFi ribbons in terms of mean time resolution, σ_{MT}, and detection efficiency. The light yield and time resolution are reported for the w.p. 1

Ribbon type	$<n_{ph}>$	$\sigma_{\Delta T}$ **[ps]**	σ_{MT} **[ps]**	eff. [%] **w.p 1**	eff. [%] **w.p. 2**
SCSF-78 3L black	15.5 ± 0.8	456 ± 9	245 ± 6	$96.8^{+0.4}_{-0.5}$	$98.3^{+0.2}_{-0.3}$
SCSF-78 4L black	20.9 ± 1.0	404 ± 9	210 ± 6	$97.7^{+0.5}_{-0.6}$	$99.0^{+0.2}_{-0.3}$
SCSF-78 4L TiO_2	23.6 ± 1.4	409 ± 9	210 ± 6	$98.0^{+0.6}_{-0.9}$	$99.2^{+0.4}_{-0.6}$
NOL-11 3L TiO_2	19.2 ± 1.2	409 ± 9	235 ± 6	$97.9^{+0.4}_{-0.6}$	$98.6^{+0.3}_{-0.4}$
NOL-11 4L TiO_2	23.4 ± 1.2	395 ± 9	200 ± 6	$98.8^{+0.4}_{-0.6}$	$99.5^{+0.3}_{-0.4}$

7 SCINTILLATING FIBER DETECTOR

In this chapter the SciFi detector for Mu3e will be presented. Mostly the mechanical design[1] will be discussed and the integration with a discussion on the requirements are presented. Also the cooling system will be discussed.

7.1 MECHANICAL REQUIREMENTS

The mechanical specifications of the SciFi detector are determined and limited by the space availability in the Mu3e experiment. The SciFi detector is located below the third pixel layer. Its size and shape are defined to fit the Mu3e experimental's geometrical acceptance. The dimensions of the geometrical envelope containing the fiber detector are dictated by the beam pipe below and the geometrical acceptance above. Figure 7.1 shows the sensitive region of the SciFi detector, which is defined by the green straight lines from the outer most pixel in the fourth layer to the center of the target. This region defines the acceptance of the central detectors. Also, space along the beampipe is required for all the services. All the data cables for the central detectors need to be routed along the beampipe, and the cooling system for the SciFi and the tile detectors is also located along the beampipe. Additionally, the helium channels need to pass also along the beampipe to deliver the cooling power to the pixel detectors.

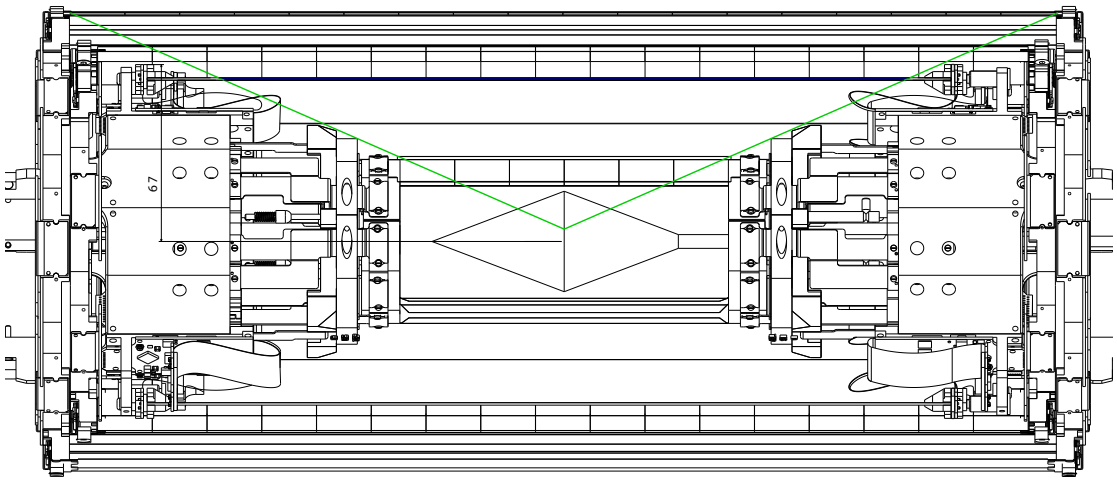

Figure 7.1: Acceptance of the Mu3e central region detectors. The straight green lines determines the acceptance region.

1 The design is made by Franck Cadoux, mechanical engineer of the University of Geneva.

7.2 MECHANICAL DESIGN

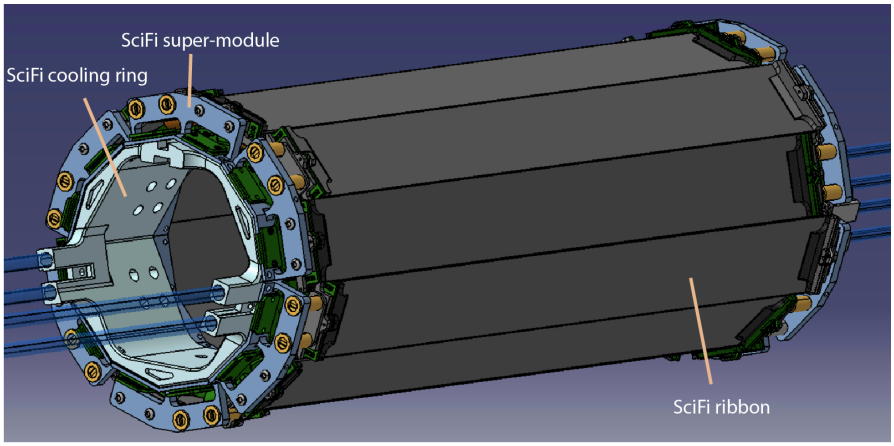

Figure 7.2: CAD rendering of the full scintillating fiber detector. 12 SciFi ribbons are arranged in a cylindrical shape and coupled to SiPMs on both sides.

Figure 7.2 presents a CAD rendering of the SciFi detector's design, detailing its key components and their integration. The detector is constructed from 12 SciFi ribbons, each measuring 300 mm in length and 32.5 mm in width. These ribbons are staggered longitudinally by approximately 10 mm. This staggering serves two purposes:

- it minimizes dead spaces between ribbons;
- it creates enough room for the spring loading mechanism that accommodates the ribbons

The spring loading is essential to prevent sagging and to address the issue of thermal expansion, as detailed in section 7.2.1. The ribbons are organized so that six are spring loaded on one side of the structure, and the remaining six on the opposite side are fixed.

The SciFi ribbons are grouped into modules, called SciFi super-modules for easier installation into the detector (see Figure 7.3). Each SciFi super-module comprises two SciFi ribbons. The coupling of the SciFi ribbons to the SiPM arrays is achieved through simple mechanical pressure without the need for grease, glue, or other optical interfaces. This simplifies the assembly process and maintains a cleaner optical path. The SiPM sensors are linked to the SciFi readout boards via flexible printed circuits. As mentioned earlier, the SiPM arrays are the Hamamatsu `S13552-HRQ`, with a high quench resistance, see section 4.8.2.

Expanding the view, the main mechanicals parts of the SciFi super-module, as illustrated in Figure 7.4, are the following:

- **L-bracket support**: Constructed from aluminum, the L-bracket support plays a crucial role in the stability and cooling of the system. Primarily, it provides robust support for the electronics boards, specifically the SciFi Module Board version

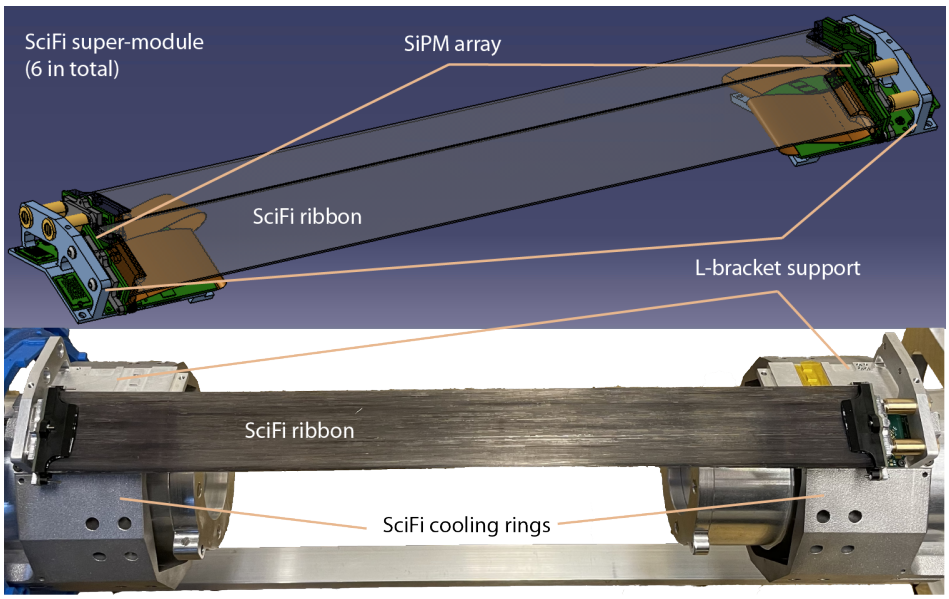

Figure 7.3: CAD rendering of the SciFi super-module (top) and a first (half) SciFi super-module made real (bottom). The SiPM arrays are coupled to the SciFi ribbons through the end-pieces.

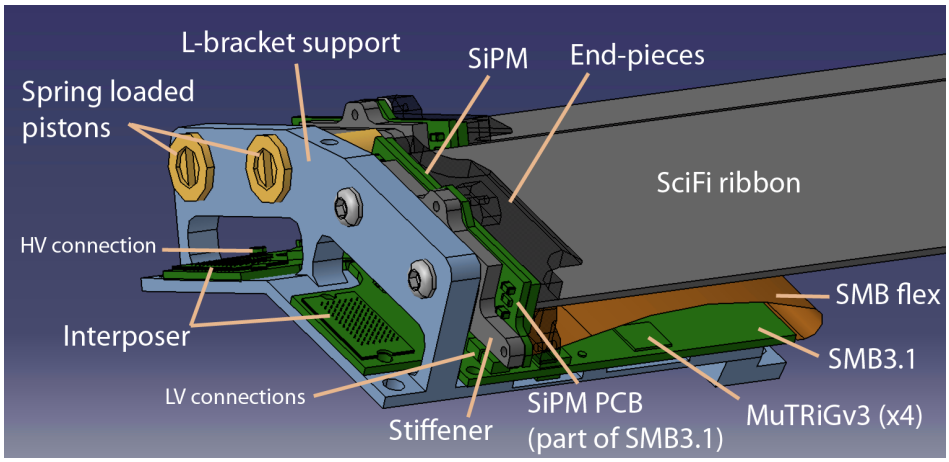

Figure 7.4: CAD rendering of the SciFi super-module closeup.

3.1. Additionally, it acts as a mechanical backbone for the SiPM arrays, enhancing their structural integrity and performance. Also, it allows to cool the SiPM arrays and the electronic boards via thermal contact with the cooling block.

- **Stiffener**: The stiffener is made in aluminium and serves as support for the SiPM arrays coupled to the SciFi ribbons. The stiffener is used for the mechanical stability and for the coupling of the SiPM arrays to the SciFi ribbons.
- **Spring loading pistons**: The pistons are part of the spring-loading mechanism. They serve a dual purpose: firstly, as guides for the screw which is encompassed by the spring, and secondly, as facilitators for the mechanism's smooth and precise operation.
- **End-pieces for the SciFi ribbons**: As already mentioned, end-pieces made in POM-C, are glued to the ribbon's ends to provide a robust and flat surface for the coupling of the SiPM arrays to the SciFi ribbons.

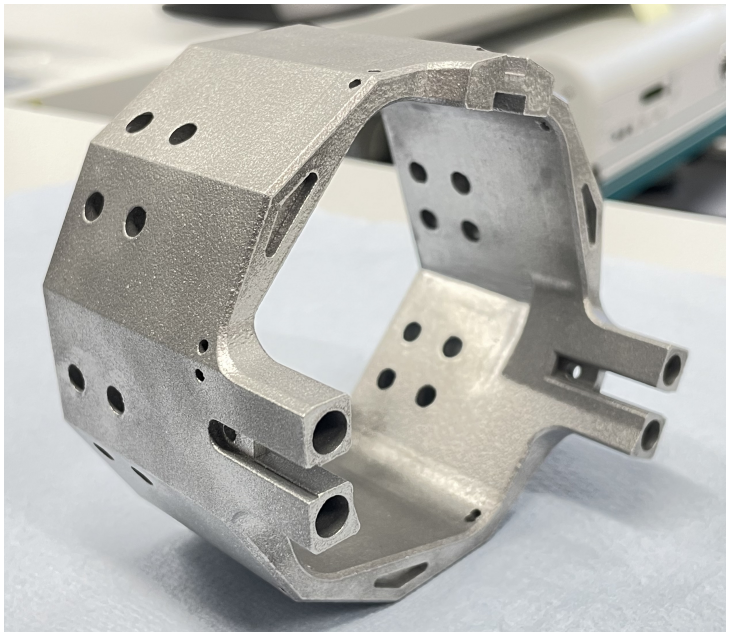

Figure 7.5: SciFi cooling block. The cooling block is 3D printed in aluminium and serves as support and cooling block for the SciFi detector. It is about 50 mm tall and has a diameter of about 100 mm. It serves not only as a support for the SciFi detector, but also facilitates the cooling of the electronic boards.

There are in total 6 super-modules, each one containing 2 SciFi ribbons. The L-bracket support are fixed on a hollow dodecagonal prism, illustrated in Figure 7.5. This prism is 3D printed in aluminium. It is about 50 mm tall and has a diameter of about 100 mm. It serves not only as a support for the SciFi detector, but also is used as cooling of the electronic boards, the SciFi Module Boards (see chapter 8). The detector includes two cooling blocks, one on each side of the beam pipe. These blocks are interconnected

with the Mu3e liquid cooling system and feature embedded piping for the circulation of the coolant, which is a mixture of silicon and oil. The cooling blocks are designed to be as compact as possible, while still providing sufficient cooling power. The primary objective of this cooling setup is to maintain the temperature of the SiPM arrays below $-10\,^{\circ}\mathrm{C}$ to ensure optimal performance.

7.2.1 *Thermal expansion and sagging of the SciFi ribbons*

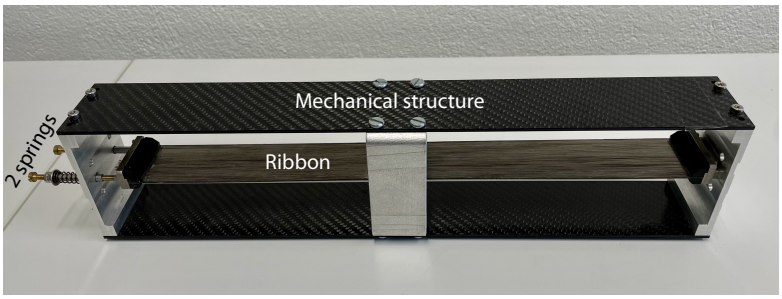

Figure 7.6: Mechanical structure used to evaluate the thermal behavior of the SciFi ribbons. The structure with a ribbon is placed in a climate chamber and one end is fitted with a pair of identical springs to apply tension.

Using a mechanical structure, the thermal behavior and sagging of the fiber ribbons is tested in a climate chamber. The structure is composed of two carbon fiber plates to ensure thermal stability, two steal holders fixed on each side of the carbon fiber plates and two other steal holders at the middle (Figure 7.6). The two steal holders at the middle on each side is placed to hold a scale on one side and a camera (inserted in a little hole) on the other side. The ribbon is placed in the middle of the holders and between the carbon fiber plates. On the final design of the Mu3e experiment, the ribbons are each spring loaded to reduce the ribbon sagging and compensate for the thermal expansion. Therefore, one side is fixed and the other is spring loaded. The ribbon is glued to the holders which is composed of a mock-up SIPM and two black holders. The two black holders are little pieces which can hold a ribbon. The ribbon used for this test is a 3-layer ribbon with 250 µm fibers, glued together with the POLYTEC EP 601-Black adhesive. The test bench has a length of 330 mm, a width of 44 mm and the distance between the two carbon fiber plates is 74 mm. The springs has a spring constant k of 1.2 N/mm. Varying forces are applied to the two spring-loaded screws by compressing the spring with a nut. This increased tension on the ribbon aims to counteract sagging and accommodate thermal expansion.

Ribbon sag is measured using a ruler fixed at the midpoint of one steel holder. Note that the ribbons exhibit orientation dependent behavior due to the curvature introduced during the gluing process. Thermal expansion of a 3-layer fiber ribbons, tested from $0\,^{\circ}\mathrm{C}$ to $60\,^{\circ}\mathrm{C}$, showed an expansion coefficient of $(65 \pm 16) \cdot 10^{-6}/\mathrm{K}$, leading to an elongation of about 1 mm for a thermal change of 50°, see left of Figure 7.7.

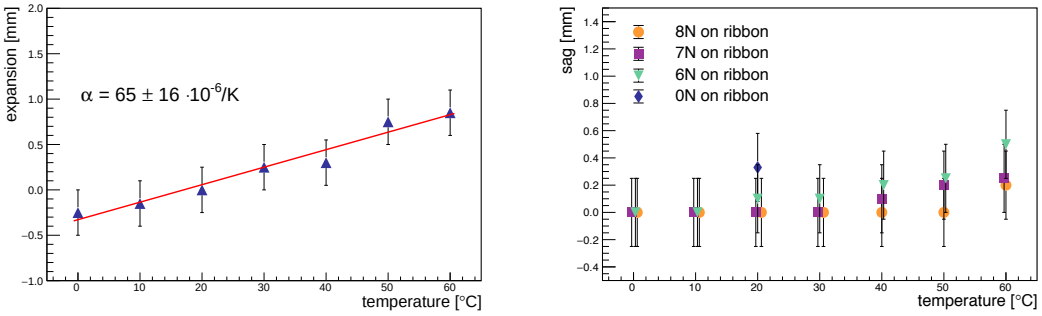

Figure 7.7: Left: elongation of a 3-layer SciFi ribbon with temperature variation. Right: ribbon sag at various tensions and temperatures, including sag at 20 °C with no tension.

To prevent sag, the ribbons use a spring-loaded mechanism, which tests indicates a minimal required tension of 8 N in total (the sum of the two springs) for stability across this temperature range, see right of Figure 7.7. Multiple cycles have been performed and the measurements are proven to be stable.

7.3 SIPM IRRADIATION

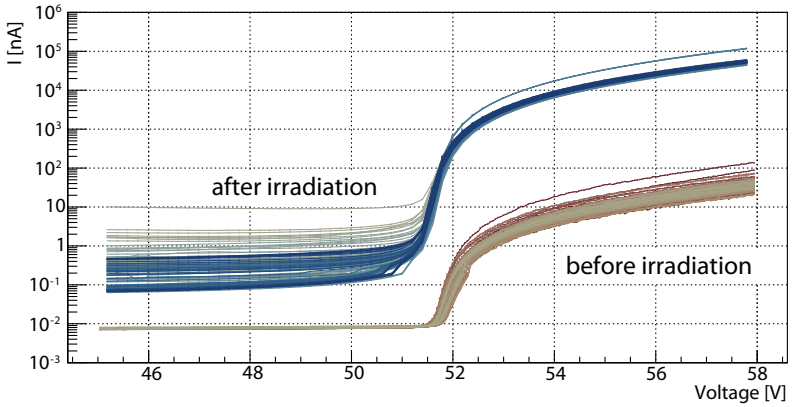

Figure 7.8: I-V curve for a SiPM array irradiated to $(1.5 \pm 0.3) \times 10^{12}$ e^+/cm^2.

The SiPMs are sensitive to radiation and can degrade over time. In the Mu3e experiment, the SiPMs arrays will operate in a very high radiation environment of low electrons and positrons from muons decays, which damages more the SiPMs than minimum ionizing particles (m.i.p.'s) , comparable to low energy neutrons. Various mechanisms can be responsible for this damage. A good candidate can be a non-ionizing energy loss in the silicon bulk material leading to dislocations. Several SiPM arrays have been exposed to positrons from muon decays at rest (Michel spectrum) and irradiated at different doses in the πE5 beamline at PSI. These irradiations were performed as part of the studies detailed in [64] and [65]. Figure 7.8 shows the I-V

curves of each channel of a SiPM before and after irradiation. This SiPM has recieved a dose of $(1.5 \pm 0.3) \times 10^{12}$ e^+/cm^2 which is the expected dose in Mu3e after one year of running at 10^8 muon decays/s. Per channel the dark current grows from 10 nA to 10 µA at overbias of 3 V.

Left of Figure 7.9 shows the DCR of one channel of the same irradiated SiPM for a threshold above 1.5 ph.e. at different temperatures. The rates have been measured by acquiring events with a random trigger over a 800 ns window and by counting the number of peaks above a threshold of 1.5 ph.e.. The DCR per channel for the irradiated SiPM array at 20 °C is ∼46 kHz[1] while at −7 °C it is ∼3 kHz. Since in Mu3e the SiPM arrays of the SciFi detector will be operated below −10 °C, the DCR further decreas. On

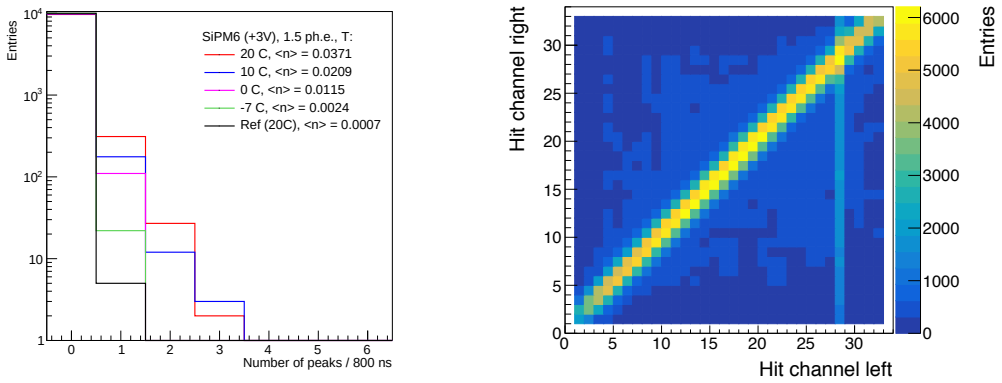

Figure 7.9: Left: DCR for a selected channel of the same irradiated SiPM array at different temperatures operated at overbias of 3 V for a 1.5 ph.e. threshold. Also the DCR for a non irradiated SiPM (in black). Right: Correlation between the two ends of the SciFi detector using the same SiPM array cooled to −6 °C with threshold set at 1.5 ph.e..

the right of Figure 7.9t he correlation between the two ends of the SciFi detector read out with the same irradiated SiPM array is shown. The SiPM is cooled to −6 °C with a 1.5 ph.e. threshold. Due to the increase of DCR minor backgrounds are introduced. Also the cluster width can be deduced which is increased by ∼ 0.5 channels. More radiation effects are discussed in [64, 65].

7.4 COOLING OF THE SCIFI DETECTOR

The cooling of the SciFi detector is achieved with a cooling circuit and a cooling chiller. The liquide cooling chiller is common for both the SciFi detector and the tile detector. The chiller used for this system is a Huber Unistat 425W. It delivers a cooling power of 2.8 kW at 20 °C and 1.9 kW at −20 °C. As seen in Figure 7.10, the maximum deliverable pressure of the chiller is 1.5 bar and the deliverable flow rate at 1 bar is 50 l/min. To be able the deliver the cooling power to the SciFi detector, the chiller needs to

1 Normalized the number of peaks to 1 s.

be operated at a pressure of $\sim$ 1.4 bar which gives a flow rate of $\sim$ 6 l/min. The cooling fluid is a low-viscosity silicon oil (Huber M80.055.03) which can be used in the temperature range from $-80\,^{\circ}\mathrm{C}$ to $55\,^{\circ}\mathrm{C}$. The control and monitoring is done by an ethernet connection, MODBUS protocol and can be integrated to the data acquisition system of `Mu3e`.

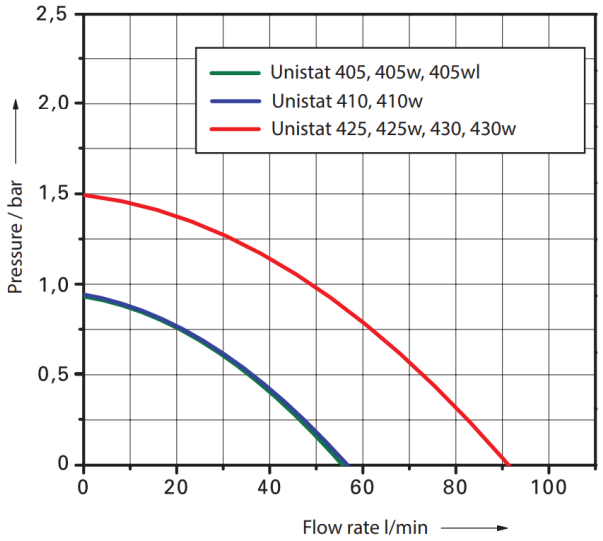

Figure 7.10: Chiller Huber Unistat 425W pump curve showing the pressure in function of the flow rate. The maximum deliverable pressure is 1.5 bar and the deliverable flow rate at 1 bar is 50 l/min. From the datasheet of the chiller [66].

Figure 7.11 shows the current foresseen cooling circuit for the SciFi detector. Starting from the chiller, the cooling subcircuit for the two detectors is separated in a manifold placed directly at the chiller, as shown in Figure 7.11. The fluid delivery to the two subsystems is then steered by external valves at the chiller manifold. Those valves would be ideal needle valves. For the upstream and downstream delivery of the fluid, valves at the SciFi US/DS manifolds (Q1, Q2, Q3, Q4 in Figure 7.11) are used to control the flow rate and the pressure in the system. The flow rate between the upstream and downstream stations must be equalized by measuring the total flow at the outside of the flanges while monitoring pressure differences downstream. Measuring the temperature at the SciFi cooling rings with the help of 3 temperature sensors per cooling ring also allows for adjusting the flow rate to ensure a uniform cooling of the detector. Following the SciFi US/DS manifolds, the cooling circuit is split into two subcircuits, one for each manifold inside the SciFi cooling rings. To control and monitor the pressure and flow rate, pressure and flow rate sensors are placed before the magnet flanges.

To make the circuit, aluminum pipes of 6 mm outer diameter and 5 mm inner diameter are directly glued on the SciFi cooling ring using `DP2216` epoxy gray glue. The pipes are then connected with the same glue to a aluminum pipe of 8 mm outer diameter and 6 mm inner diameter, which are bent to go out radially from the beampipe. Next, flexible stainless steel (SS316L) pipes connect the circuit to the manifold. With a

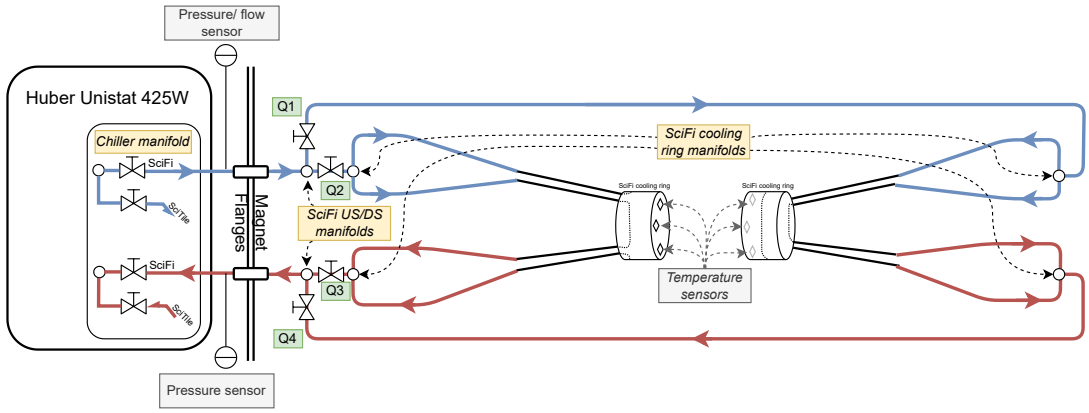

Figure 7.11: Scheme of the cooling circuit for the SciFi detector. The SciFi cooling circuit is separated from the Tiles cooling circuit at the chiller manifold. SciFi US/DS manifolds split the cooling circuit into two, for upstream and downstream cooling. Then another split is done with aditional manifolds for the SciFi cooling rings which have two embedded circuits. For clarity, lenghts and scales are not respected.

flow of 5 l/min after the magnet flanges, the total pressure drop for the SciFi circuit is estimated to be ~ 0.73 bar, and the flow at the SciFi cooling rings is respectively 1.29 l/min and 1.21 l/min for upstream and downstream rings.

8

READOUT OF THE SCINTILLATING FIBER DETECTOR

The scintillating fibers are coupled at both ends to multichannel Silicon Photo-Multiplier (SiPM) arrays , which are readout by 4 mixed mode MuTRiG (Muon Timing Resolver including Gigabit-link) ASICs. The MuTRiG ASICs are directly bonded on the SciFi Module Board (SMB). This readout board has been developed at the University of Geneva. The MuTRiG ASIC, with its $\sim$20 ps intrinsic time resolution, fullfills the requirements of the Mu3e SciFi detector. It also supports the high event rate coming from the timing detectors.

In this chapter the readout of the SciFi detector is described. First, the MuTRiG chip is described, then the SciFi Module Board and its development are presented. Laboratory tests with the latest version of the SMB and the MuTRiG chip is also presented and discussed.

8.1 MUTRIG ASIC

The MuTRiG ASIC was conceived to address the specific requirements of the Mu3e experiment, which needs both high timing resolution and the capacity to handle a significant event rate up to MHz/channel. The design of MuTRiG is the evolution of his predecessor STiCv3 ASIC [67] proven features, such as its differential analog front-end and the 50 ps binning time-to-digital converter (TDC). But also new features, such as a double data rate serializer and a custom low-voltage differential signaling (LVDS) transmitter, enables a gigabit data link with the Data Acquisition system (DAQ). These allow for a more efficient transmission of event data, a critical factor in high-rate environments. The MuTRiG ASIC has 32 channels. Further , the digital logic circuit of MuTRiG received significant upgrades. The ASIC, which his first prototype was produced in 2017, is at his third version to date (January 2023), MuTRiG version 3 (MuTRiGv3), and is the one that will be used in the Mu3e experiment.

A mixed mode ASIC, such as the MuTRiGv3, is an integrated circuit that contains both analog and digital circuits on a single chip to perform a particular function. This integration allows for efficient and compact designs, specifically in applications where both analog and digital processing are required.

The output signal of the SiPM coupled to a scintillating material gives time and energy information. The charge which can be retrived by integrating the signal, is proportional to the energy deposited in the scintillating material. The time information is given by the time of arrival of the signal.

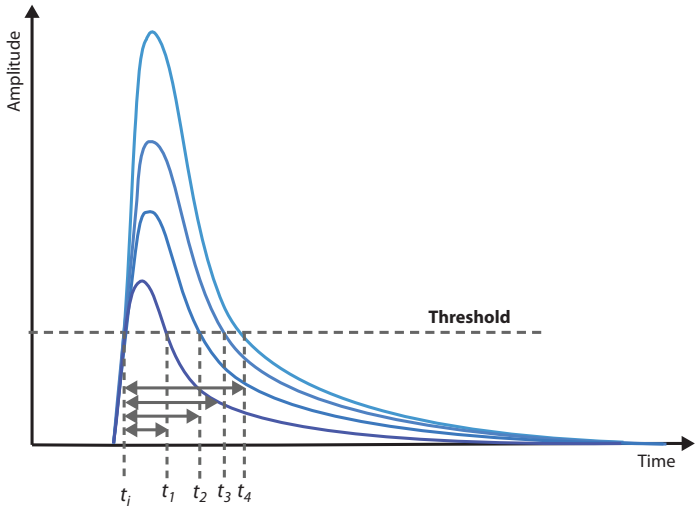

Figure 8.1: ToT measurement principle. The signal's pulse width, combined with its arrival time (t_i), is encoded in a single output signal through analog signal processing and gives the energy information.

The charge and energy is determined by using the Time over Threshold (ToT) technique. The ToT technique derives charge by measuring how long a signal exceeds a certain threshold, see Figure 8.1. This is less precise compared to the digitization of the signal's waveform or using an ADC since the ToT response to signal charge is nonlinear due to the pulse shape, which is even further accentuated the low photon statistics signals.

In scenarios where high energy resolution is not critical, this method allows for energy determination through time measurement alone, eliminating the need for both ADC and TDC modules in an ASIC, thus reducing the complexity, size, and power consumption of the readout channels. This chip uses a linearized ToT approach to enhance energy resolution. The signal's pulse width and its arrival time are merged into a single output through analog processing, enabling a single TDC channel to accurately determine both the time and energy of the incident particle.

Measuring the arrival time of particles in the MuTRiG chip involves setting a threshold for the SiPM's current pulse and detecting when this threshold is exceeded. The accuracy of the resulting time trigger signal is affected by time jitter and time walk. Time jitter, arising from random noise sources, is mitigated by optimizing the noise performance of analog circuits and the input impedance of the initial stage. Time walk, a systematic issue, requires specific discrimination techniques.

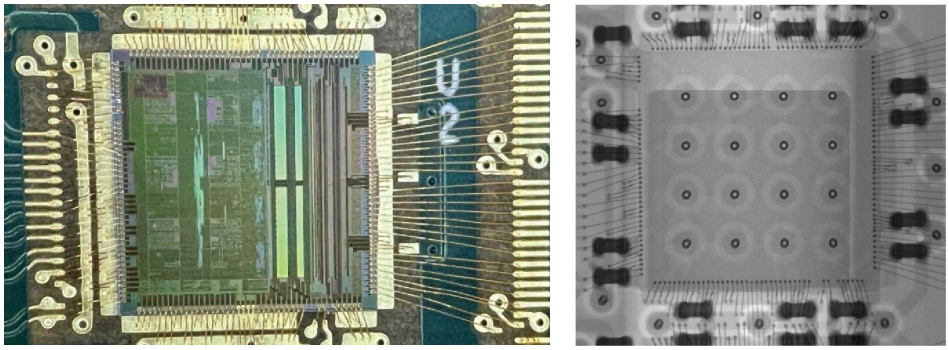

Figure 8.2: Left) The MuTRiGv3 ASIC bonded to a carrirer board. Right) The X-Ray photographie of the MuTRiGv3 ASIC bonded which is under a protective globtop on the SMB. (see Figure 8.9)

In the MuTRiG, the Leading Edge (LE) method is implemented for time of arrival determination. It utilizes two separate discriminators with adjustable thresholds to extract both time and charge information from the SiPM current pulse. Commonly they are refered to as T-Trigger for time and E-Trigger for energy. The T-Trigger uses a low-threshold LE discriminator, with a threshold range covering from below a single photon signal amplitude to multiple photons signal amplitude. For the charge measurement (E-Trigger), it employs the Time over Threshold (ToT) method. However, due to ToT's non-linearity, a higher threshold is set for the E-Trigger to prevent resolution degradation in larger signals. In the folowing, the discussions is primarily centered on the use within the SciFi detector of the MuTRiGv3.

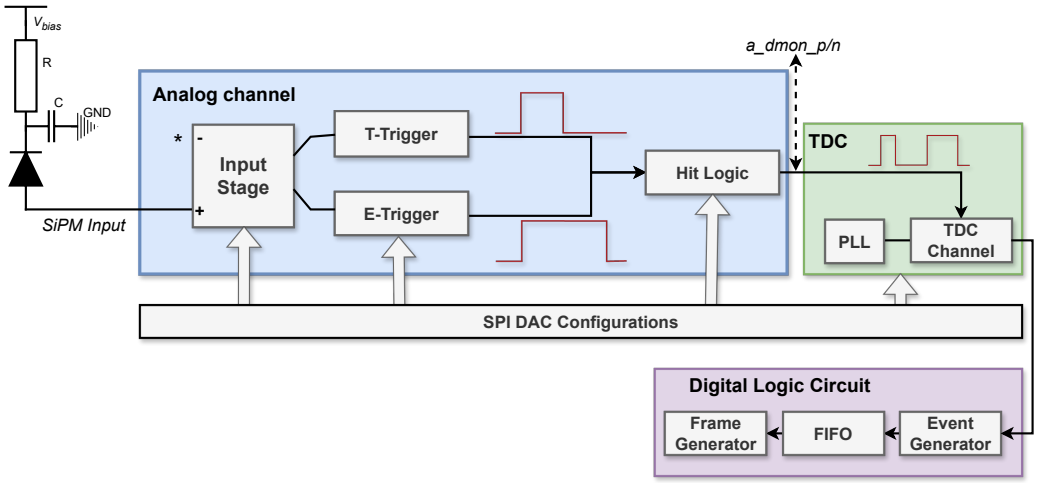

Figure 8.3: Block diagram of one channel in the MuTRiG chip. All the blocks are presented such as the analog channel, the TDC and the digital logic circuit. * only the positive input is used while the negative is left floating.

An overview of the important blocks of the MuTRiG chip is shown in Figure 8.3. First, the SiPM current signal is fed into the input stage of the analog front-end; for

clarity, only the path of one channel is shown in the Figure 8.3. Once the signal passes through the input stage, it is split into two distinct paths: one going to the timing trigger branch and the other to the energy branch. This division enables the time and energy discrimination of the signal. Following this, the discrimination signals from both branches are merged in the hit logic module which combine the signals to form a unified hit signal. A Time to Digital Converter (TDC) generates then precise timestamps corresponding to each rising edge of the hit signals. After this, the digitized timestamps from the TDC module are combined to create comprehensive hit information data. This data contains both time and energy information of each event. It is then stored temporarily in the on-chip memories, awaiting subsequent transfer out of the chip. Supporting this entire operation is the Serial Peripheral Interface (SPI). This interface serves to communicate with the various modules (blocks) within the system between the data taking periods. Those various modules include the analog channel (part of the analog front-end), the TDC, and the digital modules.

8.1.1 *Analog Front-End*

The analog front-end is the first stage of the MuTRiG chip. His role is to process the SiPM current signal to extract the time of arrival and the energy information by using the methode described in the previous section. The input of the front-end is designed differentially and so can be used in two ways: differentially or single-ended. In the case of the SciFi detector, the single-ended mode is used on the SMB because of the common cathode of the SiPMs. Each MuTRiG unit is equipped with 32 analog front-ends, with each front-end comprising an SiPM single-ended input channel and a signal discrimination mechanism.

8.1.1.1 *Input Stage*

The differential input stage of the analog front-end consists of a symmetrical structure. In the case for SciFi, the positive input is used and the negative input of the input stage is left floating.

The positive side circuit of the input stage is shown in Figure 8.4. The analog input stage uses a common gate amplifier which is a type of field-effect transistor (FET) configuration where the gate terminal of the FET is connected to a common source voltage (or ground). A FET controls the flow of current using an electric field, which is generated by the voltage between the gate and source terminals.

As seen in Figure 8.4, this transistor is identified as $M1$. The operation of this transistor is tuned through a process known as biasing. Biasing involves operating the transistor using a current known as I_{bias}, refered to as the main bias current of the input stage. This current is generated by a constant current source and can be controlled through a DAC parameter, which in turn is managed by the ASIC's digital control logic (`INPUTBIAS` in the MuTRiGv3 common parameters names). Adjusting the bias current I_{bias} optimizes the transistor's performance, notably enhances its transconductance $g_{m,M1}$. The transconductance quantifies the transistor's efficiency in regulating the

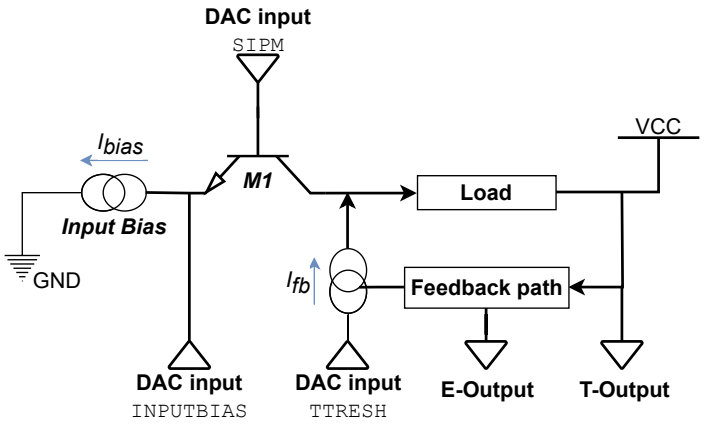

Figure 8.4: Schematic of the positive input of the MuTRiG input stage.

electric current in response to changes in the input voltage. A higher transconductance means more precise control. Moreover, the input impedance Z_{in} of the input stage is directly influenced by the transconductance of the transistor:

$$Z_{in} \sim \frac{1}{g_{m,M1}} \tag{8.1}$$

with

$$g_{m,1} = \sqrt{2\mu C_{ox} \frac{W}{L} I_{M1}} = \sqrt{2\mu C_{ox} \frac{W}{L} (I_{bias} - I_{SiPM})} \tag{8.2}$$

where μ is the mobility of the charge carriers, C_{ox} is the oxide capacitance per unit area, W and L are the width and length of the transistor, I_{M1} is the current flowing through the transistor $M1$, I_{bias} is the main bias current and I_{SiPM} is the current coming from the SiPM sensor. As seen in equation 8.1, the input impedance Z_{in} is inversely proportional to the transconductance $g_{m,M1}$ of the input transistor. This impedance can be reduced by increasing the bias current I_{bias} of the transistor. However, tuning the bias current of the input stage is a delicate process, as it changes also the bandwidth, input voltage, and the timing and energy resolution as well. Therefore, it is important to find the right balance between the input impedance and the other parameters.

The gate voltage of the input transistor, controlled by another DAC value `SIPM`, is key to the SiPM sensor's bias tuning. In a specific operational mode known as the saturation region, the behavior of the transistor is characterized by the relationship between the current flowing through it I_{M1} and the voltage difference between its gate and source terminals V_{gs}. This relationship is expressed as:

$$I_{M1} \propto (V_{gs} - V_{th})^2 \tag{8.3}$$

where V_{th} is the threshold voltage of the transistor. When the bias current I_{bias} is fixed, it sets a specific operating point for the transistor. To maintain stable operation, it is vital that the voltage difference between the gate and source terminals V_{gs} remains

constant. This stability ensures that the transistor functions effectively as an amplifier. Adjustments to the gate voltage are made through the DAC parameter `SIPM`, and these adjustments need to be mirrored by changes in the source terminal voltage to keep the V_{gs} constant. So by controlling the gate voltage through the DAC, it is possible to fine-tune the voltage across the transistor, thus controlling its operation precisely. In a large system, the bias voltage of the SiPMs are generated commonly for several channels, prohibiting to set to the precise overbias voltage for each SiPM channel individually. This feature enables to adjust the overbias voltage for each channel of the SiPM.

The circuit also includes a feedback mechanism to stabilize the circuit and maintain the output at a desired voltage level. Also, it is used to control the time trigger threshold for the time discriminator circuit in the system (T-Output). The range of the time trigger threshold is adjustable from below a single photon signal amplitude to multiple photons signals. A second copy of the signal is also generated for charge information (E-Output). The tuning of the feedback current, which defines the T-Trigger threshold, also influences the behavior of the E-Trigger path.

8.1.1.2 *Time Trigger*

The timing trigger branch is responsible for generating the T-Trigger signal, which indicates the arrival time of incident particles. The analog front-end of the system

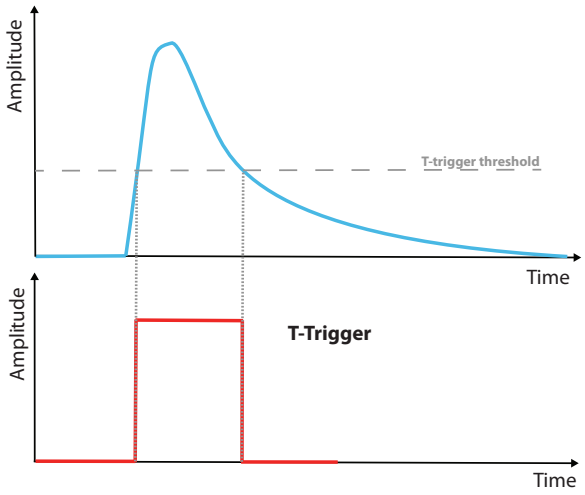

Figure 8.5: Schematic of the Time Trigger branch which is used to determine the time of arrival of the signal. Adaped from [68].

comprises two primary blocks: an amplifier and a discriminator which is a comparator circuit. To generate an accurate time trigger signal from a SiPM, the system undergoes a multi-step process. It begins with the signal from the analog input stage being increased by a high-bandwidth amplification block, essentially increasing the signal to a level suitable for further processing. The amplified output is then both fed forward for next steps and looped back into the input stage through a feedback path. This

feedback process is used to control the DC operating point of the input stage. This DC operating point is essentially the baseline voltage level of the signal when no pusles are detected by the SiPM. By tuning the feedback current via the TTHRESH DAC value, the baseline voltage level can shift up or down. The comparator's trigger threshold is set relative to this baseline. If the baseline is shifted upward, it requires a larger signal (from the SiPM) to cross the threshold and trigger the comparator. Conversely, if the baseline is shifted downward, a smaller signal is needed to trigger the comparator. The comparator itself has a set reference voltage (or threshold voltage). So when the signal exceeds this reference voltage, the comparator switches states, thus generating a time trigger signal, as seen in Figure 8.5. The threshold range is designed to be adjustable from below a single photon signal amplitude to multiple photon signal amplitude [69].

The TTHRESH DAC value has a scale and an offset providing a better control. The TTHRESH scale adjusts the slope of the feedback current's response curve to the TTHRESH DAC value, while the TTHRESH offset modifies the curve's baseline. This extends and fine-tunes the threshold ranges.

8.1.1.3 *Energy Trigger*

The energy trigger is generated by a separate circuit composed of a pulse shaper, amplifier and a discriminator. The circuit operates by employing the positive of the differential output signal obtained from the initial input stage. This is determined by a switch which is controlled by the EDGE DAC setting. Then, the selected signal is shaped using a pulse shaper to a smooth triangle-like shaped signal. During this process, the shaped signal is compared against a variable threshold voltage, adjustable through a DAC value ETHRESH. It's important to note that the time trigger's threshold value (TTHRESH) has an influence on the DC values within the input signal pathways, thereby impacting the relative discrimination threshold of the E-Trigger. So an increase of the T-trigger threshold leads to a corresponding increase in the threshold for energy discrimination. Therefore, each adjustment of the T-Trigger threshold necessitates a recalibration of the E-Trigger.

8.1.1.4 *Hit Logic*

The Hit Logic unit merges the outputs from the timing and energy trigger branches, called T-Trigger and E-Trigger respectively, to form a unified hit signal. The hit signal enables the use of one Time-to-Digital Converter (TDC) for simultaneously measuring timing and energy information. Although the TDC is only responsive to rising edges, it's crucial to sample both the rising edge of the T-Trigger signal and the falling edge of the E-Trigger signal to accurately derive both arrival times and so the energy information. The Hit Logic unit creates a combined hit signal along with an energy flag signal which is activated only during the sampling of the falling edge of the E-Trigger signal. This combined hit signal is produced through an XOR operation of the discriminator output signals.

A challenge arises due to short rise time of the SiPM signal and the proximity of the rising edges of the T-Trigger and E-Trigger signals. The narrow pulse width of the

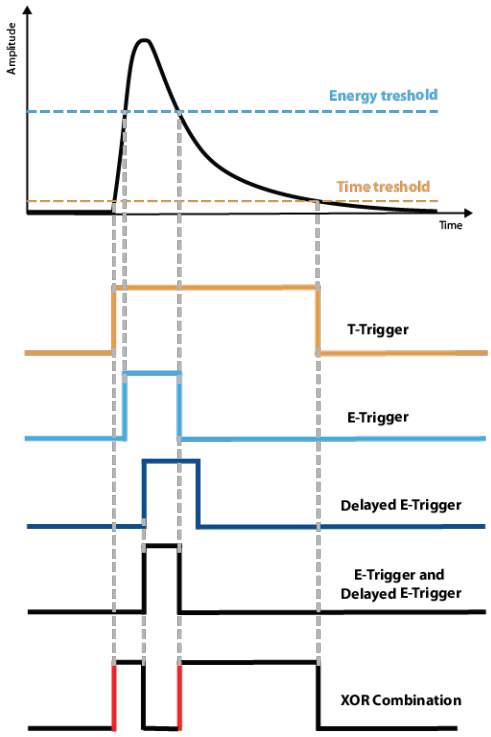

Figure 8.6: Signal processing in the Hit Logic unit. Adaped from [68].

E-Trigger signals may be insufficient to activate the TDC, especially when the pulse shaper stage in the energy branch is inactive. Conversely, when the pulse shaper is active, the E-Trigger signal might exceed the duration of the T-Trigger signal. This leads to an XOR combination that only captures the rising and falling edges of the T-Trigger signal, omitting the falling edge of the E-Trigger. To resolve this, a dedicated signal processing unit includes a delay cell and a combination of NAND and NOR gates before the output XOR gate. The NAND and NOR gates ensure the accurate capture of the E-Trigger's falling edge. The delay cell adds a 15 ns to 20 ns delay, effectively broadening the hit signal pulses. The delayed E-Trigger acts as an Energy flag, marking the start of energy measurement. Figure 8.6, illustrates the signal processing mechanics.

The entire Hit Logic unit is designed using differential Current Mode Logic (CML). CML is a differential signaling method that uses current instead of voltage to represent digital signals. This design choice offers noise rejection from the digital power supply. However, a trade-off of the CML logic is its higher power consumption compared to CMOS logic. Nonetheless, for this application, the increased power consumption is not a significant concern. When compared to the power demands of the Phase-Locked Loop (PLL) used for the TDC and the amplifiers in the timing branch of the front-end, the hit logic's power consumption remains relatively modest.

8.1.1.5 *Debug Monitors*

For functional testing and characterization, the MuTRiG chip integrates dedicated debug pads. These include two pairs of differential digital outputs and one analog single-ended output. The analog output, referred to as *a_amon*, allows observation of the analog signal after the input stage and at the amplification stages in both the time and energy discrimination paths. However, in the latest SMB version (from SMB version 2 onwards), *a_amon* is omitted due to space constraints.

The digital outputs, named *a_dmon_p* and *a_dmon_n*, enable access to the T-Trigger and E-Trigger signals after the discrimination, and their combined output signals from the Hit Logic unit, see Figure 8.3. There are 2 pairs: one for monitoring the time and charge comparator outputs and the second for the energy flag and charge output. Additionally, the digital monitor pads can directly access the TDC channel's input terminals, bypassing the analog front-end. This feature is particularly useful for calibrating and testing the digital part, including PLL lock tests, which are discussed later in the chapter. In the SMB, the first pair of *a_dmon_p* and *a_dmon_n* is used for charge injection to test the TDC.

The debug pads, when connected, are controlled by several DAC settings. The `DMON 1/2` and `DMON 1/2 enable` settings are used to configure and activate the digital monitor pad drivers for each pair. Monitoring is limited to one channel at a time, selected via the global `DMON SEL` signal, which can address a single channel from a range of 0 to 31. To disable monitoring, `DMON SEL` should be set to -1. Lastly, the `DMON SW` parameter switches the nature of the signal, choosing between charge and Energy flag or time and charge comparator outputs, with `DMON SW` set to 0 for the first pair and 1 for the second pair.

Table 8.1: Adjustable DAC values for the analog front-end discussed in this section.

Common DAC name	*Description*
INPUTBIAS	Main bias current of the input stage. Adjusting the bias current optimizes the transistor performance at the input stage. However, tuning the bias current changes also the bandwidth, input voltage, and the timing and energy resolution as well. Higher values mean higher currents.
SIPM	Gate voltage of the transistor at the input stage. Enables to adjust the overbias voltage for each channel of the SiPM. This DAC ranges from 0 to 63 with a higher values meaning higher input voltage a the terminal. The trend of the input voltage as a function of this DAC value is shown in Figure 8.22.
TTHRESH	Setting the time threshold by tuning the feedback current at the input stage. Range from 0 to 63 with lower values being higher thresholds.
TTHRESH Scale	Scaling of the time threshold. Adjusts the slope of the feedback current's response curve to the TTHRESH DAC value. Higher values correspond to higher slope.
TTHRESH Offset	Offset of the time threshold. Adjusts the baseline of the feedback current's response curve to the TTHRESH DAC value. This extends the time threshold range.
ETHRESH	Setting the energy threshold. Range from 0 to 255 with lower values being higher thresholds. For amplitudes of SiPMs signals usual values between 90 and 150 are used.
DMON 1/2	Configure the digital monitor for the selected channel. Each pair of can be configured and enabled via the DMON 1 or DMON 2. Only one channel at the time can be monitored.
DMON 1/2 enable	Enables the digital monitor for the selected channel. Only one channel at the time can be monitored.
DMON SEL	Select the channel to monitor. Only one channel at the time can be monitored.
DMON SW	Output mode of the digital monitor. Charge and flag output for value 0 or time and Energy flags for value 1.

8.1.2 *Time to Digital Converter*

Once the hit signal and Energy flag signal are generated, the next phase involves their digitization by on-chip Time-to-Digital Converter (TDC) modules. These TDC modules sample the state of an incrementally increasing counter (coarse counter) synchronized with a reference clock at the arrival of a hit signal. Additionally, the clock interval of 1.6 ns is further subdivided into smaller intervals of 50 ps (fine counter) to measure the time between the start of a clock cycle and the hit signal's arrival. Both coarse and fine counter values are recorded to timestamp the hit signal.

The TDC module comprises two main components:

1. Global Timebase unit: this unit provides uniform coarse and fine counter values across all channels, crucial for assigning accurate timestamps to each hit signal.

2. Individual Latch Units in Each Readout Channel (TDC Channel): These units capture and hold the counter values from the Timebase unit upon the arrival of a hit signal. The stored counter values are then interpreted as timestamps by the chip's digital logic circuit, which will be elaborated on later in the chapter.

The TDC's architecture, including the integration of the Global Timebase unit and the TDC channels, ensures precise time measurements of the hit signals.

8.1.2.1 *Timebase Unit*

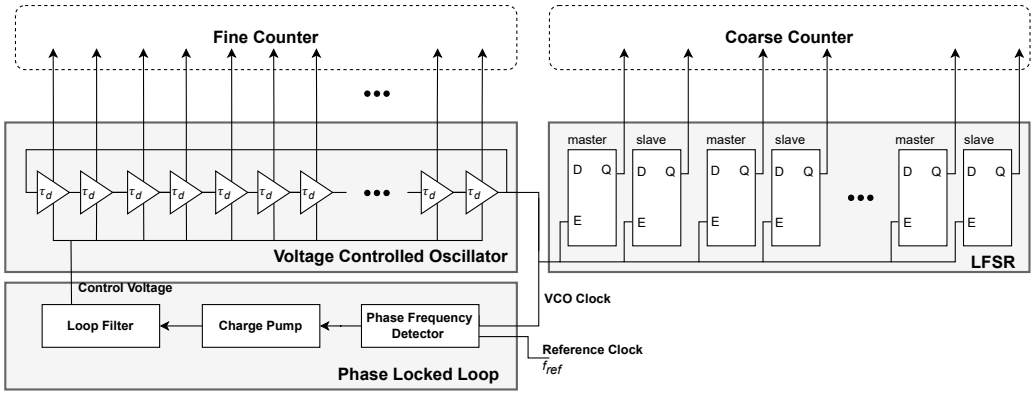

Figure 8.7: Schematic of the Timebase unit. Adaped from [68].

The Timebase unit, see Figure 8.7, in the system utilizes a Phase-Locked Loop (PLL) to generate a stable clock signal for precise timing measurements. The PLL's core component is a Voltage Controlled Oscillator (VCO), which consists of 16 delay elements (or cells) arranged in a ring structure. This configuration allows the control voltage, regulated by the PLL, to adjust the propagation delay τ_d of these delay elements. τ_d represents the time required for a signal to travel through a delay element.

As the signal completes its journey through all 16 elements, taking $16 \cdot \tau_d$ to do so, it is inverted and looped back to the start. This creates a course counter with a period of $2 \times 16 \times \tau_d$, as the signal needs to traverse the 16 delay elements twice (back and forth) to return to the initial cell. The VCO, through this mechanism, is instrumental in maintaining the precision and stability of the time measurements.

For finer time measurements in the system, the precise position of the signal within the delay element chain of the VCO is utilized. At any given moment, the signal is located in one of the delay cells. Each of these cells represents a finer subdivision of the total period of the coarse counter clock. Considering there are 16 delay elements and each element can be in one of two states (logic 0 or 1), there are a total of 32 possible states (16 elements $\times$ 2 states per element). These states are used to determine the fine counter. By knowing which delay element contains the signal at a specific time, the system can calculate a more precise time within the coarse counter clock period.

It's important to note that the output of the VCO clock signal is derived from the 8th delay element. This fine-grained approach to time measurement allows for enhanced accuracy in timing within the system.

The method employed in MuTRiG for generating a global timestamp involves combining the values of the coarse and fine counters. This can be represented in the following equation:

$$\text{Global timestamp} = T_{CC} \cdot 1.6\,\text{ns} + T_{FC} \cdot 50\,\text{ps} \tag{8.4}$$

In this equation,T_{CC} stands for the value of the coarse counter, where each increment is equivalent to 1.6 ns. T_{FC} represents the value of the fine counter, with each increment corresponding to 50 ps. By merging these values, the system accurately computes a global timestamp for each recorded event.

To ensure its frequency remains stable despite power, voltage, or temperature variations, the Voltage Controlled Oscillator (VCO) in the MuTRiG system is synchronized with a stable reference clock. This synchronization not only stabilizes the VCO but also eases the alignment of multiple Phase-Locked Loops (PLLs) with an external reference clock, ensuring a uniform time reference across different ASICs.

The VCO frequency alignment with the reference clock is managed by a Phase Frequency Detector (PFD). The PFD compares the phase of the VCO clock and the reference clock, generating a control signal that indicates whether to accelerate or decelerate the VCO's delay elements. Following this control signal, the PLL's Charge Pump (CP) either charges or discharges a capacitor in the Loop Filter, adjusting the control voltage and, in turn, the speed of the VCO's delay elements.

This feedback loop, comprising the VCO, PFD, Charge Pump, and Loop Filter, forms the PLL and each one can be tuned and controlled by several DAC settings. Once the PLL locks onto the reference clock, it maintains the VCO's frequency to match the reference.

In the latest version of the MuTRiG chip, MuTRiGv3, the Timebase unit includes a dedicated VCO output linked to a status bit. This bit indicates the PLL's locked status

and is transferred as a frame flag in the data stream's header, reset at the start of each serial data stream frame header transmission.

The PLL is designed to operate at a frequency of $f_{ref} = 625\,\text{MHz}$. This implied that the average of the propagation time of the delay elements is

$$< \tau_d >= \frac{1}{32 \cdot 625\,\text{MHz}} = 50\,\text{ps} \tag{8.5}$$

In the ideal case where all the delay elements have the same propagation time, so where it is uniform, the resolution of this time binning is

$$\sigma_{\tau_d} =< \tau_d > /\sqrt{12} = 14.4\,\text{ps} \tag{8.6}$$

However, in reality, the propagation time of the delay elements is not uniform. Due to the manufacturing process, such as differences in the interconnection of the delay elements, can cause the propagation time to vary from one element to another. Also, the propagation time of the rising and falling logic transitions can be different. Those differences are characterized and described by the differential non linearity (DNL) and the integral non linearity (INL) and are controlled by the PLL. More about the DNL and INL is discussed in [68] and [69].

The Timebase unit's coarse counter in the MuTRiG system functions using the VCO clock output and is designed as a 15-bit Linear Feedback Shift Register (LFSR). This LFSR cycles through $2^{15} - 1$ binary states, excluding the all-zero state which would halt state generation. Each state is later assigned a sequential number in the data processing phase.

The coarse counter values are reset to a pre-set initial value using a reset signal from the digital core logic. This reset is vital for synchronizing multiple TDCs to a shared reference point, ensuring consistent and precise timing throughout the system.

8.1.2.2 *TDC Channel*

Each readout channel for the SiPM in the system has a dedicated TDC channel, responsible for capturing both fine and coarse counter values of the Timebase unit when a hit signal is detected by the analog front-end. A trigger logic within this channel monitors the hit signal and generates a corresponding hit output signal. The latching process, involving capturing and holding these counter values, is initiated by the rising edge of this hit output signal.

Additionally, the Energy Flag from the analog front-end is simultaneously recorded. This trigger logic also creates a TDC Data Ready signal, indicating the timestamp and Energy Flag information is ready for processing. Following this, a TDC Reset signal is issued, serving two functions: resetting the TDC Data Ready signal and clearing the latches within the TDC channel.

After resetting, the TDC channel enters a short recovery phase, approximately 30 ns, before being ready for the next hit event. This recovery time limits the channel's maximum event occupancy to about 30 million events per second [24].

Table 8.2: Adjustable DAC values for the TDC modules discussed in this section.

Common DAC name	*Description*
`VNPFC`	This DAC value controls the bias of the Phase Frequency Detector (PFD) circuit.
`VNCnt`	This DAC value controls the bias current for the digital cells in the timebase unit. Observing spikes in the distribution of values from the coarse counter suggests instability or jitter. This can be due to inadequate biasing. Adjusting the bias might enhance the stability of the coarse counter, reducing spikes in its distribution by ensuring that the logic gates within the counter operate more reliably. Setting to 0 will make the PLL fail to maintain synchronization.
`VNVCOBuffer`	This DAC value controls the bias voltage of the buffers responsible for distributing the fine counter timestamps to all 32 channels.
`VNVD2C`	This DAC value controls the bias current of the cell responsible for converting the signal from differential logic (CML) to CMOS (single ended).
`VNPCP`	This DAC value controls the bias of the Charge Pump (CP) circuit. The CP either charges or discharges a capacitor which adjusts the control voltage of the VCO, which in turn adjusts the speed of the VCO delay elements. Adjusting this bias can help to reduce phase noise.
`VNHitLogic`	This DAC value controls the bias of the latch control in the TDC channels. Adjusting this bias can help to remove noise hits or side peaks in the difference between timestamps distribution of the PLL test.
`VNCntBuffer`	This DAC value controls the bias voltage of the buffers responsible for distributing the coarse counter timestamps to all 32 channels.
`VNVCODelay`	This DAC value controls the base current of the VCO via the Charge Pump. This is the most important DAC value to adjust for PLL tuning. Asjudting this helps to make the PLL lock in the right frequencies.
`LATCHBIAS`	This DAC value controls the bias voltage of the timestamp latch.

8.1.3 *Digital Logic Circuit*

The MuTRiG chip's digital logic circuite handles the timestamps generated by the TDCs, processes and transmits them to an external Data Acquisition (DAQ) system. It manages hit event data, with both the time of arrival of the signal and the ToT (energy) information.

In the chip, channels are grouped into four parts. Each group's hit event data from eight channels is initially stored in a Level 1 FIFO memory specific to that group. This data is then consolidated from all groups into a Level 2 FIFO memory. The frame generator module and double data rate serializer module then transmit this data in frames.

The MuTRiG chip operates on four distinct clocks:

- A 625 MHz PLL reference clock (FASTCLK) used by the Timebase unit in the TDC module and serial data link clock employed for data transmission which is inside the digital logic circuit module.
- A 125 MHz core clock that drives most digital logic modules other than the serializer in the digital logic circuit. This clock is derived from the serial data link clock using an on-chip clock divider.
- A 20 MHz clock (SPI_SCLK) for the SPI communication, used for chip configuration for example.

8.1.3.1 *Event Generator*

The event generator module, situated at the forefront of the chip's digital section, processes the TDC timestamps to generate hit event data.

The asynchronous nature of TDC signals in the system, not synchronized with the system clock, necessitates synchronization for stable data processing. A circuit transforms the TDC Data Ready signal's rising edge into a synchronous single clock cycle pulse, named TDC New Hit. This synchronization enables stable latching of new TDC timestamp data each time the TDC New Hit signal is active. The circuit also generates an active low TDC Reset signal to maintain system integrity.

The generation of the TDC New Hit signal in the chip occurs through two ways:

1. When the Energy Flag signal is set to indicate energy information (Energy Flag = 1), such as a Time-over-Threshold (ToT) timestamp following a time of arrival timestamp, and the chip's receive-all mode (`RECV ALL`) is configured to 0. This mode specifically looks for timestamps associated with energy information.
2. When the chip's receive-all mode (`RECV ALL`) is set to 1, it processes every new TDC timestamp, regardless of energy information availability. This mode ensures no timestamps are missed.

8.1.3.2 *Arbiter*

After processing in the event generator module, the hit event data in the MuTRiG system is forwarded to the arbiter module. The arbiter's function is necessary due to a limitation where only one hit event data can be sent to the first-level FIFO (L1 FIFO) per clock cycle. It decides which channel's hit event data gets prioritized for writing to the FIFO in the next clock cycle. Any hit event data not selected remains in the channel's event generator until it can be accommodated in the L1 FIFO. This arrangement ensures ordered and efficient data taking, facilitating smooth data flow to the FIFO.

8.1.3.3 *FIFO*

The MuTRiG chip uses a FIFO system to buffer hit event data, reducing individual channel deadtime. It features four Level 1 (L1) FIFOs, each associated with eight channels. These L1 FIFOs efficiently collect and temporarily store hit event data. The Level 2 (L2) FIFO consolidates data from all L1 FIFOs, transmitting it to the chip's frame generator and serializer modules. The L2 FIFO plays a role in facilitating the smooth transmission of processed data off the chip, ensuring efficient communication within the system.

8.1.3.4 *Frame Generator*

Table 8.3: Format of the data frame of the latest MuTRiGv3 chip.

Field	**Header**				**Payload**	**Trailer**		**Idel**
	Header ID	Frame ID	Frame Flag	Frame Length	Hit Events	CRC	Trailer ID	Filler
Data	K28.0	Frame Counter Value	Flag Bits	Event Counter	Event Data	CRC check value	K28.4	K28.5
Length [bit]	8	16	6	10	$0-12240$ or $0-7144$	16	8	

The MuTRiG chip transmits hit event data to the Data Acquisition (DAQ) system via a serial data link, employing a specialized communication protocol. The frame generator module formats the event data into bitstrings, adhering to the established protocol. Additionally, it prepares 8-bit bytes for the 8b/10b encoding. This encoding facilitates clock recovery at the receiver side, ensuring data integrity and synchronization. The 10-bit encoded data is then forwarded to the downstream serializer module for transmission.

To enhance the output event rate for the `Mu3e` fibre detector, while maintaining the same speed of the serial data link, the length of the hit event data can be reduced. This reduction is achieved by omitting the energy time stamp information when the frame generator module assembles the hit event data into frames. Such a measure decreases the size of a single event from 48 bits to 27 bits, thereby allowing for a higher data transmission rate (Table 8.5).

The Frame generator is composed of several blocks but the main one is the Finite State Machine (FSM) It recieves several inputs:

- COMMA: the controle signal or symbols for the 8b/10b encoding module. This is used to indicate the start or the end of a frame and also to synchronize the data link.
- Frame Counter: is a 16 bit running counter for each frame. With the help of the frame ID, this is used for merging data from different sub-detectors in the DAQ system.
- Frame Flag: Flag bits used to indicate in what configuration and in what running state the chips are.
- Frame Lenght: indicates the number of events in the current frame.
- Event data: the events data coming from 48 bit PRBS data patterns for testing (explained later) or the hit event data (short or long) stored in L2 FIFO.
- CRC: a 16 bit Cyclic Redundancy Check (CRC) value computed for the various frame components such as frame counter, frame flags, frame length, and event data to detect transmission errors. This CRC value serves as a tool for ensuring data integrity during transmission.

Table 8.3 shows the structure of the data frame used in the MuTRiG chip, which is divided into four key components: the header, the payload, the trailer, and idle words. The header contains several key elements as explained above in the input of the FSM.

Table 8.4: Definition of the frame flags.

Bit Field	***Definition***
[5]	Generate Idle Signals
[4]	Short Hit Event Lenght
[3]	PRBS Debug mode
[2]	Sending 1 PRBS Pattern Per Farme
[1]	L2 FIFO Full
[0]	PLL loss of lock

A more detailed description of the frame flags is given in Table 8.4. The payload section is filled based on the configuration settings. It can contain either PRBS debugging sequences or all hit event data from the L2 FIFO at the start of the frame. The payload length varies depending on the L2 FIFO's hit event count. In cases where there are no hit events to transmit, this section is omitted. The lenght of the payload varies depending if short mode or long mode is used.

Following the payload is the trailer section, with CRC value and a trailer ID. The CRC value is calculated for the bits from the frame counter to the end of the payload,

ensuring data integrity. The trailer ID, a k28.4 control symbol, signifies the end of a frame. Between frames, the idle period is filled with a k28.5 control symbol, aiding in clock recovery at the receiver's end.

Table 8.5: Definition of the hit event data

Long Mode		**Short Mode**	
Bit Field	***Definition***	***Bit Field***	***Definition***
[47 : 43]	Channel number	[27 : 23]	Channel number
[42]	T-BadHit	[22]	BadHit
[41 : 27]	T-Coarse Counter	[21 : 7]	Coarse Counter
[26 : 22]	T-Fine Counter	[6 : 2]	Fine Counter
[21]	E-BadHit	[1]	Energy Flag
[20 : 6]	E-Coarse Counter	[0]	0
[5 : 1]	E-Fine Counter		
[0]	E-Flag		

Left side of Table 8.5 describes long event mode configuration, where each hit event data consists of the channel number and two time stamps (one for time of arrival and the other for ToT). This configuration leads to hit event data being 48 bits (6 bytes) long, with the frame generator organizing the data byte-by-byte for encoding, starting with the highest bits first.

In contrast, the short event configuration detailed on the right side of Table 8.5 reduces hit event data to 27 bits, focusing only on the time stamp for time of arrival. Instead of detailed energy information, a single Energy Flag bit is used to indicate an energy events which are signals that pass the energy threhold. The frame generator assembles the data by placing the highest byte first.

Another mode can be enabled to monitor the event rate of each channel. This counter, a 12-bit binary unit for each channel, increments with every new event. Their values are buffered and then transmitted upon each read operation, at which point the counters are also reset.

8.1.4 *Serial Data Link*

The MuTRiG chip uses an 8b/10b encoding scheme for data transmission through a Low-Voltage Differential Signaling (LVDS) serial link. Key components include a double data rate (DDR) serializer and a custom LVDS transmitter, designed to handle high-speed data transfer necessary for high-input event rates.

The LVDS transmitter is equipped with a driver strong enough to handle the chip's load and a pre-driver that converts input signals for the LVDS driver. This system is capable of transmitting a 625 MHz clock signal, with adjustable driving strength through an additional current controled by a DAC values.

8.1.5 *Chip configuration and reset*

The MuTRiG chip communicates via a Serial Peripheral Interface (SPI). SPI operates in a master-slave setup, with the master typically being a control system (e.g., Mu3e's Front-End Board) and the slave being one or multiple MuTRiG chips. Chip selection is managed by the SPI_CSn signal. Inside the chip, the SPI slave module consists of shift registers, designed for serial bit-by-bit data transmission. Communication occurs through SPI_MOSI (Master Output Slave Input), SPI_MISO (Master Input Slave Output), and SPI_SCLK (Serial Clock) signals.

Configuration data for the MuTRiG chip is transmitted via its SPI interface. This transmission is handled by the SPI via the Front-End Board (FEB), which sends a specific configuration bit pattern to the MuTRiG. The process is controlled by the state of the SPI_CSn line. When this line is active (set to low), data begins to shift through a register. This shifting is driven by the SPI clock, SPI_SCLK. The length of this register can vary depending on the version of the MuTRiG chip being configured. Importantly, the internal settings of the MuTRiG chip are only modified when the SPI_CSn line is turned off. The data transfer to the chip starts at the SPI_MOSI line, which is connected to the beginning of a shift register, and ends at the SPI_MISO line, attached to the end of the register chain. This arrangement ensures that the configuration data is fully processed and implemented in the MuTRiG chip once the SPI_CSn line is deactivated.

The MuTRiG chip features two reset inputs: a channel reset input for synchronizing timing measurements across chips by targeting the TDC's TimeBase unit coarse counters, and a chip reset input that resets these counters and reinitializes all finite state machines in the digital part of the chip. These resets, controlled by the SPI interface, combine to form the `ASIC Reset`.

Configuring and resetting the chips are carried out through the Front-End Board (FEB). At the heart of the FEB is an Arria V FPGA, a programmable logic device, which will be elaborated in the next section. Nested within this FPGA is a NIOS processor, which is a soft microprocessor. The MuTRiG chips can be configured in two ways. Firstly, they can be directly configured via the NIOS processor embedded in the FPGA. The configurations bit pattern are then already localy stored. The second way and the way it is intended in `Mu3e`, using a graphical user interface known as the MIDAS custom page, which will also be detailed later. This interface facilitates the `Mu3e` framework in creating the required configuration bit pattern. This pattern is then transferred to the FPGA on the FEB through a Remote Procedure Call (RPC) command. This command enables the loading of the configuration bit pattern into the NIOS soft microprocessor. Following this, the NIOS processor proceeds to relay the configuration bit pattern to the MuTRiG chip using the SPI interface, thereby completing the configuration process.

8.1.6 *Pinout*

Figure 8.8 shows the pad positions of the MuTRiGv3 ASIC. The bonding pad layout is the same for MuTRiGv2 ASIC. The chip dimension is 5×5 mm. There are 3 power

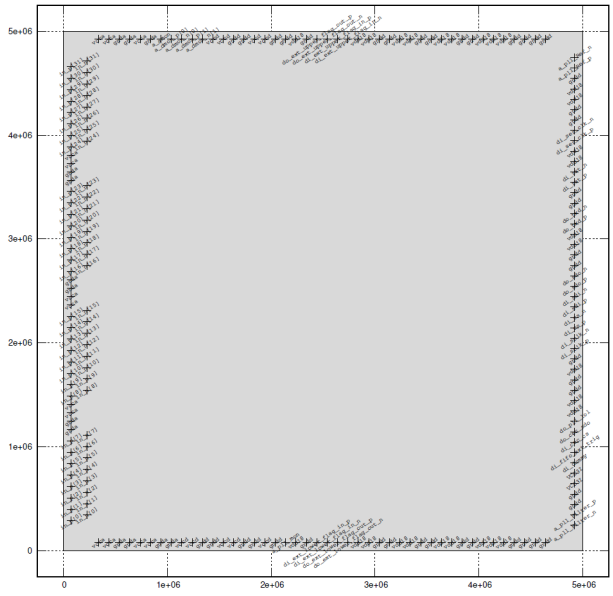

Figure 8.8: Pinout of the MuTRiGv3 ASIC with the pad positions. Units are in mm/10^6. The size is 5×5 mm.

domains for the MuTRiGv3 ASIC: an analog 1.8 V, a digital 1.8 V and a digital 3.3 V. The folowing Table 8.6 descibes the pinout of the MuTRiGv3 ASIC and what is wirebonded or left floating on the Scifi Module Board 3.1.

8.1.7 *Coincidence hit logic*

The MuTRiGv3 (as well as version 2) includes a configurable hit validation scheme, enabling basic coincidence logic. This scheme determines whether a hit or set of hits should be forwarded for further processing or discarded. The ASICs do not perform on-chip clustering of hits; hits are not combined within the ASIC itself. Hits undergo a brief holding period, typically 1-2 clock cycles, within an internal buffer. During this time, the chip evaluates hit validity based on predefined criteria. The validation process considers hits in neighboring channels within a configurable time window. If a hit occurs in any of these neighboring channels within the specified time frame, the hit under evaluation is valid. The range of neighboring channels considered for hit validation is customizable via DAC values, allowing users to define which channels are treated as neighbors. The validation signal used to determine hit validity is generated by performing a logical OR operation on the hit flags of the neighboring channels. This ensures that a hit is validated if any neighboring channel registers a hit within the designated time window. A crossbar featuring pairs of LVDS transceivers is used for the transmission of the validation signal to neighboring ASICs. This crossbar acts as a virtual channel adjacent to channels 0 and 31, enabling communication of validation information between neighboring chips. The matrix of valid neighboring channels can be programmed arbitrarily, extending up to the next-to-next-neighbor channels.

Table 8.6: Pinout of the MuTRiGv3 ASIC. Differential pairs have a positive and a negative pad marked respectively by *_p* and *_n*, for clarity, they are notated *_p/n* in the same line.

Pad name	***Direction***	***Domain/Level***	***Description***
$VCCA18$	Power	Analog	Analog 1.8 V supply voltage for the analog front-end.
$VCCD18$	Power	Digital	Digital 1.8 V supply voltage for TDC/PLL and digital parts.
$VCCD33$	Power	Digital	Digital 3.3 V supply voltage for single-ended digital I/O pads.
$GNDD$	Power	Digital	Digital ground.
$GNDA$	Power	Analog	Analog ground.
$a\_SiPM\_in\_p/n[31:0]$	Input	VCCA18	The 32 SiPM input terminals. Only the positive sides are bonded for SciFi, and the negatives are left floating.
$a\_pll\_Ref\_p/n$	Input	LVDS	The 625 MHz PLL reference clock.
$a\_pll\_Filter\_p/n$	Passive	VCCD18	PLL filter components.
$a\_pll\_mon\_p/n$	Output	VCCD18	PLL monitoring output.
di_rst_p/n	Input	LVDS	ASIC reset signal.
$di\_fifo\_ext\_trig$	Input	LVCMOS	L1 validation trigger input, not bonded.
$di\_ser\_clk\_p/n$	Input	LVDS	The 625 MHz digital system clock.
do_TxD_p/n	Output	LVDS	LVDS data link output.
a_amon	Output	VCCA18	Analog front-end monitoring, left floating.
$a\_dmon\_p/n[0]$	Bidirectional	LVDS	Time and charge monitor output and charge injection to TDC.
$a\_dmon\_p/n[1]$	Bidirectional	LVDS	Energy and flag digital monitor output and flag injection to TDC, left floating.
di_sdi_p/n	Tristate	LVDS	MOSI line of the SPI interface.
di_sdo_p/n	Input	LVDS	MISO line of the SPI interface.
di_sclk_p/n	Input	LVDS	20 MHz clock line of the SPI interface.
di_cs_p/n	Input	LVDS	Chip select line of the SPI interface, active low.
di_dummy	Input	LVCMOS	Debug line, not used.
di_cec_cs	Input	LVCMOS	Old check event counter chip select, not used (data streamed now).
di_cec_sdo	Output	LVCMOS	Old check event counter line, not used (data streamed now).
do_pll_lol	Output	LVCMOS	PLL loss of lock debug pad, left floating.
$di\_ext\_lower\_flag\_in$	Input	LVDS	Input flags used for the coincidence logic of the chip
$do\_ext\_lower\_flag\_out$	Output	LVDS	Ouput flags used for the coincidence logic of the chip

Figure 8.9: The SciFi Module Board (SMB3.1) with bonded MuTRiGv3 chips covered with globtop.

8.2 SCIFI MODULE BOARD

A deticated board has been designed hosting 4 MuTRiG ASICs which serves for the readout of the SciFi detector. This board is called the SciFi module board (SMB) and has been design from the ground up at the University of Geneva[1]. Several versions of the board have been produced and tested. The first boards which were tested, are shown in Figure 8.10. The first board was designed to host 4 MuTRiGv1 chips with connectors to connect a SiPM array. The second board, SMB2 was integrating the SiPM array via a flex print attached to the board. This was a step closer to the final design in terms of compactness. This thesis details the development process starting from the next versions of the board.

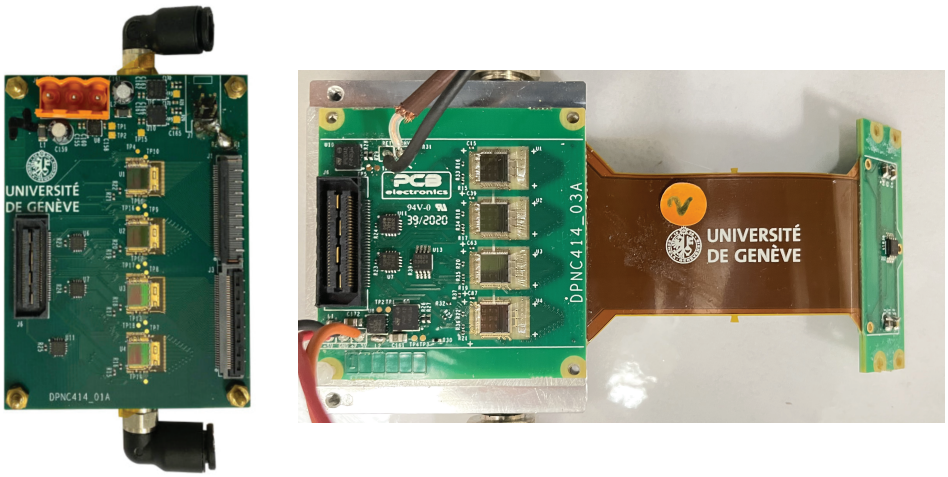

Figure 8.10: The first two SciFi Module Boards. Left) The first SMB with 4 MuTRiGv1. Right) The SMB2 with 4 MuTRiGv2. First SMB with an integrated SiPM array on the back.

1 Designed by Daniel La Marra, electronic engeneer at the University of Geneva

A board version 3.0 was developped and tested without some final mechanical dimensions such as the flex print lenght and holes positions. These exclusions did not impact the board's electronic functionality. The latest version is called the SMB version 3.1 (SMB3.1) and, at this day, is the final version for the Mu3e experiment. The board is shown in Figure 8.9 The SMB3.1 is designed to accommodate 4 MuTRiG chips and is built as an 8-layer PCB.

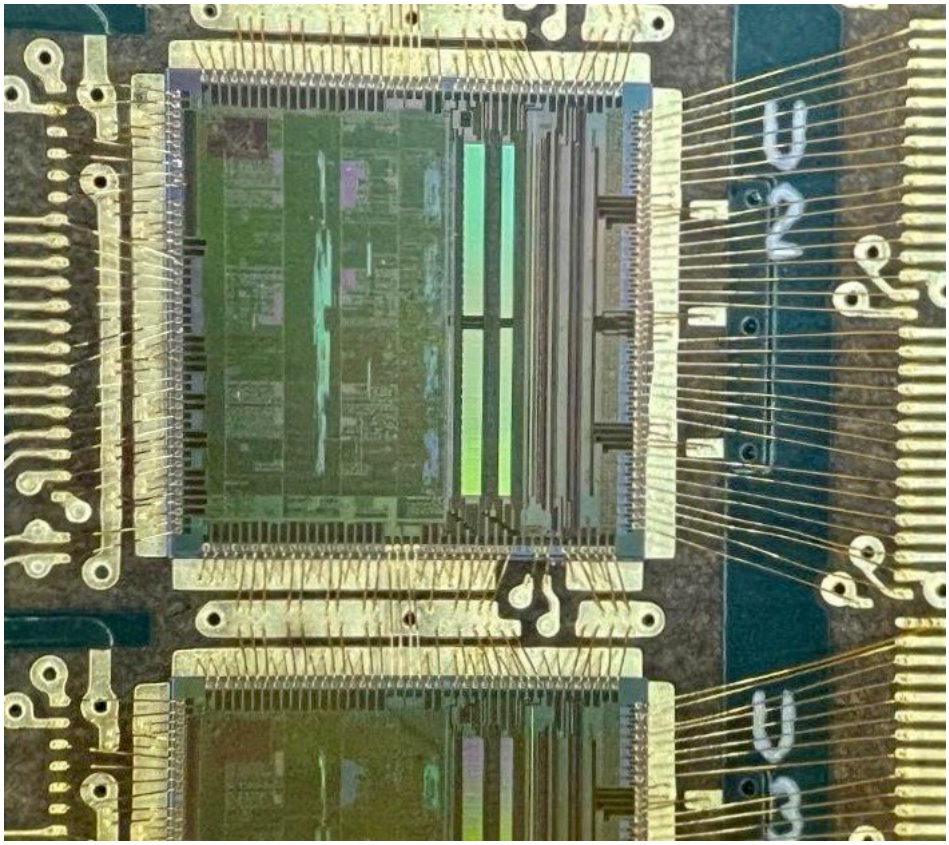

Figure 8.11: Photo of the wirebonded MuTRiGv3 ASICs, where the gold ball wire bonding technique is used and before the globtop is applied.

The design incorporates a flexprint, which terminates in a PCB for mounting the SiPM array. The end of the PCB, which has the multi-channel SiPM array mounted, is designed to be coupled directly to the surface of one side of a SciFi ribbon. As it has 4 MuTRiG chips, it can readout the 128 channels of the SiPM (S13552-HRQ) used in the SciFi detector. A primary requirement for the board was to minimize its size, particularly in width, due to space limitations. The board measures 120.9 mm in lenght and 26 mm in width. A significant achievement of this board design is the arrangement of 4 ASICs within a mere 1.2 mm of each other, giving the board it's compact design. Additionally, the precise bonding of the ASICs within this compact design stands as an achievement in its own right[2]. The four MuTRiG are bonded with a gold wire bonding

2 Thanks to Gabriel Pelleriti, electronic technician at the University of Geneva, for his role in the successful initial bonding trials on the first boards.

technique, see Figure 8.13. This method involves the use of fine gold wire and ball bonding to establish connections between the chip pads (minimum 80 µm apart in pitch) and the board pads. The four ASICs and their bonds are covered by a protective globtop known as Loctite Eccobond FP4323.

A schematic of the board is shown in Figure 8.12 where not all passif components are shown for clarity. The active components of the SMB3.1 board are the following :

- One SiPM array of 128 channels
- Four MuTRiG ASICs version 3. Note that the MuTRiG version 2 ASICs can also be used since the pinout is the same.
- Two Low-Dropout Regulator (LDO) to deliver each 1.8 V to the digital and analog part of the MuTRiG chips.
- One LDO regulator for delivering 3.3 V to some Input/Output (IO) ports on the ASIC and to power 2 temperature sensors. The IOs can be used for some monitoring or debugging purposes.
- One Single Dual 1 : 4 low skew, low additive jitter LVDS fanout buffer for the 625 MHz clock distribution and the reset to the MuTRiG chips. Named as the clock buffer.
- Two temperature sensors located on the back of the SIPM array and one on the board.

8.2.1 *Powering*

Low voltages are supplied to the SMB3.1 to power the MuTRiG chips and the temperature sensors. These voltages are delivered through three cables soldered to the board, as seen in Figure 8.9 and on the schematic in Figure 8.12. This includes one common ground cable and two separate cables for suplying the 3 LDO's, giving a regulated voltage of 1.8 V and 3.3 V. One LDO provides 1.8 V for the analog part of the ASICs (VCC18a), another supplies 1.8 V for the digital part of the ASICs (VCC18d) and a final LDO delivers 3.3 V for the single-ended digital I/O pads of the ASICs and the temperature sensors (VCC33d). The typical input voltage for the LDOs are 2.5 V and 3.5 V for the 1.8 V and 3.3 V LDOs respectively. Given that the 2.5 V supply powers both LDOs for VCC18a and VCC18d, it draws a higher current compared to the 3.5 V supply. In the configured states of the four MuTRiGv3 ASICs, VCC18a and VCC18d together have a maximum consumption of $\sim$ 3.4 A, while VCC33d has a current draw of $\sim$ 1 mA. Furtermore, a U.FL. HIROSE type of connector provides the bias voltage (HV) for the SiPM array. Before providing a bias voltage to the SiPM array, the MuTRiGv3 ASICs must be properly configured (discussed in the next sections).

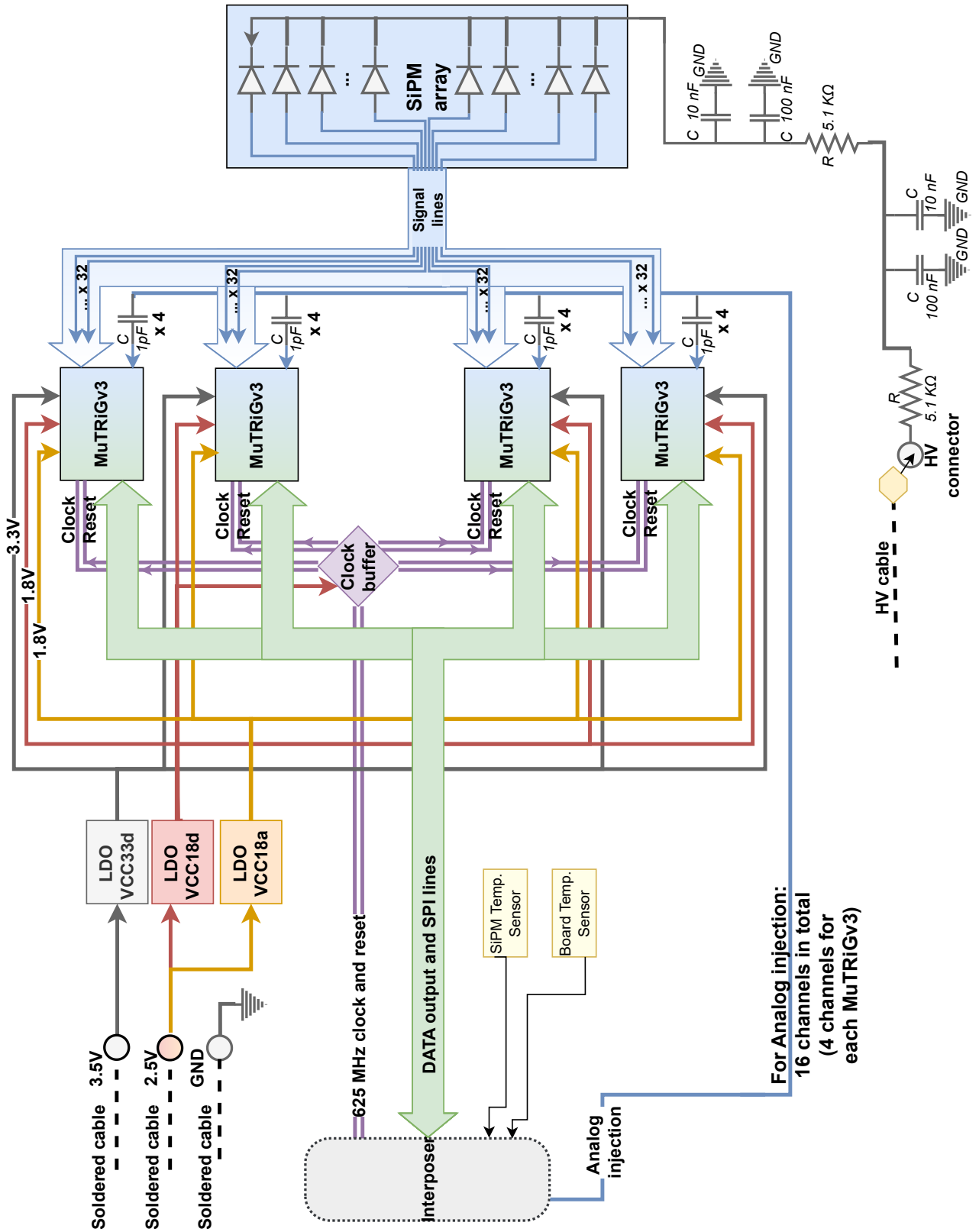

Figure 8.12: Simplified schematic of the SMB3.1 with the active components. For clarity, not all passif components are shown. Arrows indicate the inputs and outputs and colors are used to disinguish the power, the clock distribution and the digital and analog part of the MuTRiGv3 ASICs.

8.2.2 *Clock and reset distribution*

The clock and reset signals are distributed to the MuTRiG chips using a single dual 1 : 4 low skew, low additive jitter LVDS fanout buffer. It recieves two pair of differential lines (LVDS), *di_rst_n/p* and *di_ser_clk_n/p*, and distributes them to the 4 MuTRiG chips. The clock buffer is powered by the LDO which provides 1.8 V to the digital part of the MuTRiGs (VCC18d). The 625 MHz clock signal for SMB 3.1 is delivered through an interposer.

8.2.3 *Data and communication*

A interposer acts as the principal connector for upstream data transmission and electronic communication. The interposer has 7×12 pins which allow for 42 pairs of differential lines in total. For the SMB 3.1, it interfaces 17 differential pairs lines except the temperature sensor lines which are single-ended. Precise positioning of the interposer on the board is essential, and it must be fixed using the correct torque. This is because the interposer has spring loaded pins on both sides, which are used to connect the board to the additional connection PCBs. The `Mu3e` experiment will be using so called micro-twisted pair cables for transfering data between the SMBs and the upstream electronics. These cables are designed to be used in high speed data transmission applications, and are 127 µm diameter twisted pair cables with polyimide coating [24].

The signals from the SiPM array are relayed to the 4 MuTRiG chips, each equipped with 32 channels. After processing of the MuTRiG ASICs, the generated timestamps, as detailed in Section 8.1, are transmitted to the upstream electronics through the interposer. Also the SPI communication is done through the interposer.

Additionally, an analog injection is possible on the board which is performed using 16 capacitors of 1 pF arranged in parallel. These are connected to four channels on each MuTRiG ASIC, with the injection facilitated through the interposer. Space constraints on the board restrict the total number of injection channels to no more than 16. This can be used to replace the SiPM array signals with a known signal for tests of the MuTRiG ASICs, as detailed in the next section.

8.3 SCIFI RELATED ELECTRONICS

Other boards are used in the DAQ chain of Mu3e as well as for small-scale DAQ setups.

8.3.1 *Detector adaptor board*

The Detector Adaptor Board (DAB) is a board designed to interface the SMB3.1 boards with the Front-End Board (FEB) of the Mu3e experiment. They are placed inside the magnet connected to the FEBs via a backplane. On the current DAB, 2 LVDS buffer are located on the board for the incoming and outgoing signals to mitigate potential signal losses. Those buffers are able to equilize and pre-emphasize signals. The outgoing lines (from the FEB to the SMB) which are the clock, reset, charge injection, and TDC injection, pass through one buffer. The incoming lines (from the SMB to the FEB) which are the data lines, pass through the other LVDS buffer. Two connectors are located on the DAB to allow for the connection of two SMBs to each bank of the FEB. Each of these banks has enough bandwidth and electrical connections to allow the operation of one SMB.

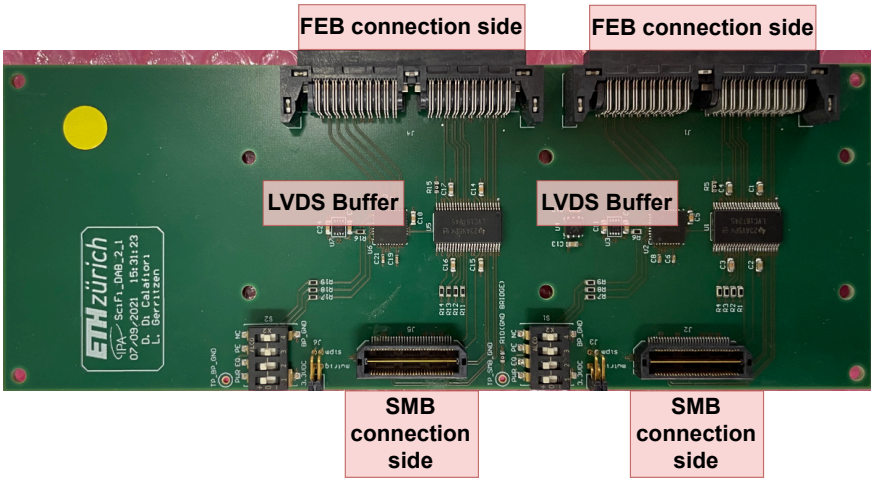

Figure 8.13: Photo of the DAB.

8.3.2 *Connector Boards*

Additional small boards facilitate the connection between the micro-twisted pair cables, the SMBs, and the DAB. On one end, the SMB-μTP connector board links the SMB interposer to the micro-twisted pair cables. On the opposite end, the DAB-μTP connector is employed to link the Samtec connector of the DAB with the micro-twisted pair cables. Each connector board will have the micro-twisted pair cables soldered.

8.3.3 *Adaptor board*

For labs with smale-scale DAQ setups, a separate small board can be used. The board connects the SMBs to the DABs and acts as an adaptor between the interposer and a samtec connection. The board mounts on the interposer of the SMB and features a Samtec QTH type of connector on the other side. This way, no micro-twisted pair cable is needed, and a Samtec cable can be used. Also two pins are available on this board which can be used to inject a signal via the analog injection circuit on the SMB 3.1.

8.4 THE MU3E DAQ SYSTEM

The Mu3e experiment uses a custom designed DAQ system and from the SMB3.1 boards, a full chain of electronics is used to readout the data. Each SciFi super-module (section 7) of the SciFi detector is composed of 4 SMB3.1, two on each side of the SciFi ribbon.

8.4.1 *General overview*

Mu3e is a triggerless experiment, meaning that it records all events in the detector. This approach necessitates a robust and efficient handling of vast amounts of data, a challenge that the DAQ system meets. The DAQ needs to decide online which events should be saved to disk.

This system's hardware architecture is unified across the SciFi, SciTile, and Mupix subdetectors, using the same MuTRiG ASIC for SiPM pulse digitization in SciFi and SciTile detector. It also employs common Readout FPGA boards across subdetectors for streamlined development and integration.

Data flow in this DAQ system (see Figure 8.14), involves layer structure. The first layer comprises 112 custom-designed frontend boards (FEBs) equipped with Arria V FPGAs, which directly interface with the Mupix chips or readout ASICs of the timing detectors, such as the SciFi detector. These FEBs are linked through high-speed optical fibers, capable of supporting data rates up to 6.25 Gbit/s, enabling efficient data transfer to the next layer of the system, which includes external switching boards. These switching boards, equipped with Arria 10 FPGAs are strategically divided to manage data from different sections of the detector. At the heart of the data transmission process are a series of PCs, the first of which connects to each switching board through optical fibers. Subsequent PCs in the chain with GPUs, maintain high-bandwidth connections, ensuring seamless data flow. The scale of data transfer is monumental, with phase I of the experiment expecting data rates of 80 Gbit/s.

8.4.2 *Data flow*

In the Mu3e experiment, a complex and well-orchestrated data acquisition and processing system is employed, featuring several key stages:

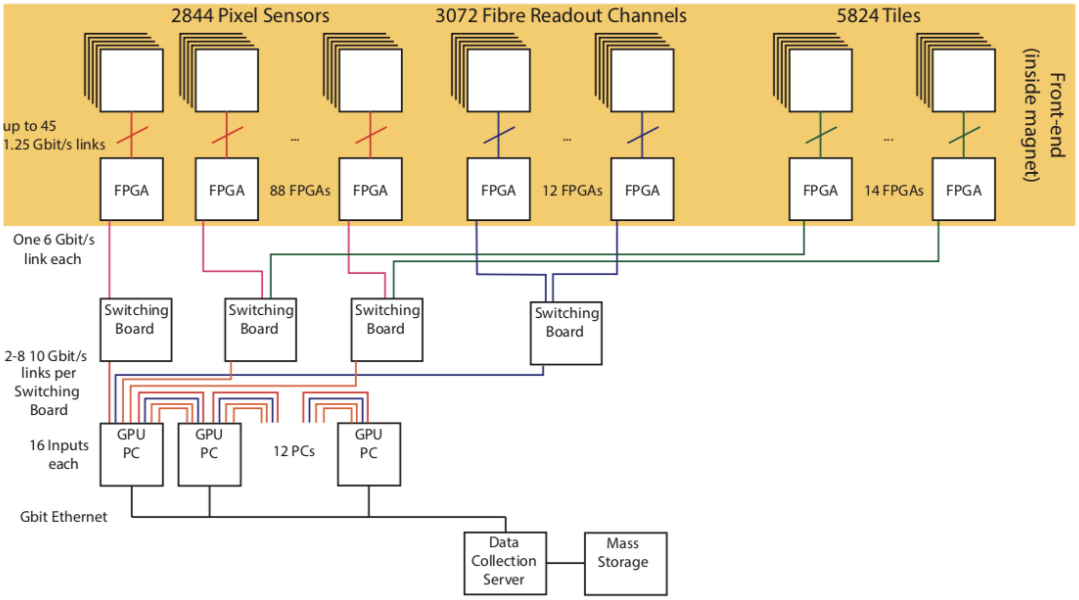

Figure 8.14: Overview of the DAQ system, from [24].

- **Initial Data Handling**: The journey of data begins with the primary detectors. For SciFi, the MuTRiG ASICs which are located on the SMB boards are responsible for acquiring data coming from the SiPM arrays. The detectors then send their data to Detector Adapter Boards (DABs), which are tailored to each specific subdetector. From the DABs, the data is then routed to generic Front-End Boards (FEBs) situated within the `Mu3e` solenoid. An FPGA on each FEB serves as the crucial interface, linking the internal system of the magnet to the external readout system through optical data links.

- **Data integration and monitoring**: A significant aspect of the data flow is the integration of hit data with monitoring data. The monitoring data originate from the detectors and the FEBs themselves, providing a comprehensive overview of the system's status. A big amount of data links converge onto each of the four Switching Boards (SWBs) located in the control room. Here, a critical process of merging and time-aligning the various data streams takes place, and the monitoring data is selectively filtered out.

- **Data Processing and Reconstruction**: The SWBs are also responsible for merging data from the upstream and downstream parts of the SciFi detector. They detect coincidences between these sections, which are then used to guide further data processing. All processed data streams are directed to a central PC in the filter farm, where data from the entire detector is analyzed in overlapping time frames. The initial stage of reconstruction involves track creation from pixel hits, executed on a GPU. If interesting events are detected, a more detailed reconstruction is

conducted using a CPU. Only the frames that pass certain selection criteria are preserved for storage.

- **Control and Configuration**: Parallel to data processing, the system also manages the flow of control and configuration commands. These commands are sent from the SWBs to the FEBs and detectors via an optical uplink. Additionally, synchronized clock and reset signals are injected into the FPGA's of the FEBs. The system is designed with flexibility, allowing for individual addressing and configuration of each MuTRiG and MuPix chips.

8.4.3 *DAQ Hardware*

8.4.3.1 *Front-end board*

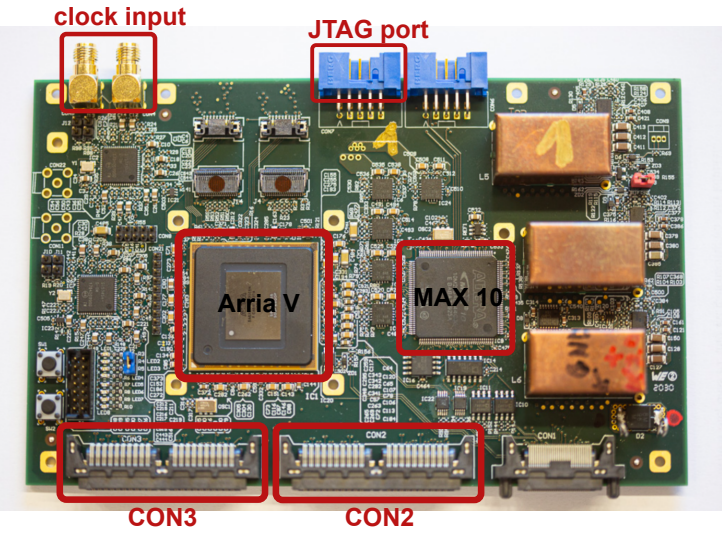

Figure 8.15: Photo of one FEB, from [24].

At the heart of the DAQ system are 114 frontend boards (FEBs), where 12 are for the SCiFi detector. Per FEB, two connections to subdetector are possible, for example two SMB (passing the DAB) for SciFi can be connected via the CON3 and CON2 connectors, see Figure 8.15. These FEBs are designed to fit the spatial limitations and fulfill the functional requirements. They are exclusively connected to either MuPix or MuTRiG chips, ensuring dedicated and efficient data handling.

Each FEB has an Arria V FPGA, serving as the core for data processing. This FPGA handles the incoming data from the detectors, received via 1.25 Gbit/s links per MuTRiG ASIC or MuPix chip. A notable aspect of the data taken by the detectors is their initial lack of temporal sorting. For instance, the MuPix system reads detected hits row by row in its pixel matrix, with the timestamps not directly correlating to the actual sequence of events. This challenge is addressed by a hit sorter implemented in

the FPGA firmware, which rearranges the incoming hits into their correct chronological order.

The FPGA can be programmed either through a debug interface or via a MAX 10 FPGA that reads from onboard flash memory. This programmability, especially the ability to remotely write to the flash memory, ensures that firmware updates are feasible even when physical access to the FEBs is restricted (without the need to connect the FEB via the JTAG port to a computer).

Beyond data readout, these FEBs are used for distributing the clock signals to the various parts of the detector. This function is essential to ensure that all components of the detector system operate synchronously, maintaining the precise timing necessary for accurate data acquisition and analysis. Alongside the clock distribution, the front-end boards also transmit slow control information to the SWB. In `Mu3e` the term "slow control" means even a broader range then just the monitoring data. It includes also the configuration data used to configure the MuTRiG chips for example, as well as the MuPix chips.

Furthermore, the FEBs are linked to an optical transceiver, which connects one FEB with four SWB, running at 6.25 Gbit/s. This transceiver used for linking the FEBs to the Switching Boards (SWBs) via optical fiber cables, ensuring a high-speed and reliable data transfer.

8.4.3.2 *Switching board*

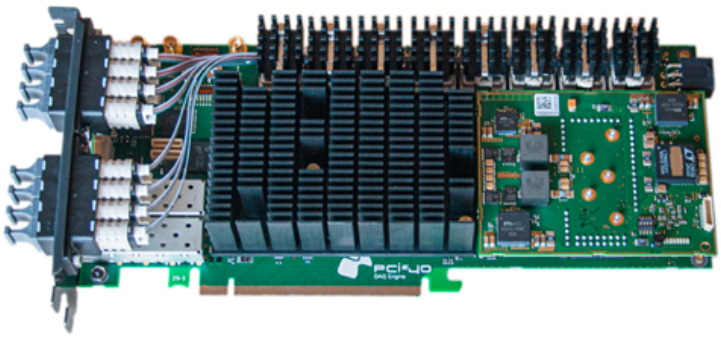

Figure 8.16: Photo of the PCIe40 developed by the LHCb collaboration and employed as switching board in `Mu3e`. A heatsink is placed above the Arria10 FPGA. Picture from [24].

The next layer of the DAQ system is composed of four switching boards (SWB). These boards are located in a PC outside the magnet and maintain a connection to the first layer of the system via optical fibers. The planned switching boards are PCIe40

board, developed by the LHCb collaboration. In the context of the SciFi detector, a single SWB is tasked with managing all 12 FEBs. This is accomplished using two optical links, each with a capacity of 6.25 Gbit/s. Comprising both an uplink and a downlink, these links enable efficient two-way communication between the SWB and the FEBs.

The PCIe40 board is equipped with an Arria10 FPGA, a PCI express interface, and 8 Avago Minipods. The Avago Minipods are high-speed optical transceivers, capable of handling data transmission rates of 6.25 Gbit/s. The primary role of these SWBs is to align and merge the multiple data streams from the connected FEBs into a singular, cohesive data stream. Notably, this layer marks the first instance where data from the upstream and downstream sections, such as in the SciFi detector, are merged. Additionally, the transmission of slow control packets and configurations to the FEBs is conducted via the PCIe interface, facilitating direct and effective communication with the boards.

8.4.3.3 *Filter farm*

Figure 8.17: Photo of the DE5a NET board built by Terasic Inc. and used as a receiving board in the filter farm PCs. Picture from [24].

The filter farm PCs are equipped with commercial Terrasic DE5a NET receiver boards with onboard an Intel Aria 10 FPGA, four QSFP optical transceivers and two banks of DDR4 memory. These receiver boards are also used in all the small-scale DAQ setups at the different institutions where they take on the role of the SWB. Additionally, the latest GPUs will also be included into the filter farm PCs.

The FPGA is responsible for executing the event-building and buffering operations, as well as the selection algorithms. The event data is then sent using Direct Memory Access (DMA) over PCIe to the main memory of the filter farm PC. The data is then subsequently copied to the memory of a GPU, where the fitting and vertex selection algorithms are run. The GPU then transmits the IDs of the selected events to the main

memory of the PC. This triggers the transmission of the corresponsing data from the buffer memory of the FPGA, through the PC main memory and Ethernet, to the central DAQ computer that operated the MIDAS software (explained later). At that computer, the data streams from the farm PCs are merged into a single data stream, along with various slow control data that is compressed and stored. More detail about the filter farm can be found in [70, 71].

8.4.4 *DAQ Software*

The `Mu3e` DAQ software framework is based on the Maximum Integrated Data Acquisition System (MIDAS) [72]. MIDAS combines tools such as run control, event building, slow control, and online monitoring. It is a data acquisition system for major experiments at PSI, T2K and CERN. The experiment operates in defined run states and transitions between them. MIDAS facilitates control over these states, enabling the system to switch from one state to another. For instance, MIDAS permits transitioning from an idle state into a running state, during which data recording occurs. In a streaming system like `Mu3e` with no trigger, the transitions to different states need to be synchronized with all subsystems. This synchronization ensures that when data from all subsystems are combined, they align and agree.

A web interface allows for control and monitoring of the experiment via Internet. Also, an Online DataBase (ODB) is utilized to store settings, chip configurations, and the general state of the experiment. MIDAS can run on a network of machines. On remote machines, programs can run and can register Remote Procedure Calls (RPC) functions, which allow for changing ODB entries. The RPC functions are used to change the configuration of the MuTRiG chips, for example. Data can also be send from remote users to the ODB via MIDAS front-ends. They allow to have acces to the ODB while running locally. The web interface allows to access the ODB and history plots. It also provides a web front-end to most of the MIDAS features. Additionally, a graphical interface can be integrated into the MIDAS web interface (custom web pages). MIDAS supports the use of JavaScript and HTML for the development of web pages, enabling users to create tailored interfaces for their experiments.

In addition to processing data at a rate of 1.25 Gbit/s per link, the DAQ system is also tasked with managing slow control data. Slow control data means parameters that change slowly and can be sampled at a lower frequency compared to the main data stream. Examples of such parameters include monitoring the temperature of the SiPMs. The system also handles detector configuration settings. These configurations are transmitted to the MuTRiG chips via an SPI interface at a slower rate of 128 kbit/s, which is significantly lower than the primary data throughput. The slow control system is integrated into MIDAS. Configuration settings must be sent to the MuTRiG chips. They are stored in the ODB and are then sent to the DAQ. The DAQ sends then commands to the FEBs to configure the MuTRiG chips. More specifically, the FEB sends a configuration bit pattern that is generated via the configurations settings stored in

the ODB. Each of different configuration settings sends out a specific bit pattern to the MuTRiG chips.

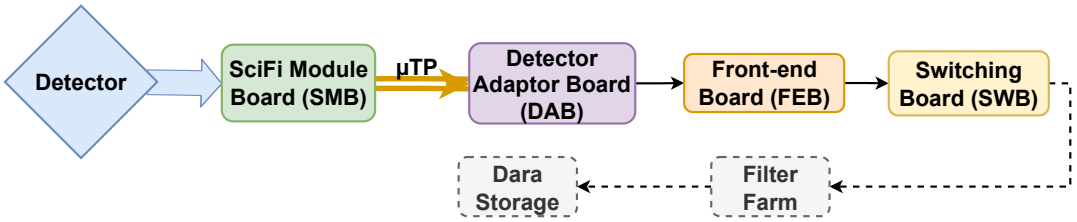

Figure 8.18: SciFi DAQ with all the main parts of the chain with the data output flow. Simplified version of 8.14 highligting SciFi related electronics.

Figure 8.18 illustrates the hardware parts of the SciFi electronic chain within the Mu3e DAQ system. Before discussing calibration and data collection, it is essential to first ensure the functionality of the SMBs.

8.5 SMB VERIFICATION PROCEDURE

After producing a SMB, several tests are conducted to ensure its functionality. The tests are conducted in a specific order, but can be developed further. This is only a basic procedure that is used with the first SMB3.0 and SMB3.1 at the University of Geneva.

8.5.1 *Power up*

A first test is to power up and check the power consumption of the board. This is done by measuring the current drawn by the board on the two low voltages (LV) lines. As first step, the power up can be done seperalty for the two input voltages. Each line is then checked for the correct voltage, gradually increasing the voltage to the typical nominal values of 2.5 V and 3.5 V. A good practice to progressively set the current limits to prevent any potential damage to the board. Also with a multimeter, one can check that the voltage outputs of the regulators are stable and has the right value. This can be done with the dedicated test points. In the small-scale DAQ setups, if the regulated outputs are already reached before the typical input values, they may be adjusted slightly lower to minimize the heat dissipation of the regulators. In the Mu3e experiment any voltage drop, if present, needs to be known.

8.5.2 *Communication with the MuTRiG chips*

The next step involves verifying the communication with the SMB through the SPI interface, which requires an operational DAQ system. For SciFi, MIDAS custom pages (graphical interfaces) are provided to monitor and configure the MuTRiG chips on the SMBs. Among these, a specific interface allows for the modification of MuTRiG settings, which are stored in the ODB and can be adjusted. These settings configure the MuTRiG chips and the DAC values linked to these parameters are listed in Table 8.1 and 8.2. The DAQ then generates the bit pattern based on the ODB-stored values, formatting

Figure 8.19: The SciFi configuration grafical interface (MIDAS custom page). The settings shown is for taking data of the MuTRiG ASICs.

it appropriately to configure the MuTRiG chips initiated via Remote Procedure Calls (RPC) to the FPGA of the FEB. Furthermore, the ODB houses global DAQ settings that can also be modified through the MIDAS graphical interface. The overall ODB settings are organized into distinct sections : DAQ, Global, PLL, and Channel, each represented by separate panels within the MIDAS custom pages for clear differentiation, see Figure 8.19. Each section is responsible for the following settings:

- DAQ section: This section contains the global settings for the DAQ system, including controlling the random data generator of the FEB for testing purposes or enabling the TDC injection (explained later). Also the possibility to reset the datapath, ASICS, LVDS lines and the counters is included. Masking hides one or several ASICs from the DAQ and is also an available option, though it can only be accessed directly in the ODB and not through the MIDAS graphical interface.

- Global section: This section contains the global settings for the SMB and MuTRiG ASICs. Here the different frame transmission modes are set, including the choice of the long, short hit event or enabling the event rate counter, discussed in section 8.1.3.4.

- PLL section: This section contains the settings for the TDCs and, more specifically, the phase-locked loop (PLL) settings. This section contains 9 parameters that are configured by 9 Digital to Analog Converters (DACs). These settings include a value, offset, and scale, which will be explained later. The purpose of these configurations is to guarantee that the Voltage Controlled Oscillator (VCO) within the MuTRiG chips successfully synchronizes with the 625 MHz clock signal, ensuring accurate operation of the TDCs. This ultimately ensures that the data has the correct timing information.

- Channel section: This section contains the settings for the individual channels of the MuTRiG chips, including the threholds (time and energy thresholds) and the SiPM biases. Also masking individual channels is possibles. This operates the analog part of the MuTRiG chips.

Additionally, two other sections are available on the interface: the monitor driver settings and LVDS driver settings sections. The monitor driver settings control all the debug pads for testing and characterization of the MuTRiG chips. More is explained in section 8.1.1.5. The LVDS driver settings section controls the LVDS drivers. The settings on this custom page can be saved into JavaScript Object Notation (JSON) files. Beforehand saved JSON files, pre-defined configurations, can also be imported to this page to set directly the ODB values. These configurations serve as initial templates for the MuTRiG chips, providing a baseline from which adjustments can be made manually on the graphical interface.

These pre-defined configuration can be organized into the following types, each with a specific purpose:

- **All off** : This configuration is used to bring the MuTRiG chips into a state that consumes little power by turing off most of the features of the chips. It will send empty frames.
- **PseudoRandom BitStream** : This configuration is used to send frames of hits containing a pseudorandom bit sequence. This sequence is basecally a test pattern that can be used to test the DAQ system and the MuTRiG chips, more about this bit sequence can be found in [68].
- **PLL test** : This configuration is used to test the PLL of the MuTRiG chips. A important step in the tests of the SMBs and explained in the next paragraph. This enables the digital part of the MuTRiG chips whitout the analog part.
- **Data** : This configuration is used to take data. It enables all the parts (digital and analog) of the MuTRiG chips.

To apply these configurations to the MuTRiG chips, the "configure" command is used on the custom page. A successful communication with the MuTRiG chips is indicated by their response to the command, at which point the new settings are applied. Notably, certain configurations may result in observable changes in the current on the low voltage lines, serving as an indicator of the adjustments.

8.5.3 *PLL test*

If configurating the MuTRiG chips is successful, the next step is to validate the PLL settings. This is done by sending a periodic signal with frequency of 100 kHz into the TDC of the MuTRiG. The signal comes from the FEB and is injected via the digital monitor pads which bypass the analog part of the MuTRiG and access directly the TDC of the channels. As the signal is periodic, the difference between timestamps

of the rising edges of the signal should be constant, as seen in the left Figure 8.20. Any deviation in this interval suggests improper PLL locking, indicated by fluctuating differences in the timestamps of the rising edges. The right Figure 8.20 shows a unsuccesful locking, where no clear peak at the right period is visible. Adjustments of the PLL settings are then needed.

The MuTRiG chips must be configured in a correct way to be able to do the test. It needs to accept the external periodic signal though the monitoring pads. This is done by switching off the `TDCTEST_N` bit for all the channels. Also the energy validation needs to be switched OFF by setting the bit of the DAC `RECV ALL` to 1. This ensures that a hit is generated at every rising edge of the injected periodic signal. The analog part of the MuTRiG chips needs to be turned off by setting the DAC `CML` value to 0. Default JSON files which include configuration settings for this PLL lock test are saved and can be used.

In the case of unsuccesful locking, the PLL settings can be adjusted. This can be done by changing some specific DAC values depending on the situation in the PLL section of the custom page. They are explained in Table 8.2. To tune the PLL, the most important DAC value to adjust are the `VNVCODelay`, `VNHitLogic` and `VNCnt`. To lock the PLL in the right frequency, the `VNVCODelay` can be adjusted. The `VNHitLogic` and `VNCnt` are used for further adjustements.

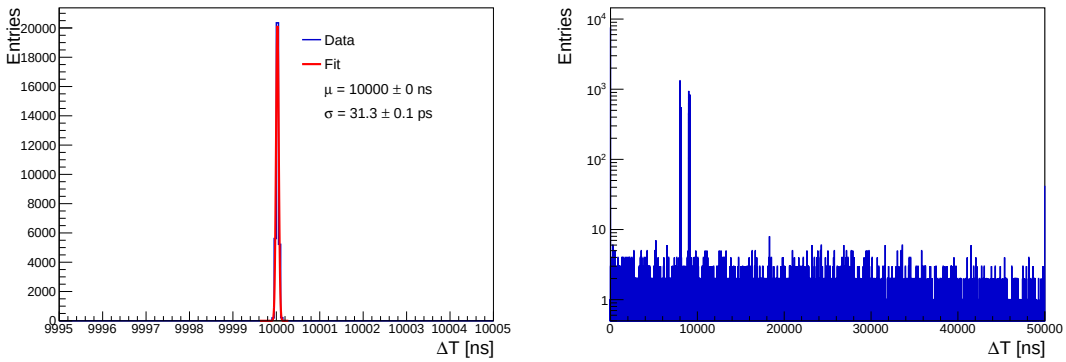

Figure 8.20: Distribution of the difference between timestamps of the rising edges of the injected periodic signal. Left when the PLL is locked, right when it is not locked (logarithmic scale).

On Figure 8.20 the distribution of the difference between timestamps of the rising edges of the injected periodic signal is shown. The left Figure 8.20 shows a PLL lock and on the right Figure 8.20 a unsuccesful locking. Figure 8.21 shows the difference between timestamps of the rising edges of the injected periodic signal for all the channels when the PLL is locked. When one channel per asic is locked in the right frequency (periode), all the other channels of the same ASIC should be locked as well since the PLL is shared between the channels of the same ASIC. The mean of the peak is at 1000 ns which correpsonds to the correct periode of the 100 kHz injected signal. The width of the peak is ∼31 ps which corresponds to the internal jitter of the MuTRiGv3 (∼20 ps) with some addtional jitter from the injection signal coming from the FPGA. Other

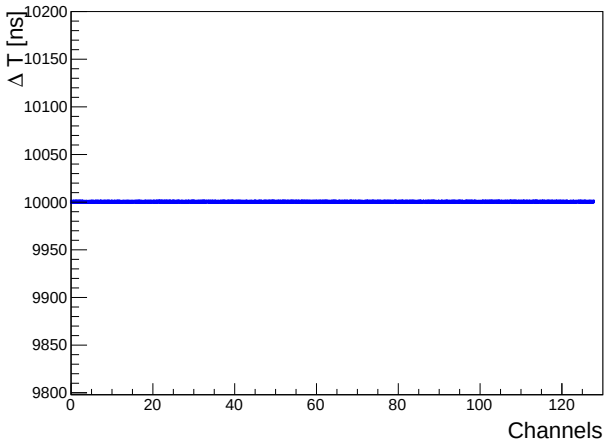

Figure 8.21: Difference between timestamps of the rising edges of the injected periodic signal for all 128 channels of one SMB3.1 when PLL is locked.

sanity checks are to check the uniformity in the fine and coarse counter distributions of all the channels. After the PLL is locked at the right frequency, the chip's digital part can be validated.

8.5.4 *Analog validation*

Following the testing of the digital part, the analogue part of the MuTRiG chips can be evaluated. This process involves setting the MuTRiG chips to data taking mode which enables the digital and analog part of the chips, utilizing the same PLL settings that have been validated beforehand. After this, a bias can be applied to the SiPM on the SMB and taking data start. It is important and good pratice to apply bias to the SiPM on the SMB only after ensuring that at least the analog part of the MuTRiG chips has been activated through configuration. The amount of hits in the data varies based on the `TTHRESH` parameter. The data can be decoded with the a ROOTANA based anaylser which has the feature to monitor online the data generating histograms on a web page. If data can be seen, the calibration and especially a threshold scan can be performed.

8.6 CALIBRATION PROCEDURES

Calibration is essential to ensure meaningful data with the SMBs. This section outlines initial calibration procedures and concepts for their implementation. Further developments in these procedures are being pursued at the time of writing this thesis. Initial calibrations can be listed as follows:

1. IV scans
2. Threshold scans
3. DNL correction: fine counter correction

8.6.1 *IV Scan*

IV scans involve measuring the leakage current through the SiPM array as a function of bias voltage under dark conditions. Before installing the SiPM on the SMB, each device is tested to determine the breakdown voltage V_{bd} for every channel. Given that all channels share a common cathode, the same bias voltage is applied to all channels. The variation in the V_{bd} value of the SiPMs is within $\pm 0.3\,\mathrm{V}$ across the entire array, see Figure 4.16.

To adjust the overbias for each channel, the gate voltage of the MuTRiG chip's input transistor can be fine tuned using a specific DAC value, named as `SiPM`. This parameter can adjust the bias by 0 to $\sim 0.9\,\mathrm{V}$ range. Figure 8.22 shows the measured voltage at the input terminals of 6 different channels (across the 4 ASICs) as function of the `SiPM` DAC value. The Figure shows the range of the bias voltage adjustments and highlights that the `SiPM` DAC value across different channels do not lead to precisely uniform adjustments. Additionally, the overall bias current of the MuTRiG chip's input stage (`INPUTBIAS`) can be modified as well, though this adjustment impacts various other parameters. By manipulating these DAC values, it is possible to adjust the overbias to a certain extend.

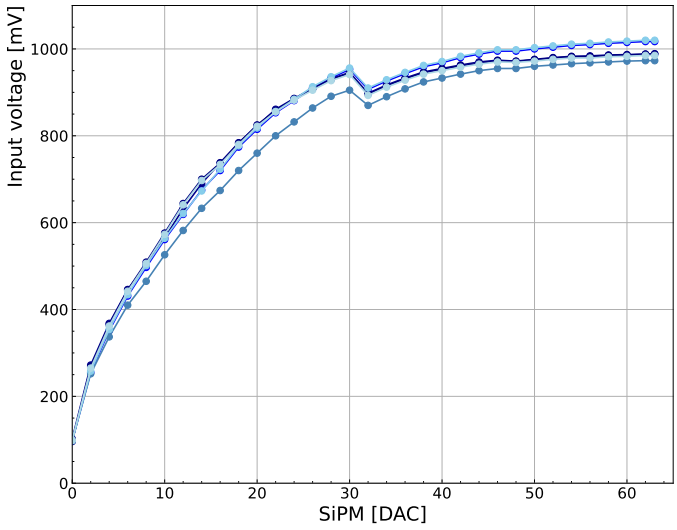

Figure 8.22: Measured voltage at the input terminals of 6 different channels (across the 4 ASICs) as function of the SiPM DAC value without applying an external bias to the SiPM.

The ultimate objective is achieving uniform gain across all channels. The intrinsic gain of each SMB channel passing through the MuTRiG chip not known. However, relative gains can be inferred from threshold scan measurements. As seen in section 6.2.3, from the slopes of the threshold scans curve the peak of the signal amplitudes can be determined. By fitting these distributions with a sigmoid function, the relative

gains can be determined from the inflection points; the separation between these points indicates the peak of the signal amplitudes therefore the channel's relative gain.

Additional IV scan are performed once the SiPM is mounted on the SMB. This guarantees that the V_{bd} remains within the initial range. In thise case, both parameters on the MuTRiG chip can be fine-tuned to their nominal values, ensuring an accurate IV scan (of all the channels at the same time) of the SiPM array exclusively, without interference from currents originating from the MuTRiG chip.

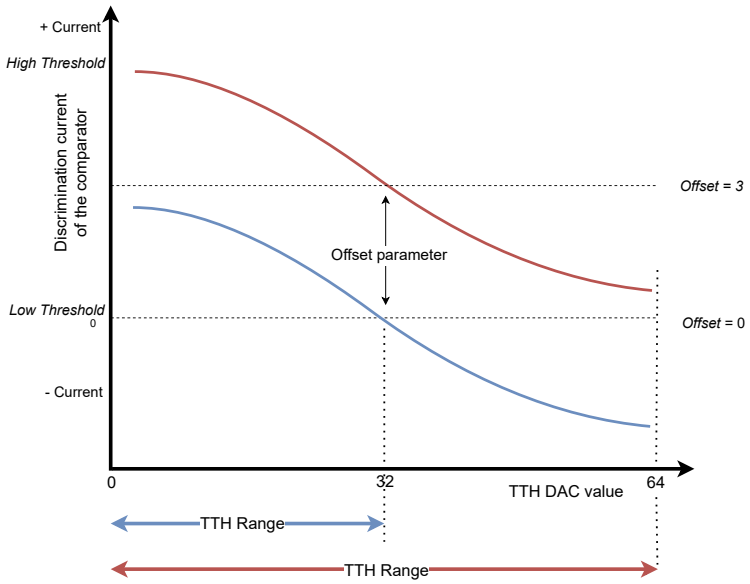

Figure 8.23: Illustration based on simualtion of the response of the comparator circuit, which is responsible for the discrimination process in the timing trigger branch of the MuTRiG chip. Serves for explantion purposes.

8.6.2 *Threshold scans*

The MuTRiG operates based on amplitude thresholds. Determining the threshold for each channel involves making scans with the SiPM array biased in dark conditions. These scans consist of measuring the rate as a function of the MuTRiG amplitude threshold, controlled by the DAC `TTHRESH`. The measured rate follows, ideally, a step function.

Threshold scans are performed through rate counters per channel in the ODB, produced by the FPGA of the FEB. The MIDAS sequencer enables ODB manipulation for configuration and to read back counter. A sequencer script automates the process, iterating over `TTHRESH` values and recording the channel rates. The result is a JSON file summarizing rates per channel for each `TTHRESH` setting.

The DAC value `TTHRESH` has 64 values with 8 offsets and 8 scales. This offset is new to the MuTRiG version 3. `TTHRESH` essentially controls the feedback current of the comparator circuit, which is responsible for the discrimination process (section 8.1.1.2).

A illustration the response of the comparator circuit as a function of the TTHRESH DAC value is shown in Figure 8.23. This illustration serves only for guidance and is based on design simulations of the MuTRiG chips. The real response curve does not have the exact same shape. By increasing the input signal through positive feedback (by lowering the TTHRESH DAC value), the comparator circuit becomes less sensitive to small changes in the input voltage, effectively raising the threshold for triggering a response. So lower the DAC TTHRESH value, higher the threshold setting in the chip. Also, the offset and scale are used to adjust the threshold. As shown in Figure 8.23, the offset is used to shift up and down the response curve, and the scale is used to adjust the slope. The blue curve in Figure 8.23 is the response curve of the MuTRiGv2 and the red curve of the MuTRiGv3. As can be observed, this offset parameter makes it possible to increase the range of the TTHRESH DAC value. With MuTRiGv3, this offset can be adjusted to go higher to reach higher discrimination currents.

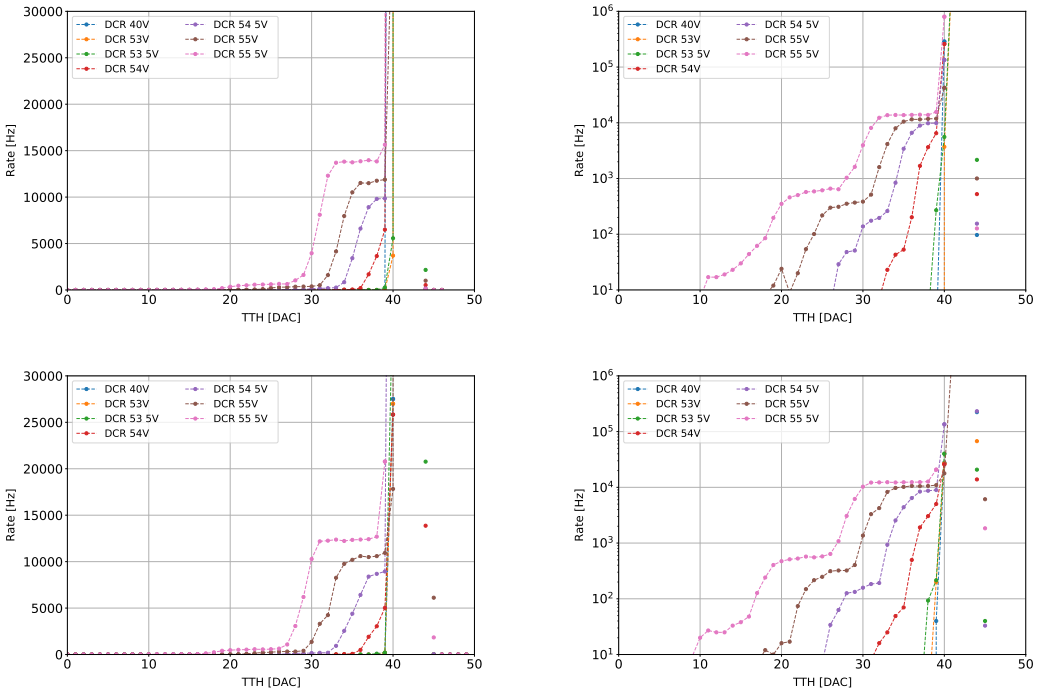

Figure 8.24: Threshold scans of two channels of a SMB3.0 in the dark. Each row is a different channel. The left column shows the rate as a function of the TTHRESH DAC value in a linear scale. The right column shows the same data in a logarithmic scale.

Figure 8.24 shows threshold scans for two channels of the SiPM array mounted on a SMB3.0 in darkness. The breakdown of the SIPM array is $\sim 52\,\mathrm{V}$. Below the breakdown, only the niose of the system can be seen, which is roughly for both channels at a TTHRESH DAC value of ~ 40. With the bias voltage exceeding the breakdown voltage, an increase in DCR is observed, marked by the appearance of a plateau level, beginning at a TTHRESH of ~ 40 until ~ 30. Also, with an increase in overbias, the gain increase, resulting in an larger plateau as the overbias level rises. The DCR, the rate at the plateau

level, is about ∼12 kHz and ∼14 kHz which, is the expected value for the SiPMs used in the SciFi detector. A second plateau can be seen (at high bias voltage of the SiPM) at a TTHRESH of ∼ 25, which corresponds to a 2 photon amplitude. A clear noise and DCR can be determined, and threshold points can be chosen. A 0.5 and 1.5 amplitude thresholds are typically chosen as they are the chosen working points for the SciFi detector. As discussed earlier, the thresholds can be set in the middle of the plateaus.

8.6.3 *DNL correction : fine counter correction*

A correction of the fine timing counter is required to address the variations within the delay elements of the TDC. While the VCO in the Timebase unit of the TDC ensures that the cumulative sum of all delay elements remains stable at a constant value when it is locked in a Phase-Locked Loop (PLL), variations can still occur among the individual delay elements. These variations are from the fabrication process.

Consequently, the width of the fine counter bins are not the same, leading to inaccuracies in the timing measurements. The variances of the fine counter bin sizes are descibed by the differential and integral non-linearity. The differential non-linearity (DNL) of the fine counter is defined as the relative deviation of its bin size to the average fine counter bin size (50 ps), which in terms of delay element τ_i is given by:

$$DNL(i) = \frac{\tau_i - < \tau_d >}{< \tau_d >} \tag{8.7}$$

The integral non-linearity is defined as the deviation between the timing measurement to the ideal correct fine time measurement and can be calculated by integrating the DNL of the fine counter bins up to the bin of interest. Typically, the DNL and INL are expressed in least significant bits (LSB) which is the smallest step of change in the digital output of the TDC. With the right adjustements of DAC values to achieve a PLL lock, DNL values are less then 1 LSB. Given the DNL values of the fine counter bins, offline correction can be implemented.

To evaluate the DNL and INL of the delay elements, the delay of the individual fin counter bins need to be measured with a code density test (CDT). During a CDT, a random number of entries are generated with a uniform distribution over a coarse counter period. The number of entries in each single fine counter bin is a direct measurement of its relative bin size which in turn is a measure of the delay element. The average number of events per fine counter bin, n_avg, is calculated as the total number of events divided by the number of available bins and serves as the benchmark for the expected ideal each bin size (50 ps). Therefore, the DNL in each fine counter bin can be derived by the deviation of the number of events in each fine counter bin to the expected average number of events per bin:

$$DNL(i) = \frac{n_i}{n_{avg}} - 1 \tag{8.8}$$

The DNL of the fine counter bins of one channel is shown in Figure 8.25. A positive DNL indicates that the bin is wider than the average bin size, while a negative DNL

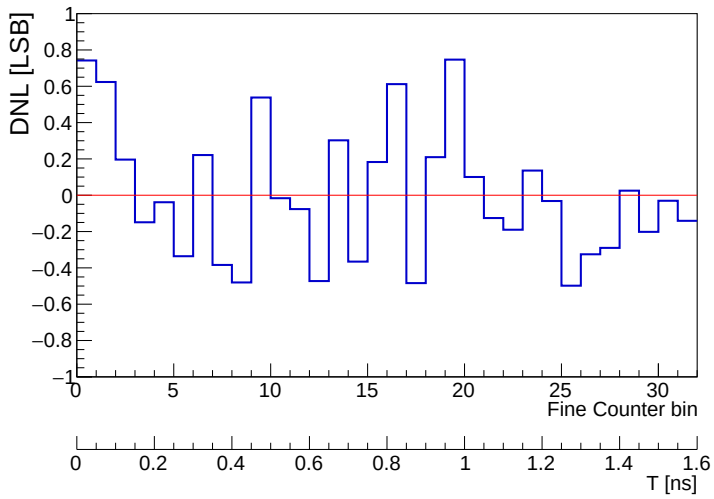

Figure 8.25: Measured non-linearities of the TDC of one channel which is represented with the differential non-linearity (DNL) of the fine counter. Bins with positive DNL are wider than the average bin size, while those with negative DNL are narrower than average. In red the corrected DNL.

indicates that the bin is narrower than average. In the ideal case, the DNL for each bin should be zero. With this injormation, corrections can be applied. One such correction involves mapping the non-uniform fine bins to uniform bins, ensuring each time interval of the fine counter bins is precisely quantized into the ideal uniform bins (50 ps). This process includes redistributing entries from smaller fine counter bins into the corresponding ideal bins, while larger fine counter bins are mapped across multiple ideal bins to achieve a more uniform distribution.

8.6.4 *Charge injection*

In the folowing additional tests with new produced SciFi boards, SMB3.0 and SMB3.1, are shown as they passed the required verification procedure, explained earlier.

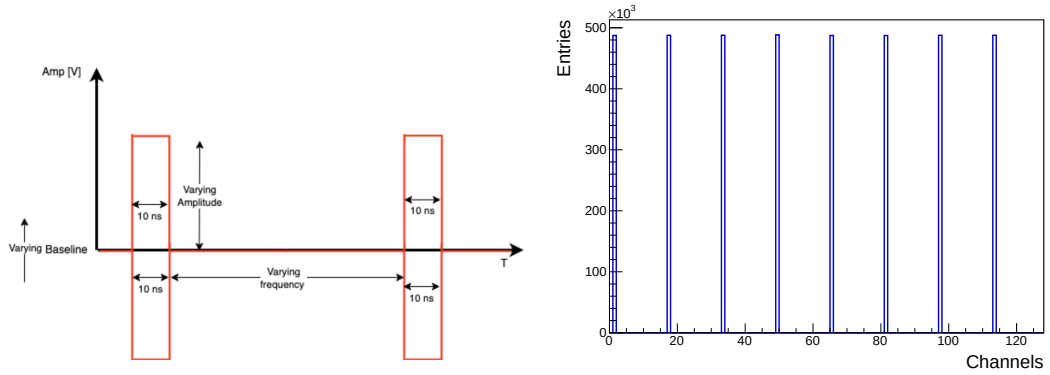

Figure 8.26: Left: sketch of the injected signal. Right: channels triggered by the injected signal.

Most of them as been done with the SMB3.0 and with a analog injection made possible with the little adaptor board. This board has two pins which enables to send a differential signal to 2 channel per MuTRiG chip, so 8 channel in total. This is possible via the design of the SMB3.0 and SMB3.1 see section 8.2.3. The injected signal is sent from a pulse generator which is connected to the adaptor board via the pins. The signal from the generator is periodic and has been adjusted to mimic a differential signal, as depicted in Figure 8.26. Amplidude, frequency and baseline of the signal can be varied. On the right of Figure 8.26, the channels triggered by the signal is visble.

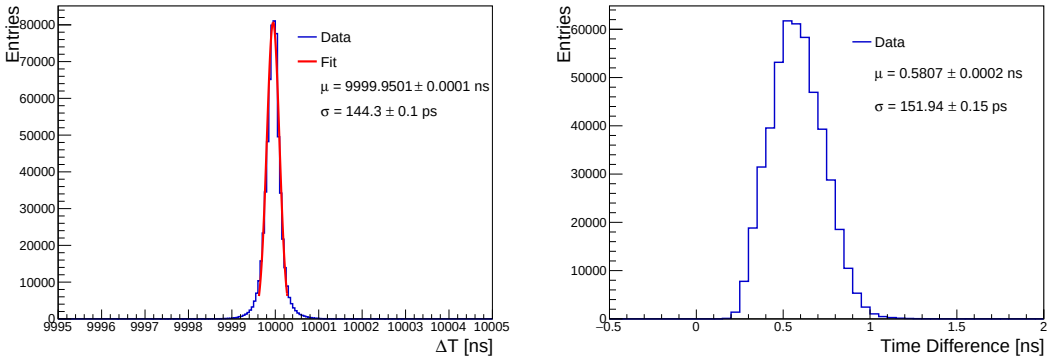

Figure 8.27: Left: distribution of the difference between timestamps of the injected analog signal. Right: distribution of the timestamps differences of two different channels of the same MuTRiG chip.

The PLL lock can be tested with the injected signal. The baseline to peak amplitude used for the injected signal is 500 mV and the frequency used for the periodique signal is 100 kHz. The distribution of the difference between timestamps of the rising edges of

the injected signal is shown in Figure 8.27 on the left. A clear peak is visible at 1000 ns, which corresponds to the right period of the injected signal. The peak is fitted with a gaussian to determine the mean and the width of the peak. The fit exludes the tails. The mean is at 1000 ns and the width is ∼150 ps. This width is mainly due to the jitter of the injected signal. This shows that the PLL can correctly lock to the injected analog signal. Also, the difference in times between two different channels can be measured, see Figure 8.27. Since it is the same injected signal, the difference in time should be the same for all channels. A difference up to 1 ns can be seen for two channels of the same MuTRiG chip because of interval delays.

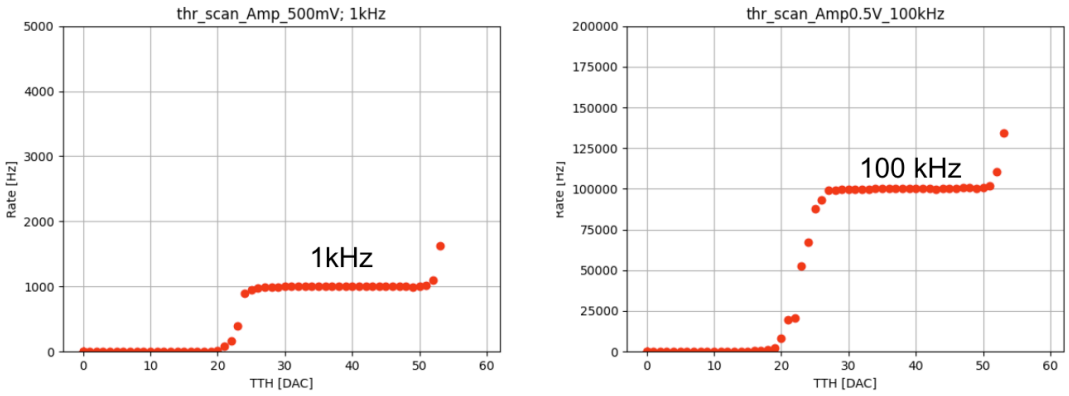

Figure 8.28: Threshold scans of one channel of a SMB3.0 with the injected signal. The frequency of the injected signal is varied.

As a next measurement, the threshold scans are performed with the controlled injection signal coming from the generator. The channels' response is observed by using different frequencies of the signal. Clear plateaus are seen in the threshold scans, see Figure 8.28. By maintaining constant values for width and amplitude at 10 ns and 500 mV respectively, the observed rates fluctuate according to the frequency of the injected pulse. The offset and scale of the TTHRESH DAC value are set to 1 and 0. The response of the channels is visible, and the correct injected frequency is seen.

The frequency fixed, the amplitude of the injected signal is varied in right Figure 8.29. Each curve is fitted with a sigmoid function. The inflection point of the sigmoid function is the peak of the signal amplitudes distribution. As the amplitude of the injected signal increases, the edge of the plateau moves to lower TTHRESH DAC values, which means a higher threshold is set. Also, the offset can be further investigated with the injected signal. With a fixed amplitude of the injected signal but varying the offset of TTHRESH DAC values as in the left Figure 8.29. A higher offset value sets the threshold higher, hence, the signal is seen at higher TTHRESH DAC values.

Figure 8.30 shows more measurements varying the amplitude of the injected signal, leaving the scale at 0. The offset of the TTHRESH DAC value is seen as the amplitude of the signal increases, the offset needs to be increased. Only the first 4 values of offset are shown. Also the effect of the scale can be seen in Figure 8.31. The slopes of the sigmoid curves are different for each scale value, appart scale 0 and 2. No differences can be seen

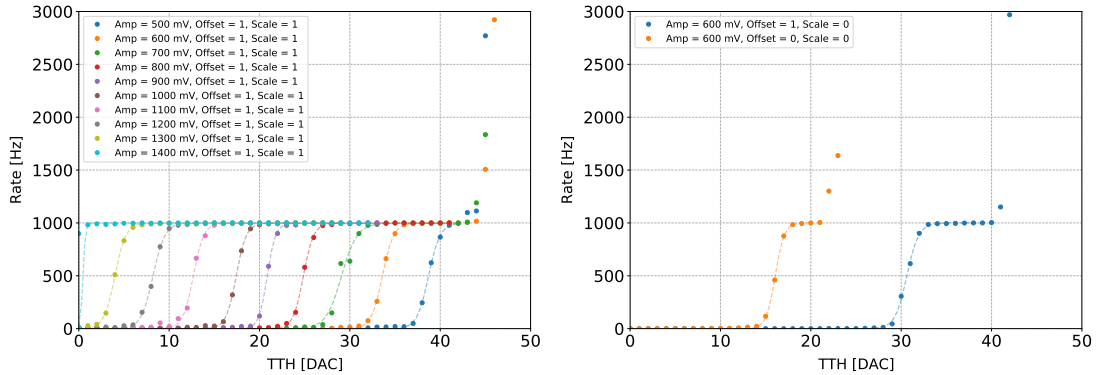

Figure 8.29: Threshold scans of one channel of a SMB3.0 with the injected signal. The amplitude of the injected signal is varied on the left and the offset of the TTHRESH DAC value is varied on the right.

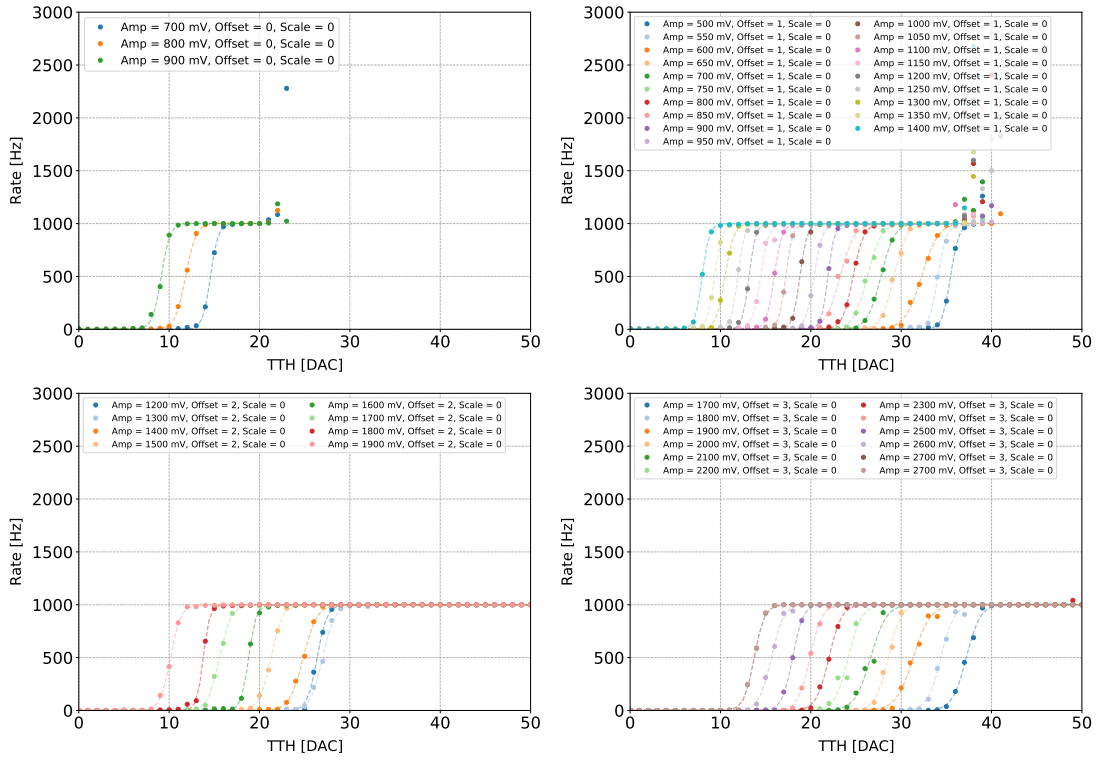

Figure 8.30: Theshold scan of one channel of the SMB3.0 with the injected signal. Different amplitudes of the signal are used and therefore different offsets are used also.

between scale 0 and 2 this might be due the fact that at the time of the measurements the scale 2 was not implemented yet in the software. The scale 0 corresponds to the steepest slope going to scale 3 and 1 which are less steep.

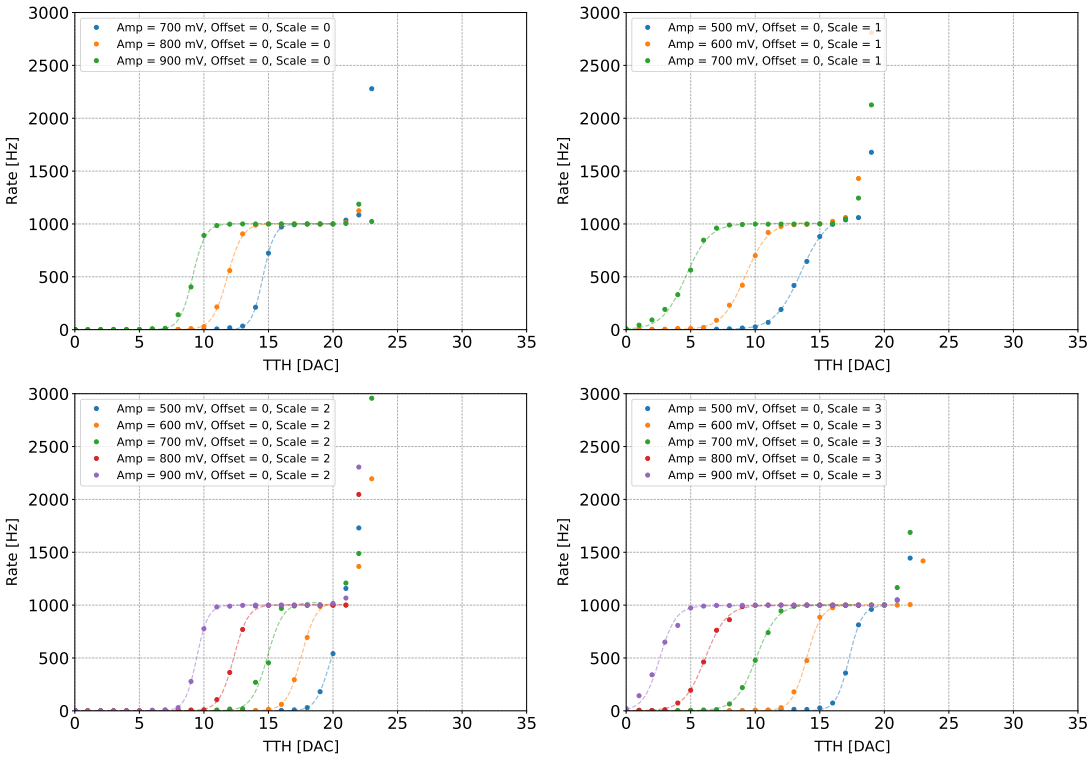

Figure 8.31: Threshold scan of one channel of the SMB3.0 with the injected signal. Varying scales for each plot is set.

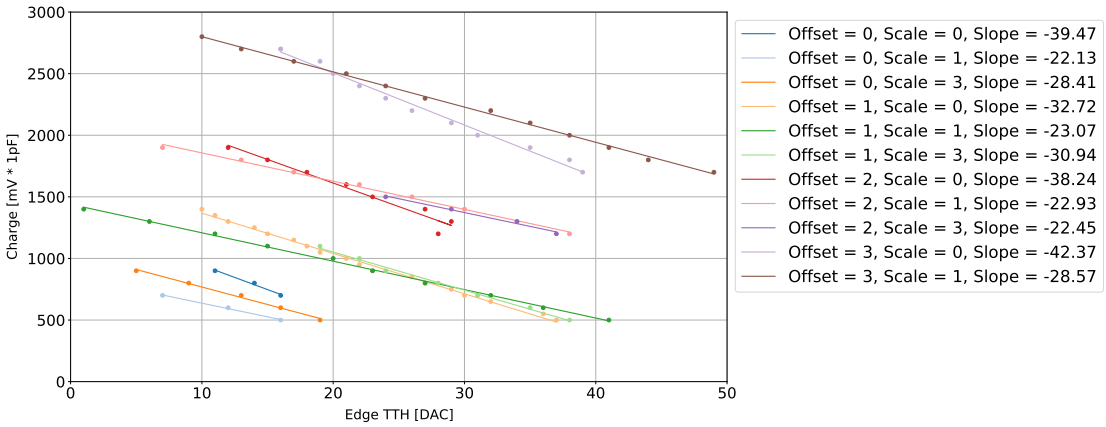

Figure 8.32: Overview of the offset and scale of the TTHRESH DAC value. The points represent the amplitude of the injected analog signal (giving a charge by multiplying with 1pF) as a function of the edge plateaus observed in the threshold scan curves. Additionally, the slopes derived from the linear fits to these data points are displayed.

A better overall view of the offset and scale of the TTHRESH DAC value can be seen in Figure 8.32. Scale 0, 1 and 3 are used since scale 2 was not different to 1. Also the offset is varied from 0 to 3. The amplitude of the injected signal passes trough a 1 pF capacitor which as a result can be related to a charge. The data points are the edges of each plateaus that are coming from the injected signal in the performed scans. The data points for every set of parameter is fitted with a linear function. The slopes of this linear fit are shown also. As the offset increases, the range of the TTHRESH DAC value increases, especially from offset 0 to 1. Also the response seems to be somewhat linear to the amplitude of the injected signal. As well the offset seems to have a linear response. The response of the scale is not so clear, but there are differences of slopes and the slope of scale 0 is also always the steepest. The scale 2 is not visible in the plot, but it is the same as scale 1. For different offsets, the scale shows varying trends, although the hierarchical relationship among them remains consistent.

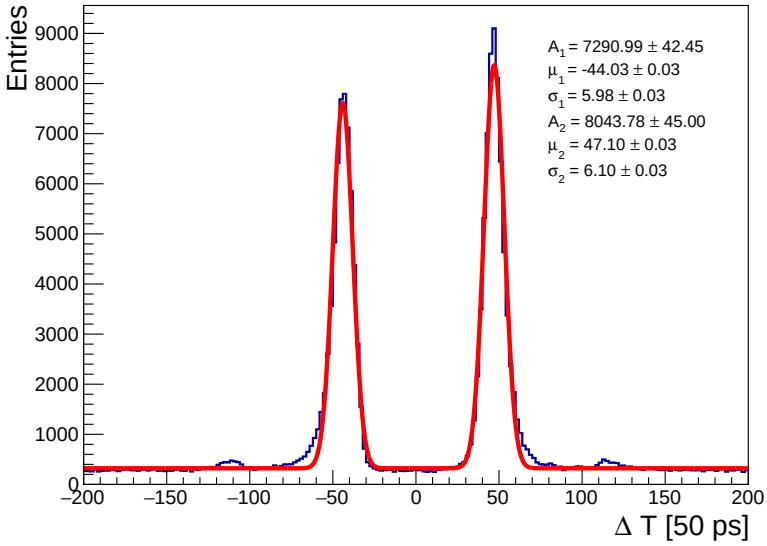

Figure 8.33: Time difference between hits in the SiPM arrays placed on both sides of the SciFi ribbon. The time difference between the two peaks is indicative of the speed of propagation of the photons in the SciFi ribbon. In red, a fit of two gaussians is performed to determine the mean and the width of the peaks.

8.6.5 *Dark count rate*

A DCR data has also been collected in the absence of ionizing particles. When a SiPM discharges (dark count), it generates polluting photons through the folowing mechanism: the electrons in the conductive band of silicon recombine with holes in the valence band, releasing energy in the form of infrared (IR) photons. These escape from the SiPM and can be trapped and transported by the scintillating fibers to the opposite

end, where they can trigger a discharge in the SiPM array coupled to the opposite side of the SciFi ribbon.

Figure 8.33 shows the time difference between the hits at the opposite ribbon's ends. Two peaks, which in this Figure 8.33 are separated by $\sim$ 4.5 ns, are due to the fact that it shows $\Delta T = T_{left} - T_{right}$ and not the time difference between the two events. With this plot, the speed of light propagation can be calculated as $v_{fiber} = L/|\Delta T| =$ 30cm /2.25 ns $\sim 0.5c$ which is in agreement with the previous studies. Also the same measurement has been performed with the DPNC 342 waveform digitizer board in previous studies [59]. The width of both of the peaks are close to $\sim$ 300 ps, which is particularly interesting regarding the jitter in the readout electronics. Considering that the intrinsic jitter of SiPM arrays (SPTR) is around 220 ps, it is evident that additional jitter arises from the MuTRiG ASICs. Therefore, this measurement can be used as an additional check in the verification procedure of the SMB and the full readout chain.

8.7 TEST BEAM

A dedicated test beam at the πM1 beamline of PSI with first (half) SciFi super-modules has been performed. The modules were composed of SMB3.0 with MuTRiGv3 ASICs. Both ends of the SciFi super-modules could be read out and a first look at data with beam is seen. Cluster widths are measured and a clear channel correlation between the two ends of the SciFi ribbon are seen in the data with beam. Efficiency studies were not possible since the sorting and a new datapath (firmware) was not fully optimized at the time of the test beam which was during the writting of this thesis. IV scans of the SiPMs arrays on the SMB3.0 were performed beforhand so an overbias of 3.5 V was set. Before the beam, locking of the PLL was once more checked and threshold scans were performed. Two working points of 0.5 and 1.5 amplitude threshold where set. The responses of the hits per side of the ribbon is similar and the beam profile is visible with the channel correlation in the left Figure 8.34 using 0.5 amplitude threshold. Also the cluster width (with a minimum hit multiplicity of 2) of the particles crossing perpendicular the SciFi ribbon are measured, see right Figure 8.34. Those are some first results and more analysis (for timing resolutions) is ongoing during the writting of this thesis. For efficiencies and timing resolutions futher laboratory tests and test beams are necessary.

8.8 SUMMARY

This chapter has presented and described to a certain level of detail the MuTRiG ASIC. It has also given a explanantion of the SciFi Module Board (SMB) used in the `Mu3e` experiment, detailing its design, components, and calibration procedures. The verification procedure for ensuring SMB functionality was outlined, the importance of power-up tests, communication verification with MuTRiG chips, PLL testing, and analog validation. Calibration procedures were then detailed, including IV scans,

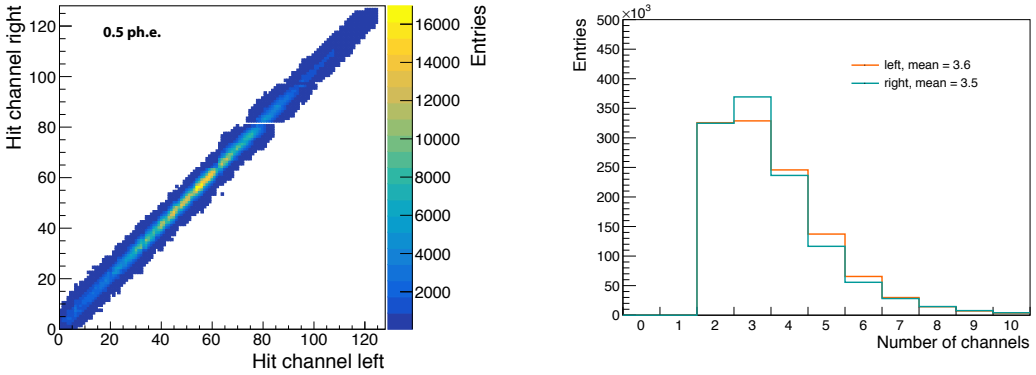

Figure 8.34: Left) Correlation between hits from beam detected by the two SiPM arrays at both ends of the SciFi ribbon with 0.5 ph.e. amplitude threshold. Right) Cluster width of both sides for particles corssing perpendicular the SciFi ribbon with amplitude threshold of 0.5.

threshold scans, and DNL correction, for the fine counter, to ensure accurate and uniform operation of the SMBs.

Additional tests conducted with the SMB3.0 and SMB3.1 versions were presented, demonstrating the SMB capabilities and the effectiveness of the calibration and verification processes. These tests included PLL lock tests using an injected analog signal, threshold scans to determine the response of the channels to varying signal amplitudes and frequencies, and exploration of the offset and scale parameters of the TTHRESH DAC value. Also the DCR measurements with the SMBs were presented and can be used as an additional check in the verification procedure of the SMB and the full readout chain.

Overall this provides thorough understanding of the SMB's functionality and of the MuTRiG ASIC. However, to gain a complete understanding of the ASIC's capabilities, particularly regarding efficiency and timing in conjunction with the SciFi ribbons, further testing and measurements will be required.

9

SUMMARY

In Phase I, the Mu3e experiment aims to seach for the cLFV decay $\mu^+ \to e^+e^-e^+$ at a Single Event Sensitivity (SES) of 2×10^{-15}. This is 3 orders of magnitude improvement over the current limit of 1.0×10^{-12} set by the SINDRUM experiment. Since the decay is forbidden in the Standard Model and has a very small branching ratio in the extended SM models with massesive neutrinos, the observation of this decay would be a clear indication of new physics beyond the SM. If it is not observed, the experiment will set an upper limit on this decay and Beyond the Standard Model theories can emerge with more stringent constraints. To achieve this, the experiment is under construction at the Paul Scherrer Institute (PSI) in Switzerland and will use the most intense continuous surface muon beam in the world delivering muons at a rate of 10^8 muons per second.

To reach the sensitivity, the detector needs to be fast enough to handle the high muon rate. In addition, an extremely low material budget of the detectors is required to minimize multiple scattering. Mu3e consits of pixel trackers based on HV-MAPS. A scintillating fiber (SciFi) detector, along with a tile detector, are used to give time information when electrons pass the detector. A very thin SciFi detector with a thickness $< 0.2\%$ of radiation length X_0 is developed for the Mu3e experiment. The SciFi detector not only has to be thin which results in small primary signal amplitudes, but it also has a very limited physical space available. The baseline design is 3 staggered layers of 250 µm diameter round scintillating fibers, type SCSF-78 from Kuraray. The detector is readout at both ends with multi-channel SiPM arrays from Hamamatsu.

This thesis presents the work done in the development and construction of the scintillating fiber detector. As first, a detailed study of different scintillating fibers, especially their timming propreties, is presented. Next, the performance of the SciFi detector with the different scintillating fiber ribbons and configurations is studied. And further, a description and some tests of the MuTRiG ASIC alongside the SciFi Module Board version 3 is presented. The next three paragraphs summarize the main results of this thesis.

Performance of scintillating fibers

A study of the propreties of the scintillating fibers is presented in this thesis. Different types of scintillating fibers were tested. It highlights the critical role of fiber properties in achieving the best timing performance. The NOL-11 fiber has the best timing performance with $\sigma_{MT} \simeq 250\,\text{ps}$ while the SCSF-78 presented a slightly higher light yield among the tested fibers. The study shows the importance of minimizing the decay time of the fiber and also maximizing the number of detected photons to enhance the timing performance of the fibers. The mean time analysis further demonstrated that it is a reliable time measurement observable, independent of the particle's crossing point.

The study also showed that scintillation light travels through the fibers at about half the speed of light in vacuum.

Performance of the scintillating fiber detector

The performance study of the SciFi detector with the scintillating fiber ribbons is presented in this thesis. Scintillating fiber ribbons with different fiber types and numbers of layers are tested. The study found that the best mean time resolution σ_{MT} of 200 ps was achieved with 4-layer SciFi ribbons made of NOL-11 fibers, whereas 3-layers ribbons using SCSF-78 fibers reached a σ_{MT} of 245 ps. Despite NOL-11 fibers having a shorter decay time than SCSF-78 fibers, the improvement in σ_{MT} is about 5%, but it came with a notable 20% reduction in the mean time distribution's tail. The addition of a fourth layer of fibers in the ribbon was found to improve σ_{MT} by around 15%, emphasizing the critical importance of light yield for achieving superior time resolution. Also, a comparison between SCSF-78 and NOL-11 fibers showed similar light yields.

Detection efficiency was observed to be high, around 97% for matching clusters from opposite sides of the ribbon wich meet a minimum hit multiplicity of two at a threshold equivalent to 0.5 photoelectrons. Furtermore, for matching clusters with at least one hit surpassing the higher threshold of 1.5 photoelectrons, the efficiency was boserved to be around 98% . Those efficiencies slighlty decreased under more a more strict time cut of $3 \times \sigma_{\Delta T}$. Importantly, the addition of a fourth layer of fibers in the ribbon not only improved detection efficiency by 1% to 3%, depending on the selected threshold working point, but also enhanced the light yield, further increasing the detector's efficiency. Moreover, the efficiency of the detector increased with the angle of particle crossing, indicating an angular dependency in its performance. The mean time, derived from time measurements at both ribbon ends, was confirmed as a reliable observable for time measurements, unaffected by the hit position. These observations underscore the balance between the choice of fiber, layering, and operational parameters in maximizing the SciFi detector's efficiency for the Mu3e experiment. From this analysis, two working points for the SciFi detector have been identified: require at least two contiguous channels to surpass a 0.5 ph.e. threshold, and require at least one channel to surpass a 1.5 ph.e. threshold.

Performance of the SiciFi module board with the MuTRiG ASICs

The final version of the SciFi Module Board (SMB) was devolopped during this thesis and tested with the MuTRiG ASICs. The design was developed to be compatible with the Mu3e experiment's requirements, with the aim to provide a reliable and efficient readout of the SciFi detector. The studies of the SciFi Module Board with the MuTRiG ASICs provided a thorough understanding of their functionalities and laid down the groundwork for future optimizations. Through verification procedures, calibration techniques, and additional tests, the capabilities of the SMB were show, marking a significant step forward. These investigations were facilitated by the prior understanding of the performance SciFi ribbons, as detailed in this thesis. However, it

was also noted that to fully understand the ASIC's in terms of efficiency and timing with the SciFi ribbons, further testing and detailed analyses are required.

Conclusion

In conclusion, SciFi detectors can be used in a variety of applications requiring very good timing and spatial resolutions, and high detection efficiency with a very low material budget, capable of operating at high rates. In addition, they can be adapted to different geometries because of their modular design and can be used in a magnetic field. Achieving very good timing properties necessitates selecting material characterized by a fast rise time and a low Signal-to-Noise Ratio (SNR), which results in a large signal amplitude and a high light yield. A critical factor when conceiving a SciFi detector comes from the light yield off the SciFi ribbons. The very constraining material budget of the Mu3e experiment requirements impose the use of SciFi ribbons consisting of only 3 staggered fiber layers. This limits the light yield of the detector, which in turn has an impact on the time resolution and efficiency of the detector. In contrast, SciFi ribbons with a greater number of staggered fiber layers would significantly increase the light yield and improve the overall performance of the detector, but at the expense of an increased overall material budget.

As the SciFi detector is a critical component of the Mu3e experiment, the results of this thesis provide a detailed understanding of the performance of the SciFi detector. With the development of the SciFi Module Board and the study of the MuTRiG ASICs, the groundwork for future optimizations is laid down. Further testbeams and laboratory tests are planned to further investigate the performance of the SciFi detector with the MuTRiG ASICs via the SciFi Module Board. The mechanical integration of the SciFi detector in the Mu3e experiment is close to completion.

BIBLIOGRAPHY

[1] David J Griffiths. *Introduction to elementary particles; 2^{nd} Rev. Ed.* Wiley, 2008.

[2] A. Zee. *Einstein Gravity in a Nutshell*. Princeton University Press, 2013.

[3] A Zee. *Quantum Field Theory in a Nutshell; 1^{st} Ed.* Princeton Univ. Press, 2003.

[4] D. Baumann. *Cosmology*. Cambridge University Press, 2022.

[5] S. Weinberg. *Gravitation and Cosmology: Principles and Applications of the General Theory of Relativity*. Wiley, 1972.

[6] Luigi Di Lella and Carlo Rubbia. *The Discovery of the W and Z Particles, Adv. Ser. Direct. High Energy Phys. 13 (2015)*. DOI: 10.1142/9789814644150_0006.

[7] M. Maggiore. *A Modern Introduction to Quantum Field Theory*. Oxford University Press, 2005.

[8] Peter W. Higgs. *Broken Symmetries and the Masses of Gauge Bosons, Phys. Rev. Lett. 13 (1964)*. DOI: 10.1103/PhysRevLett.13.508.

[9] Georges Aad et al. *Observation of a new particle in the search for the Standard Model Higgs boson with the ATLAS detector at the LHC, Phys. Lett. B 716 (2012)*. DOI: 10.1016/j.physletb.2012.08.020. arXiv: 1207.7214.

[10] Serguei Chatrchyan et al. *Observation of a New Boson at a Mass of 125 GeV with the CMS Experiment at the LHC, Phys. Lett. B 716 (2012)*. DOI: 10.1016/j.physletb.2012.08.021. arXiv: 1207.7235.

[11] B. Pontecorvo. *Electron and Muon Neutrinos, Zh. Eksp. Teor. Fiz. 37 (1959)*.

[12] Y. Fukuda et al. *Evidence for Oscillation of Atmospheric Neutrinos, Phys. Rev. Lett. 81 (1998)*. DOI: 10.1103/PhysRevLett.81.1562.

[13] Takaaki Kajita. *Discovery of neutrino oscillations, Reports on Progress in Physics (2006)*. DOI: 10.1088/0034-4885/69/6/R01. URL: https://dx.doi.org/10.1088/0034-4885/69/6/R01.

[14] Lorenzo Calibbi and Giovanni Signorelli. *Charged Lepton Flavour Violation: An Experimental and Theoretical Introduction, Riv. Nuovo Cim. 41 (2018)*. DOI: 10.1393/ncr/i2018-10144-0. arXiv: 1709.00294 [hep-ph].

[15] R.H. Bernstein and Peter S. Cooper. *Charged lepton flavor violation: An experimenter's guide, Physics Reports 532 (2013)*. DOI: https://doi.org/10.1016/j.physrep.2013.07.002.

[16] MEG II collaboration et al. *A search for $\mu^+ \to e^+\gamma$ with the first dataset of the MEG II experiment, Eur. Phys. J. C 81 (2024)*. arXiv: 2310.12614 [hep-ex].

[17] U. Bellgardt et al. *Search for the decay $\mu^+ \to e^+e^+e^-$, Nucl. Phys. B 299 (1988)*. DOI: https://doi.org/10.1016/0550-3213(88)90462-2.

[18] M. MacKenzie and P. Murat. *Search for $\mu^- \to e^+$ conversion: what can be learned from the SINDRUM-II positron data on a gold target, J. Phys. G 47 (2020)*. eprint: 2009.00214 (hep-ex).

[19] A. M. Baldini et al. *Search for the lepton flavour violating decay $\mu^+ \to e^+\gamma$ with the full dataset of the MEG experiment, Eur. Phys. J. C 76 (2016)*. DOI: 10.1140/epjc/s10052-016-4271-x. arXiv: 1605.05081 [hep-ex].

[20] Alessandro Baldini et al. *The design of the MEG II experiment, Eur. Phys. J. C 78 (2018)*.

[21] A. M. Baldini et al. *Measurement of the radiative decay of polarized muons in the MEG experiment, Eur. Phys. J. C 76 (2016)*. DOI: 10.1140/epjc/s10052-016-3947-6.

[22] L. Bartoszek et al. *Mu2e Technical Design Report, Fermilab Technical Report (2014)*. DOI: 10.2172/1172555. arXiv: 1501.05241.

[23] R Abramishvili et al. *COMET Phase-I technical design report, Progress of Theoretical and Experimental Physics 2020 (2020)*. DOI: 10.1093/ptep/ptz125.

[24] K. Arndt et al. *Technical design of the phase I Mu3e experiment, Nucl. Instr. Meth. A 1014 (2021)*. DOI: https://doi.org/10.1016/j.nima.2021.165679.

[25] R. L. Workman et al. *Review of Particle Physics, Progress of Theoretical and Experimental Physics (2022)*. DOI: 10.1093/ptep/ptac097.

[26] Cristina Martin Perez and Luigi Vigani. *Searching for the Muon Decay to Three Electrons with the Mu3e Experiment, Universe 7 (2021)*. DOI: 10.3390/universe7110420.

[27] Mu3e Collaboration internal notes.

[28] Ivan Perić. *A novel monolithic pixelated particle detector implemented in high-voltage CMOS technology, Nucl. Instr. Meth. A 582 (2007)*. DOI: https://doi.org/10.1016/j.nima.2007.07.115.

[29] Simon Corrodi. *A Timing Detector based on Scintillating Fibres for the Mu3e Experiment. Prototyping, Simulation and Integration, ETH Zurich (2018)*. DOI: 10.3929/ethz-b-000299260.

[30] William R Leo. *Techniques for nuclear and particle physics experiments: a how-to approach; 2nd ed.* Springer, 1994. DOI: 10.1007/978-3-642-57920-2.

[31] Pär-Anders Söderström. *Development of Neutron Detectors for the Next Generation of Radioactive Ion-Beam Facilities*. arXiv: 0905.2132.

[32] J.B. Birks, D.W. Fry, L. Costrell, and K. Kandiah. *The Theory and Practice of Scintillation Counting: International Series of Monographs in Electronics and Instrumentation*. Elsevier Science, 2013.

[33] C. Leroy and P.G. Rancoita. *Principles of Radiation Interaction in Matter and Detection*. World Scientific, 2009.

[34] Th. Förster. *10th Spiers Memorial Lecture. Transfer mechanisms of electronic excitation, Discuss. Faraday Soc. 27 (1959)*. DOI: 10.1039/DF9592700007.

[35] B. Wieb van der Meer. *FRET - Förster Resonance Energy Transfer*. John Wiley & Sons, Ltd, 2013. DOI: https://doi.org/10.1002/9783527656028.ch03.

[36] Heinrich Leutz. *Scintillating fibres, Nucl. Instr. Meth. A 364 (1995)*. DOI: https://doi.org/10.1016/0168-9002(95)00383-5.

[37] R. C. Ruchti. *The Use of Scintillating Fibers for Charged-Particle Tracking, An. Rev. Nucl. Part. Sci. 46 (1996)*. DOI: 10.1146/annurev.nucl.46.1.281.

[38] O. Borshchev at al. *Development of a New Class of Scintillating Fibres with Very Short Decay Time and High Light Yield, Journal of Instrumentation 12 (2017)*. DOI: 10.1088/1748-0221/12/05/P05013.

[39] A. Bravar and Y. Demets. *Timing properties of blue-emitting scintillating fibers, Journal of Instrumentation 17 (2022)*. DOI: 10.1088/1748-0221/17/12/P12020.

[40] M. Moszyński and B. Bengtson. *Status of timing with plastic scintillation detectors, Nucl. Instr. Meth. 158 (1979)*. DOI: https://doi.org/10.1016/S0029-554X(79)90170-8.

[41] B. Bengtson and M. Moszyński. *Timing properties of scintillation counters, Nucl. Instr. Meth. 81 (1970)*. DOI: https://doi.org/10.1016/0029-554X(70)90617-8.

[42] Kuraray Co. Ltd. URL: http://kuraraypsf.jp/index.html.

[43] Saint-Gobain Crystals. URL: https://www.crystals.saint-gobain.com/products/scintillating-fiber.

[44] A. Bravar, A. Buonaura, S. Corrodi, A. Damyanova, Y. Demets, L. Gerritzen, C. Grab, C. Martin Perez, and A. Papa. *Development of the scintillating fiber timing detector for the Mu3e experiment, Nucl. Instr. Meth. A 1058 (2024)*. DOI: https://doi.org/10.1016/j.nima.2023.168766.

[45] F. Corsi, A. Dragone, C. Marzocca, A. Del Guerra, P. Delizia, N. Dinu, C. Piemonte, M. Boscardin, and G.F. Dalla Betta. *Modelling a silicon photomultiplier (SiPM) as a signal source for optimum front-end design, Nucl. Instr. Meth. A 572 (2007)*. DOI: https://doi.org/10.1016/j.nima.2006.10.219.

[46] F. Corsi et al. *Electrical Characterization of Silicon Photo-Multiplier Detectors for Optimal Front-End Design, (2006)*. DOI: 10.1109/NSSMIC.2006.356076.

[47] S. M. Sze and K. K. Ng. *Physics of Semiconductor Devices, John Wiley & Sons Inc. (2006)*.

[48] First Sensors. *Introduction to silicon photomultipliers (SiPMs)*. Tech. rep. First Sensors, 2019. URL: https://www.first-sensor.com/cms/upload/appnotes/AN_SiPM_Introduction_E.pdf.

[49] Slawomir Piatek. *What is an SiPM and how does it work?, Hamamatsu Corporation (2016)*. URL: https://hub.hamamatsu.com/us/en/technical-notes/mppc-sipms/what-is-an-SiPM-and-how-does-it-work.html.

[50] K. Sato A. Ghassemi and K. Kobayashi. *Introduction to silicon photomultipliers (SiPMs)*. 2018. URL: https://hub.hamamatsu.com/content/dam/hamamatsu-photonics/sites/static/hc/resources/TN0014/mppc_kapd9005e.pdf.

[51] C. Betancourt, A. Datwyler, P. Owen, A. Puig, and N. Serra. *SiPM single photon time resolution measured via bi-luminescence, Nucl. Instr. Meth. A 958 (2020)*. DOI: https://doi.org/10.1016/j.nima.2019.162851.

[52] Slawomir Piatek. *How does temperature affect the performance of an SiPM?, Hamamatsu Corporation (2017)*. URL: https://hub.hamamatsu.com/us/en/technical-notes/mppc-sipms/how-does-temperature-affect-the-performance-of-an-SiPM.html.

[53] Hamamatsu Photonics K.K. *MPPC (multi-pixel photon counter), S13360 series, Hamamatsu Photonics K.K. (2017)*. URL: https://www.hamamatsu.com/content/dam/hamamatsu-photonics/sites/documents/99_SALES_LIBRARY/ssd/s13360_series_kapd1052e.pdf.

[54] Hamamatsu Photonics K.K. *MPPC (multi-pixel photon counter) array, S13552 series*. URL: https://www.hamamatsu.com/content/dam/hamamatsu-photonics/sites/documents/99_SALES_LIBRARY/ssd/s13552_kapd1083e.pdf.

[55] LHCb Collaboration. *LHCb Track er Upgrade Technical Design Report, CERN-LHCC-2014-001, LHCB-TDR-015 (2014)*.

[56] Axel Kevin Kuonen, G. Haefeli, Maria Elena Stramaglia, and Olivier Göran Girard. *Characterisation of the Hamamatsu MPPC multichannel array for LHCb SciFi Tracker v . 12, CERN (2015)*. 2015. URL: https://api.semanticscholar.org/CorpusID:119074500.

[57] S. Ritt, Roberto Dinapoli, and Ueli Hartmann. *Application of the DRS chip for fast waveform digitizing, Nucl. Instr. Meth. A 623 (2010)*. DOI: https://doi.org/10.1016/j.nima.2010.03.045.

[58] S. Ritt. *DRS evaluation board*. URL: https://www.psi.ch/fr/drs/evaluation-board.

[59] Antoaneta Damyanova. "*Development of the Scintillating Fiber detector for timing measurements in the Mu3e experiment*, University of Geneva (2019)." Doctoral Thesis. DOI: 10.13097/archive-ouverte/unige:125541.

[60] Intel. Cyclone V Device Overview. URL: https://www.intel.com/content/www/us/en/products/details/fpga/cyclone/v/docs.html.

[61] PSI beamline. URL: https://www.psi.ch/en/sbl/pim1-beamline.

[62] R. Gredig. *Scintillating Fiber Detector for the Mu3e Experiment, University of Zurich (2016)*.

[63] F. James. *Statistical Methods in Experimental Physics*. World Scientific, 2006.

[64] Lukas Gerritzen. *The Mu3e Scintillating Fibre Detector: Light Attenuation, Radiation Damage, and Data Acquisition*. 2022. DOI: 10.3929/ethz-b-000596779.

[65] Tiancheng Zhong. *Irradiation studies for the Mu3e Tile Detector*. 2022. DOI: 10.11588/heidok.00033605.

[66] Peter Huber Kältemaschinenbau SE. *Huber Unistat 425w datasheet*. URL: https://www.huber-online.com/en/products/dynamic-temperature-control-systems/unistats-down-to-45c/unistat-425w-1.

[67] H. Chen et al. *A dedicated readout ASIC for Time-of-Flight Positron Emission Tomography using Silicon Photomultiplier (SiPM), Nucl. Instr. Meth. A 695 (2012)*. DOI: 10.1109/NSSMIC.2014.7431045.

[68] H. Chen. *A Silicon Photomultiplier Readout ASIC for the Mu3e Experiment, University of Heidelberg (2014)*.

[69] W. Shen. *Development of Digh Performance Readout Asics for Silicon Photomultipliers (SiPMs), University of Heidelberg (2012)*. DOI: 10.11588/heidok.00014210.

[70] Valentin Henkys, Bertil Schmidt, and Niklaus Berger. *Online Event Selection for Mu3e using GPUs, 2022 21st International Symposium on Parallel and Distributed Computing (ISPDC)*. DOI: 10.1109/ispdc55340.2022.00012.

[71] Heiko Augustin et al. *The Mu3e Data Acquisition, IEEE Transactions on Nuclear Science 68 (2021)*. 2011. DOI: 10.1109/tns.2021.3084060.

[72] P. Amaudruz S. Ritt. *Maximum Integration Data Acquisition System*. 2001. URL: https://www.psi.ch/fr/lin-no-computing/midas.